Anisotropy and Interface structure in magnetic multilayers

Rozatian, Amir Sayid Hassan

Rozatian, Amir Sayid Hassan (2004) *Anisotropy and Interface structure in magnetic multilayers*, Durham theses, Durham University. Available at Durham E-Theses Online: http://etheses.dur.ac.uk/2825/

Anisotropy and Interface Structure in Magnetic Multilayers

by

Amir Sayid Hassan Rozatian

A thesis submitted in partial fulfilment of the
requirements for the degree of Doctor of Philosophy

Department of Physics
University of Durham
2004

TO MY LATE MOTHER

Abstract

It is believed that the interfacial structure can significantly affect the magnetic properties of magnetic multilayer thin films. X-ray scattering techniques provide a powerful method with which to study the bulk and interface morphology in these systems, and are therefore crucial in developing an understanding of the dominant factors influencing the magnitude of the perpendicular magnetic anisotropy (PMA).

The inter-relation between magnetic and structural properties of a series of magnetic multilayer thin films is investigated. Magnetometry measurements on a series of Fe/Au multilayers showed that some samples exhibited in-plane magnetization. X-ray data and simulations showed that the interface roughness was high in these samples. However, the formation and propagation of uncorrelated roughness followed a systematic trend for surface growth. On the other hand, x-ray data and simulations for a single 100-bilayer sample showed that the interfaces are much better defined with significantly lower roughness. This was the only sample to show perpendicular anisotropy supposing the suggestion that the absence of PMA in all other samples is associated with high interface roughness.

Magnetometry measurements of the PMA in Co/Pt multilayers show an increase in effective anisotropy at about 15 bilayers. X-ray data showed that the roughness of the interfaces was correlated in all samples and that the interfaces were sharp with no detectable interdiffusion. No systematic trend in roughness or crystallographic texture is detected with increasing bilayer repeat.

X-ray measurements on four series of Co/Pd multilayers show interface roughness independent of bilayer repeat number. For Co/Pt, the in-plane correlation length was independent of bilayer number while for Co/Pd and Fe/Au it increased. A saturation of the in-plane correlation length for the Au/Fe system where island growth of the Au occurs was observed. The out-of-plane correlation length increased with bilayer repeat for Co/Pt and Co/Pd. The interfaces in samples with higher PMA had a fractal parameter close to unity.

Acknowledgements

I would like to take this opportunity to thank all of the people without whom the past few years would not have been possible and would certainly not have been as enjoyable. If I miss anyone, out in this list of acknowledgments, my apologies.

Firstly, my deepest thanks to my supervisor, Prof. B.K. Tanner for his continual guidance, encouragement and enthusiasm throughout the course of my studies and for the provision of such excellent facilities and support within the department.

Thanks are also expressed to the University of Isfahan and the Ministry of Science, Research and Technology of Iran for the support. I would also like to express my thanks to my Iranian supervisor, Prof. J. Amighian.

I would like to thank Prof. P. J. Grundy, University of Salford, Prof. B. J. Hickey, and Dr. C. H. Marrows, University of Leeds, and their respective research groups for providing the samples.

It would not have been possible to obtain any of the data presented here had it not been for the dedication and assistance of the staff at the various Synchrotron sources. I would like to thank Dr. Chiu Tang at the Daresbury SRS, and the staff of BM16, and BM28, ESRF. I must also thank Bede Scientific Instruments Ltd and more specifically Dr. M. Wormington for providing such excellent simulation codes used to analyze the majority of the data in this thesis.

I would like to thank the many members of the department who have assisted in various ways during the past few years. Thanks go to Pauline Russell, Mike Lee and Vicki Dobby in the audio-visual department and to the secretarial staff, Penny Carse and Joanne Devlin and Norma Twomey. Also, thanks to Wayne Dobby and John Dobson.

I have been lucky enough to have had the opportunity to work with and alongside numerous people over the last few years, all of whom have contributed to making the whole experience rewarding and above all else enjoyable. My thanks to: Prof. Peter Hatton, Dr. Ian Terry, Dr. David Stockdale, Dr. Thomas Hase, Dr. Brian Fulthorpe, Dr. Andrea Li-Bassi, Dr. Luo Guangming, Dr. Sujit Halder, Dr. Gwyn Ashcroft, Dr. Dan Read, Dr. Mohammad Ghazi, Dr. James Buchanan, Dr. Neil Parkinson, Sean Giblin, Kathryn Kelly, Alex Pym, and Amit Chakraborty.

Finally, I would like to express my deepest thanks to my wife, Negin who has encouraged me over the years, without which this would not have been possible. I would also like to express my thanks to my father and my little daughter, Neshat.

Publications

The following publications relate to work presented in this thesis:

1. *The progression of interface structure through sputtered Co/Cu and Co/Pt multilayer films.*

B. D. Fulthorpe, D. E. Joyce, T. P. A. Hase, A. S. H. Rozatian, B. K. Tanner, P. J. Grundy.

Journal of Physics: Condensed Matter, Vol. 11, No. 43 (1999) 8477-8488.

2. *X-ray Probes of Magnetic Multilayer Structure.*

B. K. Tanner, T. P. A. Hase, B. D. Fulthorpe, J. Clarke, G. M. Luo, S. K. Halder, A. S. H. Rozatian, S. B. Wilkins.

Material Research Society Symposium Proceedings, Vol. 615 (2000) G 2.1.1-G2.1.12.

3. *Anisotropy and interface structure in sputtered Co/Pt multilayers on Si.*

A. S. H. Rozatian, B. D. Fulthorpe, T. P. A. Hase, D. E. Read, G. Ashcroft, D. E. Joyce, P. J. Grundy, J. Amighian, B. K. Tanner.

Journal of Magnetism and Magnetic Materials, Vol. 256, No. 1-3 (2003) 365-372.

Declaration

I hereby declare that the work contained in this thesis is my own and has not been submitted previously for any other degree. The work of collaborators is acknowledged at the appropriate point. In particular I would like to declare that the AGFM data presented in chapters 7 were performed by G. Ashcroft, University of Durham.

The samples used in this study were obtained from the following sources:

Chapter 6:	P. A. Ryan, D. T. Dekadjevi, University of Leeds.
Chapter 7:	D. E. Joyce, University of Salford.
Chapter 8:	C. H. Marrows, University of Leeds.

CONTENTS

Chapter 3 Magnetic Anisotropy in Thin Films 22

Chapter 4 Grazing incidence x-ray reflectometry 46

Appendices

Chapter 1

Aim and Outline of Thesis

1.1 Aim

Perpendicular recording media will be required for future high-density magnetic and magneto-optical recording and have therefore been studied extensively. Ferromagnetic multilayers consisting of cobalt based multilayers or alloys are seen as promising candidates for perpendicular magnetic recording media needed to overcome thermal instability at higher recording densities. Research efforts are directed at enhancing the PMA (perpendicular magnetic anisotropy) and the coercivity of hard magnetic layers, fabricating soft magnetic underlayers of high moment and creating special seed layers to control the segregation of the grains. It has recently been announced that, about two decades after the initial observation of PMA in layered systems, scientists have broken new ground in the field of magnetic data storage by demonstrating areal densities of over 100 GB/in^2 using perpendicular recording technology (Seagate Technology, SCOTTS VALLEY, Calif., 12 November 2002). Since the discovery of PMA in Co/Pd multilayers in 1985, extensive studies have been made to understand the origin of the out-of-plane magnetisation. Although the switch to perpendicular anisotropy as the magnetic layer thickness decreases is well known, the anisotropy being generally accepted as an interface phenomenon, the mechanism of this technologically important effect is not clear.

The aim of the work presented in this study was to utilise x-ray scattering techniques to characterise the structural factors that control the magnitude of the PMA in magnetic multilayers. X-ray scattering techniques provide a powerful, non-destructive, tool with which to measure the intrinsically small, Angstrom length scale structures within multilayers and, unlike scanning probe techniques, are also sensitive to the many buried interfaces within these systems. Crucial factors such as layer thickness, interface morphology and crystalline texture can be determined to a high degree of accuracy, through specular and diffuse x-ray reflectivity measurements combined with x-ray diffraction techniques. Magnetometry techniques (Torque Magnetometry, VSM, and AGFM) were used to determine the effective magnetic anisotropy of the samples.

1.2 Samples

The work presented in this study was undertaken in collaboration with research groups at the Universities of Leeds and Salford. The Fe/Au samples discussed in chapter 6 were grown, using Molecular Beam Epitaxy (MBE), by P.A. Ryan and D.T. Dekadjevi at Leeds. The Co/Pt multilayers discussed in chapters 7 were grown, by magnetron sputtering, by D.E. Joyce at Salford. The Co/Pd multilayers discussed in chapters 8 were grown, by magnetron sputtering, by C. H. Marrows at Leeds.

1.3 Outline of Thesis

Following the discussion of the aims and structure of the work presented here, chapter 2 introduces the reader to an overview of magnetic multilayer structures and the processes behind the perpendicular magnetic anisotropy effect. The different preparation methods used to produce the samples will also be reviewed.

Chapter 3 moves on to the aspects of the research performed on the magnetic anisotropy in magnetic multilayer thin films. Theoretical predictions of PMA are addressed in this chapter.

In chapter 4 the theoretical treatment of the interaction of x-rays with matter under grazing incidence conditions is reviewed. A description of specular scatter, modified to account for roughness and grading at an interface is developed from the surface and interface behaviour of x-rays via the Fresnel equations. A treatment of diffusely scattered radiation is presented through the introduction of the Born Wave and Distorted Born Wave approximations, with a description of how the fractal nature of interfaces and the correlation between them in a multilayer can be represented.

Chapter 5 presents a discussion of the experimental aspects of x-ray scattering relating to the experimental set-up and data collection methodology of the synchrotron sources at which all of the data in this study was collected.

The first results are presented in chapter 6. A series of (100) oriented Fe/Au multilayers grown, by MBE, on MgO substrates have been studied. Specular and diffuse x-ray reflectivity data and simulations, in addition to torque magnetometry and VSM (vibrating sample magnetometry) data, are presented. A relation between PMA and interfaces in Fe/Au multilayers is suggested.

Chapter 7 is concerned with the propagation of interface structure as a function of bilayer number in a series of sputter deposited Co/Pt multilayers. Specular, transverse diffuse and longitudinal diffuse x-ray scattering measurements have been used in order to follow the growth conformality of the interfaces within these systems as the number of bilayers increased. Strong evidence is found for the existence of a columnar growth mode in Co/Pt, not present in Fe/Au samples. Observations regarding the propagation of the interfaces are then discussed in relation to the magnetic properties of the Co/Pt samples. Although the magnetic measurements confirmed enhanced perpendicular anisotropy when the bilayer repeat number is about 15, the only difference observed in the interface structure was a change in the dimensionality of the roughness of the interfaces, seen in the change in fractal parameter.

Chapter 8 is concerned with the study of the relation between PMA and the interface structure in four series of sputtered Co/Pd multilayers. The evolution of interface structure as the number of bilayers increases in these samples is examined. Grazing incidence reflectivity and out-of-plane scattering measurements have been performed in an attempt to explain the exponential change in the correlation length observed in Co/Pd multilayers. The chapter then concludes with the first experimental observation of an exponential variation in the in-plane correlation length as a function of bilayer number in Co/Pd multilayers.

Finally, a summary and analysis of the important aspects of the work in this study is presented in chapter 9, along with a discussion of potential new and continued avenues of research in this field.

In order to avoid some chapters being extremely long, seven appendices are added to this thesis; some of them contain the detailed specular and diffuse scatter data and simulations.

Chapter 2

Introduction

“An insight into magnetic multilayers and superlattices”

2.1 Background

Much of modern condensed matter materials physics, basic and applied research relies on the development of new materials in unusual configurations. Magnetic materials in particular provide the underpinning science for a number of new technologies. Basic research in magnetism has been considerably revitalized recently by the preparation and discovery of novel magnetic materials as well as the exploitation of known materials in unusual geometries. The interest in artificially layered systems in particular, increased tremendously after the discovery of perpendicular magnetic anisotropy (PMA) [1] and giant magneto-resistance (GMR) [2]. Metallic superlattices and multilayers have been studied for almost 70 years [3]. However, it was not to have significant impact on magnetism research until the 1980s. Advances in vacuum technologies in the 1970s resulted in major discoveries in magnetic multilayers in 1980s, and we have witnessed an explosion of the number of publications in magnetic multilayers in the 1990s. Therefore, it is impossible to review properly the vast available literature [4-66] in this short chapter.

The term superlattice was coined originally to describe multilayers in which long range (larger than one bilayer thickness) structural coherence exists along the growth direction, but the two terms have been frequently used interchangeably [65]. It is this peculiar geometry that can modify their physical properties. Therefore, the amount of structural disorder which can be tolerated depends on the length scale which governs the physical properties being investigated. In general, the physical phenomena in superlattices can be classified as single film, interface, proximity, coupling and superlattice effects in increasing order of sample complexity. Single film effects are due to the restriction in dimensionallity. Proximity effects occur due to the contact between two unlike materials. Magnetic coupling across normal materials has been extensively investigated [2]. The phenomena described above require at most three layers, i.e., a superlattice structure is not needed. It is however easier to observe these phenomena in superlattices because they are enhanced by the increased number of layers or because most interfaces are well protected from surface contamination. For example, perpendicular magnetic anisotropy, where surface anisotropy overcomes the stronger shape anisotropy (this will be reviewed in chapter 3), or GMR, a consequence of antiferromagnetic coupling across non-magnetic spacer layer, were first observed in superlattices. Magnetic superlattices and multilayers encompass almost every combination of transition metals, and to a lesser extent, rare earth elements.

The aim of this chapter is to give the reader an overview of magnetic multilayer structures and the processes behind the perpendicular magnetic anisotropy effect. The sample preparation methods will also be reviewed.

2.2 Magnetic multilayer systems

In this section the nature of the roughness in a multilayered structure will be considered. When one or more layers are deposited onto a substrate, the effects of out of plane correlations must be considered. Figure 2.1 shows the possible out of plane correlations of the roughness that can exist in a multilayered sample. In the schematic diagram shown in figure 2.1(a) there is no interface roughness. Figure 2.1(b) shows what is termed totally correlated or conformal roughness. In this case, the roughness profile of each layer is replicated exactly from all lower layers-including the substrate. Figure 2.1(c) shows totally uncorrelated roughness. In this instance, the roughness of each layer is statistically independent of the roughness on other layers. Figure 2.1(d) represents a mixture of the two kinds of roughness, i.e. partially correlated roughness, and is the most commonly observed kind of roughness. In-plane correlation is described by an in-plane correlation function containing the in-plane correlation length, ξ, the *rms* roughness, σ, and the Hurst fractal parameter, h (with values from 0 to 1).

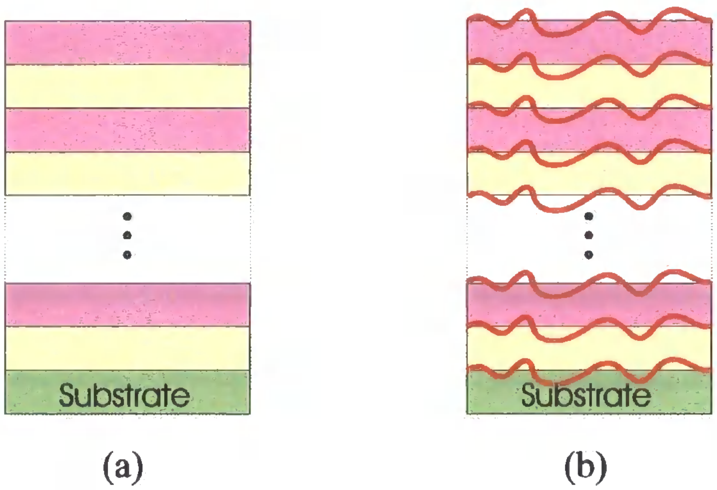

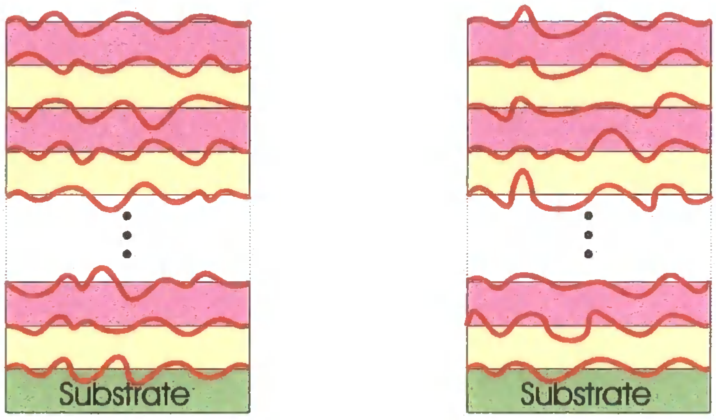

(c) (d)

Figure 2.1 Roughness in a multilayer system: **(a)** Ideally flat interfaces, **(b)** Totally correlated roughness, **(c)** Totally uncorrelated roughness, and **(d)** Partially correlated.

2.3 Preparation and structural properties of multilayers

The two main methods of multilayer growth, corresponding to the two methods by which samples discussed in this study were grown, are sputtering and molecular beam epitaxy (MBE). These methods will be reviewed briefly in this section. More details can be found in ref. [67].

2.3.1 Growth by sputtering

Sputtering is a very commonly used deposition technique. Electrically accelerated high energy ions (usually from an inert gas) bombard a target material, dislodging and ejecting material which then condenses onto a substrate to form a thin layer. By alternating sputtering of more than one target, a multilayer may be created. Alloys are sputtered from composite targets or alloy targets, however for each alloy composition a separate target must be used. Because of the high ion energies (typically several tens eV), almost all metals and metallic alloys can be readily sputtered at a relatively high deposition rate (10Å / sec). The large thickness homogeneity over several centimeters makes sputtering also a flexible, frequently employed, industrial fabrication technique.

Sputter process parameters such as sputter pressure, sputtering energy and inert gas element can be varied to modify the structure. These parameters have a major influence on the magnetic properties of the multilayers.

It is possible that the sputtering process can reduce the roughness of a surface due to erosion effects, especially if the sputtered ions are incident at oblique angles. Roughness features with an enhanced profile on the surface are preferentially removed leading to a general smoothing of the surface. However, it is also possible to roughen an already smooth surface due to fluctuations in the incident flux and this can also reduce the sputtering yield. In general, sputter deposited layers tend to have high values of fractal dimension (higher than 0.5) [68, 69].

2.3.2 Molecular beam epitaxy

In molecular beam epitaxy and other energy techniques, the deposited material is created by thermal evaporation of material from a heated source. This evaporated beam then condenses on the substrate. By using a variety of effusion cells or electron-beam evaporation sources, almost all metals can be evaporated, although the deposition rate for high melting point metals may be rather low. In general, MBE produces multilayers with atomically sharp interfaces, coherent epitaxial growth and low contamination, but with roughness on a scale which is large compared to atomic dimensions. MBE has shown to be more suited to studies relating structural and magnetic properties to details of the growth process.

The principle advantage of MBE over sputtering is that it allows materials to be deposited in such a way that retains high levels of atomic registration between adjacent layers. This routinely allows the growth of very thin layers of high epitaxial quality with inherently smooth interfaces [68, 69]. When depositing a selected material onto a substrate a high degree of lattice match is required for successful epitaxial deposition.

2.3.3 Sputtering versus molecular beam epitaxy

As stated before, Sputtering (DC or RF) and molecular beam epitaxy are the main techniques used to fabricate metallic superlattices. Growth by both MBE and sputtering followed by detailed characterization can yield complementary information.

Ultrahigh vacuum (UHV) MBE uses atomic beams to deposit epitaxial films on a substrate at typically elevated temperature. Low growth rates (submonolayer per second) combined with surface migration enable layer-by-layer growth to be achieved. Film growth, far from thermodynamic equilibrium, is governed mainly by the surface kinetics occurring when the impinging atoms encounter the substrate. Sputtering permits higher throughput, which is easy to rate-control and allows tunability of the energy distribution of particles arriving at the substrate. The presence of sputtering gas generally excludes the use of *in situ* structural characterization techniques and is more susceptible to contamination. However, it is fair to state that the structural and physical properties of metallic superlattices prepared by both techniques are comparable, if the same care is taken in the growth process. Probably the reason for this is that, contrary to semiconductors, most properties of metals are relatively insensitive to small amounts of contamination. Metallic superlattices have been grown from a large variety of combinations of metallic elements, without consideration for their crystallographic structures. On one hand, elements that are closely lattice matched and have the same crystal structure, generally have equilibrium thermodynamic phase diagrams forming continuous sets of solid solutions. Therefore, they are driven thermodynamically towards interdiffusion, although thin film growth is kinetically limited. On the other hand, as known for many years, lattice matching is not a necessary condition for epitaxy. Therefore, if the superlattice components form no alloys, it may be expected that they will be more segregated. Another important issue is that the growth of a superlattice is somewhat different from that of a bilayer. The structure is affected by the momentary substrate and the temperature at which a layer is growing, i.e., different interfaces and layers have different growth conditions. At elevated growth temperatures, self annealing and interdiffusion may occur in the buried layers. Therefore, it is important to characterize the structure once the whole superlattice is grown. For relatively thick multilayers, detailed knowledge of the interface structure is not important because physical properties are not significantly affected by interface quality. On the other hand, multilayers with constituents approaching single monolayer (ML) level are routinely fabricated these days. In such cases, structural characterization is crucial. Non-destructive diffraction techniques, such as x-ray reflectivity (which will be discussed in chapters 4 and 5), are commonly used to analyze multilayered structure. Powerful tuneable photon sources are capable of element specific characterization and polarized photons or neutrons are available to probe the magnetic structure. Since quantitative diffraction studies require modelling and a priori knowledge of the probed length scale, complementary techniques, such as cross-sectional transmission electron (TEM) or scanning probe microscopies (SPM) are helpful. The major types of structural imperfection present in superlattices are interfacial roughness, interdiffusion, imperfect crystallinity, and crystalline orientation. The distinction between interdiffusion and roughness is of great importance. At short length scales, smaller than the lateral coherence length of a particular probe, an interface with roughness ‘looks' like a homogeneous interface with an average scattering function given by the relative proportion of the constituents. In a naive interpretation, interdiffusion affects only the peak intensities, while layer thickness fluctuations broaden the peaks. Rocking curve widths are affected by the angular distribution of crystallites and crystalline orientation, while variations in interatomic spacing change the peak position. In realistic situations, however, there is no such clear distinction between the particular type of disorder and its effect on a particular feature; all diffraction features are affected to some degree. Therefore, quantitative analysis of diffraction data requires comparison to simulated diffraction patterns with detailed modelling of defect structures. Superlattices are routinely checked using laboratory x-ray diffractometers, while synchrotron sources provide tunability, polarization and increased intensity, to improve diffraction quality or provide diffuse scattering data (which will be discussed in chapter 5). Conventional diffraction (specular) and diffuse scattering (off specular) data contains complementary information. The specular peaks contain information on defect structures along the growth direction, while the lateral length scale being probed is rather uncertain, whereas diffuse scattering data shed light on lateral correlation lengths. Quantitative disorder parameters can be extracted from the data by detailed refinement techniques. There are exploratory reports on the use of ion scattering to investigate interface roughness by low and medium energy ion scattering. Powerful tunable photon sources become more important in spectroscopic areas to probe the superlattice electronic structure, i.e. in x-ray fluorescence spectroscopy (XFS), x-ray emission spectroscopy (XES), x-ray absorption spectroscopy (XAS), diffraction anomalous fine structure spectroscopy (DAFS), x-ray resonance magnetic scattering (XRMS) and near edge x-ray absorption fine structure (NEXAFS). It can be noted that the magnetic profile could be different from the chemical profile of the superlattice and polarized neutron reflectivity (PNR) and soft x-ray resonant scattering techniques have been applied to the question.

2.4 Physical properties of magnetic multilayers

Magnetic superlattices composed of ferromagnetic/non-magnetic (F/N) materials have been studied for the effects of dimensionality, magnetic anisotropy associated with the F/N interface, magnetic coupling through the non-magnetic spacer layer, and to a much lesser extent, for superlattice electronic or spin structure effects. Ferromagnetic/ferromagnetic (F/F) or rare-earth superlattices have attracted much less attention. In this section, PMA, one of the most important physical properties of magnetic multilayers will be reviewed.

Metallic multilayers composed of alternating layers of a ferromagnetic transition metal (FT = Fe, Co, Ni) and noble metals (NM = Cu, Ag, Pd, Pt, Au) exhibit perpendicular magnetic anisotropy (PMA) and maybe useful as magneto-optic recording media. In these multilayers, the easy direction of interfacial magnetic anisotropy may be perpendicular to the film plane and is controlled by the nature of interface. This PMA is an example of an interface effect, which does not require multilayer structure but it is commonly investigated for convenience in multilayers. Comparing the observed interface anisotropies (which will be discussed in chapter 3), one notes that for Co and Fe these are often positive, i.e. favouring a perpendicular easy direction, whereas for the Ni-based multilayers they are usually negative.

2.4.1 The Co-based multilayers

Co-based thin film and multilayer systems are not only interesting from a fundamental basic research point of view, but are also candidates as components in high density magneto-optical (MO) storage media. This is because of the particular magnetic properties these systems exhibit.

Recent experiments have revealed that strong perpendicular magnetic anisotropy occurs due to the existence of the interfaces in X / {(Co/X)*N} magnetic multilayers, when X denotes nonmagnetic layers (Pt, Pd, Au, Cr) and N is the number of bilayers [1, 70-73]. By contrast, for X = Cu, Ag, these multilayers showed in-plane easy magnetization. The perpendicular magnetic anisotropy observed for very thin Co layers in magnetic multilayers is necessary for MO recording.

Much attention has been devoted to understanding the origin of the observed perpendicular anisotropy [74-76]. It has been shown that the magnetic properties depend on the thickness of the Co layers [77, 78] as well as on the detailed structural properties of the Co film. The crystalline orientation [79], the amount of alloying between magnetic and nonmagnetic layers [80] and the exact thickness of the Co layers (possibly related to the fcc-to-hcp transition) [81, 82] have been observed to influence the magnetic properties.

Co/Pt multilayers attracted much attention because of the simultaneous large magneto-optical Kerr rotation and PMA which has been interpreted using theoretical band structure calculations [83]. In fact, the structure and morphology of thin Co deposits on Pt(111) has been studied extensively in the past [35, 55, 84-96]. In the studies of Co/Pt sputtered multilayers, grown on Si [60] and on glass [90, 97] high values of effective anisotropy between 10 and 18 bilayers were observed (Figure 2.2). The authors suggested a possible relationship between the high value of effective anisotropy and the loss of conformal roughness for $N \geq 15$ (N, number of bilayers).

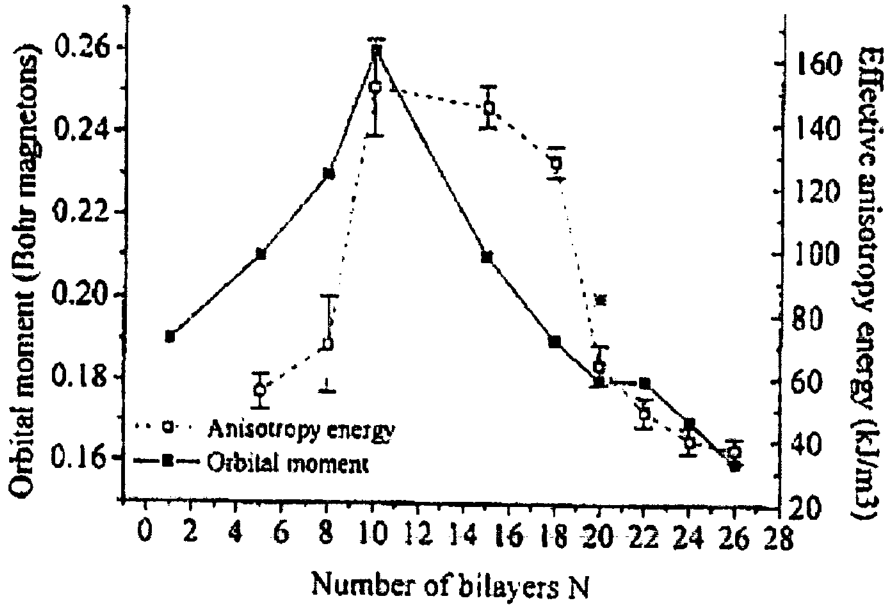

Figure 2.2 Effective anisotropy for Co/Pt multilayers as a function of N, taken from Ref. [60].

Moreover, the use of Pd as the nonmagnetic element is particularly interesting. Although Pd is non-magnetic, it is well known to possess unusually high susceptibility. Ferromagnetic impurities or proximity to ferromagnetic materials can produce a magnetic moment in otherwise nonmagnetic Pd. Co/Pd, the first system showing PMA [1], is still investigated [98-101] and since the Pd polarization is sensitive to structural defects, considerable emphasis is made on structural characterization [52, 102-105].

On the other hand, the discovery of PMA in Co/Ni is intriguing, as both the multilayer components are magnetic [106].

2.4.2 The Fe-based multilayers

Since the discovery of giant magnetoresistance (GMR) in ferromagnetic multilayers [2], Fe-based thin film multilayers have attracted a great deal of attention. Interface mixing in Fe/Ni multilayers [107], GMR [2, 108-112], and the effect of interface roughness on the observed GMR in Fe/Cr superlattices have also been studied extensively [113-120]. PMA has also been observed in Fe/Au multilayers [46, 121, 122] and will be discussed in chapter 6.

2.5 Conclusions

Disorder is a key parameter in multilayers and superlattices. Although striving for even higher perfection is a commendable effort, it is safe to state that absolute perfection will not be achieved in the near future. Therefore, developing theories and experimental situations which probe the effect of disorder at varying length scale is of crucial importance. The question of how interfacial effects manifest themselves in the measurement of the physical properties of superlattices remains an interesting one.

REFERENCES

[1] P. F. Carcia, A. D. Meinhaldt, and A. Suna, *Appl. Phys. Lett.*, **47 (2)**, 178-180 (1985).

[2] M. N. Baibich, J. M. Broto, A. Fert, F. N. Vandau, F. Petroff, P. Eitenne, G. Creuzet, A. Friederich, and J. Chazelas, *Phys. Rev. Lett.*, **61 (21)**, 2472-2475 (1988).

[3] W. M. DuMound, *Phys. Rev.*, **48** , 703 (1935).

[4] W. R. Bennett, C. D. England, D. C. Person, and C. M. Falco, *J. Appl. Phys.*, **69 (8)**, 4384-4390 (1991).

[5] G. A. Bertero and R. Sinclair, *Appl. Phys. Lett.*, **64 (24)**, 3337-3339 (1994).

[6] G. A. Bertero and R. Sinclair, *IEEE Trans. Magn.*, **31 (6)**, 3337-3342 (1995).

[7] S. S. Bogomolov, R. J. Highmore, W. C. Shih, A. L. Greer, R. E. Somekh, and J. E. Evetts, *J. Appl. Phys.*, **73 (10)**, 6841-6843 (1993).

[8] M. Bohm and U. Krey, *J. Magn. Magn. Mater.*, **192 (1)**, 27-34 (1999).

[9] C. N. Borca and P. A. Dowben, *J. Magn. Magn. Mater.*, **199** , 258-260 (1999).

[10] H. Brandle, D. Weller, J. C. Scott, S. S. P. Parkin, and C. J. Lin, *IEEE Trans. Magn.*, **28 (5)**, 2967-2969 (1992).

[11] E. Bruno and B. L. Gyorffy, *Appl. Surf. Sci.*, **75** , 320-325 (1994).

[12] P. F. Carcia, Z. G. Li, M. Reilly, and W. B. Zeper, *J. Appl. Phys.*, **73 (10)**, 6424-6426 (1993).

[13] P. F. Carcia, Z. G. Li, and W. B. Zeper, *J. Magn. Magn. Mater.*, **121 (1-3)**, 452-460 (1993).

[14] P. F. Carcia, M. Reilly, Z. G. Li, and H. W. Vankesteren, *IEEE Trans. Magn.*, **30 (6)**, 4395-4397 (1994).

[15] P. F. Carcia, Z. G. Li, and H. W. Vankesteren, *Thin Solid Films*, **246 (1-2)**, 126-130 (1994).

[16] P. F. Carcia, Z. G. Li, H. W. Vankesteren, and M. T. Johnson, *J. Magn. Magn. Mater.*, **145 (1-2)**, 231-238 (1995).

[17] P. F. Carcia, D. Coulman, R. S. McLean, and M. Reilly, *J. Magn. Magn. Mater.*, **164 (3)**, 411-419 (1996).

[18] N. H. Cho, K. M. Krishnan, C. A. Lucas, and R. F. C. Farrow, *J. Appl. Phys.*, **72 (12)**, 5799-5807 (1992).

[19] N. H. Cho, K. M. Krishnan, C. H. Lee, and R. F. C. Farrow, *Appl. Phys. Lett.*, **60 (19)**, 2371-2373 (1992).

[20] S. B. Choe and S. C. Shin, *J. Appl. Phys.*, **81 (8)**, 5743-5745 (1997).

[21] S. B. Choe and S. C. Shin, *Phys. Rev. B*, **57 (2)**, 1085-1089 (1998).

[22] S. B. Choe and S. C. Shin, *Phys. Rev. Lett.*, **86 (3)**, 532-535 (2001).

[23] P. Dehaan, Q. Meng, T. Katayama, and J. C. Lodder, *J. Magn. Magn. Mater.*, **113 (1-3)**, 29-35 (1992).

[24] F. J. A. Denbroeder, W. Hoving, and P. J. H. Bloemen, *J. Magn. Magn. Mater.*, **93** , 562-570 (1991).

[25] A. Dinia, S. Zoll, and K. Ounadjela, *J. Magn. Magn. Mater.*, **148 (1-2)**, 327-328 (1995).

[26] B. N. Engel, C. D. England, R. Vanleeuwen, M. Nakada, and C. M. Falco, *J. Appl. Phys.*, **69 (8)**, 5643-5645 (1991).

[27] M. Enrech, R. Skomski, J. M. D. Coey, and J. G. Lunney, *J. Appl. Phys.*, **73 (10)**, 6421-6423 (1993).

[28] C. M. Falco and J. M. Slaughter, , **126 (1-3)**, 3-7 (1993).

[29] J. Ferre, C. Chappert, H. Bernas, J. P. Jamet, P. Meyer, O. Kaitasov, S. Lemerle, V. Mathet, F. Rousseaux, and H. Launois, *J. Magn. Magn. Mater.*, **199** , 191-193 (1999).

[30] C. F. J. Flipse, J. J. Devries, G. Vanderlaan, M. Surman, A. Partridge, and W. J. M. Dejonge, *J. Magn. Magn. Mater.*, **148 (1-2)**, 141-142 (1995).

[31] R. A. Fry, L. H. Bennett, E. Della Torre, R. D. Shull, W. F. Egelhoff, R. F. C. Farrow, and C. H. Lee, *J. Magn. Magn. Mater.*, **193 (1-3)**, 162-165 (1999).

[32] R. A. Fry, L. H. Bennett, E. Della Torre, and R. F. C. Farrow, *J. Appl. Phys.*, **87 (9)**, 5765-5767 (2000).

[33] B. D. Fulthorpe, P. A. Ryan, T. P. A. Hase, B. K. Tanner, and B. J. Hickey, *J. Phys. D-Appl. Phys.*, **34 (10A)**, A203-A207 (2001).

[34] J. Geshev, A. Morrone, and J. E. Schmidt, *J. Magn. Magn. Mater.*, **226** , 1711-1713 (2001).

[35] V. Georgescu, V. Mazur, and B. Pushcashu, *Mater. Sci. Eng. B-Solid State Mater. Adv. Technol.*, **68 (3)**, 131-137 (2000).

[36] S. J. Greaves, P. J. Grundy, and R. J. Pollard, *J. Magn. Magn. Mater.*, **121 (1-3)**, 532-535 (1993).

[37] S. J. Greaves, A. K. Petfordlong, Y. H. Kim, R. J. Pollard, P. J. Grundy, and J. P. Jakubovics, *J. Magn. Magn. Mater.*, **113 (1-3)**, 63-71 (1992).

[38] P. J. Grundy, *J. Alloy. Compd.*, **326 (1-2)**, 226-233 (2001).

[39] G. Guntherodt, B. Hillebrands, P. Krams, J. V. Harzer, F. Lauks, R. L. Stamps, W. Weber, D. Hartmann, D. A. Wesner, A. Rampe, U. A. Effner, H. P. Oepen, D. Weller, F. C. Farrow, B. N. Engel, and C. M. Falco, *Philos. Mag. B-Phys. Condens. Matter Stat. Mech. Electron. Opt. Magn. Prop.*, **70 (3)**, 767-772 (1994).

[40] S. A. Gusev, A. A. Fraerman, D. B. Rozenstein, and M. G. Teitelman, *Phys. Lett. A*, **198 (5-6)**, 437-440 (1995).

[41] S. Hashimoto, A. Maesaka, K. Fujimoto, and K. Bessho, *J. Magn. Magn. Mater.*, **121 (1-3)**, 471-478 (1993).

[42] P. He, Z. S. Shan, J. A. Woollam, and D. J. Sellmyer, *J. Appl. Phys.*, **73 (10)**, 5954-5956 (1993).

[43] R. T. Heap and S. J. Greaves, *J. Phys. D-Appl. Phys.*, **27 (7)**, 1343-1347 (1994).

[44] S. Honda, H. Tanimoto, J. Ago, M. Nawate, and T. Kusuda, *J. Appl. Phys.*, **70 (10)**, 6047-6049 (1991).

[45] S. Honda, Y. Tamura, T. Takeuchi, and M. Nawate, *IEEE Trans. Magn.*, **29 (6)**, 3364-3366 (1993).

[46] S. Honda, K. Koguma, M. Nawate, and I. Sakamoto, *J. Appl. Phys.*, **82 (9)**, 4428-4434 (1997).

[47] M. A. Howson, *Contemp. Phys.*, **35 (5)**, 347-359 (1994).

[48] M. A. Howson, B. J. Hickey, J. Garfield, J. Xu, P. A. Ryan, D. Greig, A. Yelon, and N. Wiser, *J. Phys.-Condes. Matter*, **11 (30)**, 5717-5722 (1999).

[49] Y. Jyoko, S. Kashiwabara, Y. Hayashi, and W. Schwarzacher, *Electrochem. Solid State Lett.*, **2 (2)**, 67-69 (1999).

[50] Y. Jyoko and W. Schwarzacher, *Electrochim. Acta*, **47 (1-2)**, 371-378 (2001).

[51] V. Kambersky, P. Dehaan, J. C. Lodder, J. Simsova, and R. Gemperle, *IEEE Trans. Magn.*, **29 (6)**, 3138-3140 (1993).

[52] S. K. Kim and S. C. Shin, *J. Appl. Phys.*, **89 (5)**, 3055-3057 (2001).

[53] B. M. Lairson, J. Perez, and C. Baldwin, *Appl. Phys. Lett.*, **64 (21)**, 2891-2893 (1994).

[54] Z. G. Li, P. F. Carcia, and Y. Cheng, *J. Appl. Phys.*, **73 (5)**, 2433-2437 (1993).

[55] C. J. Lin, G. L. Gorman, C. H. Lee, R. F. C. Farrow, E. E. Marinero, H. V. Do, H. Notarys, and C. J. Chien, *J. Magn. Magn. Mater.*, **93** , 194-206 (1991).

[56] T. Salditt, T. H. Metzger, J. Peisl, and X. Jiang, *J. Phys. III*, **4 (9)**, 1573-1580 (1994).

[57] T. Salditt, D. Lott, T. H. Metzger, J. Peisl, G. Vignaud, P. Hoghoj, O. Scharpf, P. Hinze, and R. Lauer, *Phys. Rev. B*, **54 (8)**, 5860-5872 (1996).

[58] T. Salditt, D. Lott, T. H. Metzger, J. Peisl, G. Vignaud, J. F. Legrand, G. Grubel, P. Hoghoi, and O. Scharpf, *Physica B*, **221 (1-4)**, 13-17 (1996).

[59] B. K. Tanner and J. M. Hudson, *IEEE Trans. Magn.*, **28 (5)**, 2736-2741 (1992).

[60] C. J. Tatnall, D. E. Joyce, P. J. Grundy, J. P. Schille, and G. van der Laan, *J. Magn. Magn. Mater.*, **177** , 1181-1182 (1998).

[61] W. B. Zeper, H. W. Vankesteren, and P. F. Carcia, *Adv. Mater.*, **3 (7-8)**, 397-399 (1991).

[62] B. Zhang, K. M. Krishnan, C. H. Lee, and R. F. C. Farrow, *J. Appl. Phys.*, **73 (10)**, 6198-6200 (1993).

[63] M. Zheng, Y. Xu, Z. H. Guo, and Y. J. Wang, *Chin. Phys. Lett.*, **13 (9)**, 711-713 (1996).

[64] L. M. Falicov, D. T. Pierce, S. D. Bader, R. Gronsky, K. B. Hathaway, H. J. Hopster, D. N. Lambeth, S. S. P. Parkin, G. Prinz, M. Salamon, I. K. Schuller, and R. H. Victora, *J. Mater. Res.*, **5 (6)**, 1299-1340 (1990).

[65] I. K. Schuller, *Solid State Commun.*, **92 (1-2)**, 141-147 (1994).

[66] M. T. Johnson, P. J. H. Bloemen, F. J. A. denBroeder, and J. J. deVries, *Rep. Prog. Phys.*, **59 (11)**, 1409-1458 (1996).

[67] C. H. Marrows, *Ph. D. Thesis,* University of Leeds (1997).

[68] *Fractal Concepts in Surface Growth*, A.-L. Barabasi and H. E. Stanley, Cambrige University Press (1995).

[69] *Fractals, scaling and growth far from equilibrium*, P. Meakin, Cambridge University Press (1998).

[70] W. B. Zeper, F. Greidanus, P. F. Carcia, and C. R. Fincher, *J. Appl. Phys.*, **65 (12)**, 4971-4975 (1989).

[71] N. W. E. McGee, M. T. Johnson, J. J. Devries, and J. A. Destegge, *J. Appl. Phys.*, **73 (7)**, 3418-3425 (1993).

[72] A. Murayama, K. Hyomi, J. Eickmann, and C. M. Falco, *Phys. Rev. B*, **58 (13)**, 8596-8604 (1998).

[73] T. Zeidler, F. Schreiber, and H. Zabel, *J. Appl. Phys.*, **79 (8)**, 4793-4795 (1996).

[74] F. J. A. den Broeder, D. Kuiper, A. P. Vandemosselaer, and W. Hoving, *Phys. Rev. Lett.*, **60 (26)**, 2769-2772 (1988).

[75] C. Chappert and P. Bruno, *J. Appl. Phys.*, **64 (10)**, 5736-5741 (1988).

[76] C. H. Lee, H. He, F. J. Lamelas, W. Vavra, C. Uher, and R. Clarke, *Phys. Rev. B*, **42 (1)**, 1066-1069 (1990).

[77] D. Weller, Y. Wu, J. Stohr, M. G. Samant, B. D. Hermsmeier, and C. Chappert, *Phys. Rev. B*, **49 (18)**, 12888-12896 (1994).

[78] D. Weller, J. Stohr, R. Nakajima, A. Carl, M. G. Samant, C. Chappert, R. Megy, P. Beauvillain, P. Veillet, and G. A. Held, *Phys. Rev. Lett.*, **75 (20)**, 3752-3755 (1995).

[79] D. Weller, G. R. Harp, R. F. C. Farrow, A. Cebollada, and J. Sticht, *Phys. Rev. Lett.*, **72 (13)**, 2097-2100 (1994).

[80] S. Ferrer, J. Alvarez, E. Lundgren, X. Torrelles, P. Fajardo, and F. Boscherini, *Phys. Rev. B*, **56 (15)**, 9848-9857 (1997).

[81] N. Nakajima, T. Koide, T. Shidara, H. Miyauchi, I. Fukutani, A. Fujimori, K. Iio, T. Katayama, M. Nyvlt, and Y. Suzuki, *Phys. Rev. Lett.*, **81 (23)**, 5229-5232 (1998).

[82] D. Weller, A. Carl, R. Savoy, T. C. Huang, M. F. Toney, and C. Chappert, *J. Phys. Chem. Solids*, **56 (11)**, 1563-1566 (1995).

[83] S. Uba, L. Uba, A. N. Yaresko, A. Y. Perlov, V. N. Antonov, and R. Gontarz, *Phys. Rev. B*, **53 (10)**, 6526-6535 (1996).

[84] J. F. Ankner, J. A. Borchers, R. F. C. Farrow, and R. F. Marks, *J. Appl. Phys.*, **73 (10)**, 6427-6429 (1993).

[85] L. H. Bennett, E. Della Torre, and R. A. Fry, *Physica B*, **306 (1-4)**, 228-234 (2001).

[86] G. A. Bertero, R. Sinclair, C. H. Park, and Z. X. Shen, *J. Appl. Phys.*, **77 (8)**, 3953-3959 (1995).

[87] P. F. Carcia, *J. Vac. Sci. Technol. A-Vac. Surf. Films*, **5 (4)**, 1975-1976 (1987).

[88] C. H. Chang and M. H. Kryder, *J. Appl. Phys.*, **75 (10)**, 6864-6866 (1994).

[89] I. B. Chung, Y. M. Koo, and J. M. Lee, *J. Appl. Phys.*, **87 (9)**, 4205-4209 (2000).

[90] B. D. Fulthorpe, D. E. Joyce, T. P. A. Hase, A. S. H. Rozatian, B. K. Tanner, and P. J. Grundy, *J. Phys.-Condes. Matter*, **11 (43)**, 8477-8487 (1999).

[91] S. Hashimoto, Y. Ochiai, and K. Aso, *J. Appl. Phys.*, **66 (10)**, 4909-4916 (1989).

[92] J. C. A. Huang, C. H. Lee, and K. L. Yu, *J. Appl. Phys.*, **89 (11)**, 7059-7061 (2001).

[93] J. H. Kim and S. C. Shin, *J. Appl. Phys.*, **80 (5)**, 3121-3123 (1996).

[94] E. T. M. Lacey and P. J. Grundy, *IEEE Trans. Magn.*, **26 (5)**, 2356-2358 (1990).

[95] E. Lundgren, J. Alvarez, X. Torrelles, K. F. Peters, H. Isern, and S. Ferrer, *Phys. Rev. B*, **59 (3)**, 2431-2435 (1999).

[96] R. Atkinson, S. Pahirathan, I. W. Salter, P. J. Grundy, C. J. Tatnall, J. C. Lodder, and Q. Meng, *J. Magn. Magn. Mater.*, **162 (1)**, 131-138 (1996).

[97] C. J. Tatnall, J. P. Schille, P. J. Grundy, and D. G. Lord, *J. Magn. Magn. Mater.*, **165 (1-3)**, 391-393 (1997).

[98] M. Cinal and D. M. Edwards, *Phys. Rev. B*, **55 (6)**, 3636-3648 (1997).

[99] V. O. Golub, R. Gontarz, G. N. Kakazei, and N. A. Lesnik, *J. Magn. Magn. Mater.*, **174 (1-2)**, 95-99 (1997).

[100] M. Cinal, *J. Phys.-Condes. Matter*, **13 (5)**, 901-916 (2001).

[101] S. Boukari, E. Beaurepaire, H. Bulou, B. Carriere, J. P. Deville, F. Scheurer, M. De Santis, and R. Baudoing-Savois, *Phys. Rev. B*, **6414 (14)**, art. no.-144431 (2001).

[102] J. R. Childress, R. Kergoat, O. Durand, J. M. George, P. Galtier, J. Miltat, and A. Schuhl, *J. Magn. Magn. Mater.*, **130 (1-3)**, 13-22 (1994).

[103] S. K. Kim, Y. M. Koo, V. A. Chernov, J. B. Kortright, and S. C. Shin, *Phys. Rev. B*, **62 (5)**, 3025-3028 (2000).

[104] J. Y. Kim, B. K. Lee, G. S. Park, M. Uchida, T. Kurosawa, S. Watanabe, J. Ariake, N. Honda, and K. Ouchi, *J. Magn. Magn. Mater.*, **235 (1-3)**, 53-58 (2001).

[105] T. Onoue, J. Kawaji, K. Kuramochi, T. Asahi, and T. Osaka, *J. Magn. Magn. Mater.*, **235 (1-3)**, 82-86 (2001).

[106] G. H. O. Daalderop, P. J. Kelly, and F. J. A. Denbroeder, *Phys. Rev. Lett.*, **68 (5)**, 682-685 (1992).

[107] B. R. Acharya, S. N. Piramanayagam, A. K. Nigam, S. N. Shringi, S. Prasad, N. Venkataramani, G. Chandra, and R. Krishnan, *J. Magn. Magn. Mater.*, **140** , 555-556 (1995).

[108] A. Barthelemy, A. Fert, M. N. Baibich, S. Hadjoudj, F. Petroff, P. Etienne, R. Cabanel, S. Lequien, F. N. Vandau, and G. Creuzet, *J. Appl. Phys.*, **67 (9)**, 5908-5913 (1990).

[109] G. Oomi, Y. Uwatoko, Y. Obi, K. Takanashi, and H. Fujimori, , **126 (1-3)**, 513-515 (1993).

[110] J. M. Colino, I. K. Schuller, V. Korenivski, and K. V. Rao, *Phys. Rev. B*, **54 (18)**, 13030-13033 (1996).

[111] B. G. Almeida, V. S. Amaral, J. B. Sousa, J. Colino, I. K. Schuller, R. Schad, V. V. Moshchalkov, and Y. Bruynseraede, *J. Appl. Phys.*, **81 (8)**, 5194-5196 (1997).

[112] J. Santamaria, M. E. Gomez, M. C. Cyrille, C. Leighton, K. M. Krishnan, and I. K. Schuller, *Phys. Rev. B*, **6501 (1)**, art. no.-012412 (2002).

[113] E. E. Fullerton, D. M. Kelly, J. Guimpel, I. K. Schuller, and Y. Bruynseraede, *Phys. Rev. Lett.*, **68 (6)**, 859-862 (1992).

[114] D. M. Kelly, E. E. Fullerton, F. T. Parker, J. Guimpel, Y. Bruynseraede, and I. K. Schuller, *Int. J. Mod. Phys. B*, **7 (1-3)**, 419-424 (1993).

[115] H. Nakajima, K. Nonaka, Y. Obi, and H. Fujimori, , **126 (1-3)**, 176-179 (1993).

[116] N. M. Rensing, A. P. Payne, and B. M. Clemens, *J. Magn. Magn. Mater.*, **121 (1-3)**, 436-439 (1993).

[117] A. Gupta, A. Paul, S. M. Chaudhari, and D. M. Phase, *J. Phys. Soc. Jpn.*, **69 (7)**, 2182-2187 (2000).

[118] A. Paul, A. Gupta, S. M. Chaudhari, and D. M. Phase, *Vacuum*, **60 (4)**, 401-405 (2001).

[119] A. Paul, *J. Magn. Magn. Mater.*, **240 (1-3)**, 497-500 (2002).

[120] D. Olligs, D. E. Burgler, Y. G. Wang, E. Kentzinger, U. Rucker, R. Schreiber, T. Bruckel, and P. Grunberg, *Europhys. Lett.*, **59 (3)**, 458-464 (2002).

[121] R. Krishnan, A. Das, J. P. Eymery, M. Porte, and M. Tessier, *IEEE Trans. Magn.*, **33 (5)**, 3697-3699 (1997).

[122] I. Chibe, K. Himi, K. Saito, S. Mitani, K. Takanashi, K. Hayata, K. Sato, and H. Fujimori, *J. Magn. Magn. Mater.*, **226** , 1720-1721 (2001).

Chapter 3

Magnetic Anisotropy in Thin Films

3.1 Introduction

Magnetic anisotropy is one of the key properties exploited in ferromagnetic nanostructures. Reduced dimensionality may greatly alter the effective magnetic anisotropy of such structures. For layered systems, numerous investigations demonstrate that reduced thickness and complex interactions on surfaces and interfaces induce uniaxial magnetic anisotropy that, by orders of magnitude, exceeds the values of the intrinsic anisotropy in the corresponding bulk materials [1, 2]. High anisotropy is important in media in order to avoid reversal i.e., to get high coercivity. During the last decade, a large variety of magnetic thin films and multilayers have been synthesized and investigated experimentally. They have already found applications in modern magnetoelectronics and magnetic recording media [3, 4].

Recent first principle numerical calculations have proved the reliability of the quantum-mechanical microscopic theory in its applications to magnetic nanostructures [5-7]. They are offering considerable insight into the phenomena of the induced anisotropy. However, these *ab initio* calculations are still unable to give a complete description of the magnetization structures and processes in real layered systems. Hence, our understanding of and control over the magnetic anisotropy of nanostructures is rather incomplete. Up to now, the analysis of experimental data on anisotropy effects in magnetic multilayer systems is mostly based on the effective volume anisotropy method introduced by Néel about fifty years ago [8]. Within this approach, the value of the average induced uniaxial anisotropy (the effective magnetic anisotropy energy), K_{eff} can be modelled phenomenologically by deconvolution of a volume term K_V, independent of magnetic layer thickness t, and an interface (surface) term K_S, proportional to $1/t$. The volume anisotropy is composed of the magnetocrystalline K_C, the shape K_d, and the magnetoelasic K_γ anisotropies ($K_\gamma = -3/2\,\gamma\,\delta$, where γ is the saturation magnetization coefficient and δ is the stress existing in the magnetic layer). The effective magnetic anisotropy energy K_{eff} of a multilayer thin film can be expressed phenomenologically as follows:

$$K_{eff} = K_V + \frac{2}{t} K_S \tag{3.1}$$

with:

$$K_V = K_C - \alpha M_S^2 - \frac{3}{2}\,\gamma\,\delta \tag{3.2}$$

where M_S and α represent the saturation magnetization and the demagnetization factor, respectively, t is the thickness of the ferromagnetic layer, and K_S is Néel's surface anisotropy. The demagnetization factor α is commonly considered to be 2π for an imperfect film. It should be pointed out that the value of α could be determined from Equations (3.1) and (3.2) once K_{eff}, K_C, M_S, and K_γ are known.

The Equations (3.1) and (3.2) just represent a weighted average of the magnetic anisotropy energy of the interface atoms and the inner atoms of a magnetic layer thickness t. The relation is presented under the convention that K_S/t represents the difference between the anisotropy of the interface atoms with respect to the inner or bulk atoms. Also the layer is assumed to be bounded by two identical interfaces, accounting for the factor 2. Equation (3.1) is commonly used in experimental studies, and the determination of K_V and K_S can be obtained by a plot of the product $K_{eff} * t$ versus t. Figure 3.1 shows a typical example of such a plot for Co/Pd multilayers, series 2 (chapter 8). Here, a positive K_{eff} describes the case of a preferred direction of the magnetization perpendicular to the plane of sample. The negative slope indicates a negative volume anisotropy K_V, favoring in-plane magnetization, while the intercept at $t_{Co} = 0$ indicates a positive interface anisotropy K_S, favoring out-of-plane magnetization. Below a certain thickness $(t_\perp = -2K_S / K_V)$, in this case about 8 Å , the interface anisotropy contribution outweighs the volume contribution, resulting in a perpendicularly magnetized system. In other words, the strong demagnetizing fields which are created when tilting the magnetization out of the plane and which are usually responsible for the orientation of the magnetization parallel to the film plane, are overcome. The volume energy corresponding to these demagnetizing fields form the major contribution to K_V in most cases.

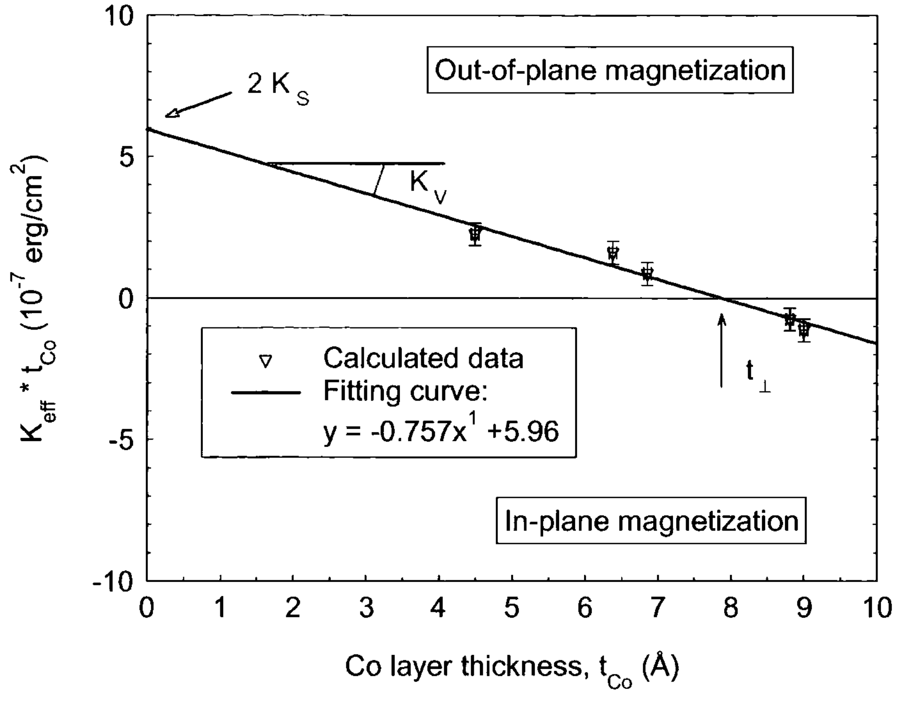

Figure 3.1 The effective anisotropy energy times the individual Co layer thickness versus the Co layer thickness of Co/Pd multilayers, series 2 (chapter 8).

The experimental results of the type shown in Figure 3.1 considerably stimulated theoretical work. For the bulk transition metals, it appeared very difficult to calculate the magnetic anisotropy from first principles, as the corresponding energies are very small (about 1 meV per atom). On the other hand, for multilayer thin films, which generally exhibit larger anisotropies, some progress has been made [9-11]. However, for many layered systems with reduced thickness, the function K_S / t becomes strongly nonlinear which is at variance with Equation (3.1) [1, 12-16]. Perhaps the most interesting feature that shows up in some systems is that the magnetization goes back in the plane in the thin film limit [17]. Two major models, one by Jungblut *et al* [13] and the other by Bochi *et al* [14, 15] have been proposed to explain the thickness dependence of the anisotropy, particularly the reappearance of the in-plane magnetization for thinner nickel films. Moreover, the general validity of the Néel's theory has been questioned in a number of articles [1, 18]. The separation of the uniaxial anisotropy into volume and surface contribution and the reduction of surface anisotropy into an effective volume contribution should be considered as an excessive simplification. Furthermore, equation (3.1) implies that the anisotropy is constant within a magnetic layer and, thus, stabilizes a homogenous distribution of the magnetization. However, it has been shown that the competition between volume and surface anisotropies may induce inhomogeneous states in magnetic films and multilayer structures [19]. On the whole, Néel's approach and similar models have succeeded in giving qualitative explanations of some general features of the induced anisotropy. However, they do not account for many other observed effects and they fail to give a quantitative description of the magnetization structures in magnetic nanostrutures.

This chapter is concerned with both the theoretical and experimental aspects of the research performed on the magnetic anisotropy in Fe/Au, Co/Pt, and Co/Pd multilayers. Moreover, the perpendicular uniaxial magnetic anisotropy is emphasized although in-plane anisotropies will also be addressed.

The chapter is organized as follows: in section 2, the origin of the magnetic anisotropy will be reviewed. Section 3 is devoted to several aspects of growth conditions and film structure which influence PMA in magnetic multilayers. Theoretical predictions of PMA will be addressed in section 4. The most commonly used experimental techniques to quantitatively determine the magnetic anisotropy are briefly introduced in section 5.

3.2 Origin of the Magnetic Anisotropy

When a physical property of a material is a function of direction, that property is said to exhibit anisotropy. The preference for the magnetization to lie in a particular direction in a sample is called magnetic anisotropy. A parameter that describes the magnetization process could be the permeability, μ or the susceptibility, κ. Thus, in general, these parameters are functions of the direction in which the field is applied to the material [20]:

$$\mu = \mu(\phi, \theta) \tag{3.3}$$

$$\kappa = \kappa(\theta, \phi) \tag{3.4}$$

Magnetic anisotropy can have its origin in sample shape, crystal symmetry, stress, or directed atomic pair ordering. Basically the two main sources of the magnetic anisotropy are the magnetic dipolar interaction and the spin–orbit interaction. Due to its long range character, the dipolar interaction generally results in a contribution to the anisotropy, which depends on the shape of the sample. It is of particular importance in thin films, and is largely responsible for the in-plane magnetization usually observed. In the absence of spin–orbit and dipolar interaction, the total energy of the electron–spin system does not depend on the direction of the magnetization. In a localized picture the spins are coupled via the spin–orbit interaction to the orbits which, in turn, are influenced by the crystal lattice. For itinerant materials the spin–orbit interaction induces a small orbital momentum, which then couples the total (spin plus orbital) magnetic moment to the crystal axes. This results in a total energy which depends on the orientation of the magnetization relative to the crystalline axes, and which reflects the symmetry of the crystal. This is known as the magnetocrystalline contribution to the anisotropy. The lowered symmetry at an interface strongly modifies this contribution as compared to the bulk, yielding a so-called interface anisotropy as pointed out by Néel [8]. In conjunction with the overlap in wavefunctions between neighbouring atoms, the spin–orbit interaction is also responsible for the magneto-elastic or magnetostrictive anisotropy induced in a strained system, a situation which is frequently encountered in multilayers due to the lattice mismatch between the adjacent layers. In the following subsections each of these anisotropy terms will be discussed in somewhat more detail.

3.2.1. Shape anisotropy

Among the most important sources of the magnetic anisotropy in thin films is a magnetic dipolar interaction, which senses the outer boundaries of the sample. Neglecting the discrete nature of matter, magnetization can be treated as a field $M(r)$, which obeys Maxwell's equations. At the interfaces between two regions with different magnetization we have the usual boundary conditions: the normal component of B and the tangential component of H should be continuous. The magnetostatic energy is the total energy difference between the situations in which the sample has a given magnetization distribution to the situation in which there is no sample at all [21]. This involves both the magnetic field inside and outside the sample, but by taking the appropriate expressions for the energy, the volume of integration can be limited to the sample volume. When a field M is given, the solution for B and H are often formulated with the use of the magnetic potential ψ, defined by:

$$H = -\nabla \psi \tag{3.5}$$

The function ψ is a solution of Laplace's equation:

$$\nabla^2 \psi = 0 \tag{3.6}$$

The shape effect of the dipolar interaction in ferromagnetic samples can be described, via an anisotropic demagnetizing field, H_d. A magnetized body produces magnetic charges or poles at the surface. This surface charge distribution, acting in isolation, is itself another source of a magnetic field, called a demagnetizing field and is given by:

$$H_d = -N * \mathrm{M} \tag{3.7}$$

Here M is the magnetization vector and N is the shape-dependent demagnetizing factor and in general it is a tensor function of sample shape [20]. For a thin film all tensor elements are zero except for the direction perpendicular to the layer:

$$N_\perp = 1 \tag{3.8}$$

Since the magnetostatic energy can be expressed as:

$$E_d = -\frac{\mu_0}{2V}\int M \cdot H_d \, dV = \frac{\mu_0}{2V}\int (-\nabla \cdot M)\, \psi \, dV \tag{3.9}$$

Where μ_0 $\left(=4\pi\times10^{-7}\right)$ and V are the permeability of vacuum and volume of the sample, respectively. When the magnetization is saturated and θ is the angle between the axis normal to the plane of the film and M, the average anisotropy energy contribution per unit volume V of the thin film becomes:

$$E_d = \frac{1}{2}\mu_0\, M_S^2 \cos^2\theta \tag{3.10}$$

Here the magnetization is assumed to be uniform with a magnitude equal to the saturation magnetization M_S, and subtends an angle θ with the film normal. The anisotropy energy E_a is the difference between the magnetostatic energy for the parallel orientation $(\theta = \pi/2)$ and the perpendicular orientation $(\theta = 0)$, which yields:

$$E_a = -\frac{1}{2}\mu_0\, M_S^2 \tag{3.11}$$

According to this expression, the contribution favours an in-plane preferential orientation for the magnetization. Because the thickness of the film does not enter into the continuum approach employed above, it contributes only to K_V. It is this contribution which is mainly responsible for the negative slope of the K_{eff} versus t plot in Figure 3.1. This continuum approach is common in the analysis of the experimental data.

However, when the thickness of the ferromagnetic layer is reduced to only a few monolayers, the film should not, in principle, be considered as a magnetic continuum, but has to be treated as a collection of discrete magnetic dipoles on a regular lattice. Calculations made on the basis of discretely summing the dipolar interactions for films in the range of 1–10 MLs lead to the following results [22]. Depending on the symmetry of the interface, the outer layers experience a dipolar anisotropy which can be appreciably lower than the inner layers. For the inner layers, the dipolar anisotropy is rather close to the value based on the continuum approach. Consequently, the average dipolar anisotropy can be phenomenologically expressed by a volume and an interface contribution. The magnitude of the dipolar interface contribution, however, is of minor importance, and other sources of interface anisotropy, such as spin–orbit coupling, appear to be dominant.

3.2.2. Magnetocrystalline anisotropy

Magnetocrystalline anisotropy is the energy necessary to deflect the magnetic moment in a single crystal from the easy to hard direction. The easy and hard directions arise from the interaction of the spin magnetic moment with the crystal lattice (spin-orbit coupling). In principle, there are two contributions to the magnetocrystalline anisotropy energy: the magnetic dipolar and the electronic band structure part. The first comes from the classical magnetic dipolar interaction and, except for systems with a large anisotropy; it is much smaller than the second one. Van Vleck already pointed out that the physical origin of the electronic magnetocrystalline anisotropy energy and the orbital moment is the spin-orbit coupling. Van Vleck discussed the magnetocrystalline anisotropy (in the case of bulk) in a pair interaction model assuming localized magnetic moments [23]. Néel extended this model to surfaces and showed that the reduced symmetry at the surface should result in magnetic anisotropies at the surface differing strongly from the bulk atoms [8]. Nowadays it is well established that the electronic contribution and the orbital moment come from the simultaneous occurrence of spin-orbit coupling and spin polarization. For that reason, calculations of the electronic magnetocrystalline anisotropy energy (MAE) and orbital moment of bulk materials and transition-metal thin-film multilayers from first principles became possible only after the development of spin-polarized relativistic band structure methods. At the same time, several authors derived and proposed expressions, which relate the electronic MAE to other quantities also induced by the spin-orbit coupling and spin-polarization, as, *e.g.*, the orbital moment [1].

As stated, the tendency for M_S to lie along an easy axis can be described using the magnetocrystalline anisotropy constant. For the simplest case of a purely uniaxial crystal, with no anisotropy normal to the single easy axis, an appropriate expression for the anisotropy energy density is:

$$E = K \sin^2 \theta \qquad (3.12)$$

where θ is the angle between M_S and a coordinate axis parallel to the easy axis. E is zero when M_S is parallel or antiparallel to the arbitrarily directed coordinate axis and maximum for $\theta = \frac{\pi}{2}$, i.e. has appropriate symmetry. This would apply with other even terms and a more general form of Equation (3.12) is as follows:

$$E = K_1 \sin^2 \theta + K_2 \sin^4 \theta + \cdots \tag{3.13}$$

For cobalt at room temperature experiments indicate [24]:

$$K_1 = 55 \times 10^5 \; erg / cm^3$$

$$K_2 = 12 \times 10^5 \; erg / cm^3$$

Anisotropy fields may be regarded as those fields which, when applied along an easy axis, give the same torques as those corresponding to the anisotropy and thus may be taken to represent the anisotropy. The torque due to the anisotropy can be defined as follows:

$$T = -\frac{\partial E}{\partial \theta} \tag{3.14}$$

3.2.3 Magneto-elastic anisotropy (stress anisotropy)

Strain in a ferromagnet changes the magnetocrystalline anisotropy and may thereby alter the direction of the magnetization. This effect is the 'inverse' of magnetostriction, the phenomenon that the sample dimensions change if the direction of the magnetization is altered. The energy per unit volume associated with this effect can, for an elastically isotropic medium with isotropic magnetostriction, be written as:

$$E_{me} = -K_{me} \cos^2 \theta \tag{3.15}$$

with:

$$K_{me} = -\frac{3}{2}\,\gamma\,\delta \tag{3.16}$$

Alternatively:

$$K_{me} = -\frac{3}{2}\,\gamma\,\varepsilon\,Z \tag{3.17}$$

Here δ is the stress which is related to the strain, ε, via the elastic modulus Z by: $\delta = \varepsilon\,Z$. The magnetostriction constant γ depends on the orientation and can be positive or negative. The angle θ measures the direction of the magnetization relative to the direction of uniform stress. If the strain in the film is non-zero, the magneto elastic coupling contributes in principle to the effective anisotropy. When the parameters are constant (not depending on the magnetic layer thickness, t) this contribution can be identified with a volume contribution K_V (compare with the Equations (3.1) and (3.2)). Strain in thin films can be induced by various sources. Among them are thermal strain associated with differences in thermal expansion coefficients, intrinsic strain brought about by the nature of the deposition process and strain due to non-matching lattice parameters of adjacent layers [1, 25].

3.3 Effects of the interface structure on the magnetic anisotropy

It should be realized that the structure of the magnetic layers is extremely important for the actually observed magnetic anisotropies. The importance of the topology of the interfaces and of the crystallographic structure of the magnetic layers was already mentioned. The structural properties are strongly determined by the complex interplay between the growth technique employed (e.g. sputtering and evaporation), the preparation conditions (temperature, growth rate, sputtering pressure), the elements which are grown, their thicknesses and lattice mismatch, the symmetry and quality of the substrate and the resulting growth mode. In this section the effect of interface roughness and interdiffusion will be discussed.

So far, it was assumed that the layers have ideal flat interfaces. In practice, films cannot be grown perfectly. Roughness and/or interdiffusion will be present and will modify the magnetic properties. Here, a brief comment will be made on their effects on the magnetic anisotropy.

3.3.1 Theory

The effect of roughness on the dipolar anisotropy has been studied theoretically by Bruno [26]. A rough surface can be characterized by the roughness σ, which is the mean square deviation from the ideally flat surface, and the correlation length ξ, the average lateral size of flat areas on the surface (terraces) (Figure 3.2).

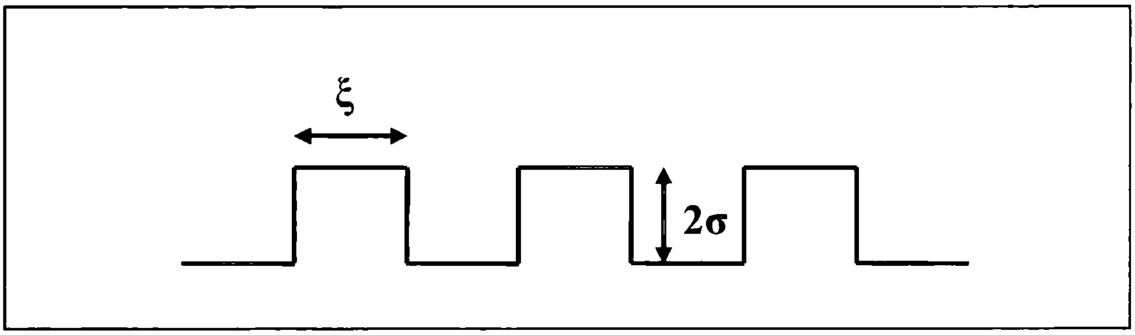

Figure 3.2 Schematic surface profile in the Bruno model, showing the characteristic parameters σ and ξ.

Roughness creates in-plane demagnetizing fields at the edges of terraces, thereby reducing the *shape* anisotropy. The shape anisotropy contribution resulting from the roughness will, therefore, always be positive (favoring PMA). In addition, due to its presence at the interfaces only it will scale as $1/t$. The magnitude of the corresponding dipolar interface anisotropy is a complicated function of σ and ξ, which can be found in Ref. [26]. Under 'normal' conditions ($\sigma < 5$ Å, and $\xi \approx 20$ Å), however, the contribution appears to be small. Roughness also introduces step atoms at the interface. It has been derived [27], using the pair interaction model, that these step atoms should reduce the interface anisotropy contribution of *magnetocrystalline* origin. The extent of this reduction will be determined by the change of the anisotropy of the step atoms relative to terrace atoms and by the number of step atoms relative to the number of terrace atoms. The former depends on the geometry of the interface; the latter is determined by the height of the steps σ, their length ξ and the number of steps per unit length $(1/\xi)$. Bruno [27] derived the relative reduction in K_S for a simple cubic (100) interface is given by:

$$\frac{\Delta K_S}{K_S} = -\frac{2\sigma}{\xi}$$

This prediction has been quantified in a series of elegant experiments on Fe/Au multilayers [28]. As mentioned, interdiffusion might occur during the deposition of the layers. It is clear that diffuse interfaces introduce randomness in the magnetic pair bonds according to Néel's model, which obviously reduces the interface anisotropy. Draaisma and de Jonge [22] have paid attention to this problem and have demonstrated via calculations based on the pair interaction model a strong dependence of K_S on the degree of mixing. Although the application of the pair interaction model in the latter two cases demonstrated the importance of the topology of the interface, it would be interesting to compare the results with the outcome of more advanced calculations such as in Ref. [29]. The first calculations of this type predict a reduction in magnetocrystalline anisotropy resulting from the presence of defects [30].

3.3.2 Experiments

It has been reported that the interface anisotropies observed for samples grown on single crystals are generally larger than those observed for polycrystalline samples. This indicates the importance of the interface quality. Examples expressing this are a study on Co/Au multilayers [31] and work on a wedge-shaped Co layer [32].

3.3.3 Non-linear Kt versus t behavior

As stated before, a deviation from the linear behavior of $K*t$ versus t at small Co thicknesses can be observed in some systems. This feature is often encountered in the anisotropy studies of transition metal multilayers. Apart from a possible coherent–incoherent transition, with the accompanying changes in the magneto-elastic anisotropy contributions as discussed earlier, several explanations can be given. Assuming, for instance, that at small Co thickness the film is no longer a continuous flat layer but is broken up into islands, necessarily yielding a lower effective magnetic/non-magnetic interface area, a lower interface contribution and a correspondingly lower total anisotropy than expected from Equation (3.1). Apart from interdiffusion, which can also account for nonlinear behaviour if the magnetic-layer thickness becomes comparable to the thickness of the diffusion zone, a lowering of the Curie temperature with the magnetic layer thickness, which is a well known finite-size effect, can also play a role in the case of room temperature measurements [33]. Moreover, one should realize that for ultrathin magnetic layers it is not at all apparent that one is allowed to separate the MAE into interface and volume contributions.

3.4 Theoretical predictions of perpendicular magnetic anisotropy

The magnetic anisotropy energy is a relatively small energy term in an *ab initio* calculation. Pioneering work by Gay and Richter [34] on the calculation of magnetic anisotropy energy in free standing magnetic monolayers, was later extended to a series of first-principles calculations on Co-based multilayers [9-11, 35-38]. In these calculations, the magnetic anisotropy is of the order of $1\,meV/Co\,atom$ and can be related to the spin–orbit interaction induced splitting and shifting of electronic states which depend on the magnetization direction. As such, only those systems with relatively large PMA (Co/Pt, Co/Pd, Co/Ni) have been extensively investigated from the theoretical point of view. It should be noted that each calculation determines only the total magnetic anisotropy energy for a given multilayer structure. As a consequence, the separation of this anisotropy into a volume and interface contribution is somewhat arbitrary. However extending our understanding of perpendicular magnetic anisotropy beyond the phenomenological approach of volume and interface-anisotropies requires caution. Experimentally, many factors such as roughness, formation of interface alloys, or patchiness of ultrathin layers may cause a reduction in PMA. Where stresses are present in multilayer growth, these may, under particular circumstances, contribute to both K_V and K_S. Theoretically, the difficulty in modelling incoherently grown materials prevents a detailed quantitative comparison with most experimental systems. Therefore, an evaluation of the underlying approximations common to all of the theoretical quantitative studies becomes very difficult. Of the theoretical predictions which may be tested experimentally, perhaps the most important are the electronic structure effects on PMA and their associated orientational dependence. Originally, Néel discussed the anisotropy within a pair interaction model, the reduced symmetry at the interface resulting in anisotropies differing greatly from that of the bulk, which were furthermore predicted to be orientationally dependent. Such a simple pair model is, however, less suited to transition metal multilayers, where the itinerant electron model is more appropriate. The predictions and orientational dependence of the PMA are discussed for a wide variety of systems and could be found in [1, 39].

3.5 Measurement of magnetic anisotropy

Magnetic anisotropy can be deduced from the dynamical response of the magnetic system or from the static response. The dynamic response of the magnetic layers can be measured by ferromagnetic resonance (FMR) and Brillouin light scattering (BLS) [1]. The static response can be measured by torque magnetometry [40, 41], torsion oscillating magnetometry [42], the magneto optical Kerr effect (MOKE) [32] and various techniques which measure the magnetic moment, such as vibrating sample magnetometry (VSM), superconducting quantum interference device (SQUID) magnetometry, alternating gradient field magnetometry (AGFM), etc. Much of the experimental data so far has been obtained from static measurements. In particular magnetization and torque measurements are frequently employed to determine the magnetic anisotropy and will be discussed briefly in this section.

3.5.1 Magnetization methods

The magnetic anisotropy is most frequently determined from magnetization measurements, e.g. by VSM, AGFM, or SQUID, along two orthogonal directions of the magnetic field relative to the sample. Examples of such measurements, with the field parallel and perpendicular to the film plane, are shown in Figure 3.3.

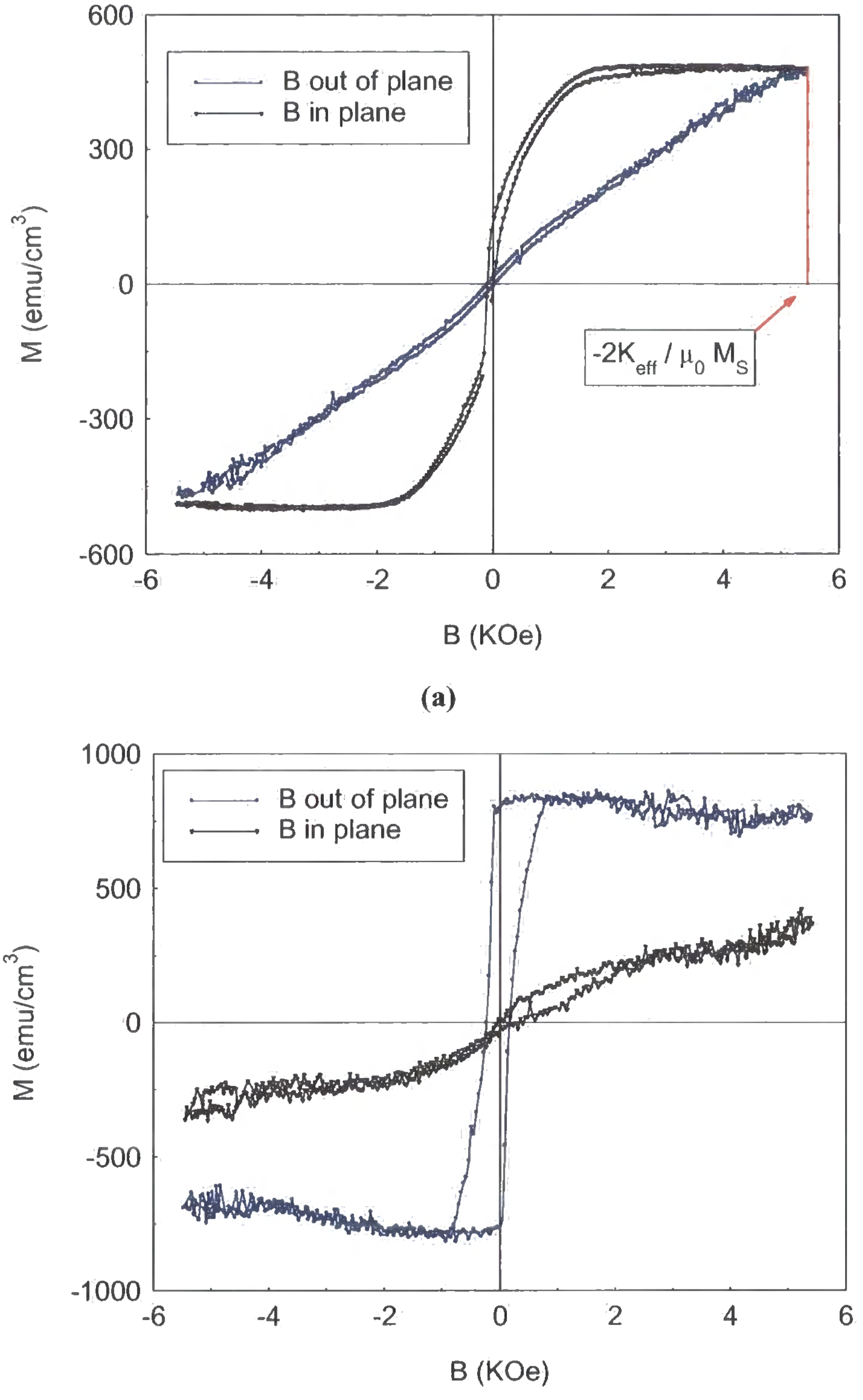

(a)

(b)

Figure 3.3 Hystersis loops measured with the applied field perpendicular and parallel to the plane of Co/Pd samples **(a)** with 30 bilayers repeats (series 3), **(b)** with 12 bilayers repeat (series 1).

The MAE is given by the area enclosed between the parallel and perpendicular loops. This is based on elementary electromagnetic considerations which show that the energy needed to change the sample magnetization in an applied field H by an amount dM is given by $\mu_0\, H\, dM$. In some cases, the MAE can also be obtained from the fields at which saturation occurs. The angle-dependent part of the energy E of the magnetization of the thin film can be written as:

$$E = \left(-K_i + \frac{1}{2}\mu_0\, M_S^2 \right) \cos^2\theta - \mu_0\, M_S\, H \cos(\phi - \theta) \tag{3.18}$$

In this expression, K_i contains all first-order (intrinsic) anisotropy energy contributions except the shape anisotropy or magnetostatic energy contribution, which is given by $\frac{1}{2}\mu_0\, M_S^2$ ($2\pi M_S^2$ in cgs) for a saturated film. The last term describes the interaction between the applied field and the resulting magnetization; θ and ϕ denote the angles subtended by the magnetization and field, respectively, and the film normal. Energy minimization as a function of the applied field H yields the field dependence of the equilibrium angle $\theta_{eq}(H)$ and the field component of the magnetization $M = M_S \cos(\theta_{eq} - \phi)$.

For samples with an in-plane easy axis $\left(K_{eff} = K_i - \frac{1}{2}\mu_0\, M_S^2 \langle 0 \right)$ this procedure gives the magnetization curves shown in Figure 3.3(a). The area enclosed between the two curves clearly equals the effective magnetic anisotropy energy (MAE), K_{eff}. As seen in Figure 3.3(a), the MAE could in this case (in-plane magnetization) also be obtained from the hard-axis saturation field, the so-called anisotropy field $H_A = -\frac{2\, K_{eff}}{\mu_0\, M_S}$. In the case of samples with a perpendicular easy axis$\left(K_{eff} \rangle\, 0\right)$, one should be careful in applying this analysis as the magnetostatic energy contribution used in Equation (3.18) is not valid in general because it depends on the size of the domains [1].

Summarizing, the MAE can in principle be determined from the field dependence of the magnetization by measuring the saturation fields or the area between the in-plane and perpendicular magnetization curves. However, in general, no one-to one relation exists between the hard-axis saturation field and the total effective magnetic anisotropy energy K_{eff}. The area between the loops, on the contrary, yields K_{eff} in all cases. In practice, problems are encountered using the 'area method'. For instance, as Figure 3.3 illustrates, the experiments can show a considerable hysteresis and the available field is in some cases not sufficient to saturate the sample in the hard axis direction. In order to determine the MAE in such cases, the hysteresis is removed by averaging the hysteresis loop branches, and the hard axis loop is extrapolated, which is often rather arbitrary for nonlinear curves. These problems can be circumvented by measuring the angular dependence of the magnetization. In this method the applied field is set at a constant value but its angle with respect to the film normal is varied by rotating the sample. During this rotation, the component of the magnetization along the field is measured. The magnetic anisotropy is then determined by fitting the obtained angular dependence by minimization of Equation (3.18).

3.5.2 Torque magnetometry

More accurate anisotropy measurements are often made using a torque magnetometer. A torque magnetometer works on the principle of balancing a known mechanical torque from a suspension wire against an unknown torque associated with the magnetization being rotated away from its easy axis. Torque magnetometery is one of the most direct methods for the measurement of crystalline anisotropy. The sample is suspended by a torsion wire in a rotating magnetic field, and the torque on the sample is recorded as a function of angle. In the analysis of the torque data, we consider terms to second order in the phenomenological expansion of the anisotropy energy. The torque $\left(T = -\frac{\partial E}{\partial \theta}\right)$ can be calculated [20, 43, 44] from a total energy E written as:

$$E = K_{eff} \sin^2 \theta + K_2 \sin^4 \theta - BM\{\cos(\theta - \phi)\} \tag{3.19}$$

where θ is the angle of the magnetization M and ϕ is the angle of the applied magnetic field B with respect to the normal of the plane of sample. As the anisotropy is high, the angle between magnetization and field direction $(\theta-\phi)$ is significant and it is essential to incorporate this shear correction when fitting the data. Shear is the distortion which can occur in a torque curve. It arises when the magnetization in the sample lags behind or moves ahead of the applied field direction. All experimental torque curves were therefore numerically fitted to the equation:

$$T=-K_{eff}\sin 2\left\{\phi+\arcsin\left(-\frac{T}{MB}\right)\right\}+\frac{1}{2}K_2\sin 4\left\{\phi+\arcsin\left(-\frac{T}{MB}\right)\right\} \qquad (3.20)$$

in order to extract values of K_{eff} and K_2 (in cgs). A typical torque curve along with a fit to Equation (3.20), including a shear correction can be seen in Fig. 3.4.

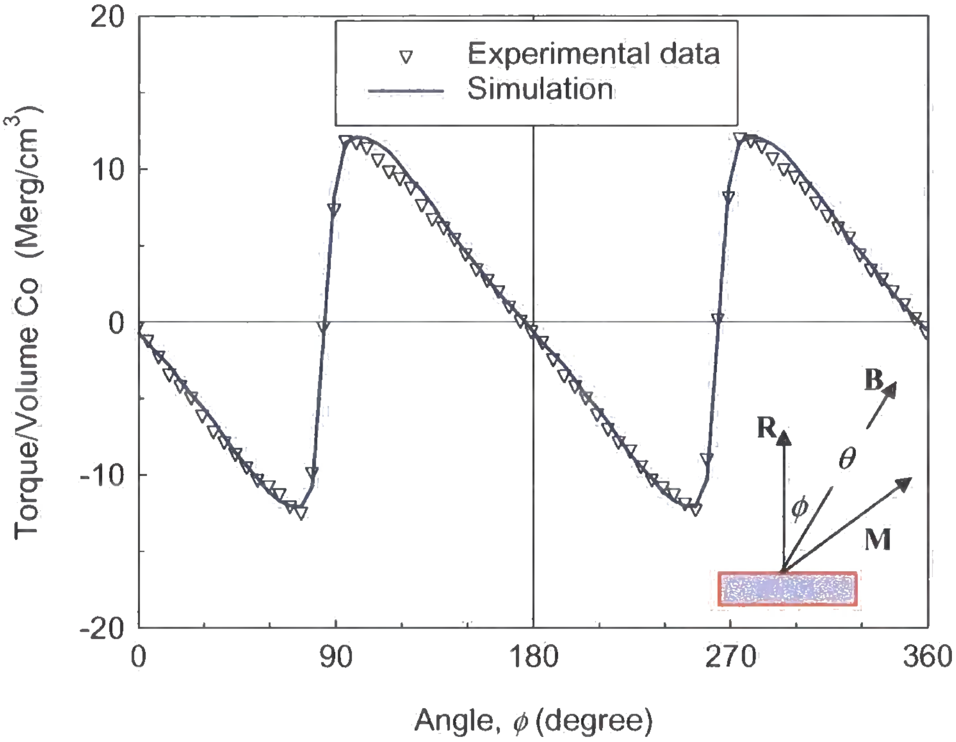

Figure 3.4 Torque curve for a Co/Pt sample at B=7.6KOe. The inset shows the orientation of magnetisation and applied field directions.

3.6 Summary

In this chapter, a discussion has been given of the important contributions to the anisotropy of magnetic thin films, such as the magnetic dipolar, the magnetocrystalline and the magnetostrictive contributions. Of particular importance appeared a contribution scaling with the reciprocal magnetic-film thickness: a so-called interface anisotropy. The many experiments have made it clear that interface anisotropies generally exist at all interfaces irrespective of the elements forming the interface. They are not restricted to magnetic/non-magnetic interfaces, a finding which is consistent with the general belief that the interface anisotropy basically originates from the lack of translational symmetry at the interface. The experiments have also shown that the magnetic-interface anisotropies can be several orders of magnitude larger than the magnetocrystalline anisotropies found in bulk crystals and can easily induce perpendicular preferential orientations. It is found that the experimental determination of PMA, which is intrinsically material and orientation dependent, is sensitive to experimental artifacts such as sample roughness, microstructure (patches and columns), formation of interface alloys and mechanical stresses. Although the influence of several of these factors on the measured anisotropy may be quantified (e.g. roughness, patchiness, mechanical stresses), direct comparison with the predictions from *ab initio* calculations demands caution. Whilst the orientational dependence of the PMA is theoretically confirmed, and encouraging quantitative agreement is established with the measured PMA in several MBE-grown sample series, the major uncertainty associated with the *ab initio* calculations remains the necessity to use a coherent epitaxial structural model, which is infrequently encountered in many important cases: Co/Pd(111), Co/Pt(111). As most of the experimental artifacts result in a reduction of the measured PMA, theoretically predicted values should generally exceed those obtained experimentally. The *ab initio* calculations also predict enhanced orbital moments in several systems which display strong PMA, which have subsequently been confirmed experimentally using MCXD (Weller *et al* 1994). However, enhanced moments are not directly related to large PMA: it is the orbital moment anisotropy which determines the magnitude of the PMA (Weller *et al* 1995). Finally, it was demonstrated that where relaxation from coherent to incoherent epitaxial growth is encountered, the stress apparently contributes to both volume and interface anisotropies, the latter of which may therefore further be separated into a magneto-elastic term (the misfit interface anisotropy) and an electronic term (in fact the result of *ab initio* calculations). Such examples illustrate how recent insights are taking us beyond the phenomenological approach to perpendicular anisotropy.

REFERENCES

[1] "Ultrathin Magnetic Structures", Eds.: J. A. C. Bland and B. Heinrich, Springer-Verlag (1994).

[2] P. Poulopoulos and K. Baberschke, *J. Phys.-Condes. Matter*, **11 (48)**, 9495-9515 (1999).

[3] F. J. Himpsel, J. E. Ortega, G. J. Mankey, and R. F. Willis, *Adv. Phys.*, **47 (4)**, 511-597 (1998).

[4] P. J. Grundy, *J. Phys. D-Appl. Phys.*, **31 (21)**, 2975-2990 (1998).

[5] G. Y. Guo, *Phys. Rev. B*, **55 (17)**, 11619-11628 (1997).

[6] G. Y. Guo, *J. Phys. IV*, **7 (C2)**, 117-120 (1997).

[7] P. Weinberger and L. Szunyogh, *Comput. Mater. Sci.*, **17 (2-4)**, 414-437 (2000).

[8] L. Néel, *J. Phys., Rad.*, **15** , 376 (1954).

[9] G. H. O. Daalderop, P. J. Kelly, and M. F. H. Schuurmans, *Phys. Rev. B*, **42 (11)**, 7270-7273 (1990).

[10] G. H. O. Daalderop, P. J. Kelly, and M. F. H. Schuurmans, *Phys. Rev. B*, **41 (17)**, 11919-11937 (1990).

[11] G. H. O. Daalderop, P. J. Kelly, and F. J. A. Denbroeder, *Phys. Rev. Lett.*, **68 (5)**, 682-685 (1992).

[12] F. J. A. den Broeder, W. Hoving, and P. J. H. Bloemen, *J. Magn. Magn. Mater.*, **93** , 562-570 (1991).

[13] R. Jungblut, M. T. Johnson, J. A. Destegge, A. Reinders, and F. J. A. Denbroeder, *J. Appl. Phys.*, **75 (10)**, 6424-6426 (1994).

[14] G. Bochi, C. A. Ballentine, H. E. Inglefield, C. V. Thompson, and R. C. Ohandley, *J. Appl. Phys.*, **79 (8)**, 5845-5847 (1996).

[15] G. Bochi, C. A. Ballentine, H. E. Inglefield, C. V. Thompson, and R. C. Ohandley, *Phys. Rev. B*, **53 (4)**, R1729-R1732 (1996).

[16] K. Ha and R. C. O'Handley, *J. Appl. Phys.*, **87 (9)**, 5944-5946 (2000).

[17] K. Ha and R. C. O'Handley, *J. Appl. Phys.*, **85 (8)**, 5282-5284 (1999).

[18] G. T. Rado, *J. Magn. Magn. Mater.*, **104** , 1679-1683 (1992).

[19] A. Thiaville and A. Fert, *J. Magn. Magn. Mater.*, **113 (1-3)**, 161-172 (1992).

[20] *Modern Magnetic Materials, Principles and Applications.*, R. C. O'Handley, JOHN WILEY & SONS, INC. (2000).

[21] *Classical Electrodynamics*, J. D. Jackson, 2nd ed., Wiley (1975).

[22] H. J. G. Draaisma and W. J. M. Dejonge, *J. Appl. Phys.*, **64 (7)**, 3610-3613 (1988).

[23] J. H. van Vleck, *Phys. Rev.*, **52** , 1178-1198 (1937).

[24] D. M. Paige, B. Szpunar, and B. K. Tanner, *J. Magn. Magn. Mater.*, **44 (3)**, 239-248 (1984).

[25] *Magnetism, Principles and Applications*, D. Craik, John Wiley & Sons (1995).

[26] P. Bruno, *J. Appl. Phys.*, **64 (6)**, 3153-3156 (1988).

[27] P. Bruno, *J. Phys.: F*, **18 (6)**, 1291-1298 (1988).

[28] G. Lugert, W. Robl, L. Pfau, M. Brockmann, and G. Bayreuther, *J. Magn. Magn. Mater.*, **121 (1-3)**, 498-502 (1993).

[29] G. H. O. Daalderop, P. J. Kelly, and M. F. H. Schuurmans, *Phys. Rev. B*, **44 (21)**, 12054-12057 (1991).

[30] J. M. Maclaren and R. H. Victora, *J. Appl. Phys.*, **76 (10)**, 6069-6074 (1994).

[31] F. J. A. den Broeder, D. Kuiper, A. P. Vandemosselaer, and W. Hoving, *Phys. Rev. Lett.*, **60 (26)**, 2769-2772 (1988).

[32] S. T. Purcell, M. T. Johnson, N. W. E. McGee, W. B. Zeper, and W. Hoving, *J. Magn. Magn. Mater.*, **113 (1-3)**, 257-263 (1992).

[33] P. J. H. Bloemen, W. J. M. Dejonge, and F. J. A. Denbroeder, *J. Magn. Magn. Mater.*, **93** , 105-108 (1991).

[34] J. G. Gay and R. Richter, *Phys. Rev. Lett.*, **56** , 2728-2731 (1987).

[35] G. H. O. Daalderop, P. J. Kelly, and M. F. H. Schuurmans, *Phys. Rev. B*, **50 (14)**, 9989-10003 (1994).

[36] R. H. Victora and J. M. Maclaren, *Phys. Rev. B*, **47 (17)**, 11583-11586 (1993).

[37] R. H. Victora and J. M. Maclaren, *J. Appl. Phys.*, **73 (10)**, 6415-6417 (1993).

[38] K. Kyuno, R. Yamamoto, and S. Asano, *J. Phys. Soc. Jpn.*, **61 (6)**, 2099-2103 (1992).

[39] M. T. Johnson, P. J. H. Bloemen, F. J. A. denBroeder, and J. J. deVries, *Rep. Prog. Phys.*, **59 (11)**, 1409-1458 (1996).

[40] S. R. Hoon and D. M. Paige, *IEEE Trans. Magn.*, **23 (1)**, 183-185 (1987).

[41] P. Poulopoulos, N. K. Flevaris, R. Krishnan, and M. Porte, *J. Appl. Phys.*, **75 (8)**, 4109-4113 (1994).

[42] R. Bergholze and U. Gradmann, *J. Magn. Magn. Mater.*, **45** , 389-398 (1984).

[43] D. M. Paige and B. K. Tanner, *J. Phys. E: Sci. Instrum.*, **15 (1)**, 128-131 (1982).

[44] *Introduction to Magnetism and Magnetic Materials*, D. Jiles, Interpharm/CRC (1998).

Chapter 4

Grazing Incidence X-ray Reflectometry

4.1 Introduction

X-ray reflectivity has become an important tool in studying the structure and organization of materials that are grown as thin films at nanoscales. In thin film materials research, the trend is to design solid films of increasing complexity having specific properties for technical applications. The nature of the materials deposited on substrates and the techniques of deposition for such applications are extremely variable. Molecular beam epitaxy deposition generally provides extremely well-crystallized materials of semiconductor and metallic heterostructures. As stated in chapter 2, this technique, which is expensive, is used in general for making specific materials such as quantum wells and artificial superlattices. For industrial applications the sputtering technique is widely used for coating metallic films, for making oxide thin films and for creating heterogeneous materials like cermets (ceramic metals). The perfection of layered super-structures is defined both by the quality of the interfaces and by the reproducibility with which one can achieve the deposition of the layers (control of thickness, crystallinity, voids or various defects, which may appear during the growth process). In particular, the roughness of the interfaces is of crucial importance for many technological applications. In the following two chapters, the technique of specular x-ray reflectivity will be presented and it will be shown through various examples how the technique can be used to determine the thickness of the individual layers and the roughness of the interfaces. The measurement of diffuse x-ray scattering will be presented as a good way to analyse the correlation of interfacial roughness between successive layers.

4.2 Basic principles of x-ray reflectivity

4.2.1 The index of refraction

X-rays are part of the broad spectrum of electromagnetic waves. X-rays can be produced by the acceleration or deceleration of electrons either in vacuum (synchrotrons) or in metallic targets (tubes). The most widely used x-rays in materials science have a typical wavelength, λ, of the order of $1\,\text{Å}$. This wavelength is associated with a very high frequency of the order of $10^{19}\ Hz$ which is at least four orders of magnitude greater than the eigen frequency of an electron bound to a nucleus. As a consequence, the interaction of x-rays with matter can be well described (in a classical way) by an index of refraction which characterizes the change of direction of the x-ray beam when passing from air to a material. The time independent part of electromagnetic plane wave given by $E(r)=E_0\exp(ik\cdot r)$, which penetrates into a medium characterized by an index of refraction, n, propagates according to the Helmholtz equation:

$$\nabla^2 E(r)+|k|^2\,E(r)-V\,E(r)=0 \tag{4.1}$$

where $V=|k|^2\left(1-n^2\right)$ describes the interaction with the material for a homogenous material with a refractive index n so:

$$\nabla^2 E(r) + k^2\, n^2(r)\, E(r) = 0 \tag{4.2}$$

where $k = 2\pi/\lambda$. A very simple classical model in which an electron of the material is considered to be accelerated by the x-ray field shows that the index of refraction for x-rays can be written as:

$$n = 1 - \delta - i\,\beta \tag{4.3}$$

where δ and β account for the scattering and absorption of the material, respectively. The sign preceding β depends on the convention of signs used to define the propagation of the electric field. The values of δ and β (which are positive) depend on the electron density and linear absorption coefficient of the material through the following relations [1]:

$$\delta = \frac{N_A}{2\pi} r_e\, \lambda^2 \sum_j \frac{\rho_j}{m_j}\left(Z_j + f_j'\right) \tag{4.4}$$

$$\beta = \frac{N_A}{2\pi} r_e\, \lambda^2 \sum_j \frac{\rho_j}{m_j} f_j'' \tag{4.5}$$

All the units are defined in cgs units and $r_e = 2.813\times10^{-13}\ cm$ is the classical radius of the electron, N_A is Avogadro's number, ρ_j is the density of element j, m_j is its atomic mass and Z_j is the atomic number. The f' and f'' terms are the real and imaginary parts of the absorption for the specific energy of incident radiation such that:

$$f = f_0 + f' + f'' \tag{4.6}$$

When the frequency of the incident radiation is well away from any absorption edges within the material the absorption and dispersion of x-rays can essentially be neglected and the scattering factor is equal to f_0, the Fourier transform of the electron density function. Equation (4.6) becomes important when the frequency of the incident radiation is close to an absorption edge. The f'' factor can also be important elsewhere in any regime where high absorption occurs. A detailed treatment of the method by which these correction terms are calculated can be found elsewhere [1, 2]

4.2.2 The critical angle of reflection

For x-rays, the refractive index of a material is slightly less than unity [3]. Passing from air $(n=1)$ to the reflecting material $(n<1)$, it is possible to reflect totally the beam if the incident angle θ_i (which is the angle between the surface of the sample and the incident beam) is small enough (Figure 4.1). This is known as the *total external reflection* of x-rays. For this to occur, the incident angle must be smaller than the critical angle θ_c defined as (neglecting absorption):

$$\cos\theta_c = n = 1-\delta \tag{4.7}$$

Since n is very close to unity, this angle is very small and a Taylor approximation in θ_c yields:

$$\theta_c^2 = 2\,\delta = \frac{r_e\,\lambda^2}{\pi}\,\rho \tag{4.8}$$

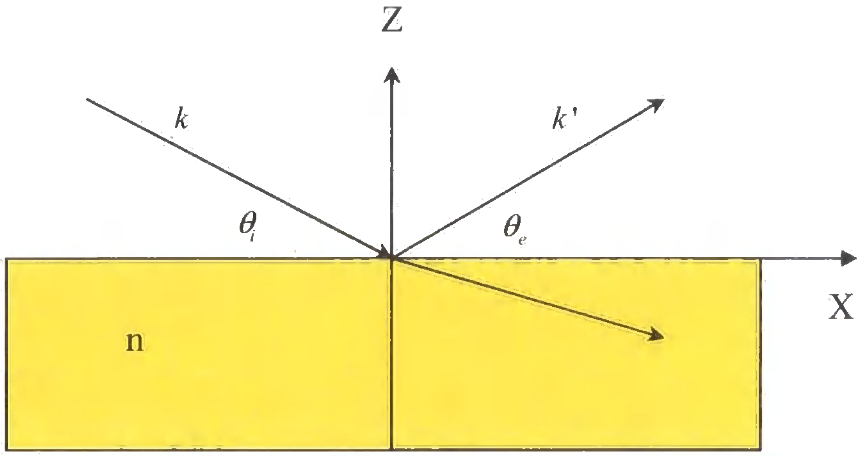

Figure 4.1 X-ray reflectivity from a flat surface.

4.2.3 Reflected intensity from ideally flat surface

When an x-ray beam impinges on a flat material, part of the incoming intensity is reflected and part transmitted through the material. If the surface of the reflecting material is flat, the reflected intensity will be confined in a direction symmetric from the incident one and will be labelled as *specular*. The specular reflectivity is conventionally defined as the ratio of scattered intensity over the incident intensity:

$$R(\theta)=\frac{I(\theta)}{I_0} \tag{4.9}$$

The domain of validity of x-ray reflectivity is limited to small angles of incidence where it is possible to consider the electron density as continuous. In this approximation, the reflection can be treated as a classical problem of reflection of an electromagnetic wave at an interface. The reflected amplitude is obtained by writing the continuity of the electric field and of the magnetic field at the interface. This leads to the classical Fresnel relationship which gives the reflection coefficient in amplitude for the (s) and (p) polarization (Appendix B). The reflectivity, which is the modulus square of this coefficient, can be formulated in the case of x-rays as:

$$R^{flat}(\theta) = r\,r^* = \left| \frac{\theta - \sqrt{\theta^2 - \theta_C^2 - 2\,i\,\beta}}{\theta + \sqrt{\theta^2 - \theta_C^2 - 2\,i\,\beta}} \right|^2 \qquad (4.10)$$

This expression is independent of the polarization. Since the reflectivity is only observed in specular conditions (incident angle equal to the exit angle), one obtains, after introduction of the wave vector transfer:

$$q = (0, 0, q_z = 4\pi \sin\theta/\lambda) \qquad (4.11)$$

$$R^{flat}(q_z) = \left| \frac{q_z - \sqrt{q_z^2 - q_c^2 - \dfrac{32\,i\,\pi^2\,\beta}{\lambda^2}}}{q_z + \sqrt{q_z^2 - q_c^2 - \dfrac{32\,i\,\pi^2\,\beta}{\lambda^2}}} \right|^2 \qquad (4.12)$$

4.2.4 Importance of surface roughness

Ideal flat surfaces are fictitious especially when they are analysed with x-rays or neutron reflectometry. Such techniques are indeed extremely sensitive to any defects of flatness. It is easy to realize that rough surfaces will be less reflecting than an ideally flat surface. It is thus important to describe the effect of roughness on the measured reflected intensity. The *roughness*, σ, of the surface can be comprehended statistically with the help of the moments of the distribution, $P(z)$, and of altitude $z(x,y)$ with respect to the mean altitude $\bar{z}$ by the following relation:

$$\sigma^2 = \left\langle \left[z(x,y) - \bar{z} \right]^2 \right\rangle = \int P(z) \left[z(x,y) - \bar{z} \right]^2 dz \qquad (4.13)$$

It is usual to introduce a height difference correlation function $g(X,Y)$, which correlates the two heights, $z(x,y)$ and $z(x' = x + X\ ,\ y' = y + Y)$ on the surface, as:

$$g(X,Y)=\left\langle\left[z(x,y)-z(x',y')\right]^2\right\rangle$$
$$=\left\langle z^2(x,y)\right\rangle+\left\langle z^2(x',y')\right\rangle-2\left\langle z(x,y)\,z(x',y')\right\rangle \tag{4.14}$$

where the averaging is taken over the area coherently illuminated by the beam. It can be assumed that the surface presents the property of stationarity, i.e. the mean value of the square of the altitude does not depend on the position, so that $\left\langle z^2(x,y)\right\rangle=\left\langle z^2(x',y')\right\rangle=\sigma^2$ represents the root-mean-squared (*rms*) of the vertical roughness. As a result:

$$g(x,y)=2\,\sigma^2-2\left\langle z(x,y)\,z(x',y')\right\rangle=2\,\sigma^2-2\,C(X,Y) \tag{4.15}$$

where $C(X,Y)$ is the *height–height correlation function* defined as:

$$C(X,Y)=\frac{1}{L_x}\frac{1}{L_y}\int_{-\frac{L_y}{2}}^{\frac{L_y}{2}}\int_{-\frac{L_x}{2}}^{\frac{L_x}{2}} z(x,y)\,z(x',y')\,dx\,dy \tag{4.16}$$

As shown in Figure 4.2, the effect of surface roughness is to reduce the specular reflectivity by a kind of Debye–Waller factor. When the correlation length of the height fluctuations is not very large then:

$$R^{rough}(q_z)=R^{flat}(q_z)\,e^{-\left[q_{z,0}\,q_{z,1}\right]\sigma^2} \tag{4.17}$$

where $q_{z,0}$ and $q_{z,1}$ are the wave vector transfers in air and in the material. For large q_z this may be simplified as:

$$R^{rough}_{spec}(q_z)=R^{flat}(q_z)\,e^{-q_z^2\,\sigma^2} \tag{4.18}$$

where $R^{flat}(q_z)$ is the Frenel reflection coefficient as defined above. The term $e^{-q_z^2\sigma^2}$ is defined as a Debye-Waller factor [2, 4].

Figure 4.2 shows the simulated reflectivity of a silicon wafer with different interface roughness. One can see that the roughness plays a major role at high angles (high wave vector q).

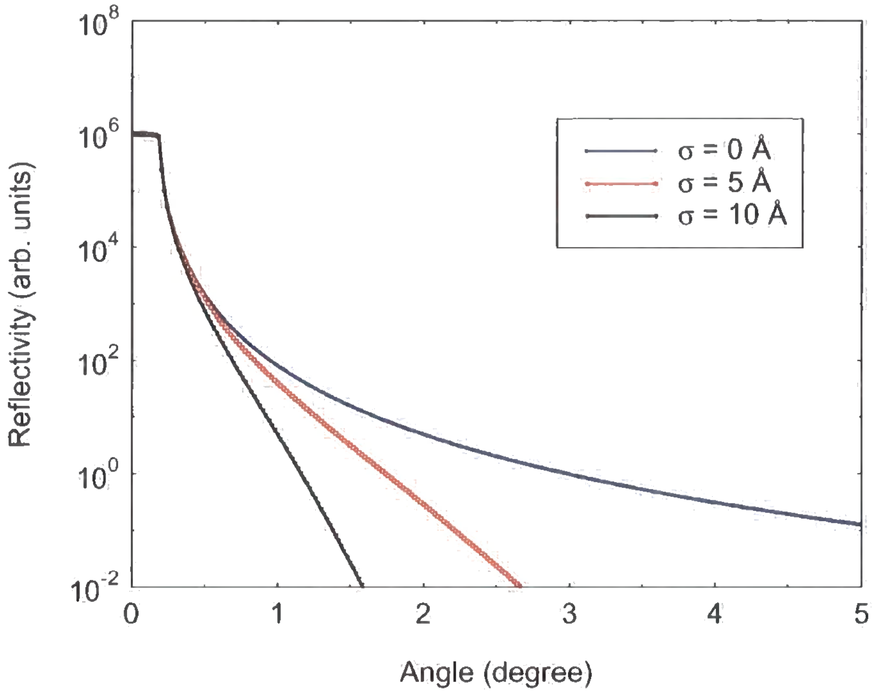

Figure 4.2 X-ray reflectivity from a silicon wafer for no surface roughness, $\sigma = 5$Å, and $\sigma = 10$Å, $\lambda = 1.3$Å.

4.2.5 X-ray reflection by multilayers with flat and rough interfaces

When the wave propagates in a heterogeneous medium containing regions of different electron densities, it is not possible to use the Fresnel coefficients directly. The calculation is performed by applying the boundary conditions of the electric and magnetic fields at each interface. The fact that multiple reflections are taken into account in the calculation leads to the *dynamical theory* of reflection and the result is usually presented as the product of matrices. For this let us consider a plane wave polarized in the direction perpendicular to the plane of incidence and propagating in the medium j of a stratified material and let us choose the axes so that the wave is travelling in the xz

plane (Figure 4.3). For the electric field in medium j, solution of the Helmholtz equation is:

$$\begin{aligned} E_j(x,z) &= \left(A_j^+ e^{ik_{z,j} z} + A_j^- e^{-ik_{z,j} z}\right) e^{i(\omega t - k_{x,j} x)} \\ &= \left[U_j^+(z) + U_j^-(z)\right] e^{i(\omega t - k_{x,j} x)} \end{aligned} \tag{4.19}$$

where $k_{z,j}$ and $k_{x,j}$ are the z and x component of the wave vector in medium j. The condition of the tangential component of the electric and magnetic fields and the conservation of $k_{x,j}$ at interface j, $j+1$ located at $z = z_{j+1}$ yield:

$$U_j^+(z_{j+1}) + U_j^-(z_{j+1}) = U_{j+1}^+(z_{j+1}) + U_{j+1}^-(z_{j+1}) \tag{4.20}$$

$$k_{z,j}\left[U_j^+(z_{j+1}) - U_j^-(z_{j+1})\right] = k_{z,j+1}\left[U_{j+1}^+(z_{j+1}) - U_{j+1}^-(z_{j+1})\right] \tag{4.21}$$

These two equations can be combined in a matrix form yielding:

$$\begin{pmatrix} U_j^+(z_{j+1}) \\ U_j^-(z_{j+1}) \end{pmatrix} = \begin{pmatrix} p_{j,j+1} & m_{j,j+1} \\ m_{j,j+1} & p_{j,j+1} \end{pmatrix} \begin{pmatrix} U_{j+1}^+(z_{j+1}) \\ U_{j+1}^-(z_{j+1}) \end{pmatrix} \tag{4.22}$$

with:

$$p_{j,j+1} = \frac{k_{z,j} + k_{z,j+1}}{2k_{z,j}}$$

and:

$$m_{j,j+1} = \frac{k_{z,j} - k_{z,j+1}}{2k_{z,j}}$$

and:

$$k_{z,j} = k_j \sin\theta_j = k\sqrt{\theta_j^2 - 2\delta_j - 2i\beta_j}$$

The matrix which transforms the amplitude of the electric field from medium j to medium $j+1$ can be denoted as by the refraction matrix $R_{j,j+1}$. In addition, in medium j, the amplitude of the electric field varies with altitude t as follows:

$$\begin{pmatrix} U_j^+(z) \\ U_j^-(z) \end{pmatrix} = \begin{pmatrix} e^{-ik_{z,j}t} & 0 \\ 0 & e^{ik_{z,j}t} \end{pmatrix} \begin{pmatrix} U_j^+(z+t) \\ U_j^-(z+t) \end{pmatrix} \tag{4.23}$$

The transfer matrix which is involved here is denoted by the translation matrix T_j. It can be shown that the cosine terms appear in the reflected intensity $\left(R^{flat} = rr^* \propto \cos 2k_{z,1}\, t\right)$, with $r = \dfrac{U_0^+(z_1)}{U_0^-(z_1)}$ indicating that the reflectivity does present periodic oscillations in reciprocal space [2, 5, 6].

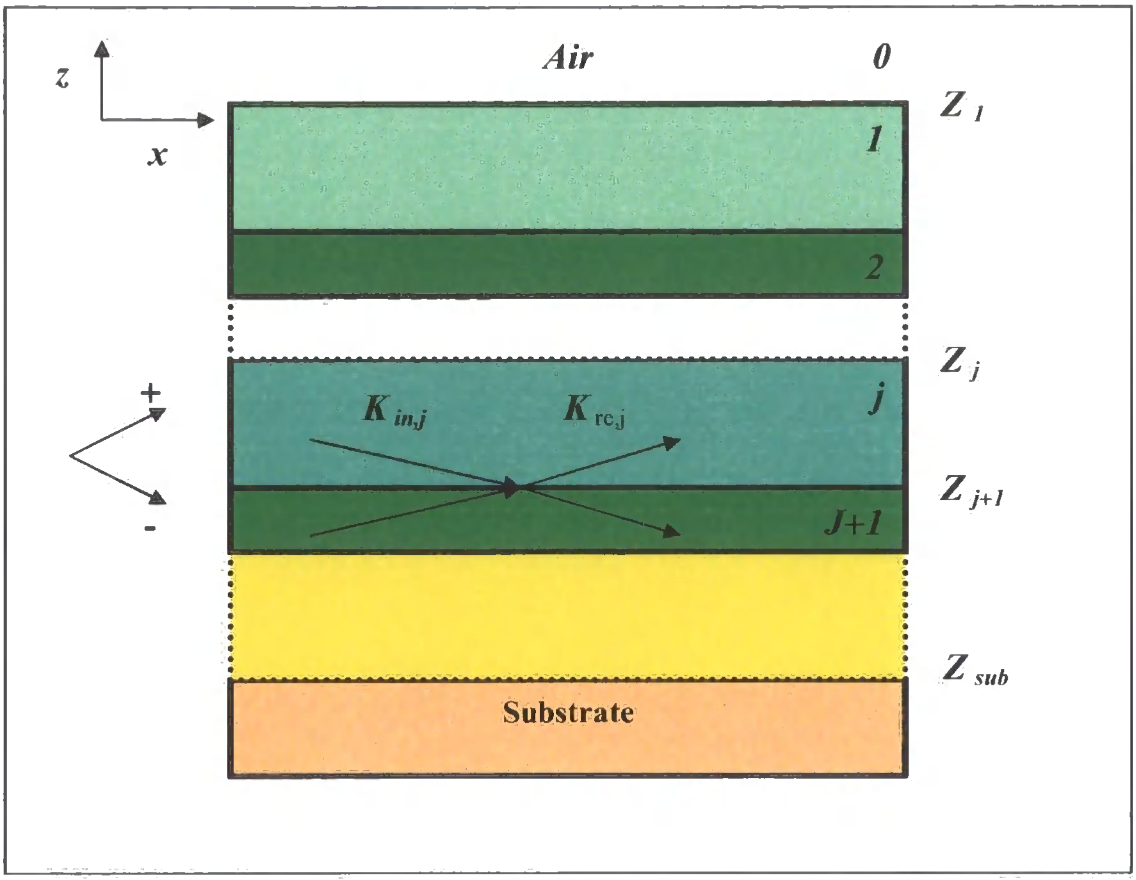

Figure 4.3 schematic of a multilayer system and the conventions used in the text concerning the labels of the layers and of the propagation directions of the incident and reflected waves.

The oscillations are the result of constructive interference between the reflected waves at interfaces 1 and 2 and their period gives the thickness of the film. Figure 4.4 corresponding to the reflectivity of a 200Å platinum layer on silicon is a good illustration of observable interference. The fact that the observed reflectivity is less than 1 below the critical angle is related to a surface effect. At very shallow angles, it frequently happens that the footprint of the beam is larger than the sample surface so that only part of the intensity is reflected. A correction must then be applied to describe this part of the reflectivity curve [7]. Figure 4.5 shows the influence of surface and interface roughness on the reflectivity of a gold thin film deposited on a silicon substrate. Here σ_0 and σ_1 represent roughness at film surface and film/substrate interface, respectively.

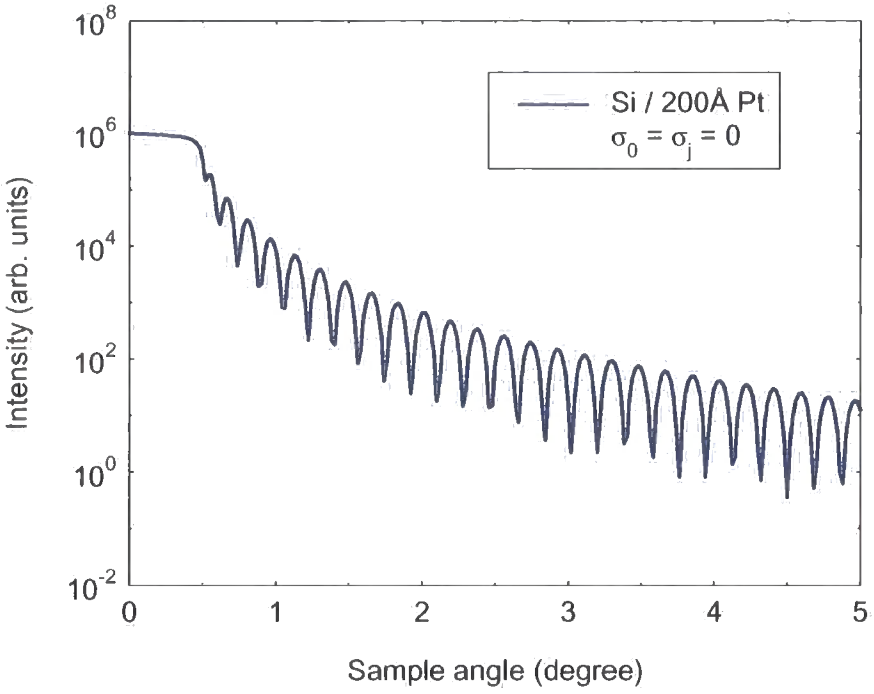

Figure 4.4 X-ray reflectivity simulation from a thin film platinum layer deposited on a silicon wafer.

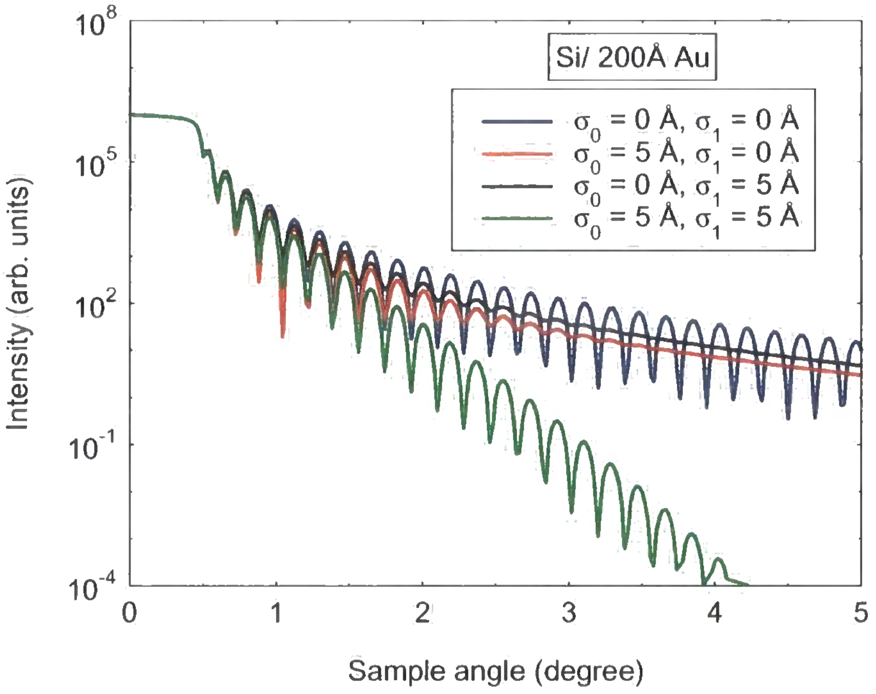

Figure 4.5 The effect of surface and interface roughness on the reflectivity of a 200Å gold deposited on a silicon substrate, $\lambda = 1.3$Å.

The reflectivity curve of a multilayer exhibits a typical shape in which one can find Bragg peaks separated by Kiessig fringes [2, 8]. The distance in q space between two Bragg peaks is inversely proportional to the period of the multilayer and the one between Kiessig fringes gives the thickness of the film (one should expect $N-2$ fringes between two Bragg peaks, N being the number of repeated bilayers). Figure 4.6 shows a simulated reflectivity curve of a 10-bilayer Co/Pt multilayer thin film deposited on Si substrate.

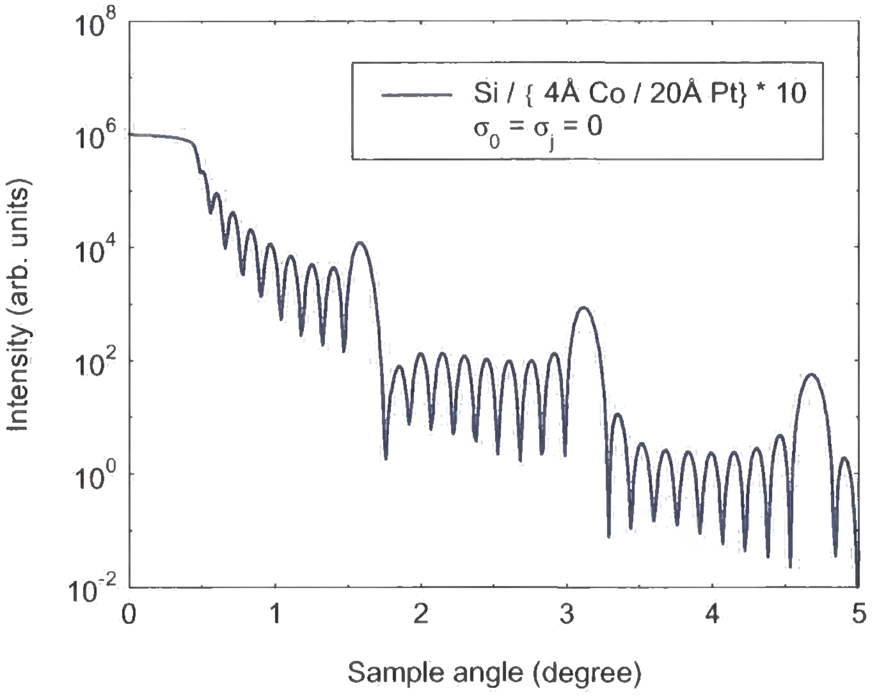

Figure 4.6 A simulated reflectivity curve from a 10-bilayer Co/Pt multilayer thin film deposited on silicon.

4.3 Born approximation

The Born approximation (BA), considers only the scattering from separate electrons, and neglects the processes of extinction, refraction and multiple scattering. This approach is valid when the incident angle θ_i and the exit angle θ_e are larger than the critical angle of total reflection θ_c, and it cannot explain the existence of Yoneda wings (which appear at $\theta_i = \theta_c$ or $\theta_e = \theta_c$), the Kiessig interference fringes, or the Bragg peaks from multilayers. Several theoretical models based on this approach have been published [9-11]. Born approximation expressions for both the x-ray specular reflectivity and the x-ray diffuse scattering from a single smooth surface were derived by Sinha *et al* [9]. A simple generalization of the BA for multilayers was proposed by Savage *et al* [10]. They have introduced the concept of the interface roughness as composed of two parts: uncorrelated and correlated (i.e. which propagates from layer to layer). Spiller *et al* [11] have proposed the use of the power spectral density (PSD) function for description of the roughness of each interface instead of height-to-height correlation function. In their opinion, the PSD function is more appropriate for the description of the roughness than the correlation functions, because the latter one describes the measuring tool and not the surface. A Monte-Carlo simulation of the interface roughness of multilayer structures and BA calculation of the x-ray diffuse scattering intensity was used [12] for studying partially correlated roughnesses.

4.4 Distorted wave Born approximation

The distorted-wave Born approximation (DWBA), or the dynamic approach, was first applied for the description of x-ray diffuse scattering by Sinha *et al* [9]. This approach takes into account the processes of X-ray refraction and multiple scattering. The DWBA approach is suitable for small θ_i and θ_e and fails if both θ_i and θ_e are significantly larger than θ_c (in this region BA simulations are applicable). The main idea of the DWBA is in the splitting of the scattering potential in the stationary wave-equation into two parts: (i) undisturbed, which describes ideally smooth interfaces; and (ii) disturbed, which can be considered as a small perturbation due to the roughness. The electrodynamic formulation of the reciprocity theorem was used by Kaganer *et al* [13] to derive a model for description of the x-ray diffuse scattering from multilayers. Several authors have developed the DWBA approach very intensively in the last decade. Sinha has proposed a generalized equation for the evaluation of the intensity of the x-ray diffuse scattering from a multilayer. Weber and Lengeler [14] were able to obtain consistent results for the out-of-plane roughness from both x-ray diffuse scattering and x-ray reflectivity scattering measurements by proposing a model in which both transmitted amplitudes are replaced with those for a rough surface by using correction terms. Several publications on the DWBA model of the x-ray diffuse scattering from multilayers were published by Holý and co-workers [15-18] and by de Boer and co-workers [19]. Holý *et al* [15] have proposed a first order DWBA model for the x-ray diffuse scattering from multilayers, and have derived a simpler approximation for the case $|q_z \sigma| < 1$. A formalism for combining the kinematic x-ray diffraction with the DWBA approach for description of the roughness was proposed by Holý [16], and was used for modelling the x-ray diffuse scattering from periodic crystalline multilayers. The effect of the out-of-plane correlation of the roughness in multilayers was also studied numerically [17]. The DWBA formalism was used in [18] for calculation of the x-ray diffuse scattering contribution from randomly rough multilayers to x-ray reflection, strongly asymmetric x-ray diffraction, and grazing incidence x-ray diffraction.

4.5 Diffuse scattering

4.5.1 Theoretical basis

In contrast to the x-ray specular reflectivity, the x-ray diffuse scattering gives information on the in-plane and out-of-plane structure of the interface. A short description of x-ray diffuse scattering theory will be reviewed in this section. More details can be found in several references [4, 9, 10, 15, 20-24].

4.5.2 Scattering cross-section within the Born approximation

In the Born approximation where the multiple reflections are neglected, the scattering cross-section ($S(q)$, which is proportional to $\frac{d\sigma}{d\Omega}$) is the Fourier transform of the density–density autocorrelation function and is defined as:

$$S(q) = r_e^2 \iint \rho(r)\, \rho(r')\, r^{iq\cdot(r-r')}\, dr\, dr' \tag{4.24}$$

At small angles, x-rays are only sensitive to the mean electron density which is a constant if the material is homogeneous. In the above equation, the phase factor defines the phase shift between the waves scattered at the two points r and r' when one looks at the position q in reciprocal space. It is possible to show that when the integration along the z direction is performed from $-\infty$ to $z(X,Y)$ the scattering cross-section yields:

$$S(q)=\frac{\rho^2 r_e^2 L_x L_y}{q_z^2}\iint_S e^{-\frac{q_z}{2}g(R)}\, e^{i\left(q_x X+q_y Y\right)}\,dX\,dY \tag{4.25}$$

With $g(R)$ and $C(R)$ defined in section 4.2.4, this leads to:

$$S(q)=\frac{\rho^2 r_e^2 L_x L_y}{q_z^2}\, e^{-q_z^2\sigma^2}\iint_S e^{q_z^2 C(R)}\, e^{i\left(q_x X+q_y Y\right)}\,dX\,dY \tag{4.26}$$

For the purposes of modelling the sample roughness, each individual interface can be described by the shape function $z(x,y)$, where the *XY*-plane is parallel to the sample surface. For many isotropic surfaces [9], it can be assumed that:

$$g(R)=2\sigma^2\left[1-e^{-\left(\frac{R}{\xi}\right)^{2h}}\right] \tag{4.27}$$

and the height-height correlation function is given by the isotropic self-affine correlation function:

$$C(R)=\sigma^2\, e^{-\left(\frac{R}{\xi}\right)^{2h}} \tag{4.28}$$

where $R=\left(X^2+Y^2\right)^{\frac{1}{2}}$.

Here, the roughness σ governs the amplitude of the fluctuations and the correlation length of the height fluctuations, ξ, is the distance in the XY plane at which the correlation has decayed with $1/e$. The Hurst parameter h (which is related to the surface fractal dimension by $h=D-3$) determines the texture of the surface. The roughness exponent h is the key parameter which describes the height fluctuations at the surface and takes a value from 0 to 1. Parameter h close to 0 means an extremely jagged surface, while h close to 1 means a slowly oscillating smooth surface with hills and valleys. More details about the different models for description of the surface and interface roughness and the growth of thin films can be found in [9, 25-28].

4.5.3 Ideally flat surfaces

For ideally flat surfaces $g(R)$ is zero everywhere at the surface and the scattering cross-section yields:

$$S(q)=\frac{\rho^2 r_e^2 L_x L_y}{q_z^2}\iint_S e^{i(q_x X+q_y Y)}\,dX\,dY \tag{4.29}$$

The integral is the Fourier transform of a constant so that:

$$S(q)=\frac{4\pi^2\rho^2 r_e^2 L_x L_y}{q_z^2}\,\delta q_x\,\delta q_y \tag{4.30}$$

leading to the following well-known reflectivity:

$$\mathrm{I}(q)=\frac{16\pi^2\rho^2 r_e^2}{q_z^4} \tag{4.31}$$

The reflectivity decreases as a power law with q_z and is defined by Dirac distributions in the orthogonal directions, thus showing that for a flat surface the reflectivity is strictly *specular*.

4.5.4 Rough surfaces without cut-off

Consider self-affine rough surfaces presenting a correlation length large in comparison with the coherence length. As previously shown, $g(R)$ is given by

$g(R)=2\sigma^2\left[1-e^{-\left(\frac{R}{\xi}\right)^{2h}}\right]$, and if $R/\xi \ll 1$ then:

$$g(R)=2\sigma^2\left[\frac{R}{\xi}\right]^{2h} \tag{4.32}$$

This function can be written as:

$$g(R)=\frac{2\sigma^2}{\xi^{2h}}R^{2h}=AR^{2h} \tag{4.33}$$

The scattering cross-section yields:

$$S(q)=\frac{\rho^2 r_e^2 L_x L_y}{q_z^2}\iint_S e^{-\frac{q_z}{2}AR^{2h}}\, e^{i(q_x X+q_y Y)}\,dX\,dY \tag{4.34}$$

and can be expressed in polar coordinates as:

$$S(q)=\frac{\rho^2 r_e^2 L_x L_y}{q_z^2}\int e^{-\frac{q_z}{2}AR^{2h}}\, J_0(q_r R)\, R\,dR \tag{4.35}$$

$q_r=\left(q_x^2+q_y^2\right)^{\frac{1}{2}}$ is the in-plane scattering wavevector and J_0 the zero order Bessel function. The above integral has analytical solutions for $h=0.5$ and $h=1$ and has to be calculated numerically in other cases. For $h=1$:

$$S(q)=\frac{2\pi\rho^2 r^2 L_x L_y}{Aq_z^4}e^{-\frac{q_r^2}{2Aq_z^2}} \tag{4.36}$$

and for $h=0.5$:

$$S(q)=\frac{A\pi\rho^2 r_e^2 L_x L_y}{\left[q_r^2+\left(\frac{A}{2}\right)q_z^4\right]^{\frac{3}{2}}} \tag{4.37}$$

The above expressions clearly show that for surfaces of this kind the scattering is purely *diffuse*. The case $h = 0.5$ is of particular interest since it corresponds to self-affine rough surfaces presenting a random walk character. Examples of such a surface have been encountered in Langmuir–Blodgett films [29, 30].

4.5.5 Rough surfaces with cut-off

For rough surfaces presenting a cut-off length ξ, the development of $g(R)$ is no longer possible and the scattering cross-section becomes:

$$S(q) = \frac{\rho^2 r_0^2 L_x L_y}{q_z^2} e^{-q_z^2 \sigma^2} \iint_S e^{q_z^2 C(X,Y)} e^{i(q_x X + q_y Y)} dX\, dY \tag{4.38}$$

It is possible to separate this expression into the specular and the diffuse off-specular components by using the following method:

$$e^{q_z^2 C(X,Y)} = 1 + \left[e^{q_z^2 C(X,Y)} - 1 \right] \tag{4.39}$$

which yields:

$$S(q) = S_{spec}(q) + S_{diff}(q) \tag{4.40}$$

with:

$$\begin{aligned} S_{spec}(q) &= \frac{\rho^2 r_e^2 L_x L_y}{q_z^2} e^{-q_z^2 \sigma^2} \iint_S e^{-i(q_x X + q_y Y)} dX\, dY \\ &= \frac{4\pi^2 \rho^2 r_e^2 L_x L_y}{q_z^2} e^{-q_z^2 \sigma^2} \delta q_x\, \delta q_y \end{aligned} \tag{4.41}$$

and:

$$S_{diff}(q) = \frac{\rho^2 r_e^2 L_x L_y}{q_z^2} e^{-q_z^2 \sigma^2} \iint_S \left[e^{q_z^2 C(X,Y)} - 1 \right] e^{i\left(q_x X + q_y Y\right)} \, dX \, dY \tag{4.42}$$

The specular part is similar to that of a flat surface except that it is reduced by the $e^{-q_z^2 \sigma^2}$ roughness factor which is somewhat identical to a Debye–Waller factor. The diffuse scattering part may be determined if one knows the functional form of the height–height correlation function. If a stretched exponential is chosen, the parameters h and ξ are obtained by fitting the above expression to the data. This approach has been used to analyse a variety of thin films and multilayers. A nice example concerning W/Si multilayers is presented in Salditt *et al.* [31]. A more precise treatment can be made within the distorted wave Born approximation (DWBA) [9]. This allows one to take into account the Yoneda wings which appear in the transverse scans [32]. The DWBA is extremely useful to explain strong effects of multiple scattering visible in thin films [15, 33].

Finally, the effect of the instrumental resolution on the reflectivity analysis has to be considered. One must understand that this effect is of particular importance in the analysis of the diffuse scattering (for more details see ref. [7]). It is also important to realize that for very rough surfaces 'true specular reflectivity' may not exist and that only diffuse scattering would be observed (this will be evidenced in chapter 6 for Fe/Au multilayers). For this reason, any analysis of the specular reflectivity can only be valid under the condition that the diffuse scattering has been subtracted from the data.

4.5.6 Experimental techniques in the x-ray diffuse scattering

Several different types of diffuse scans are commonly used. The more detailed experimental aspects of x-ray scattering techniques will be presented in chapter 5.

1. Longitudinal scan (off-specular scan, or diffuse-nearspecular scan). In this case the incident angle θ_i is slightly different from the exit angle θ_e, i.e. $\theta_i = \theta_e + \Delta\theta$, where the offset angle $\Delta\theta$ is usually around -0.1°.

2. Transverse diffuse scan (rocking curve). In this case the source and the detector are fixed, and the sample is rocked, i.e. the scattering angle, $\theta_i + \theta_e$, is constant.

3. Radial scan (detector scan). In this case the source and the sample are fixed, and the detector is moved, i.e. only θ_e changes.

4. Full scan. In this case the sample is fixed, and both the source and the detector are moved, i.e. both θ_i and θ_e change.

5. Out-of-plane scan. In this case both angles θ_i and θ_e are fixed, and only the out-of plane angle (i.e. q_y) changes.

4.6 Summary

X-ray reflectometry is now widely used for the analysis of surfaces and interfaces. Its main advantage is that it allows one to determine the surface and interface roughness (when σ is typically less than 25 Å), the layer thickness, and the structural arrangement of complex architectures. Since measurements are made at small angles of incidence, it is not necessary for the analysed materials to be crystallized, which is also an advantage of the technique over classical diffraction methods.

The diffuse scattering which corresponds to the signal which is not specularly reflected gives additional information. In particular, one can learn from the diffuse scattering how the roughness of the interfaces is correlated both within one interface and from one interface to the next. From the x-ray diffuse scattering one can extract information on roughness, in-plane and out-of-plane correlation lengths and fractal parameter (σ , ξ, ζ, h respectively), correlation between the roughness of different interfaces (i.e. the conformal roughness), and in some cases separate information on roughness and grading at the interfaces, or separation of the roughness from the particles on the surface. Basic expressions for the x-ray diffuse scattered intensity and review of the possible applications of x-ray scattering for characterization of interfaces were presented in ref. [34]. A discussion on the out-of-plane scans (q_y- scans), from which one can obtain information on smaller lateral length scales, was published in refs. [35, 36].

REFERENCES

[1] B. Lengeler, in "*Photoemission and Absorption Spectroscopy of Solids and Interfaces with Synchrotron Radiation*", Eds.: M. Campagna and R. Rosei, North-Holland, 1991, pp. 157-202.

[2] *Elements of Modern X-ray Physics*, J. Als-Nielsen and D. McMorrow, John Wiley & Sons, Ltd. (2000).

[3] A. H. Compton, *Philos. Mag.*, **45** , 112 (1923).

[4] D. K. G. de Boer, *Phys. Rev. B*, **49 (9)**, 5817-5820 (1994).

[5] L. G. Parratt, *Phys. Rev.*, **95 (2)**, 359-369 (1954).

[6] *Principles of optics*, M. Born and E. Wolf, 6 ed., Pergamon (1980).

[7] A. Gibaud, G. Vignaud, and S. K. Sinha, *Acta Crystallogr. Sect. A*, **49** , 642-648 (1993).

[8] H. Kiessig, *Ann. Phys.*, **10**, 769 (1931).

[9] S. K. Sinha, E. B. Sirota, S. Garoff, and H. B. Stanley, *Phys. Rev. B*, **38 (4)**, 2297-2311 (1988).

[10] D. E. Savage, J. Kleiner, N. Schimke, Y. H. Phang, T. Jankowski, J. Jacobs, R. Kariotis, and M. G. Lagally, *J. Appl. Phys.*, **69 (3)**, 1411-1424 (1991).

[11] E. Spiller, D. Stearns, and M. Krumrey, *J. Appl. Phys.*, **74 (1)**, 107-118 (1993).

[12] G. Gladyszewski, *Thin Solid Film*, **275**, 184 (1996).

[13] V. M. Kaganer, S. A. Stepanov, and R. Kohler, **221 (1-4)**, 34-43 (1996).

[14] W. Weber and B. Lengeler, *Phys. Rev. B.*, **46 (12)**, 7953 (1992).

[15] V. Holý, J. Kubena, I. Ohlidal, K. Lischka, and W. Plotz, *Phys. Rev. B*, **47 (23)**, 15896-15903 (1993).

[16] V. Holý, *Appl. Phys. A-Mater. Sci. Process.*, **58 (3)**, 173-180 (1994).

[17] V. Holý and T. Baumbach, *Phys. Rev. B*, **49 (15)**, 10668-10676 (1994).

[18] V. Holý, T. Baumbach, and M. Bessiere, *J. Phys. D-Appl. Phys.*, **28 (4A)**, A220-A226 (1995).

[19] D. K. G. deBoer and A. J. G. Leenaers, *Physica B*, **221 (1-4)**, 18-26 (1996).

[20] G. H. Vineyard, *Phys. Rev. B*, **26 (8)**, 4146-4159 (1982).

[21] M. Kopecky, *J. Appl. Phys.*, **77 (6)**, 2380 (1995).

[22] M. Rauscher, T. Salditt, and H. Spohn, *Phys. Rev. B*, **52 (23)**, 16855-16863 (1995).

[23] D. K. G. de Boer, *Phys. Rev. B.*, **53 (10)**, 6048 (1996).

[24] T. A. Leskova and A. A. Maradudin, *Waves Random Media*, **7 (3)**, 395-434 (1997).

[25] G. Palasantzas, *Phys. Rev. B*, **48 (19)**, 14472-14478 (1993).

[26] G. Palasantzas, *Phys. Rev. B*, **49 (15)**, 10544-10547 (1994).

[27] *Fractal Concepts in Surface Growth*, A.-L. Barabasi and H. E. Stanley, Cambrige University Press (1995).

[28] *Fractals, scaling and growth far from equilibrium*, P. Meakin, Cambridge University Press (1998).

[29] A. Gibaud, *Phys. Rev. Lett.*, **74** , 2305 (1995).

[30] J. K. Basu, *Phys. Rev. Lett.*, **82** , 4675 (1999).

[31] T. Salditt, D. Lott, T. H. Metzger, J. Peisl, G. Vignaud, P. Hoghoj, O. Scharpf, P. Hinze, and R. Lauer, *Phys. Rev. B*, **54 (8)**, 5860-5872 (1996).

[32] Y. Yoneda, *Phys. Rev.*, **131 (5)**, 2010-2013 (1963).

[33] J. P. Schlomka, M. Tolan, L. Schwalowsky, O. H. Seeck, J. Stettner, and W. Press, *Phys. Rev. B*, **51 (4)**, 2311-2321 (1995).

[34] G. Renaud, *J. Phys. III*, **4 (10)**, 1795-1810 (1994).

[35] T. Salditt, T. H. Metzger, and J. Peisl, *Phys. Rev. Lett.*, **73 (16)**, 2228-2231 (1994).

[36] T. Salditt, T. H. Metzger, J. Peisl, and G. Goerigk, *J. Phys. D-Appl. Phys.*, **28 (4A)**, A236-A240 (1995).

Chapter 5

X-ray Experiments and Analysis

5.1 Introduction

When Röntgen discovered x-rays just before the beginning of the 20th century, it took him and others only a few months to realize their importance for the investigation of medical and applied problems. In the first 50 years after this event, the intensity of these x-rays was increased by about two orders of magnitude until the classical method of producing x-rays reached its natural technological limits with the rotating anode tube. The major problems were firstly that most of the energy of the electrons is converted to heat and secondly that only a small fraction of the x-rays produced can be used for experiments because the source emits radiation in a large solid angle. In x-ray tubes, x-rays are emitted by decelerating electrons in an anode (e.g. copper or cobalt). The emission cone spans the full half space [1, 2]. With the exception of radiology on large objects, only a small fraction of this emission cone is used. If samples are small and irradiation occurs, e.g. in crystallography, these sources are far from ideal.

In the 1950s, synchrotrons and later storage rings for electrons, which emit x-rays due to a large centripetal acceleration came into operation. Synchrotron radiation takes its name from a specific type of particle accelerator. At relativistic energies, this acceleration can become enormous while, unlike in an anti-cathode, the electrons are not lost. During 1970s, pioneering experiments in many different research fields demonstrated the usefulness of this new tool.

Besides synchrotrons themselves, synchrotron radiation is produced in storage rings where electrons or positrons are kept circulating at constant energy. In a storage ring the synchrotron radiation is produced either in the bending magnet needed to keep the electrons in a closed orbit, or in insertion devices such as wigglers or undulators, situated in the straight section of the storage ring. In these devices, an alternately directed magnetic field forces the electrons to follow oscillating paths rather than moving in a straight line. In a wiggler, the amplitude of the oscillations is rather large, and the radiation from different wiggler magnets adds incoherently. More information on x-ray sources can be found in many articles [2-8].

The x-ray experimental work in this thesis has been carried out on both laboratory and synchrotron sources. This chapter is divided into three parts. A brief review is given of 1) the x-ray sources used in this thesis, 2) x-ray data collection, and 3) the analytical software which was used for analysing x-ray data.

5.2 X-ray sources

The x-ray experimental work in this thesis has been carried out on a Bede GXR1 laboratory reflectometer at the University of Durham, station 2.3 at the SRS (Daresbury), and beamline BM16 at the ESRF in Grenoble. In this part a brief review of these sources will be presented.

5.2.1 Laboratory Sources

After the discovery of x-rays by Röntgen, for several years the only source for producing x-rays was a hot-cathode tube. The x-ray tube that Röntgen used was difficult to run reliably. It was a tremendous practical step forward when in 1912; W. D. Coolidge developed a new tube in the General Electric Research Laboratories in New York. In this new tube, electrons were produced by a glowing filament and subsequently accelerated towards a water-cooled metal anode. The spectrum of x-rays generated from electrons impinging on the metal anode has two distinct components. There is a continuous part due to the electrons being decelerated, and eventually stopped in the metal. This is known as *bremsstrahlung* radiation (after the German *bremsen* for brake), and has a maximum energy that corresponds to the high voltage applied to the tube. Superimposed on this broad spectrum is a sharper line spectrum (Figure 5.1(a)). As can be seen in Figure 5.1(b), in a collision with an atom the incident electron may also cause an atomic electron to be removed from one of the inner shells, creating a vacancy. The subsequent relaxation of an electron from an outer shell into the vacancy produces an x-ray with a characteristic energy equal to the difference in energy between the two shells (the fluorescent radiation). As the characteristic shells are labeled **K**, **L**, **M**, etc, a transition from the **L** (**M**) level to the K level corresponds to a line denoted $\mathbf{K}_\alpha$ ($\mathbf{K}_\beta$). The intensity of the X-ray radiation is proportional to the beam current; the larger the number of electrons striking the target, the greater the number of x-rays that are produced. However, most of the energy of the electrons is converted to heat within the target and so a generator operating at 40KV and 25 mA produces almost 1KW of power.

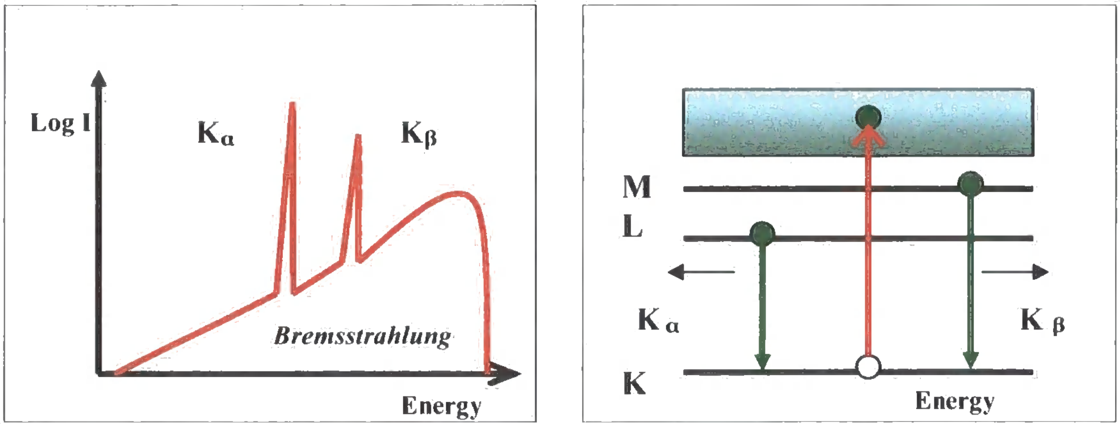

(a) **(b)**

Figure 5.1 (a) The spectrum from an x-ray tube. **(b)** Schematic atomic energy level diagram (reproduced from Ref. [2]).

It is possible to produce a more powerful x-ray generator, by using a rotating anode target. In a rotating anode, the target has a cylindrical shape, which rotates. The point of impact of the electron beam therefore moves, effectively increasing the target area and reducing the localized heat load. In these systems, the power can be increased up to around 18 kW, depending on focal spot size. However , they are much more costly to run, and require regular servicing [2, 9].

5.2.1.1 Bede GXR1

The x-ray experiments were carried out, firstly, on a Bede Scientific laboratory reflectometer (GXR1). A schematic of the GXR1 reflectometer can be seen in Figure 5.2. The x-ray reflectometer measures the intensity reflected in the specular direction $(\theta_i = \theta_r)$ as a function of the grazing incidence angle. The source was a copper target x-ray tube operated at 40 kV and 40 mA, monochromatized to $Cu\ K_\beta$ (λ=1.3926 Å). The specular reflectivity curves were taken as a function of incidence angle using a $\theta/2\theta$ scan, with the detector stepped at twice the step of the specimen. Specular and off-specular reflectivity curves were taken for each sample, with θ_i usually varying in the range 0 - 10000 arc seconds, with a step of 20 arcseconds. A -360 arc seconds offset of the sample angle was used for the off-specular measurements. This type of scan collects the diffuse scatter just off the specular ridge. The true specular reflectivity curves were obtained by subtracting the off-specular measurement from the specular, to remove the forward diffuse scatter. Transverse diffuse data were taken by fixing the scattering angle, i.e., the detector and scanning the sample from grazing incidence to grazing exit. The specular peak is typically 100 arc seconds in width.

The x-ray reflectometer probes a macroscopic area of sample, as the x-ray beam is 1-5 mm wide and 100 μm high (as defined by beam slits), with a divergence of about 50". A more detailed description of the GXR1 concerning the experimental requirements and alignment can be found elsewhere [10-12].

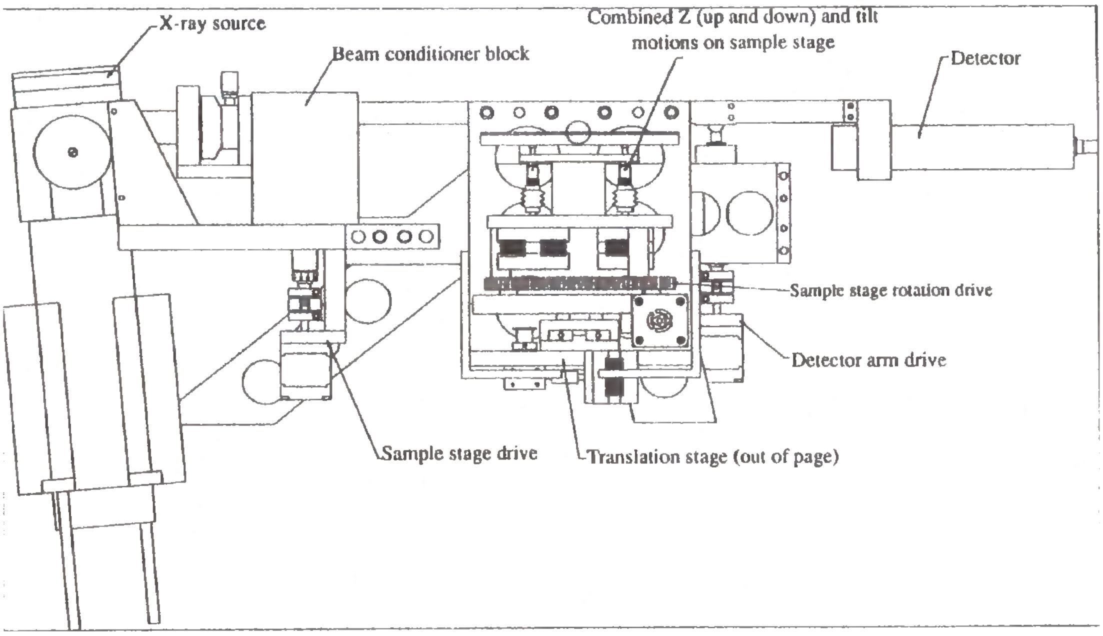

Figure 5.2 A schematic of the GXR1 reflectometer [11].

5.2.2 Synchrotron radiation source

Nowadays stronger sources of x-rays are synchrotrons and storage rings. At this moment, three third generation storage rings are in operation worldwide: the ESRF, in Grenoble, France, the APS in Argonne, USA, and Spring-8 in Harma, Japan. The majority of x-ray data presented in this thesis were obtained from synchrotron sources (at the ESRF and at the SRS).

5.2.2.1 Station 2.3 at the SRS, Daresbury, UK

A large proportion of x-ray data presented in this thesis, was obtained from station 2.3 at the Daresbury synchrotron radiation source. Station 2.3 was initially designed as a Powder Diffraction beamline [13]. At the SRS in Daresbury, the energy of the electrons is 2 GeV and the ring has a circumference of 96m. The station is situated about 15m tangentially from a 1.2T dipole magnet in the electron storage ring receiving x-rays ranging from 0.7Å to 2.5Å. Figure 5.3 shows the measured intensity distribution on the station. The intensity of the beam was monitored as the monochromator angle was varied. The peak flux of the station occurs at a wavelength of approximately 1.3Å.

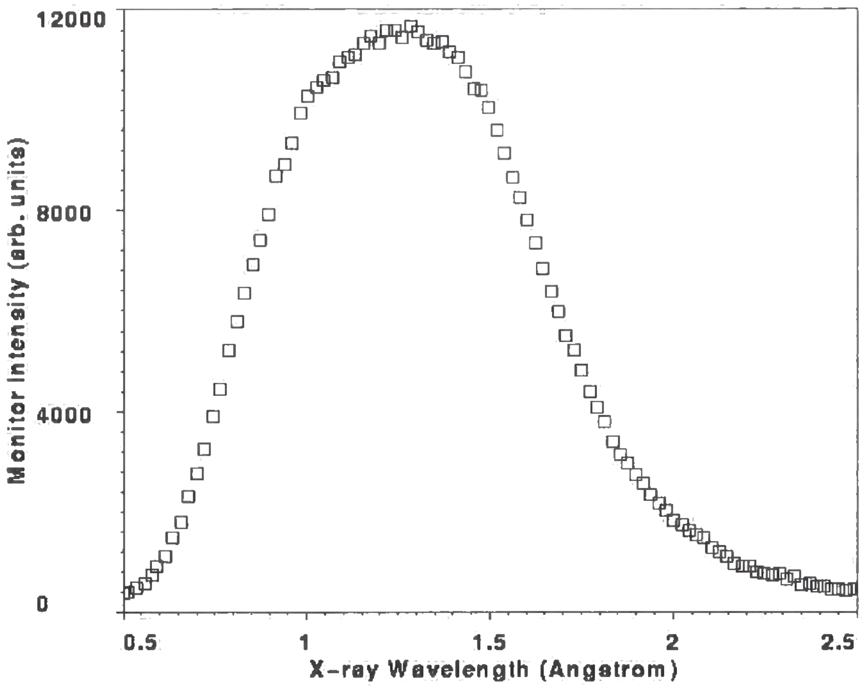

Figure 5.3 The intensity distribution from the station 2.3 [14].

For experimental purposes, a monochromatic, low divergence beam is required before the generated x-ray beam reaches the sample. Due to the relativistic nature of the electrons, this low divergence is achieved inherently at a synchrotron (i.e. approximately 200" vertical divergence at SRS beamline 2.3). The wavelength can then be selected by using a monochromating crystal (e.g. a water-cooled Si (111) monochromator at SRS 2.3; after monochromation the angular divergence of the incident beam, at this station, is about 10"). A schematic of the station set up for reflectometry studies is shown in Figures 5.5.

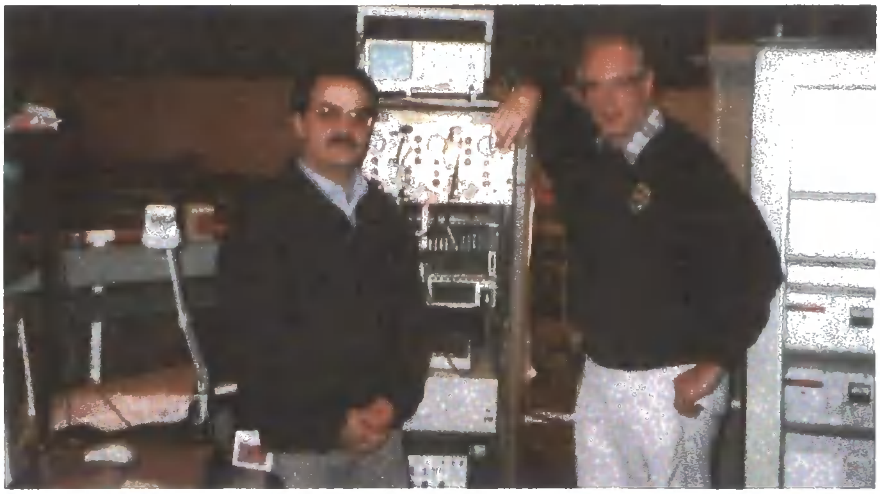

Figure 5.4 Station 2.3 control area.

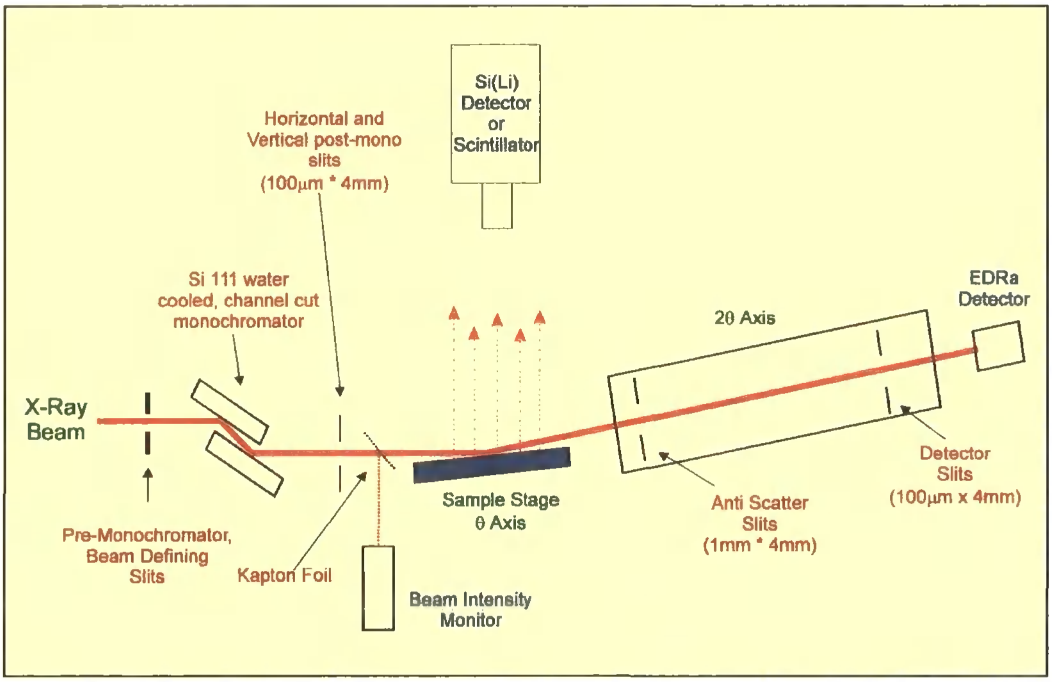

Figure 5.5 A schematic of the station 2.3 for reflectivity geometry [14].

As can be seen in Figure 5.5, the conditioned beam passes through a set of beam defining slits. These slits can be varied in height and width to give the required beam size and energy bandpass on the sample. The detection of x-rays is also very important. In a typical reflectivity experiment the detector must be able to detect a totally reflected beam and then be sensitive enough to handle the low intensity of the diffuse scatter. The detector used in all the experiments was the Bede EDR [15]. This high dynamic range detector has a minimum count rate of about 0.15 counts per second and was found to be non-linear for count rates greater than 4×10^5 counts per second. In order to define the resolution of the instrument, a series of slits are placed immediately in front of the detector, as shown in Figure 5.5, the height of the slits being the same as that of the incident beam. In addition, anti-scatter slits are placed on the detector arm close to the sample, in order to reduce the noise at the detector by eliminating extraneous scatter. In order to reduce further the absorption, the air path from the sample to the detector was evacuated [12, 13, 16].

5.2.2.2 BM16 (now ID31) at the ESRF, Grenoble, France

The ESRF is a third generation synchrotron radiation source consisting of an 850-metre circumference storage ring fed from a 300-metre circumference booster synchrotron [6, 17-19]. The main storage ring operates at 6 GeV giving a critical wavelength shorter than that of the Daresbury SRS and more intensity at the higher end of the energy spectrum.

BM16 at the ESRF, was similar to station 2.3 in the sense that it was designed for high resolution powder diffraction studies. However, there are some differences. Firstly, at the experimental end of the beamline there was an additional analyser system comprising nine germanium (111) crystals with a 2 degree separation. This enabled true triple axis diffraction measurements to be undertaken although in this study analyser slits were used in order to avoid the loss of intensity associated with an analyser crystal arrangement [8]. BM16 also differed from station 2.3 in terms of the design of the optical elements. A monochromator, comprising of two Si(111) crystals, was used. One crystal was cooled to dissipate the heat load from the incident beam and the other could be curved to focus sagitally the beam. The focusing was in the horizontal plane of the beam, the vertical angular divergence of which remained unchanged. The beam could be focused vertically to increase the incident flux at the sample, using a mirror placed further down the line at a cost to the angular resolution. A schematic of BM16 can be seen in Figure 5.6.

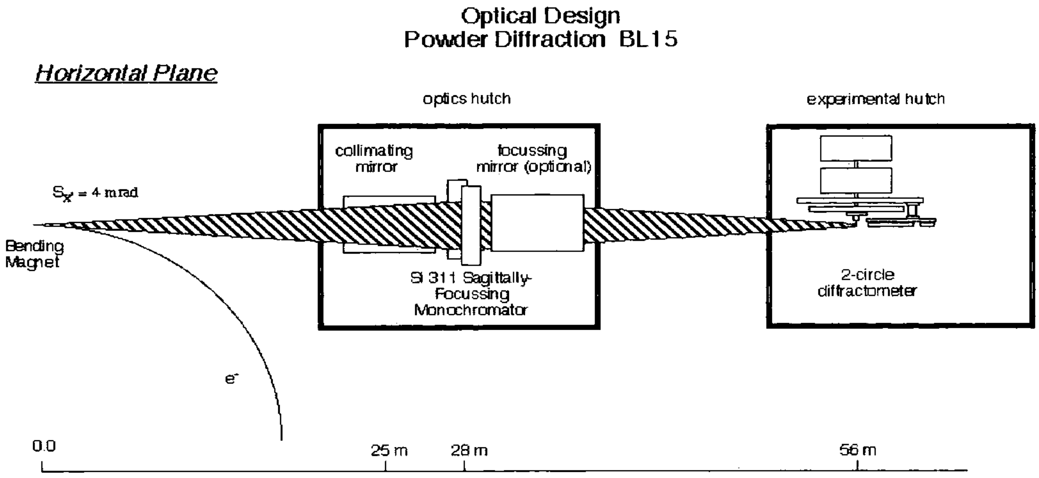

Figure5.6 A schematic of beamline BM16 at the ESRF.

Another detector used for experiments at BM16 was a CCD camera for the collection of 2-dimensional diffraction patterns. This device has the advantage of collecting the whole diffraction pattern in a few seconds, which is useful for example in measurements where the experimental conditions change very rapidly (e.g. temperature, pressure, chemical reactions).

5.3 X-ray data collection

The first step was to carry out x-ray scans by using the laboratory reflectometer, GXR1. It will be shown in the next section that, for Co/Pt and most of the Co/Pd multilayers, these scans were not suitable for curve fitting as the maximum range of the variation of detector (2θ) in GXR1 is approximately seven degrees. In addition, the intensity of laboratory based x-ray sources is not enough for studying the interface roughness of the samples used in this study (except for very rough interfaces e.g. Fe/Au multilayers). A comparison between two off-specular (longitudinal) diffuse scatter data sets taken in the laboratory and at the synchrotron source can be seen in Figure 5.7. The off-specular fringes can clearly be seen in the synchrotron source data, while one could conclude that the conformality is lost by analyzing the laboratory off-specular data. Many papers have reported such a conclusion which, of course, is wrong.

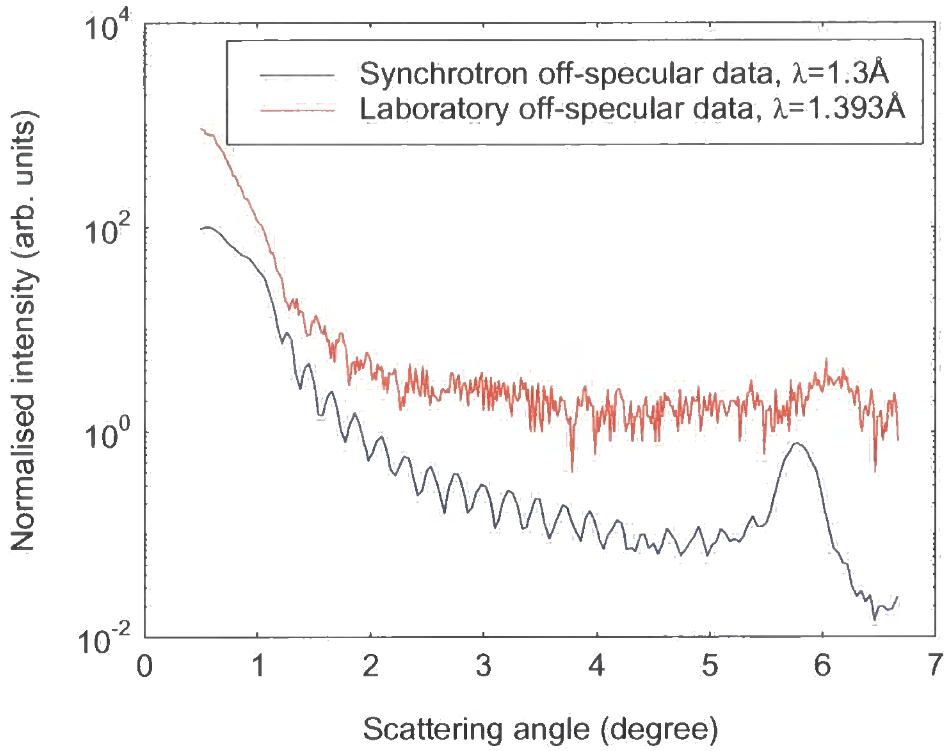

Figure 5.7 A comparison between off-specular scans taken at the synchrotron source and in the laboratory.

The reason for running samples on the GXR1 was to select a series of samples with good interface structure. It was found that one Co/Pt sample (with 22 bilayers), five Fe/Au samples, and several samples from the Co/Pd series had very poor interfaces. The second step was then to run the selected samples on the station 2.3 and BM16.

5.4 Alignment issues with synchrotron data

A very careful alignment is needed for x-ray scans when using both laboratory and synchrotron sources. The most important part of the aligning procedure is to ensure that the sample holder is at the centre of rotation of all diffractometer axes. The diffractometer is a two-circle machine with a sample (omega or theta) axis and a detector (2theta) axis. By fixing the cross hairs of a telescope on the sample holder and then rotating the omega (theta) axis through 180 degrees it is possible to ensure that the holder does not move either laterally or vertically. Any adjustments that are required can be made via a goniometer on the sample stage until no observed movement of a reference point on the holder occurs with respect to the telescope cross hairs. This ensures that the alignment is accurate to within approximately 10μm both laterally and vertically. The entire diffractometer is raised or lowered until the sample holder half cuts the incident beam. The position of the diffractometer is then fixed and any further alterations to the sample height are made via the goniometer on the holder until the sample itself half cuts the beam. Once the diffractometer is aligned it is a relatively trivial process to align the actual sample to the beam. An attenuator is placed in the incident beam (not for the GXR1, where the tube current is reduced) and the detector scanned across the beam in order to find the detector zero position. The sample, mounted on the holder is raised into the beam until the beam is half cut. The sample angle is rocked and the count maximised to ensure that the sample is lying flat with respect to the beam. This position is set as the omega zero point. The detector is driven out to a small angle, typically 2 degrees and any attenuation removed. Small increments to the sample angle are made until the intensity reaches a maximum. At this point the sample angle is set as half of the detector angle. This process is then repeated at higher scattering angles to verify that the alignment is correct. The entire process assures that the sample is at the centre of rotation of the diffractometer, flat to the beam at zero angle and accurately aligned to the specular condition [12, 20].

At the higher scattering angles, alignment is more difficult when using synchrotron sources (easy to slip off specular ridge due to higher resolution). In the case of Co/Pd samples, it was much more difficult to align samples at higher degrees. In some cases the laboratory specular data was better to achieve the best fits. Two examples of the case are illustrated in Figures 5.8 and 5.9. The second Bragg peak can clearly be seen in the laboratory data while, it did not appear in the synchrotron data. This may be due to the different scattering factors at the different energies.

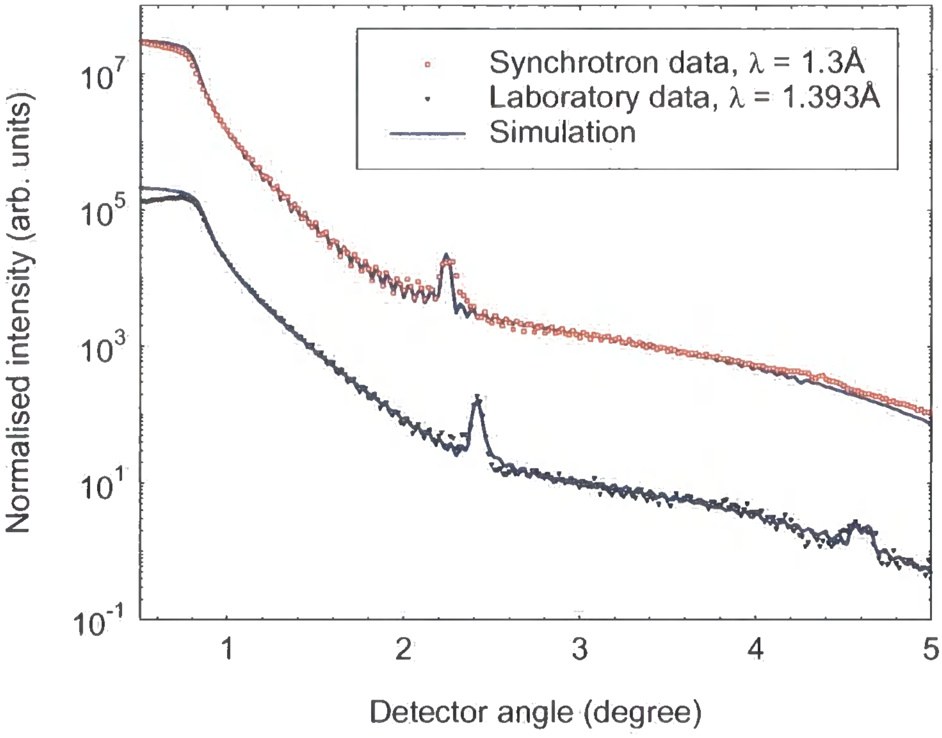

Figure 5.8 A comparison between synchrotron and laboratory data for a Co/Pd multilayer (series 1) with 30 bilayers.

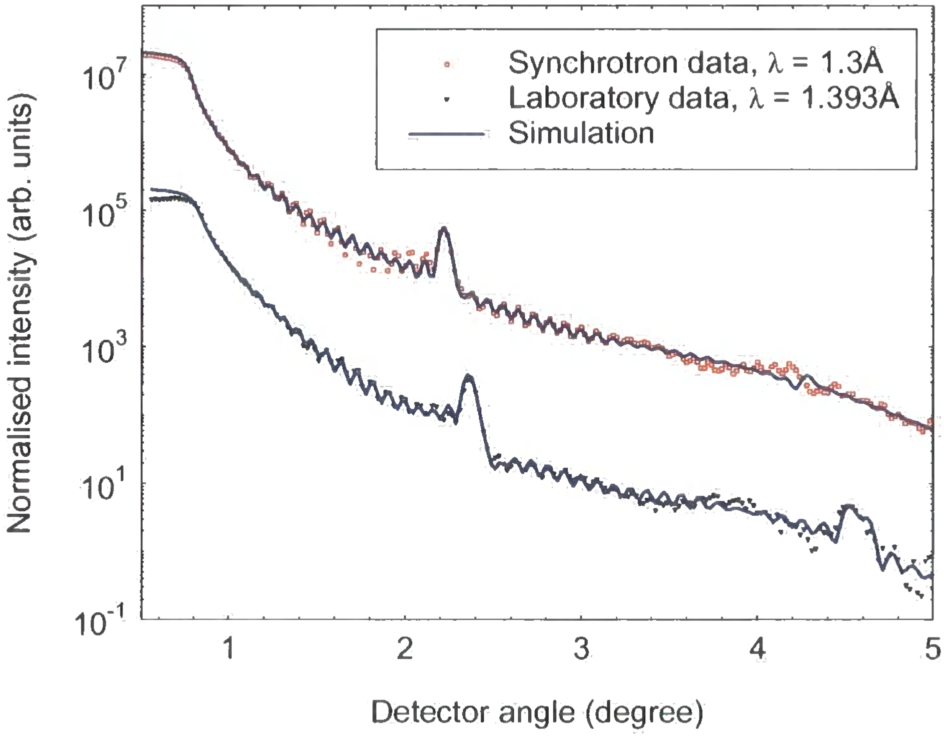

Figure 5.9 A comparison between synchrotron and laboratory data for a Co/Pd multilayer (series 2) with 20 bilayers.

As is shown in Table 5.1 for the 30-bilayer Co/Pd sample (from series 1), very different interface parameters could be found by simulating these two experimental data. In chapter 8, it will be shown in details that the model is compatible with the interface parameters obtained from laboratory data. As expected, the thickness values are close but the interface parameters deduced from simulation of diffuse data (both longitudinal and transverse) seems to be very different. This could lead to very different conclusions while studying the effect of interface roughness on very important phenomena such as magnetic anisotropy.

Table 5.1 A comparison between the interface parameters deduced from the simulations of Synchrotron and Laboratory data.

Data type	t_{Buffer} *Pd* ±0.3Å	$t_{bil.}$ *Co* ±0.3Å	$t_{bil.}$ *Pd* ±0.3Å	σ_{Buffer} *Pd* ±0.3Å	$\sigma_{bil.}$ *Co* ±0.3Å	$\sigma_{bil.}$ *Pd* ±0.3Å	ζ ±10%	ξ ±10Å	h ±10%
Synch.	34.4	3.5	32.1	4.9	9.3	10.0	250	125	0.40
Lab.	26.7	1.5	33.8	8.7	4.1	5.2	250	900	0.75

In order to ensure that the specular data that were collected at the synchrotron radiation source are reliable, one should consider that the higher reflected intensity near the critical angle gives rise to the saturation of the first Bragg peak (and the Kiessig fringes close to the critical angle). An example of such saturation can be seen in Figure 5.10. No curve can be fully fitted to such experimental data. The specular scan can be corrected by using the attenuators, over the required range and then patched together.

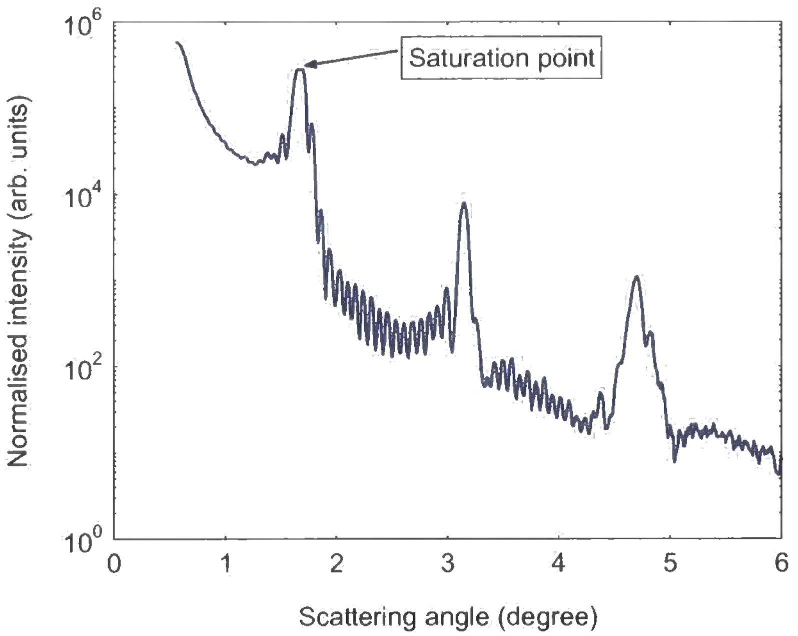

Figure 5.10 Saturation occurred at the first Bragg peak for a Fe/Au sample.

5.5 X-ray data analysis

The final step was to deduce the layer and interface structural parameters of the samples by fitting the specular and transverse diffuse data to profiles simulated from model structures using Bede REFS and REFS Mercury codes. These codes are based on a fractal model of the interfaces within the Distorted Wave Born Approximation (DWBA) [21-27]. Both codes use Parrat's recursive formalism of the Fresnel equations to calculate the reflected wave amplitude and thus the reflected intensity [28-31]. Usually, the individual layers in a multilayer system are expected to grow as stratified media with continuous interfaces, which do not intersect each other. Thus, the Parratt optical formalism combined with distorted wave born approximation (DWBA) is typically applied for evaluation of the reflectivity curves. In this model, surface and interface roughnesses are incorporated by assuming a Gaussian variation of the electron density gradient at each interface. This permits an analytic solution of the modified Fresnel reflectivity in both the Born and the distorted wave Born approximation (DWBA). A genetic algorithm is used to minimise automatically the logarithm of the difference in the absolute intensity between the simulated and experimental curve as the model parameters are adjusted by the computer. By fitting of the simulated curves to the experimental data, not only the film thickness and electron density but also the surface and interface roughness (*rms)* can be deduced.

This final step is in some ways the most important part of the work. Although the MERCURY code is automated, the deduced layer model may not be unique. As the specular data should then be used to simulate transverse diffuse data manually, reliable simulation of the specular scatter is crucial. In other words, incorrect simulation of specular data could lead to a significant error in analysis (see for example references [32, 33]). In this final part of the chapter, the certain aspects of the simulation procedure using MERCURY and REFS codes will be discussed.

5.5.1 Grazing incidence x-ray specular reflectivity analysis using Bede mercury code

Grazing incidence specular reflectivity is the most widely used of the x-ray scattering techniques. In the specular scattering geometry the scattering vector is directed normal to the sample surface at all times (chapter 4). Specular scans, in which the detector is scanned at twice the rate of the sample, provide information on near surface electron density, layer thickness and average interface width. They do not distinguish between compositional grading and true roughness as there is no component of scattering vector in the surface (Appendix C). From these measurements, the bilayer and total stack thickness are determined from the Bragg peak and Kiessig fringe period, respectively. For a multilayer system, consisting of many individual bilayer repeats, the reflectivity signal can be thought of in two distinct parts. Firstly, high frequency Kiessig, or thickness, fringes arise from interference between x-rays reflected from the top surface and substrate. In addition to this, the bilayer repeats act as a pseudo crystal structure with a large lattice spacing out of the plane of the film. At certain scattering vectors, this large d spacing gives rise to constructive interference, described by Bragg's law and produces a specular Bragg peak. The intensity and sharpness of the Bragg peak depends on the number of bilayers, period dispersion and interface roughness within the structure. The structural parameters are deduced by fitting the specular data to profiles simulated from model structures using the Bede Mercury code, which is an automated program. By defining the range of variations for thickness, roughness, and density of different layers, the programme uses a genetic algorithm to minimize the difference between the experimental and simulated data. Although statistically equivalent best fits can be achieved in most cases, the structural parameters are not always correct. The data are always limited in extent and this truncation can lead to significant error in the analysis. Two best fits to the laboratory specular data, for a 10-bilayer Co/Pt sample can be seen in Figure 5.11(a) and (b). Figure 5.11(a) shows a simulation which has a lower cost function (representing the normalised deviation between experiment and simulation). It is clear that the thickness values are very different from the nominal growth values and from the values in Figure 5.11(b). However, as can clearly be seen in Figure 5.12, an extension of these two simulations will not fit to the experimental data at higher scattering angles. Indeed the one with the lower cost function fits worst. The cost function could not be always considered as the only or best parameter for achieving the best fits. Finally, Figure 5.13 shows the best fit to the synchrotron specular data.

As stated before, in case of Co/Pd multilayers, it has been much more difficult to achieve the best fits. Co/Pd samples consist of four series showed different layer structure for each series of samples.

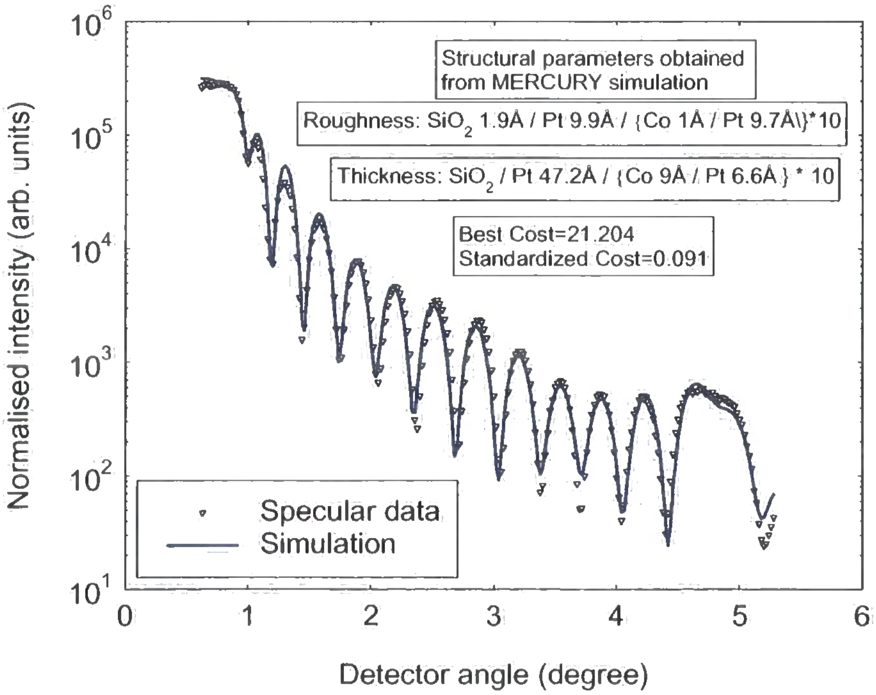

(a)

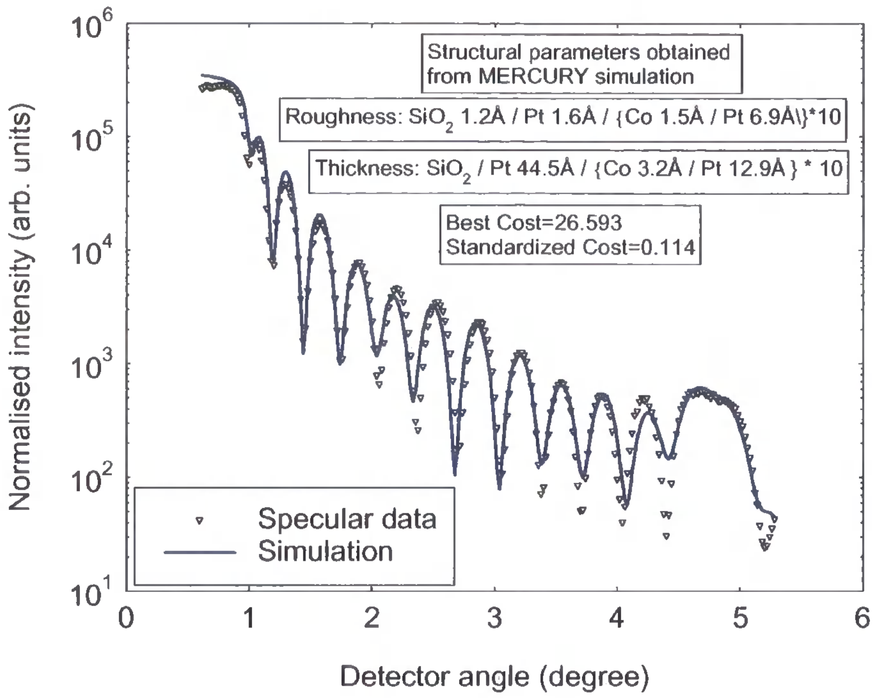

(b)

Figure 5.11 Two best fits to the laboratory data.

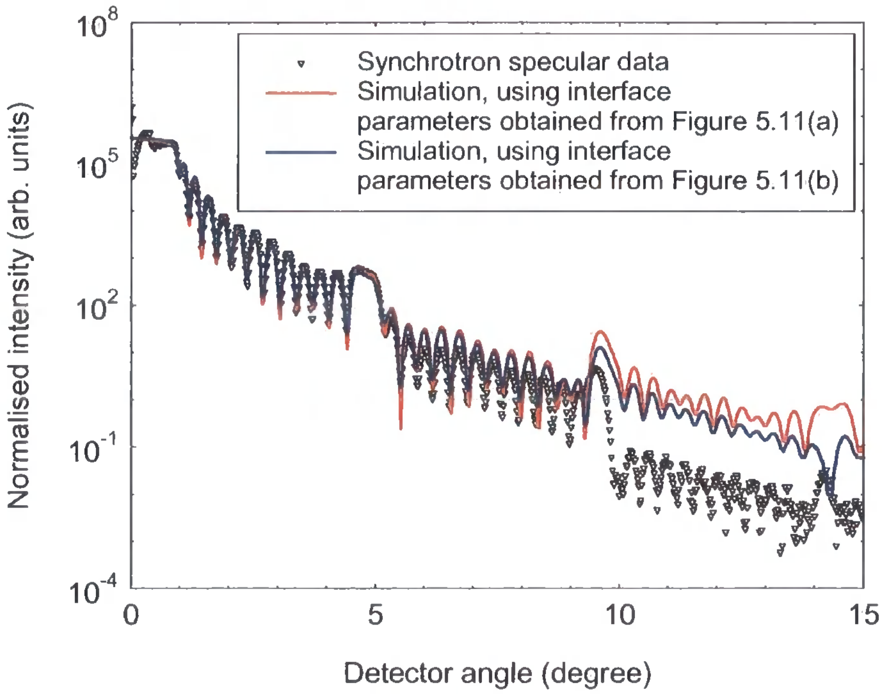

Figure 5.12 Synchrotron data and fits by using parameters obtained from Figure 5.11.

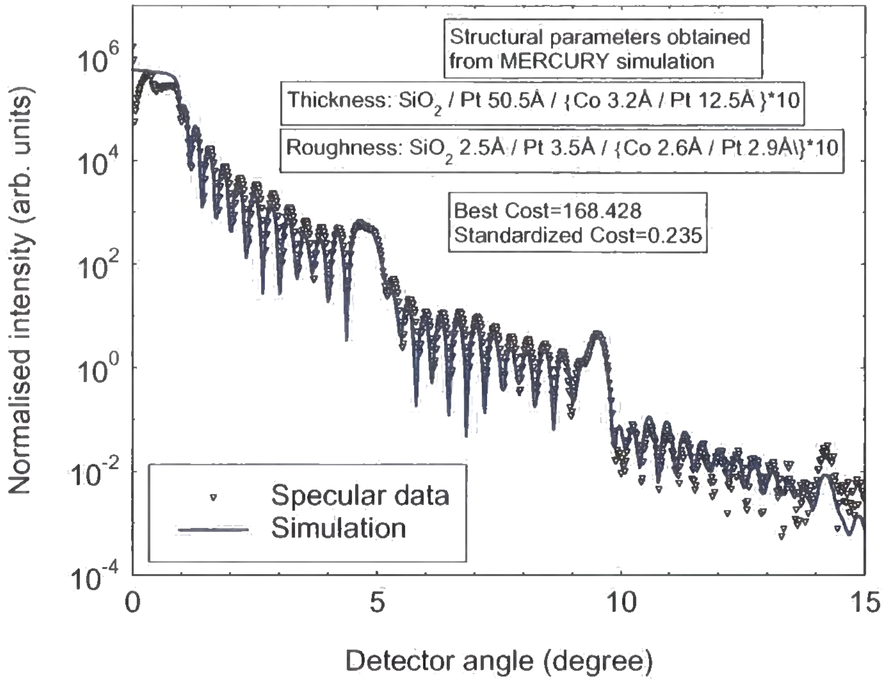

Figure 5.13 Synchrotron specular data and the best fit.

5.5.2 Non-specular (longitudinal and transverse) x-ray diffuse scattering analysis using Bede REFS code

Non-specular diffuse scattering measurements have been widely used for the investigation of surface and interfacial roughness in various multilayers. In the magnetic multilayers, the interfacial roughness originating from atomic disorder is expected to cause magnetic disorder at the surface or interfaces as well as the enhancement or reduction of magnetic moments. A typical way to determine the interface structure is to construct a model that describes the structure and from which the x-ray data can be simulated (chapter 4).

From qualitative investigation of the off-specular data, a great deal of information about interface propagation and conformality can be releaved. An immediate qualitative estimate as to the degree of conformal growth within a multilayer stack can be made by looking at the grazing incidence off-specular scan. However, it is the simulation of transverse diffuse measurements that yields the most important information about the in-plane structure and the degree of conformality both within the bilayer and across the total stack thickness. By using simulation software, extensive work is needed to construct a model based on the simulated data. The Bede REFS software [34] uses the theory of Sinha *et al* [22] based on a fractal model for the interfaces and use the DWBA. The Bede REFS code considers three models for roughness: correlated, uncorrelated, and partially correlated (model I and II). By simulating diffuse scattered data, four further parameters can be deduced: in-plane (lateral) correlation length (ξ), out-of-plane (vertical) correlation length (ζ), Hurst fractal parameter (h), and vertical correlation fraction (*VCF*). The best simulations could be achieved by choosing the correct model.

5.5.2.1 Longitudinal diffuse scans (off-specular)

An example of an off-specular data and simulation is shown in Figure 5.14. Both Kiessig fringes and Bragg peaks can clearly be seen in the off-specular data. By using the partially correlated roughness (model I) and changing the vertical correlation fraction (VCF), the off-specular data could be simulated (Figure 5.14(a)). By varying the VCF, the amount of roughness that is correlated at any interface can be specified as a proportion of the total interface roughness. In this model the in-plane correlation length and fractal parameter are held constant at each interface.

In the absence of any interdiffusion between layers, the average interface width represents the topological roughness and can be written as follows:

$$\sigma_{rms}^2 = \sigma_{Correlated}^2 + \sigma_{Uncorrelated}^2 \qquad (5.1)$$

A series of off-specular simulations using the partially correlated roughness (model II) are shown in Figure 5.14(b). This model allows more parameters to be varied and gives a better description of the interface correlations (i.e. both lateral and vertical correlation lengths). However, a small increase in the number of layers leads to a large increase in the computational time involved in simulation (especially for simulating diffuse scatter data). By using both of these models (model I and II) for simulation of the off-specular data, the ratio of the vertically correlated to the *rms* roughness (vertical correlated fraction, *VCF*) and vertical correlation length (ζ) could be obtained, respectively. These values are then held constant when simulating diffuse scatter in a series of data sets for one sample.

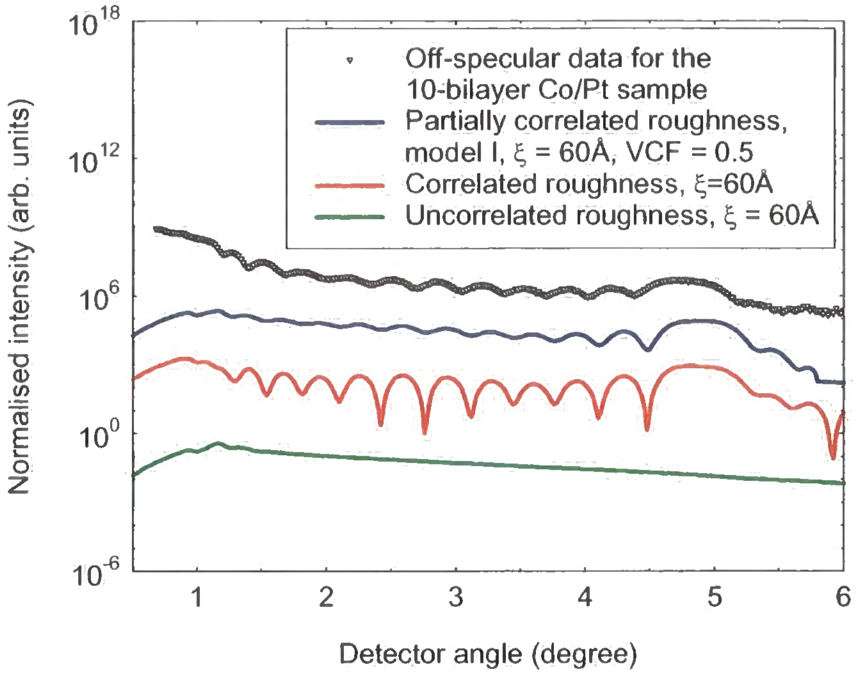

(a)

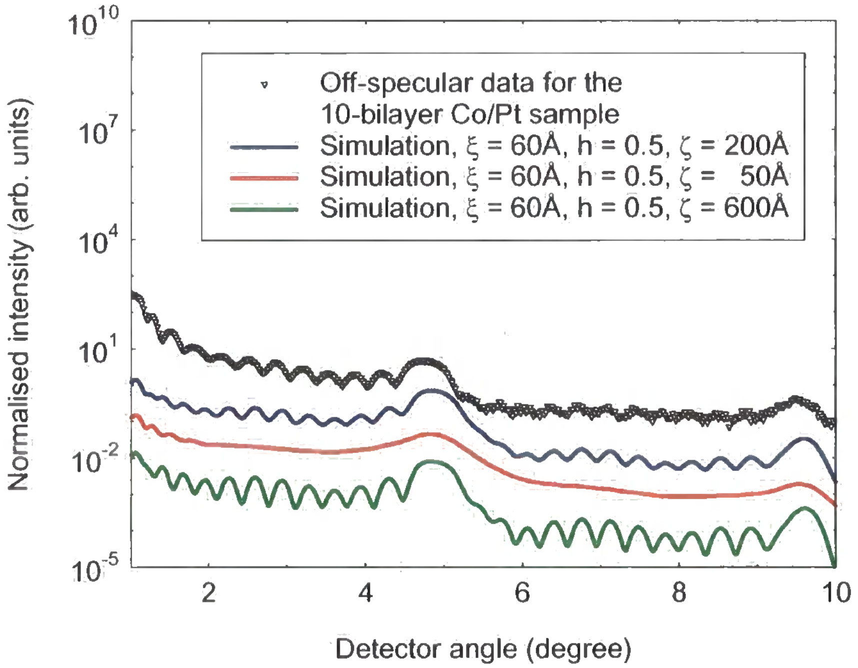

(b)

Figure 5.14 Off-specular data and simulations for 10-bilayer Co/Pt multilayer using Bede REFS models: **(a)** Correlated, uncorrelated, and partially correlated model I, and **(b)** Partially correlated model II.

5.5.2.2 Transverse diffuse scans

To distinguish true interface roughness from compositional grading, it is essential to measure the diffuse scatter. Simulating the diffuse scatter data is a very long process and the most difficult and time-consuming part of data analysis. First, the intensity of the diffuse data has to be fixed. This can be done by matching the specular ridge to the specular point at which the diffuse data has been taken. An example of such process is shown in Figure 5.15.

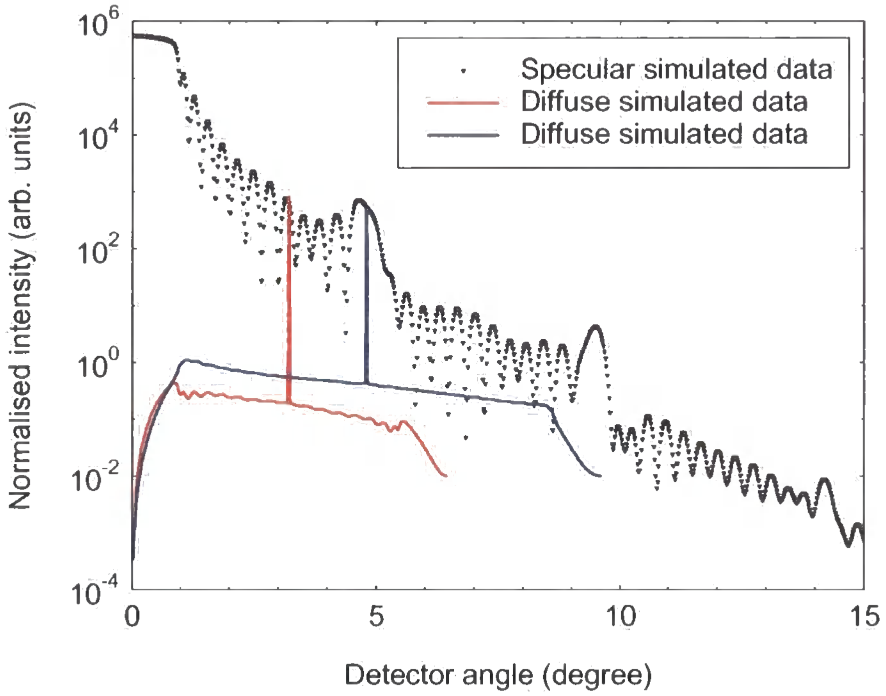

Figure 5.15 Specular and transverse diffuse simulations.

The final step is to simulate the diffuse scatter data that were taken at different points (usually at the two first Bragg peaks and two Kiessig fringes). As can be seen in Figure 5.16, many sets of parameter values fit one diffuse scan. It was shown in Figures 5.7 and 5.14 that the off-specular data plays a key role in determining whether the interface roughness is correlated or uncorrelated. Choosing the correct simulation model for simulating the diffuse data depends on the off-specular simulations. Except for the highly uncorrelated systems, a combination of the two models (model I and II) for partially correlated roughness, was found to be the best model for obtaining the best fits although it is highly time consuming. It is necessary to fit at least three diffuse scans (taken at two Kiessig fringes and first Bragg peak). By taking transverse diffuse scans passing perpendicularly through a maximum of a multilayer Bragg peak, the interfacial properties of the multilayer stack are dominant. In the case of the scans through a maximum or a minimum of the Kiessig fringes, the total layer thickness properties are determined. Thus, at the position of a Kiessig minimum, where the scattering from the total layer thickness is small and resonance scattering from a multilayer Bragg peak is absent, the surface properties are mainly reflected in the simulation of the transverse diffuse scans. When the correct model is chosen, more than one diffuse scatter data sets (taken at different specular angles) could be fitted simultaneously. In some cases, the parameter values do not fit the diffuse scans taken at or around second Bragg peak. The reason is not yet clear.

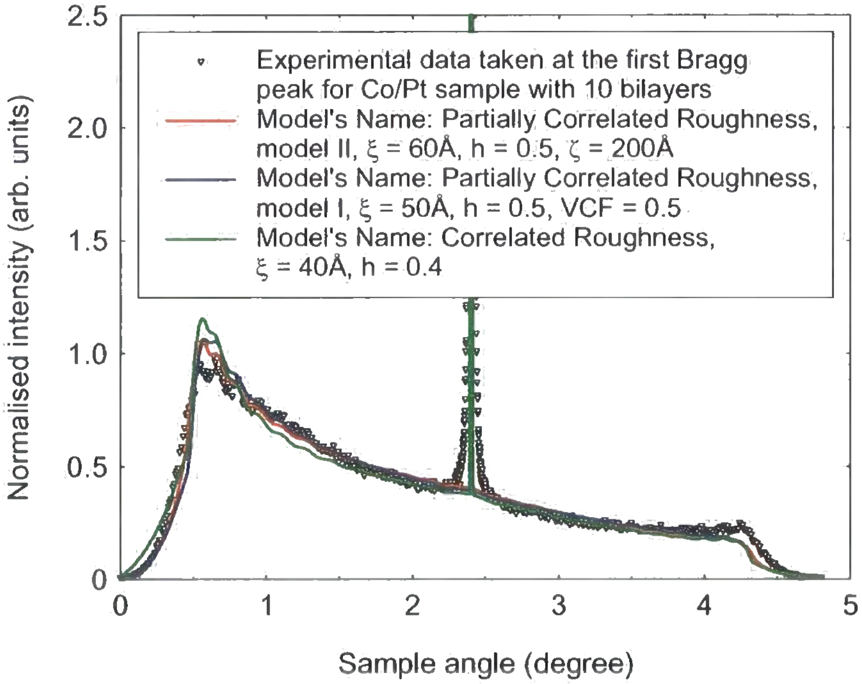

Figure 5.16 Transverse diffuse data taken at the first Bragg peak along with simulations using three different models for the 10-bilayer Co/Pt sample.

5.5.3 Additional x-ray techniques

During the course of this study, additional x-ray techniques other than those of Grazing Incidence Reflectivity have been used. Such techniques will be summarised below and in each case the reader is referred to more detailed texts for a more comprehensive description.

5.5.3.1 Symmetric high angle x-ray diffraction (HAXRD)

High angle diffraction experiments are performed using the same geometry as the specular scan, only at much higher angles and after initially aligning the diffractometer on a known reflection from the sample. Once again, with the sample and detector being scanned out-of-the plane of the sample, such experiments are sensitive to the out-of-plane crystal structure and hence measure the spacing of the crystal planes scattering normal to the surface of the sample. As expected from Bragg's law, diffraction peaks occur in such high angle scans at a position corresponding to these out of plane lattice spacing. By comparing the position of the reflections in these scans with those calculated from tabulated values, it is also possible to obtain information on out-of-plane lattice strain within the sample. Information on out-of-plane grain size and sample mosaicity can also be obtained from such scans [35, 36].

5.5.3.2 Soft x-ray scattering

Soft x-ray scattering experiments are performed using the same geometry as the specular scan, only at much higher wavelength ($\lambda \approx 15$Å). The greater range in reciprocal space that can be probed when the x-ray energy is of the order of 700 eV allows the Fourier transform of the correlation function to be probed directly. In the case of soft x-ray experiments, the interface parameters (i.e. fractal parameter and correlation length) are calculated directly from the scans at the second Bragg peak [12]. As seen in Figure 5.17, both Lorentzian and Gaussian curves can be fitted to the experimental data. Calculation of the in-plane correlation length from these two functions could lead to a ten times difference between the values obtained from the two fits.

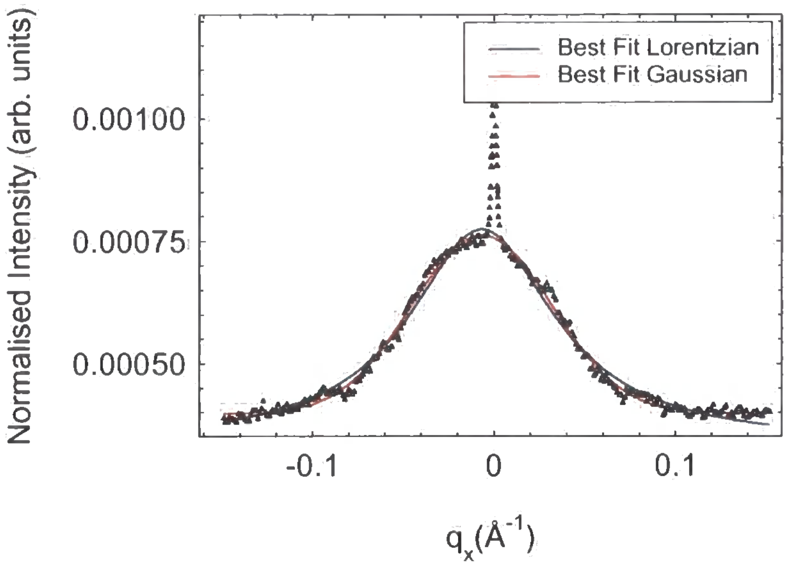

Figure 5.17 Best fits to the experimental data at soft energies.

5.5.3.3 Diffuse x-ray out of the scattering plane

By measuring the intensity out of the scattering plane, a greater range of the in-plane component of reciprocal space can be probed, without the need to change the energy. This geometry (Figure 5.18) can be used to extract the fractal parameter [37-39] but this technique is not sensitive to the correlation length (chapter 8).

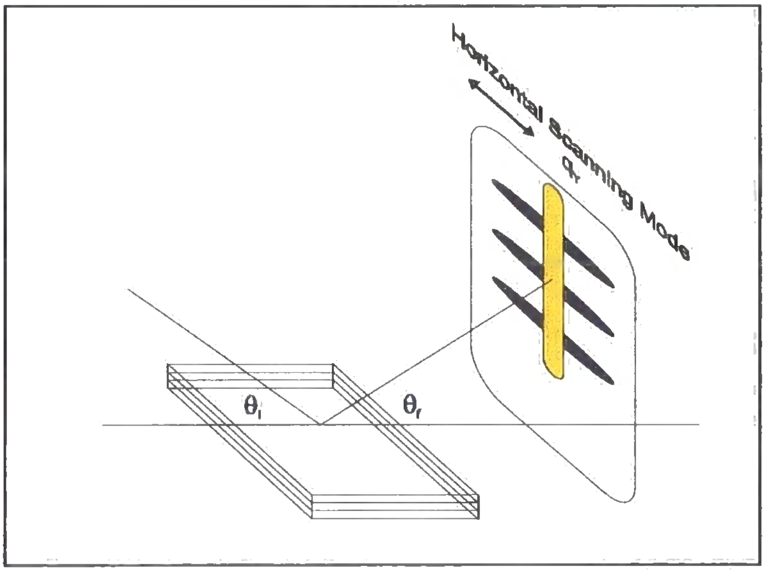

Figure 5.18 The geometry of diffuse x-ray out of the scattering plane.

5.6 Conclusions

This chapter has introduced the reader to the x-ray sources and benefits of synchrotron radiation as a very active tool that can be used for studies of dynamics in materials in the era of nanoscience. The x-ray data presented in this thesis have been taken on a variety of x-ray scattering instruments based on both in the laboratory, and at synchrotron radiation sources. It was found that for the study of interface structure, the synchrotron radiation source was a more powerful device. The x-ray data analysis and simulation process was also discussed in this chapter. It can be concluded that in the case of grazing incidence specular reflectivity, the data are always limited and this truncation can lead to significant error in the analysis. In the case of diffuse scattering, it was necessary to fit at least three diffuse scans. They fit simultaneously only when the correct model is used. Except for the case of totally uncorrelated systems, a very accurate description of the interface correlations could be obtained by using two models (partially correlated roughness, model I and II). By using model I firstly, the amount of roughness that is correlated at any interface can be specified as a proportion of the total interface roughness. Secondly, by using model II, the values of correlation lengths (vertical and lateral) along with the fractal parameter could be obtained for each sample. Other techniques do not seem to be as powerful as the grazing incidence scattering for the study of buried interfaces. However, wrong interface parameters are the consequence of an inappropriate model.

REFERENCES

[1] *Elements of X-ray Diffraction*, B. D. Cullity, Addison-Wesley (1978).

[2] *Elements of Modern X-ray Physics*, J. Als-Nielsen and D. McMorrow, John Wiley & Sons, Ltd (2000).

[3] B. K. Tanner and D. K. Bowen, *Materials Science Reports*, **8 (8)**, 369-407 (1992).

[4] "Synchrotron Radiation Research", Eds.: H. Winick and S. Doniach, Plenum Press (1980).

[5] *Introduction to Synchrotron Radiation*, G. Margaritondo, Oxford University Press (1988).

[6] C. Kunz, *J. Phys.: Condens. Matter*, **13**, 7499-7510 (2001).

[7] "Neutron and Synchrotron Radiation for Condensed Matter Studies", Eds.: J. Baruchel, J.-L. Hodeau, M. S. Lehmann, J. R. Ragnard, and C. Schlenker, Springer-Verlag (1993).

[8] *High Resolution X-ray Diffractometry and Topography*, D. K. Bowen and B. K. Tanner, Taylor & Francis Ltd. (1998).

[9] T. P. A. Hase, "Condensed Matter Physics Course; Lecture Notes", University of Durham, Durham (2002).

[10] J. M. Hudson, *Ph. D. Thesis,* University of Durham (1994).

[11] I. Pape, *Ph. D. Thesis,* University of Durham (1997).

[12] T. P. A. Hase, *Ph. D. Thesis,* University of Durham (1998).

[13] C. C. Tang, S. P. Collins, B. M. Murphy, N. D. Telling, R. A. Wogelius, and S. J. Teat, *Rev. Sci. Instrum.*, **69 (3)** (1998).

[14] http://srs.dl.ac.uk/XRD/2.3/Manual

[15] S. Cockerton and B. K. Tanner, *Adv. X-ray. Ana*, **38**, 371 (1995).

[16] B. K. Tanner, T. P. A. Hase, B. D. Fulthorpe, J. Clarke, G. M. Luo, S. K. Halder, A. S. H. Rozatian, and S. B. Wilkins, *Mater. Res. Soc. Symp. Proc.*, **615** , G 2.1.1-G 2.1.12 (2000).

[17] M. Altarelli, *J. Magn. Magn. Mater.*, **233** , 1-7 (2001).

[18] S. Ferrer and Y. Petroff, *Surf. Sci.*, **500 (1-3)**, 605-627 (2002).

[19] B. K. Tanner, *Acta Phys. Pol. A*, **86 (4)**, 537-544 (1994).

[20] B. D. Fulthorpe, *Ph. D. Thesis,* University of Durham (1999).

[21] G. H. Vineyard, *Phys. Rev. B*, **26 (8)**, 4146-4159 (1982).

[22] S. K. Sinha, E. B. Sirota, S. Garoff, and H. B. Stanley, *Phys. Rev. B*, **38 (4)**, 2297-2311 (1988).

[23] W. Weber and B. Lengeler, *Phys. Rev. B.*, **46 (12)**, 7953 (1992).

[24] D. K. G. de Boer, *Phys. Rev. B*, **49 (9)**, 5817-5820 (1994).

[25] S. K. Sinha, *Curr. Opin. Solid State Matter. Sci.*, **1 (5)**, 645 (1996).

[26] S. K. Sinha, *Acta Phys. Pol. A*, **89 (2)**, 219-234 (1996).

[27] M. Wormington, C. Panaccione, K. M. Matney, and D. K. Bowen, *Philos. Trans. R. Soc. Lond. Ser. A-Math. Phys. Eng. Sci.*, **357 (1761)**, 2827-2848 (1999).

[28] L. G. Parratt, *Phys. Rev.*, **95 (2)**, 359-369 (1954).

[29] J. H. Underwood and T. W. Barbee, *Appl. Optics*, **20 (17)**, 3027-3034 (1981).

[30] P. Lee, *Appl. Opt.*, **22** , 1241 (1983).

[31] B. Vidal and P. Vincent, *Appl. Opt.*, **23** , 1794 (1984).

[32] F. Prokert, J. Noetzel, N. Schell, E. Wieser, W. Matz, and A. Gorbunov, *Thin Solid Films*, **394 (1-2)**, 164-173 (2001).

[33] F. Prokert, J. Noetzel, N. Schell, E. Wieser, and A. Gorbunov, *Thin Solid Films*, **416 (1-2)**, 114-121 (2002).

[34] M. Wormington, D. K. Boen, and B. K. Tanner, *Mater. Res. Soc. Symp. Proc.*, **238** , 119 (1992).

[35] *X-ray diffraction in Crystals, Imperfect Crystals and Amorphous Bodies*, A. Guinier, Dover Pub. (1994).

[36] *X-ray Diffraction*, P. E. Warren, Dover Pub. (1990).

[37] T. Salditt, D. Lott, T. H. Metzger, J. Peisl, R. Fischer, J. Zweck, P. Hoghoj, O. Scharpf, and G. Vignaud, *Europhys. Lett.*, **36 (8)**, 565-570 (1996).

[38] T. Salditt, D. Lott, T. H. Metzger, J. Peisl, G. Vignaud, P. Hoghoj, O. Scharpf, P. Hinze, and R. Lauer, *Phys. Rev. B*, **54 (8)**, 5860-5872 (1996).

[39] T. Salditt, T. H. Metzger, C. Brandt, U. Klemradt, and J. Peisl, *Phys. Rev. B*, **51 (9)**, 5617-5627 (1995).

Chapter 6

Interfaces in Fe/Au Multilayers

6.1 Introduction

In recent years, there have been many studies of systems comprising single or multilayered Fe and Au. Since the discovery of large perpendicular magnetic anisotropy (PMA) [1] and giant magnetoresistance (GMR) [2] in ferromagnetic multilayers, they have attracted a great deal of attention. In particular, there are a lot of reports on Fe/Au systems; e.g. magnetic exchange coupling [3], magneto-optical Kerr effect [4-9], giant magnetoresistance [10, 11], and both in-plane [12] and perpendicular magnetic anisotropy [13-19]. Furthermore, the electronic states and electron transport properties of Fe/Au multilayers have attracted much attention over the last few years [20-23]. Electron band calculations predict enhanced magnetic moments in monolayered Fe/Au structures due to the reduction of the number of next neighboring atoms [24-26] and the creation of a large out-of-plane anisotropy [27]. Magnetic properties of Fe/Au multilayers vary very much depending on the Fe and Au layer thicknesses. It has been shown that the magnetic easy axis changes from in-plane to the perpendicular direction as the thickness of the Fe layer is reduced below 10 Å [28]. Takanashi *et al* reported that the perpendicular magnetic anisotropy of Fe/Au superlattices oscillated as a function of the layer thickness with a period of one monatomic layer (1 ML: $d_{Fe} = 1.43$Å and $d_{Au} = 2.04$Å) [29]. They also found that the interface roughness for noninteger values of ML reduced the number of Fe atoms with strictly uniaxial crystal symmetry, leading to the reduction in effective perpendicular magnetic anisotropy energy.

On the other hand, the formation and propagation of roughness during atomic deposition has been the subject of intense interest and investigation, due to their importance in the study of perfection of Fe/Au thin films and multilayers [30, 31]. Interfacial roughness is believed to plays an important role in the transport properties of metallic multilayers [32, 33].

In order to resolve the open questions related to PMA, on one hand in this chapter, the magnetic anisotropy and interfacial features of a series of MBE (Molecular Beam Epitaxy) Fe/Au multilayers grown on (100) MgO will be discussed. The interface structure of another Fe/Au sample with 100 bilayers will also be followed. On the other hand, some surprising results related to the evolution of interface structure in these samples will be presented.

6.2 Samples

A series of Fe/Au multilayer films were grown on a single crystal (100) oriented MgO using the MBE technique at the University of Leeds by P.A. Ryan and D.T. Dekadjevi.

All samples were nominally:

$$\text{MgO (100)} / 10\text{Å Fe} / 500\text{Å Au} / N \times \{1.4\text{Å Fe} / 2.04\text{Å Au}\} / 15\text{Å Au}$$

$$\text{with } N = 3, 5, 10, 20, 40$$

Another sample was also grown separately by the same technique, with 100 bilayers.

6.3 X-ray experiments

The three specific types of x-ray reflectivity scans were performed, namely the specular, longitudinal diffuse and transverse diffuse. These are discussed extensively in chapters 4 and 5 and the reader is referred to these chapters for more details. All of the data in this section were carried out on a Bede GXR1 laboratory reflectometer using a wavelength of 1.393Å.

6.3.1 GIXR results

A series of grazing incidence specular and off-specular x-ray scans along with simulations for these samples is shown in Figure 6.1. These scans provide information concerning the development of the multilayer stack as the number of bilayers was increased from 3 to 40. As can be seen, the off-specular data overlapped the specular scan quickly, indicating high interface roughness. Two different types of Kiessig fringes (short and long period) can clearly be seen in the specular data while only the long period fringes were appeared in the off-specular data. The true specular data (for which the off-specular data has been subtracted from the specular data) will thus consist of short period fringes only. No off-specular Kiessig fringes (short period) corresponding to the total stack thickness are seen in any of the samples, suggesting that the roughness is uncorrelated in all cases. On the other hand, the observation of the long period off-specular Kiessig fringes suggests that some kind of conformal roughness could be present in these Fe/Au multilayers. In order to understand the origin of these long period Kiessig fringes, the off-specular data are modeled and will be discussed later.

Structural parameters were obtained by fitting the experimental data to simulations from a model structure. Values of thickness and interface width were first found by automatic refinement using the Bede MERCURY code for the true specular data and these parameters then used to fit the diffuse scatter and off-specular data manually (sections 6.3.2 and 6.3.3).

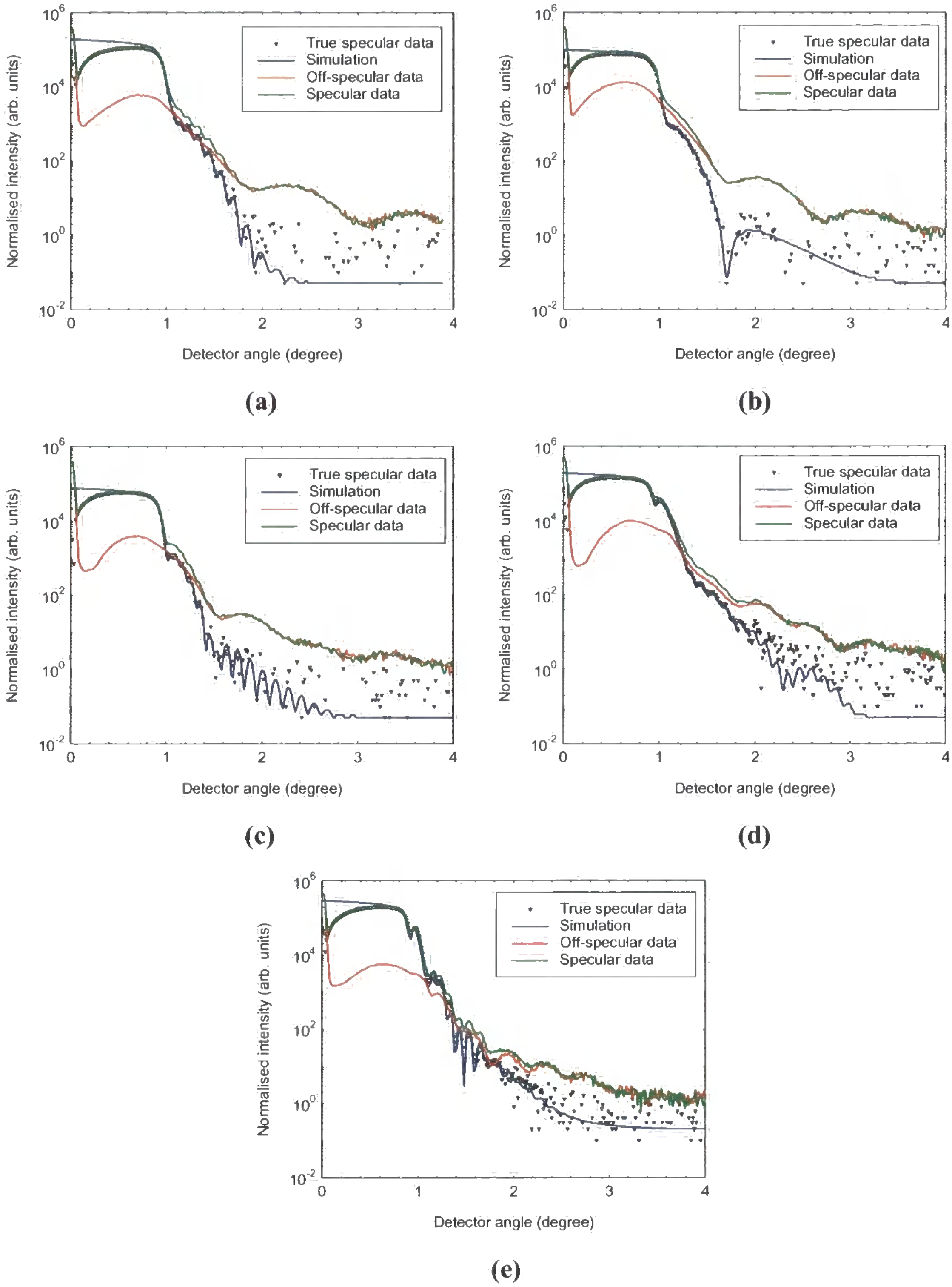

(a)

(b)

(c)

(d)

(e)

Figure 6.1 Specular data, Off-specular data, true specular data and simulations for samples with **(a)** 3 bilayers, **(b)** 5 bilayers, **(c)** 10 bilayers, **(d)** 20 bilayers, and **(e)** 40 bilayers.

6.3.2 GIXS results

Across the series of five samples, transverse diffuse measurements were made at different values of scattering vector. Through a combination of specular and diffuse scans, many aspects of the interface morphology in the multilayer structures could be characterised. For each sample, at least two transverse diffuse scans were taken at selected Kiessig fringes (one maximum and one minimum) as due to the very thin bilayer thicknesses, Bragg peaks were not observed in the range of scattering angle. These scans are primarily sensitive to correlated and uncorrelated roughness. The Bede REFS code (which was used to fit the transverse diffuse data), considers four different models for interfaces. Best fits were achieved using the model for uncorrelated roughness. A selection of transverse diffuse scans and best fits to the experimental data are shown in Figure 6.2.

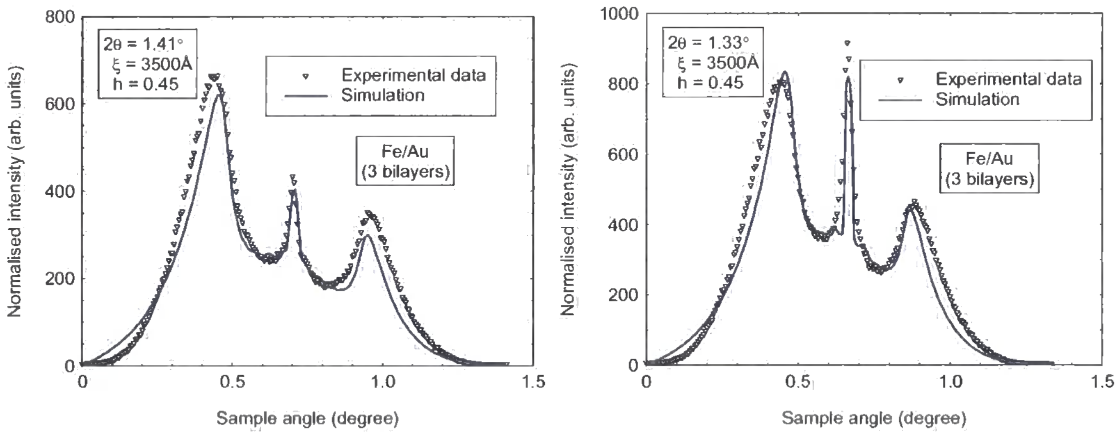

(a) **(b)**

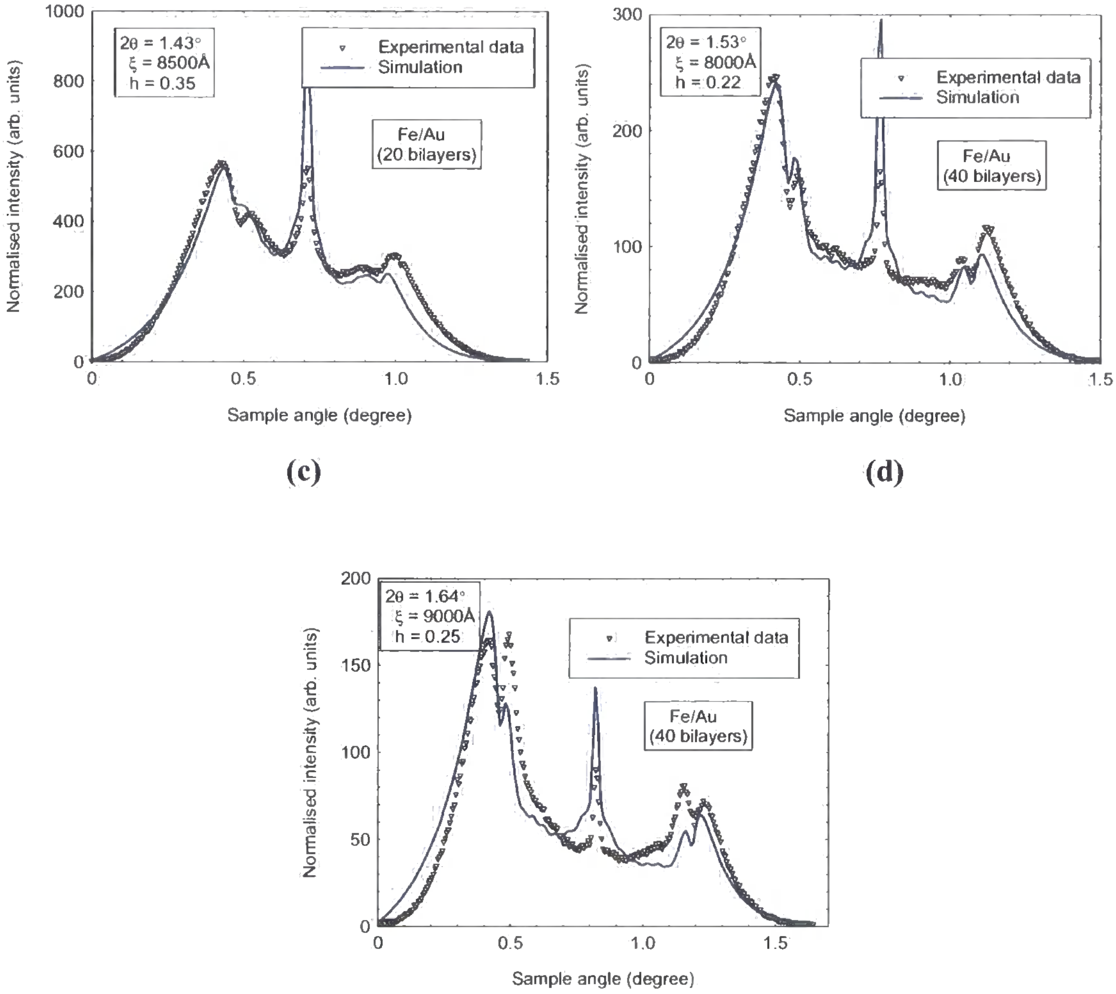

(c) **(d)**

(e)

Figure 6.2 Transverse diffuse scans and simulations using Bede REFS.

As can be seen in Figures 6.1 and 6.2, good fits have been achieved in most cases. Structural parameters, such as thickness (t), *rms* interface width (true roughness, σ), in-plane correlation length (ξ), and fractal parameter (h) determined from the GIXR and GIXS fitting procedure are summarized in table 6.1. All of the roughness (σ) was found to be uncorrelated.

Table 6.1

Multilayer structure parameters determined from x-ray scattering simulations.

N	t_{Seed} *Fe* ±0.3Å	t_{Buffer} *Au* ±0.3Å	$t_{Bilayer}$ *Fe* ±0.3Å	$\sigma_{Bilayer}$ *Fe* ±0.3Å	$t_{Bilayer}$ *Au* ±0.3Å	$\sigma_{Bilayer}$ *Au* ±0.3Å	t_{Cap} *Au* ±0.3Å	*h* ±10%	ξ (Å) ±10%
3	35.8	475.4	1.8	24.2	2.0	22.3	47.0	0.45	3500
5	28.8	546.9	2.2	10.7	2.2	10.3	31.2	0.45	5500
10	22.3	540.5	1.1	12.7	2.4	19.4	20.2	0.35	7500
20	28.6	489.1	1.5	14.0	2.2	10.7	47.5	0.35	8500
40	28.4	443.5	1.60	16.8	1.9	20.9	39.2	0.22	8000

6.3.3 Off-specular results

In order to understand the origin of the long period Kiessig fringes appearing in both the specular and off-specular data (but not in the true specular data), the off-specular data were simulated using the Bede REFS code. The results are shown in Figure 6.3.

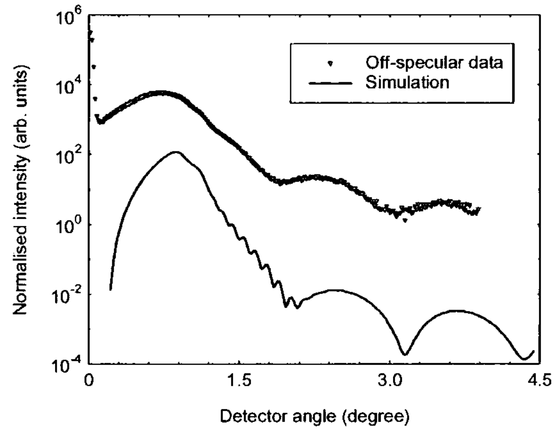

(a)

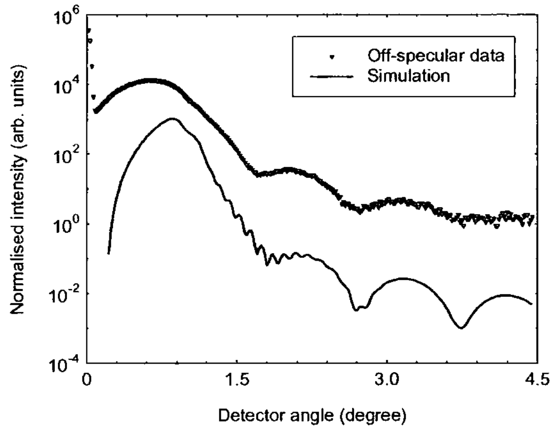

(b)

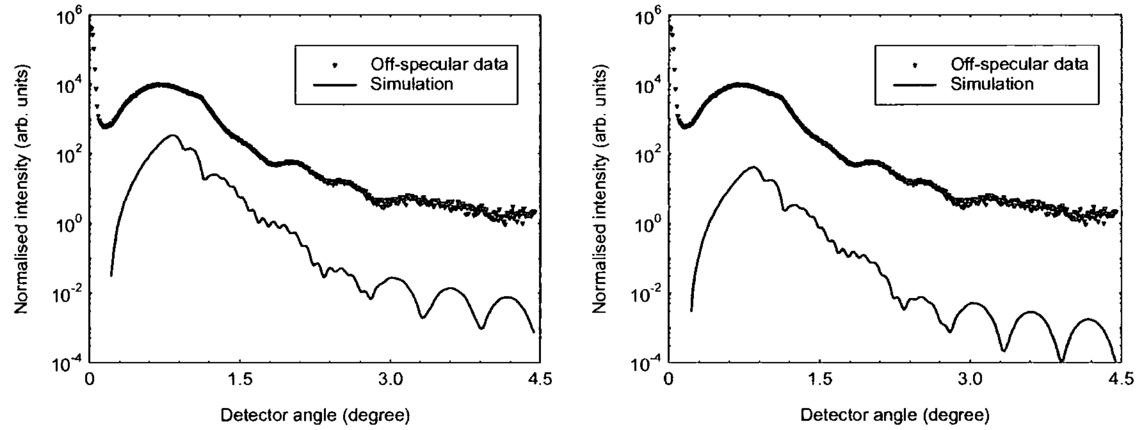

(c) (d)

Figure 6.3 Off-specular scans and simulations using Bede REFS for Fe/Au multilayers with **(a)** 3 bilayers, **(b)** 5 bilayers, **(c)** 20 bilayers, and **(d)** 40 bilayers.

The long period fringes in the x-ray reflectivity data do not seem to have come from the cap layer (as the thickness is about 15Å). They also do not seem to result from the seed layer. Neither can they be supposed to be the tails in the specular data. The specular and off-specular data showed that the short period fringes are superimposed on the long period fringes in all cases.

In order to simulate the off-specular data, a model was constructed based on the assumption that the roughness was totally correlated. To achieve the best simulations, it was necessary to add another layer between the Fe and Au in the multilayer structure. The results are shown in Table 6.2. The in-plane correlation length, ξ_c, was found to be about 300Å (± 150Å).

Table 6.2

Multilayer structure parameters determined from off-specular simulations.

N	t_{Seed} *Fe* ±0.3Å	t_{Buffer} *Au* ±0.3Å	$t_{Bil.}$ *Fe* ±0.3Å	$\sigma_{Bil.}$ *Au* ±0.3Å	t Fe_XAu_{1-X} ±0.3Å	σ Fe_XAu_{1-X} ±0.3Å	$t_{Bil.}$ *Au* ±0.3Å	$\sigma_{Bil.}$ *Au* ±0.3Å	$t_{Cap.}$ *Au* ±0.3Å
3	38.5	534.4	2.0	21.0	2.0	21.4	1.8	24.7	49.1
5	38.5	534.4	2.0	21.0	2.0	21.4	1.8	24.7	49.1
10	38.5	534.4	2.0	21.0	2.0	21.4	1.8	24.7	49.1
20	38.5	534.4	1.5	17.0	1.5	17.0	1.5	17.0	49.1
40	38.5	534.4	1.0	20.0	1.0	20.0	1.0	20.0	49.1

As seen in Tables 6.1 and 6.2, different bilayer parameters (thickness and roughness) were achieved. A possible explanation for the long period Kiessig fringes is illustrated in Figure 6.4. Figure 6.4(a) shows a typical fractal interface (totally uncorrelated) with an in-plane (lateral) correlation length, ξ_{uc}. In Figure 6.4(b) the idea of a non-fractal interface (totally correlated with an in-plane correlation length, ξ_c) is illustrated. A superposition of the two types of roughness is proposed in 6.4(c). This type of roughness has recently been proposed for Si/SiO_2 interfaces by using AFM analysis [34]. The additional $Fe_xAu_{(1-x)}$ layer seems to be responsible for the long period Kiessig fringes in the specular and off-specular data. As the interface roughness is much greater than the thickness of bilayers, these long period fringes do not appear in the true specular data. In the specular scattering geometry, the scattering vector is directed normal to the sample surface at all times. Specular reflectivity measurements are sensitive principally to near surface electron density, layer thickness and average interface width.

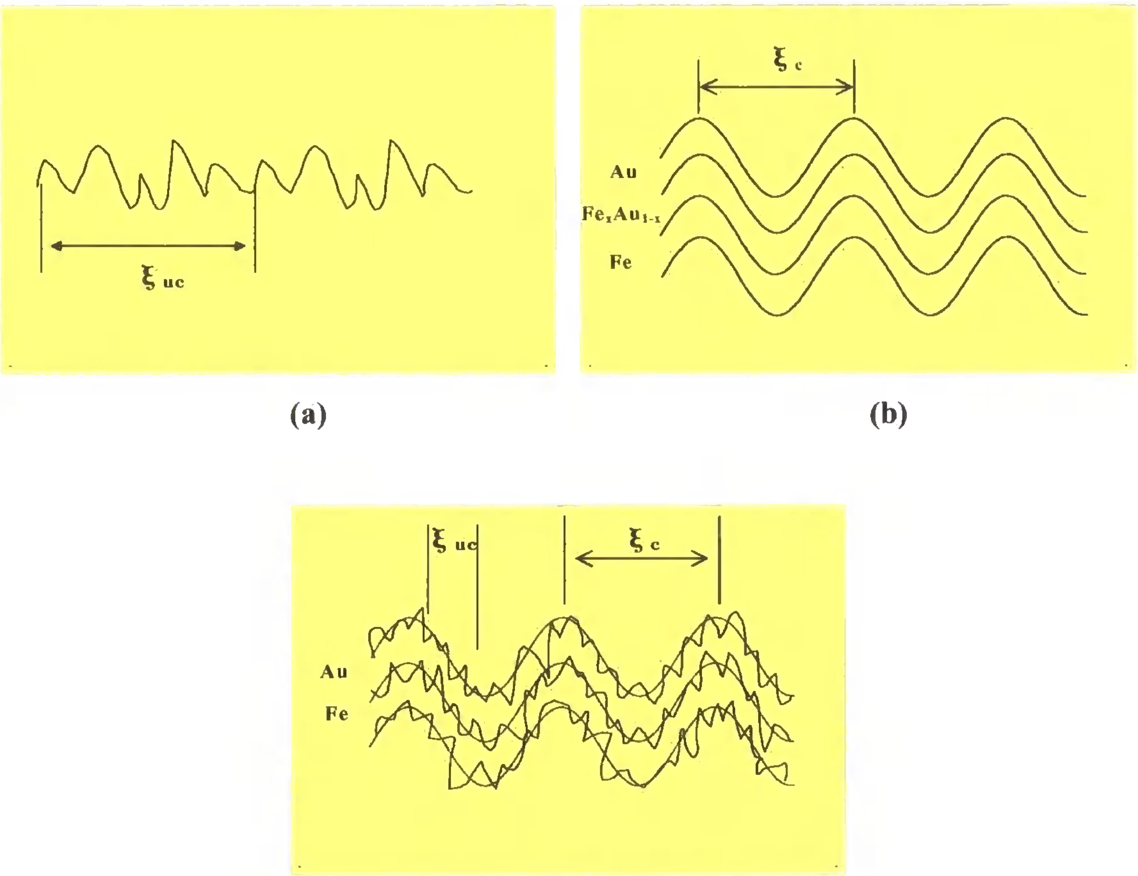

(a) **(b)**

(c)

Figure 6.4. Schematic illustration of different profiles of interface. **(a)** Short period roughness. **(b)** Long period roughness. **(c)** Superposition of two types of roughness.

Proposing a model for this series of Fe/Au multilayers considering a virtual $Fe_xAu_{(1-x)}$ layer between iron and gold layer, is consistent with a recent work done by Rafaja *et al* [35]. The Fe/Au system has been reported as an example of a binary system having a wide miscibility gap at low temperature. The solubility of iron in gold depends on the temperature. Usually, the individual layers in a multilayer system are expected to grow as stratified media with continuous interfaces, which do not intersect each other. In the case of Fe/Au multilayers, some authors consider these gaps as a result of breaking up of the magnetic layers due to the grain boundary diffusion and formation of a discontinuous magnetic layers with a granular structure [36, 37]. The structure model of a multilayer with non-continuous interfaces is illustrated in Figure 6.5(b) along with schematic of a continuous interface (Figure 6.5(a)). For evaluation of the x-ray reflectivity from multilayers with non-continuous interfaces, a modified model has recently been suggested [35].

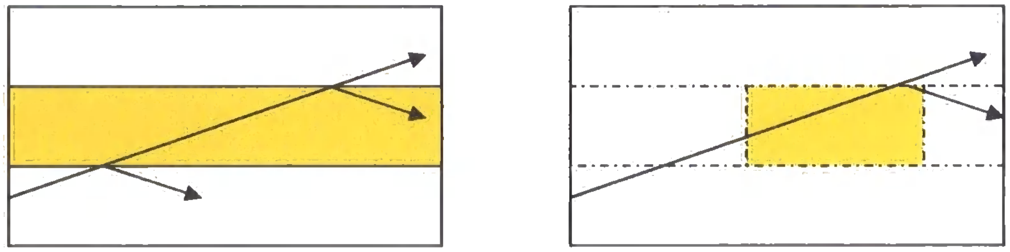

(a) (b)

Figure 6.5. Transmission and refraction of x-rays in multilayers with **(a)** Continuous interfaces, and **(b)** Non-continuous interfaces. Dashed lines show positions of virtual (continuous) interfaces [35].

On the other hand, proposing a model assuming the presence of two types of roughness (correlated and uncorrelated), is in good agreement with a work done by Schreyer *et al* on Fe/Cr multilayers [38]. However, unlike their Fe/Cr system, in these series of Fe/Au multilayers, the in-plane correlation length associated with the uncorrelated interfaces is found to be much greater than the one for correlated interfaces $(\xi_{uc} \gg \xi_{c})$. These two types of roughness were clearly separated by simulating diffuse scattering data (both longitudinal and transverse). This can be described in the reciprocal space (Figure 6.6). ξ_c can be determined using longitudinal diffuse scattering along q_z, while ξ_{uc} is obtained from transverse diffuse scan along q_x.

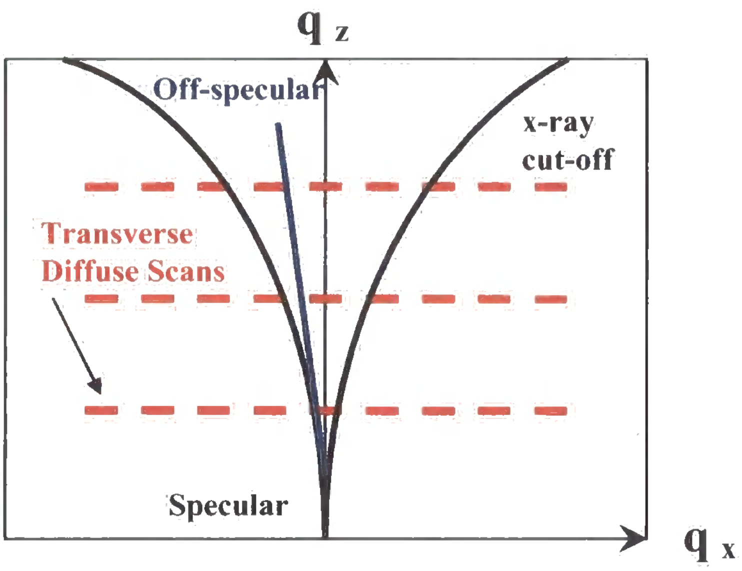

Figure 6.6. Plan of reciprocal space showing the specular, off-specular and transverse diffuse scan modes.

Proposing two different models (one for simulating specular and another model for off-specular) may seem to be rather unusual. It could be proposed that the correlated roughness was induced by the buffer layer and propagated through all successive layers. The uncorrelated roughness then originated from the growth of the individual Fe and Au layers. This is mainly done as the Bede REFS and REFS Mercury codes are based on a fractal model of the interfaces within the distorted wave Born approximation assuming only one in-plane correlation length in the model [39-44].

6.4 Magnetic measurements

Anisotropy measurements were performed at room temperature using the torque magnetometer. All experimental torque curves were numerically fitted to the following equation (discussed in chapter 3):

$$T = -K_{eff}\sin 2\{\phi + arcsin(-T/MB)\} + \tfrac{1}{2}K_2 \sin 4\{\phi + arcsin(-T/MB)\} \qquad (6.1)$$

where T is the torque, M is the magnetization and ϕ is the angle of the applied magnetic field B with respect to the normal of the plane of sample. The two lowest order uniaxial anisotropy terms are K_1 and K_2 with $K_{eff} = K_1 - 2\pi M_s^2$.

6.4.1 Torque magnetometry results

Samples were run under applied magnetic fields ranging from 4.8 KOe to 8.0KOe. The torque curves for the 40-bilayer sample are shown in Figure 6.7(a). As can be seen in Figure 6.7(b), the amplitude of all torque curves increased with increasing magnetic field up to ~ 7.0 KOe and then remained constant indicating that saturation of the magnetization had been achieved. The torque curve along with a fit to equation (6.1) for the 40-bilayer sample, including a shear correction is illustrated in Figure 6.7(c). The positive slope at $\phi = 0.0^\circ$ confirms that the easy axis lies in the plane of the samples in all cases. Torque data were normalized to the magnetic volume deduced from the Fe thickness determined from the X-ray reflectometry data.

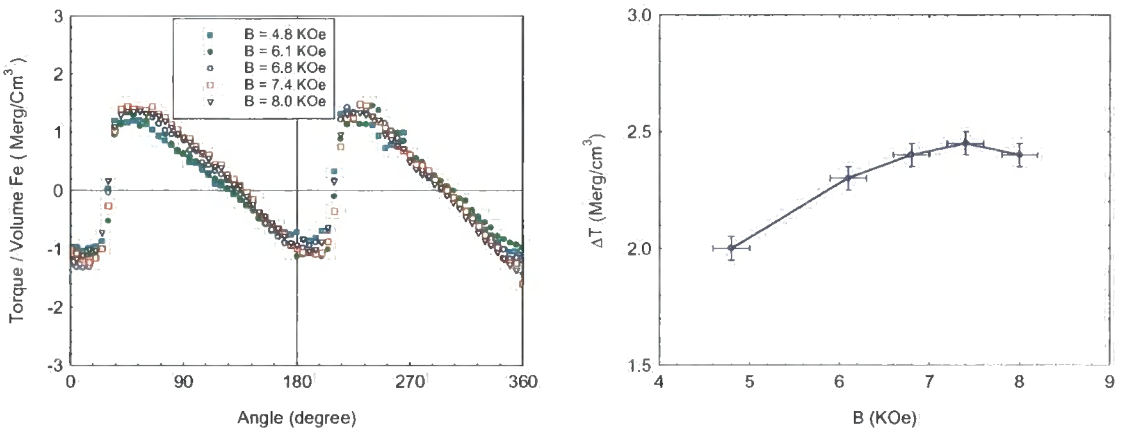

(a) **(b)**

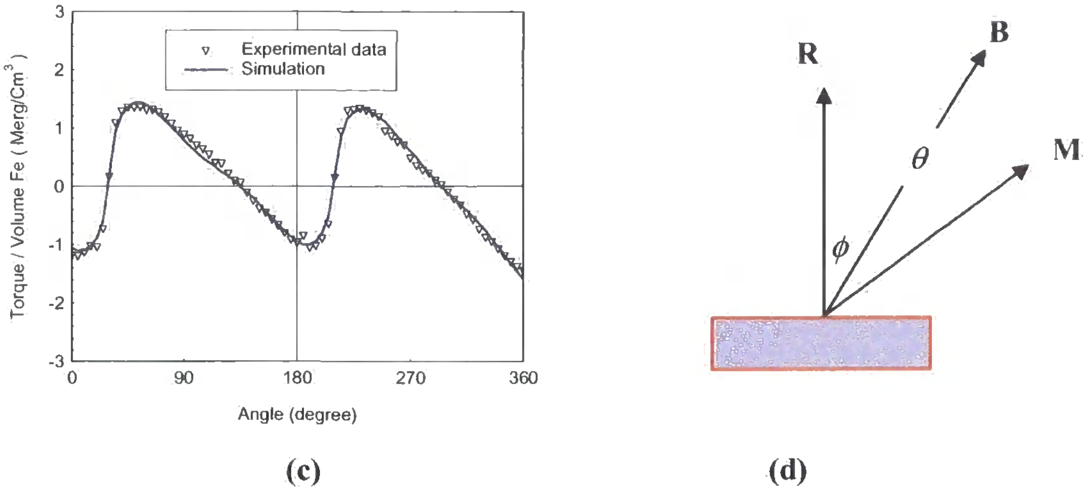

(c) (d)

Figure 6.7 (a) Torque curves at different magnetic fields for Fe/Au multilayer with 40 bilayers. **(b)** Relation between the amplitude of torque curves and magnetic field . **(c)** Torque curve and best fit for the sample with 40 bilayers at B = 7.4 kOe. **(d)** Orientation of magnetisation and applied field directions.

As seen in Figure 6.8, K_{eff} is negative and constant in all cases, again confirming that the magnetic moments are in the plane for all samples. A value of $K_2 = (0.4 \pm 0.1)\, Merg/cm^3$ was measured for all samples at $B = 7.4\, KOe$ indicating the presence of a small component of 4ϕ in the torque curves. Torque curves for samples with 3 and 5 bilayers were noisy and it was not possible to simulate the data for anisotropy energy measurements.

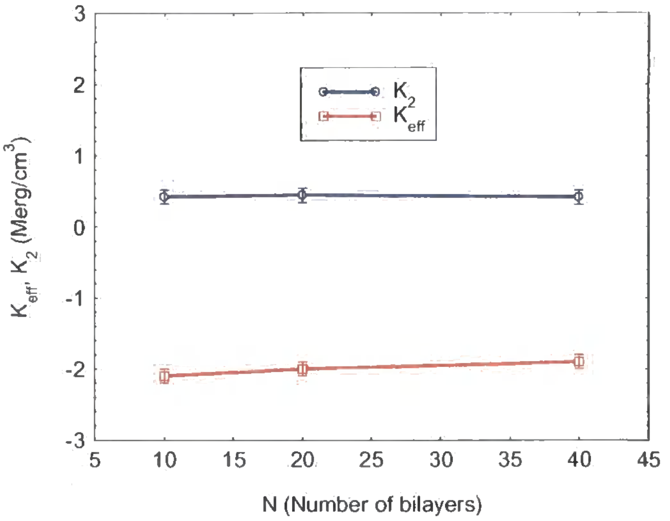

Figure 6.8 Relation between K_{eff} , K_2 and number of bilayers at B = 7.4 KOe.

6.5 Discussions

Magnetic measurements showed that all samples exhibited in-plane magnetization; with the easy axis lying in the plane of the sample. Unlike the perpendicular magnetic anisotropy material Co/Pt (chapter 7) [45], there is no variation of anisotropy with bilayer number. The results are in contrast to the previous studies of Fe/Au multilayers. These have shown that Fe/Au multilayers exhibit an easy axis of magnetization perpendicular to the thin film plane when the Fe layer is smaller than 10Å [28, 46].

Honda *et al* [28] studied the magnetic properties of a series of Fe/Au multilayers grown on glass substrates. Riedling *et al* [46] investigated the magnetic ordering and anisotropies of a series of {MgO / Fe 10Å / Au 500Å / 30*(Fe x Å / Au y Å) / Au 20 Å} multilayers (with x =1,2 and y =1-6) using the MBE technique. They observed perpendicular anisotropy in all samples except one (with x =2Å and y =1Å). However, Riedling *et al* did not study the interface structure of their multilayers. No information was available concerning the change of magnetization direction from out-of-plane to in-plane observed in that sample as to whether this was associated with a change in the interface roughness or not. However, Amitesh Paul has recently reported that the PMA in Fe/Tb multilayers decreased with the increase in the interface roughness [47].

In all samples studied here, the Fe and Au layer thicknesses were in the range of those studied by Riedling *et al* and one would expect these multilayers to exhibit PMA. As seen in Table 6.1, grazing incidence x-ray experiments and simulations showed that although the samples had very thin bilayers, they also had very poor and rough interfaces. It can be concluded that the interface roughness reduced the effective perpendicular magnetization leading samples with very rough interfaces to changing the direction of easy axis from out-of-plane to in plane. This is consistent with a theoretical work done by Uba *et al* [48]. They reported the high sensitivity of magnetization direction to the roughness of the interfaces in Fe/Au multilayers. However generalizing this conclusion to different systems is a challenging proclaim. Paul *et al* studied the effect of interface roughness on perpendicular magnetic anisotropy of a series of Fe/Tb multilayers [49] and reported the observation of strong PMA in their samples with high interface roughness (greater than 12Å).

The previous study of a series of (100) oriented Fe/Au multilayers grown, by Molecular Beam Epitaxy (MBE), on (001) MgO with a nominal structure:

MgO (100) / 10Å Fe / 500Å Au / { 7.2Å Fe / X Å Au }*20 with 0Å<X<60Å

showed that a high proportion of the interface roughness was correlated in nature [21-23]. No interdiffusion between iron and gold layer was observed. The interface width (σ) and in-plane correlation length (ξ) was found to be about 5Å and 200Å respectively, much lower than the values measured for the 20-bilayer sample studied here (~10Å and 8500Å respectively).

Matching of simulations to the present experimental off-specular $\theta/2\theta$ scans shows that the correlated roughness is retained for all samples (regarding the long period off-specular Kiessig fringes). The in-plane correlation length remaining constant in a highly correlated system has been seen in many systems, i.e. Co/Cu [50] and Co/Pt [45]. On the other hand, the transverse diffuse data and simulations led to the proposal of the existence of a component of uncorrelated roughness in the plane. As seen in Table 6.1, transverse diffuse data and simulations showed that the in-plane correlation length associated with the uncorrelated roughness, ξ_{uc}, increased as a function of bilayer repeat, N, and then remained constant as it reached to a maximum value (Figure 6.9). The calculated data for in-plane correlation length obtained from the simulations of transverse diffuse scattering x-ray data was fitted to the following equation:

$$\xi_{uc} = a * \{1 - \exp(-b * N)\} \qquad (6.2)$$

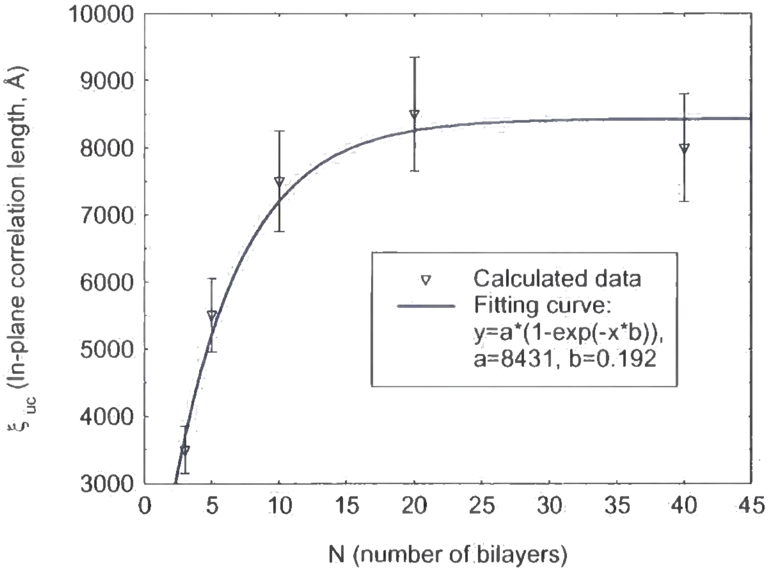

Figure 6.9 Relation between in-plane correlation length (ξ_{uc}) and number of bilayers.

Moreover, the variation of in-plane correlation length with the layer thicknesses (Figure 6.10(a)) shows that the lateral interfacial correlation length increased as the multilayer was grown. From the inequality of lateral correlation lengths in these samples, it can be concluded that the roughness of the interfaces are not correlated. This is in good agreement with the work done on Fe/Cr multilayers using Scanning Tunneling Microscopy (STM) by Schmidt *et al* [51]. Equation 6.2 is again the best fitting curve to the calculated data. This effect has been seen in both MBE grown Fe/Au [23] and sputtered Fe/Au multilayers and has been shown to follow the Kardar-Parisi-Zhang (KPZ) model (appendix G) for surface growth [31, 52]. In their extensive studies of interfacial morphology in metallic multilayers (especially Fe/Au and NiFe/Au), Paniago *et al* reported that small interfacial features tend to be less replicated, with an increasing growth correlation length for larger features. Thicker multilayers are required to determine the growth correlation length for very large interfacial features. This is an important factor in the determination of the mode of growth. If the multilayer is too thin, the roughness correlation length is saturated and is equal to the total thickness of the film [31]. However, as can be seen in Figure 6.10(b), in the case of this study of Fe/Au multilayers, this saturation was not observed. The in-plane correlation lengths were found to be much greater than the total thickness of each sample, possibly because of the presence of very rough interfaces. By employing RHEED analysis for a series of Fe/Au multilayers, Dekadjevi *et al* observed a similar increase in the lateral correlation length as a function of Au thickness [23].

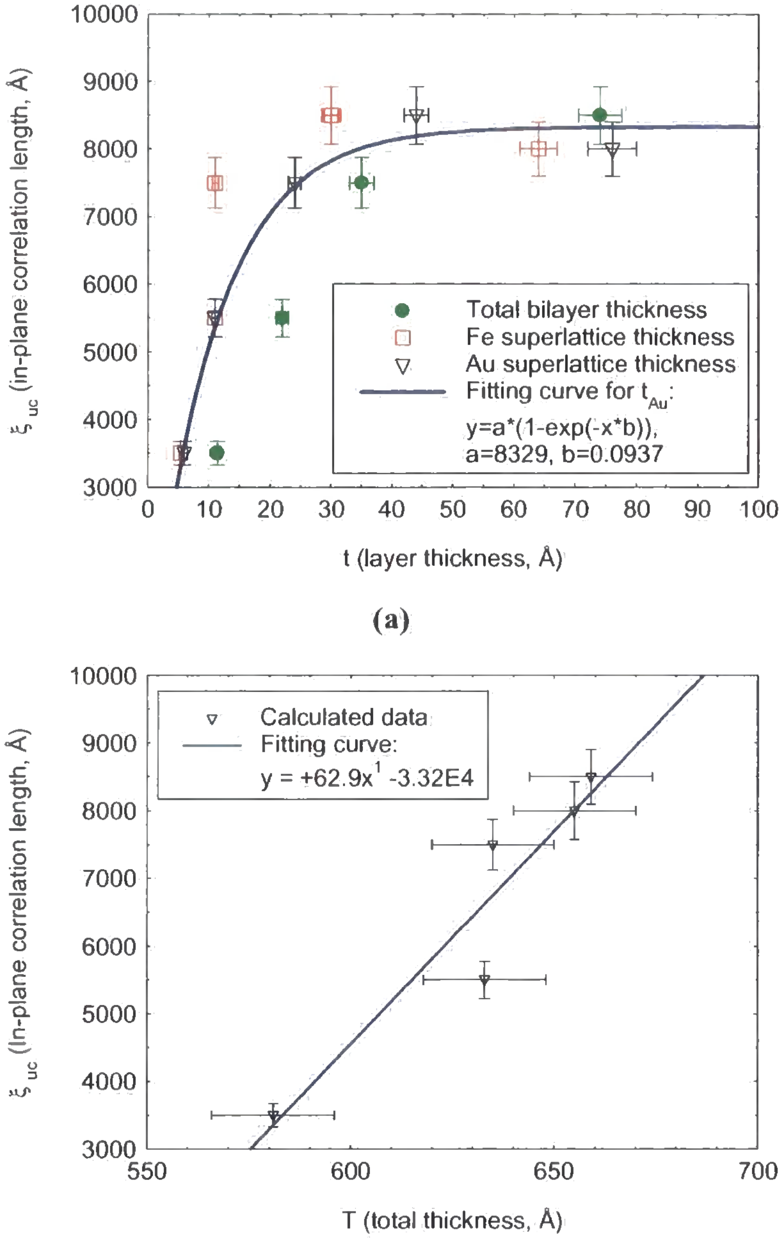

(a)

(b)

Figure 6.10 Variation of in-plane correlation length (ξ_{uc}) with **(a)** Individual and bilayer thicknesses (t), and **(b)** Total thickness T.

The relation between the fractal parameter (h) and number of bilayers is shown in Figure 6.11. It can be seen that h decreased as the number of bilayers increased indicating that the interfaces become more 3-dimensional in nature as the correlation length increases. Fractal parameter is typically lower than 0.5 for samples grown by MBE techniques while in the case of sputtered Fe/Au multilayers, Paniago *et al* observed a tendency toward saturation in the growth and interfacial smoothing after the deposition of 40 bilayers [52].

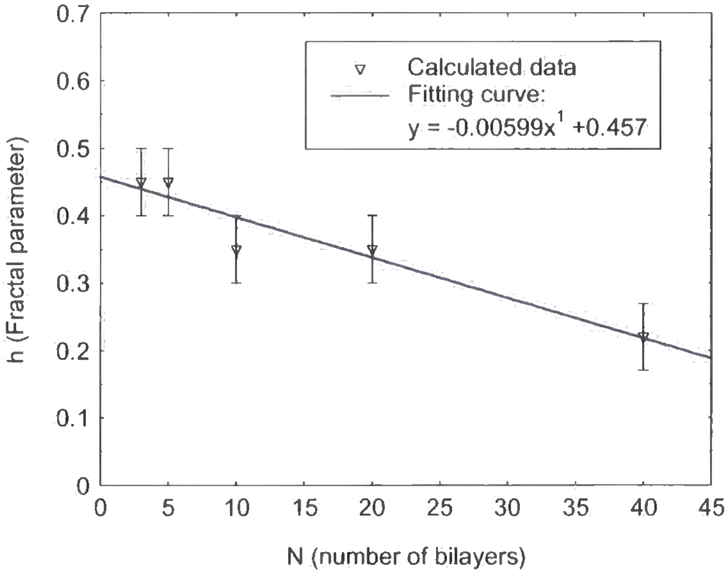

Figure 6.11 Relation between the fractal parameter (h) and number of bilayers.

6.6 100-bilayer sample

The sample was run on the Bede GXR1 reflectometer with λ=1.393Å and the x-ray data are illustrated in Figure 6.12. As can be seen, excellent fits have been achieved. In figure 6.12(b), the off-specular simulated data has been shifted downward for better visibility. The presence of off-specular Kiessig fringes in both experimental and simulated data indicated that the roughness was partially correlated with the fraction of $3/10$ (vertical correlation fraction). The vertical correlation roughness was found to be about 500Å. Structural parameters determined from the GIXR and GIXS fitting procedure are listed in Table 6.3.

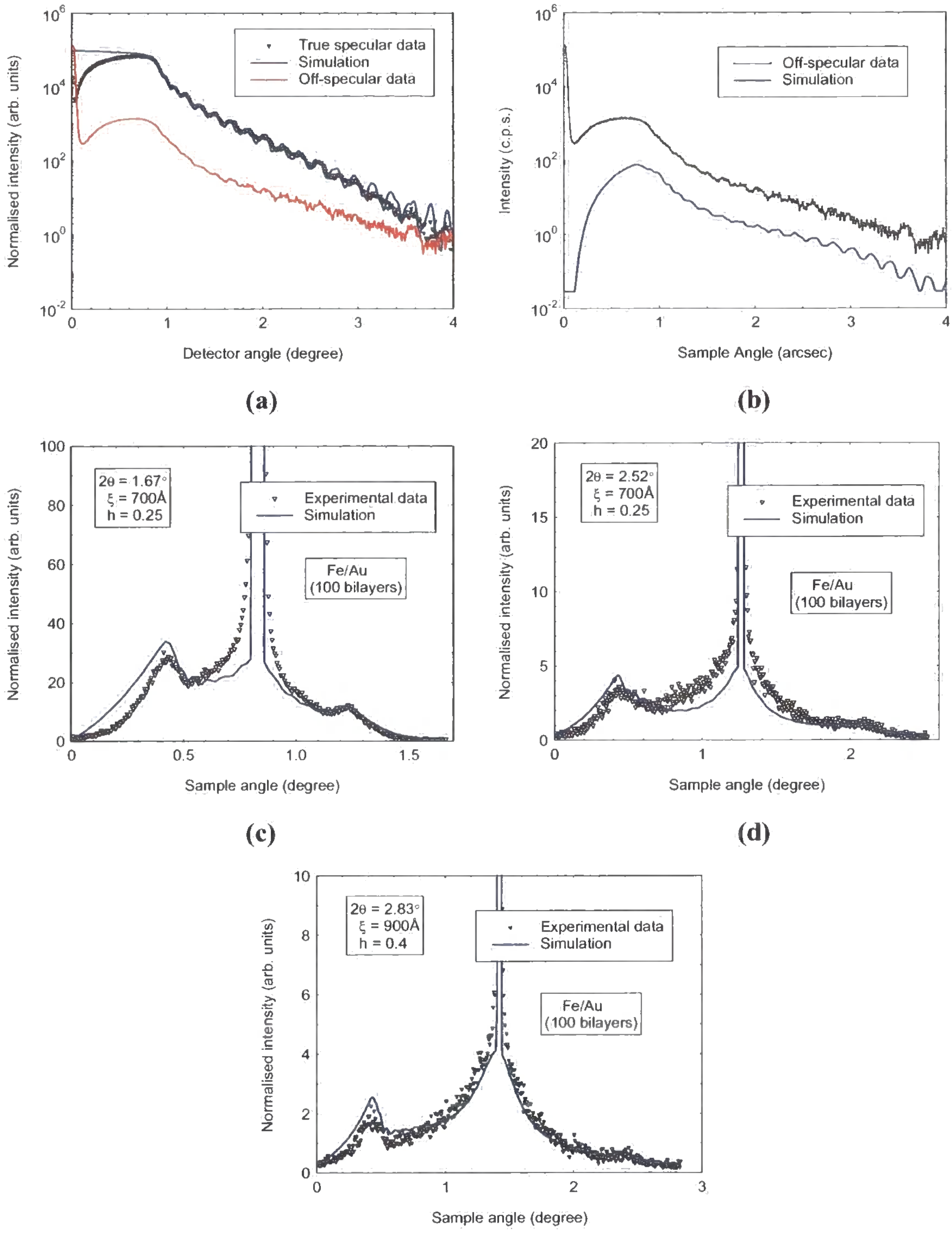

(a) **(b)**

(c) **(d)**

(e)

Figure 6.12 (a) Specular scan and simulation, **(b)** Off-secular data and simulation, **(c)**, **(d)**, and **(e)** Transverse diffuse scans and simulations at three Kiessig fringes.

Table 6.3

Multilayer structure parameters determined from x-ray scattering simulations.

N	t_{Seed} *Fe* ±0.3Å	t_{Buffer} *Au* ±0.3Å	$t_{Bil.}$ *Fe* ±0.3Å	$\sigma_{Bil.}$ *Fe* ±0.3Å	$t_{Bil.}$ *Au* ±0.3Å	$\sigma_{Bil.}$ *Au* ±0.3Å	t_{Cap} *Au* ±0.3Å	h ±10%	ξ (Å) ±10%
100	12.1	530.2	1.9	8.1	1.7	7.2	21.7	0.25	700

6.7 Discussions

The 100-bilayer sample showed a very different interface structure. As seen in Table 6.3, the interface parameters seem to be closer to the nominal parameters compared to the other series of Fe/Au samples (Table 6.1). The roughness of the interfaces and the in-plane correlation length are much lower. The most interesting feature appeared in this sample is illustrated in Figure 6.12(b). Excellent simulation of off-specular data gave indication of a major difference between the evolution of interfaces during the growth in this sample and the other series of Fe/Au multilayers discussed in this chapter. Exactly the same model was used for fitting the specular and diffuse data (unlike the other series of samples), suggesting that the interfaces of 100-bilayer sample are well defined with no detectable interdiffusion.

On the other hand, VSM measurements at room temperature confirmed that the 100-bilayer sample exhibited PMA. The hystersis loops are illustrated in Figure 6.13.

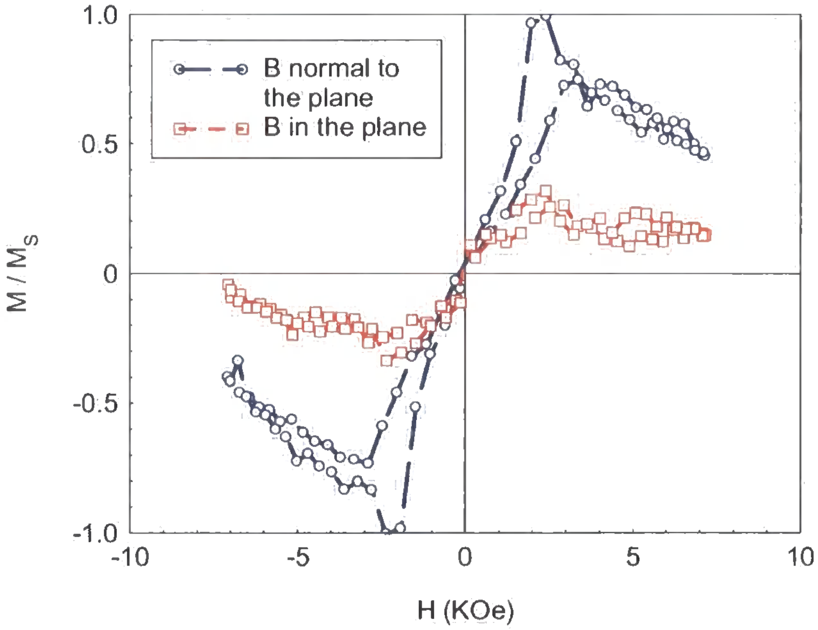

Figure 6.13 Hysteresis loops for the Fe/Au sample with 100 bilayers at room temperature.

The magnetization and interface structure of MBE grown Fe/Au multilayers with 100 bilayers have rarely been investigated in recent years. Honda *et al* studied the magnetic properties of 100-bilayer Fe/Au multilayers prepared on glass by electron-beam evaporation techniques and reported that PMA was induced when the Fe layer thickness became as small as 5Å [28].

6.8 Conclusions

The aim of the work reported in this chapter has been to study the effect of the interface structure on perpendicular magnetic anisotropy in a series of MBE grown Fe/Au multilayers as the number of bilayers changes. However, torque magnetometry measurements showed that not all samples exhibited out-of-plane magnetization. The easy axis remained in the plane with constant effective anisotropy energy in all cases.

Grazing incidence x-ray reflectivity and diffuse scattering data and simulations showed that the interface roughness was high and it is postulated that this results in the easy axis of magnetization remaining in the plane. However, the formation and propagation of uncorrelated roughness followed a systematic trend for surface growth. From the specular and off-specular data, it was found that there was a high degree of vertical correlation of the interfaces throughout the layer stack in all samples as a result of the presence of long period fringes. ξ_c was determined to be about equal in all samples while ξ_{uc} increased as the number of bilayers increased.

On the other hand, x-ray data and simulations for a single 100-bilayer sample showed that although the Fe and Au layers have the same thicknesses close to the other samples in the first series, the interfaces are much better defined with significantly lower roughness. This was the only sample to show perpendicular anisotropy supposing the suggestion that the absence of PMA in all other samples is associated with high interface roughness.

Finally, once again, Grazing Incidence x-ray Scattering is proved to be a very powerful technique for investigating the interface structure of thin films in details.

REFERENCES

[1] P. F. Carcia, A. D. Meinhaldt, and A. Suna, *Appl. Phys. Lett.*, **47 (2)**, 178-180 (1985).

[2] M. N. Baibich, J. M. Broto, A. Fert, F. N. Vandau, F. Petroff, P. Eitenne, G. Creuzet, A. Friederich, and J. Chazelas, *Phys. Rev. Lett.*, **61 (21)**, 2472-2475 (1988).

[3] Z. Celinski and B. Heinrich, *J. Magn. Magn. Mater.*, **99 (1-3)**, L25-L30 (1991).

[4] A. Fuss, S. Demokritov, P. Grunberg, and W. Zinn, *J. Magn. Magn. Mater.*, **103 (3)**, L221-L227 (1992).

[5] K. Takanashi, S. Mitani, H. Fujimori, K. Sato, and Y. Suzuki, *J. Magn. Magn. Mater.*, **177** , 1199-1200 (1998).

[6] V. I. Gavrilenko and R. Wu, *J. Appl. Phys.*, **85 (8)**, 5112-5114 (1999).

[7] M. F. Thomas, J. Bland, G. S. Case, J. A. Hutchings, and O. Nikolov, *Hyperfine Interact.*, **126 (1-4)**, 377-386 (2000).

[8] L. Uba, S. Uba, V. N. Antonov, A. N. Yaresko, A. Y. Perlov, T. Slezak, and J. Korecki, *Solid State Commun.*, **114 (8)**, 441-445 (2000).

[9] J. Grondilova, M. Rickart, J. Mistrik, K. Postava, S. Visnovsky, T. Yamaguchi, R. Lopusnik, S. O. Demokritov, and B. Hillebrands, *J. Appl. Phys.*, **91 (10)**, 8246-8248 (2002).

[10] K. Shintaku, Y. Daitoh, and T. Shinjo, *Phys. Rev. B*, **47 (21)**, 14584-14587 (1993).

[11] N. Hosoito, K. Mibu, T. Ono, T. Emoto, and T. Shinjo, *J. Magn. Magn. Mater.*, **156 (1-3)**, 325-326 (1996).

[12] W. Durr, M. Taborelli, O. Paul, R. Germar, W. Gudat, D. Pescia, and M. Landolt, *Phys. Rev. Lett.*, **62 (2)**, 206-209 (1989).

[13] S. Araki, T. Takahama, H. Dohnomae, T. Okuyama, and T. Shinjo, *Mater. Res. Soc. Symp. Proc.*, **151** , 123 (1989).

[14] H. Kikuchi, Y. Suzuki, and T. Katayama, *J. Appl. Phys.*, **67 (9)**, 5403-5405 (1990).

[15] G. Lugert, W. Robl, L. Pfau, M. Brockmann, and G. Bayreuther, *J. Magn. Magn. Mater.*, **121 (1-3)**, 498-502 (1993).

[16] C. Chappert, P. Bruno, B. Bartenlian, P. Beauvillain, R. Megy, and P. Veillet, *J. Magn. Magn. Mater.*, **148 (1-2)**, 165-166 (1995).

[17] R. Krishnan, A. Das, J. P. Eymery, M. Porte, and M. Tessier, *IEEE Trans. Magn.*, **33 (5)**, 3697-3699 (1997).

[18] R. Krishnan, A. Das, and M. Porte, *J. Magn. Magn. Mater.*, **168 (1-2)**, 15-17 (1997).

[19] I. Chibe, K. Himi, K. Saito, S. Mitani, K. Takanashi, K. Hayata, K. Sato, and H. Fujimori, *J. Magn. Magn. Mater.*, **226** , 1720-1721 (2001).

[20] N. Hosoito, S. Ogawa, and T. Shinjo, *Hyperfine Interact.*, **57 (1-4)**, 1865-1870 (1990).

[21] B. D. Fulthorpe, *Ph. D. Thesis,* University of Durham (1999).

[22] B. D. Fulthorpe, P. A. Ryan, T. P. A. Hase, B. K. Tanner, and B. J. Hickey, *J. Phys. D-Appl. Phys.*, **34 (10A)**, A203-A207 (2001).

[23] D. T. Dekadjevi, P. A. Ryan, B. J. Hickey, B. D. Fulthorpe, and B. K. Tanner, *Phys. Rev. Lett.*, **86 (25)**, 5787-5790 (2001).

[24] C. L. Fu, A. J. Freeman, and T. Oguchi, *Phys. Rev. Lett.*, **54 (25)**, 2700-2703 (1985).

[25] J. M. Maclaren, M. E. McHenry, S. Crampin, and M. E. Eberhart, *J. Appl. Phys.*, **67 (9)**, 5406-5408 (1990).

[26] Z. P. Shi, J. F. Cooke, Z. Y. Zhang, and B. M. Klein, *Phys. Rev. B*, **54 (5)**, 3030-3032 (1996).

[27] L. Szunyogh, B. Ujfalussy, and P. Weinberger, *Phys. Rev. B*, **51 (15)**, 9552-9559 (1995).

[28] S. Honda, K. Koguma, M. Nawate, and I. Sakamoto, *J. Appl. Phys.*, **82 (9)**, 4428-4434 (1997).

[29] K. Takanashi, S. Mitani, K. Himi, and H. Fujimori, *Appl. Phys. Lett.*, **72 (6)**, 737-739 (1998).

[30] J. Krim and G. Palasantzas, *Int. J. Mod. Phys. B*, **9 (6)**, 599-632 (1995).

[31] R. Paniago, P. C. Chow, R. Forrest, and S. C. Moss, *Physica B*, **248** , 39-47 (1998).

[32] M. Suzuki and Y. Taga, *Phys. Rev. B.*, **52** , 361 (1995).

[33] Z. H. Yang and M. R. Scheinfein, *ibid*, **52** , 4263 (1995).

[34] X. H. Liu, J. Chen, M. Chen, and X. Wang, *Appl. Surf. Sci.*, **187 (3-4)**, 187-191 (2002).

[35] D. Rafaja, H. Fuess, D. Simek, J. Kub, J. Zweck, J. Vacinova, and V. Valvoda, *J. Phys.-Condes. Matter*, **14 (21)**, 5303-5314 (2002).

[36] A. Berkowitz and e. al, *Phys. Rev. Lett.*, **68** , 3745 (1992).

[37] J. W. Dykes and e. al, *J. Appl. Phys.*, **79** , 5584 (1996).

[38] A. Schreyer, J. F. Ankner, T. Zeidler, H. Zabel, M. Schafer, J. A. Wolf, P. Grunberg, and C. F. Majkrzak, *Phys. Rev. B*, **52 (22)**, 16066-16085 (1995).

[39] S. K. Sinha, E. B. Sirota, S. Garoff, and H. B. Stanley, *Phys. Rev. B*, **38 (4)**, 2297-2311 (1988).

[40] S. K. Sinha, *Curr. Opin. Solid State Matter. Sci.*, **1 (5)**, 645 (1996).

[41] S. K. Sinha, *Acta Phys. Pol. A*, **89 (2)**, 219-234 (1996).

[42] D. K. G. de Boer, *Phys. Rev. B*, **49 (9)**, 5817-5820 (1994).

[43] W. Weber and B. Lengeler, *Phys. Rev. B.*, **46 (12)**, 7953 (1992).

[44] M. Wormington, C. Panaccione, K. M. Matney, and D. K. Bowen, *Philos. Trans. R. Soc. Lond. Ser. A-Math. Phys. Eng. Sci.*, **357 (1761)**, 2827-2848 (1999).

[45] A. S. H. Rozatian, B. D. Fulthorpe, T. P. A. Hase, D. E. Read, G. Ashcroft, D. E. Joyce, P. J. Grundy, J. Amighian, and B. K. Tanner, *J. Magn. Magn. Mater.*, **256** , 365-372 (2003).

[46] S. Riedling, N. Knorr, C. Mathieu, J. Jorzick, S. O. Demokritov, B. Hillebrands, R. Schreiber, and P. Grunberg, *J. Magn. Magn. Mater.*, **199** , 348-350 (1999).

[47] A. Paul, *J. Magn. Magn. Mater.*, **240** , 497-500 (2002).

[48] L. Uba, S. Uba, V. N. Antonov, A. N. Yaresko, T. Slezak, and J. Korecki, *Phys. Rev. B*, **62 (20)**, 13731-13747 (2000).

[49] A. Paul, A. Gupta, P. Shah, K. Kawaguchi, and G. Principi, *Hyperfine Interact.*, **139 (1-4)**, 205-213 (2002).

[50] B. D. Fulthorpe, D. E. Joyce, T. P. A. Hase, A. S. H. Rozatian, B. K. Tanner, and P. J. Grundy, *J. Phys.-Condes. Matter*, **11 (43)**, 8477-8487 (1999).

[51] C. M. Schmidt, D. E. Burgler, D. M. Schaller, F. Meisinger, H. J. Guntherodt, and K. Temst, *J. Appl. Phys.*, **89 (1)**, 181-187 (2001).

[52] R. Paniago, R. Forrest, P. C. Chow, S. C. Moss, S. S. P. Parkin, and D. Cookson, *Phys. Rev. B*, **56 (20)**, 13442-13454 (1997).

Chapter 7

Interfaces in Co/Pt Multilayers

7.1 Introduction

Co/Pt and Co/Pd multilayers that display perpendicular magnetic anisotropy (PMA), high coercivity and significant Kerr rotations in the range of visible light are candidates for high-density magnetic and magneto-optical recording media. Since the discovery of PMA in multilayer thin films [1], there have been numerous experimental and theoretical studies some of which have been reviewed in chapters 2 and 3. However, recent work has suggested that PMA cannot be explained solely by Néel surface anisotropy. A different electronic structure [2] or strain and interface dislocations [3] at the magnetic-non-magnetic interfaces have also been suggested as the possible origin, especially for samples produced by sputtering [4-6]. This is supported by the observation that stress and strain induced by the mismatch between magnetic and non-magnetic layers can be used to change the properties of Co/Pd multilayers and thus play a role in obtaining the desired anisotropy [7].

Depending on the thickness of the magnetic layer, the anisotropy of the film changes from in-plane to the perpendicular direction as the thickness of the Co layer reduces below a critical value [8, 9]. It has been shown that Co/Pd and Co/Pt multilayers have an easy axis of magnetization perpendicular to the thin film plane only when the Co layers are very thin (t_{Co}< 8Å for Co/Pd and t_{Co}< 14Å for Co/Pt) [3, 8, 9]. Greaves *et al* found that the PMA in Co/Pt multilayers peaked for a Co thickness of around 4Å [10]. At greater thicknesses a smaller proportion of the Co atoms are at the interfaces and the surface anisotropy contribution decreases.

On the other hand, defect structures such as the roughness of the interface [11, 12], and the degree of mixing of the atoms at the interface (the sharpness of the interface) [13] have been predicted to affect the anisotropy. Baker *et al* showed that grain boundaries in polycrystalline Co/Pd films appear to act as preferential sites for intermixing, reducing the thermal stability of the films [14]. Oh and Joo [15] studied the importance of the sputtering pressure during the preparation of the Pd or Pt underlayer on the magnetic properties of Co/Pd and Co/Pt multilayers. They found that the coercivity of Co/Pd multilayers was very sensitive to the surface roughness of the underlayer, in contrast to Co/Pt multilayers, which were insensitive to the effect.

In the studies of Co/Pt sputtered multilayers, grown previously at Salford on Si [16] and on glass [17, 18] high values of effective anisotropy between 10 and 18 bilayers were observed (see section 2.4.1). In this chapter, the structural and interface parameters of the underlayer and bilayers and their relation to the magnetic properties of (Co 4Å/ Pt 12Å) multilayers sputtered on silicon will be studied. The results will also be compared with the other series of Co/Pt multilayers.

7.2 Samples

A series of Co/Pt multilayer films were grown on a single crystal (001) oriented silicon using the magnetron sputtering technique at the University of Salford by D. E. Joyce. All samples were nominally:

SiO_2/50Å Pt/ $N \times$ {4Å Co / 12Å Pt} where $N = 5, 10, 12, 15, 20, 25$

The base pressure in the sputtering chamber was 4×10^{-8} mbar with 3 mTorr Ar Partial pressure.

7.3 Magnetic measurements

Anisotropy measurements were made using the torque magnetometer, VSM and home-built AGFM. Magnetic measurements were performed at room temperature and all experimental torque curves were numerically fitted to the Equation (3.20) discussed in chapter 3.

7.3.1 Torque magnetometry results

Samples were run on the torque magnetometer with magnetic field ranging from 0KOe to 8.8KOe. The torque curves for the 12 and 15 bilayer samples can be seen in Figure 7.1. The reason for choosing these data is to show the reader how sensitive the torque magnetometer is to the sample size and presence of other instruments in the laboratory. For small samples and at low magnetic fields, the torque data becomes noisy, as can be seen in Figure 7.1(a). In addition, running VSM, AGFM and other magnetic instruments during torque data collection, can cause some noise in the torque data.

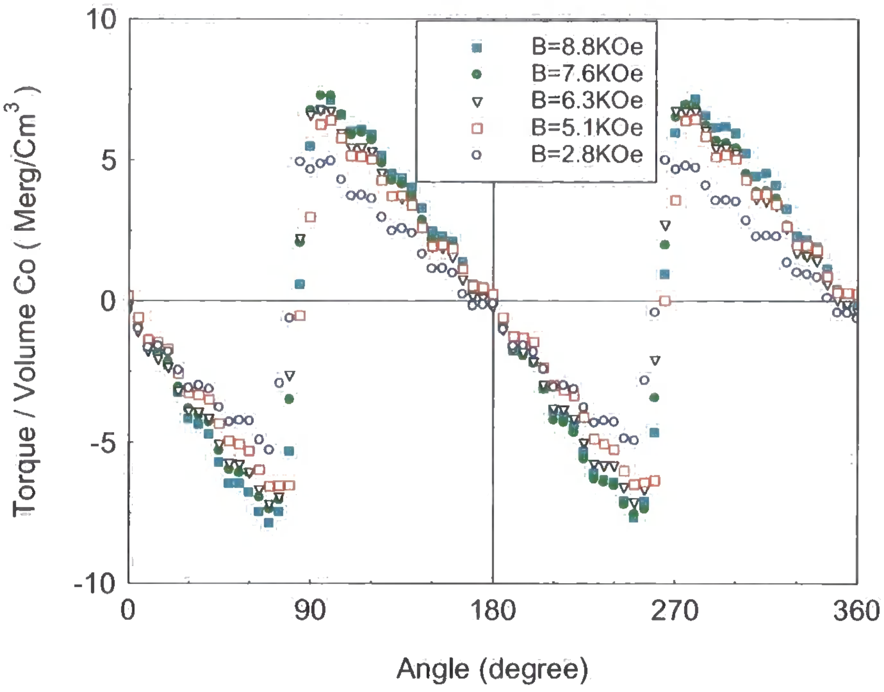

(a)

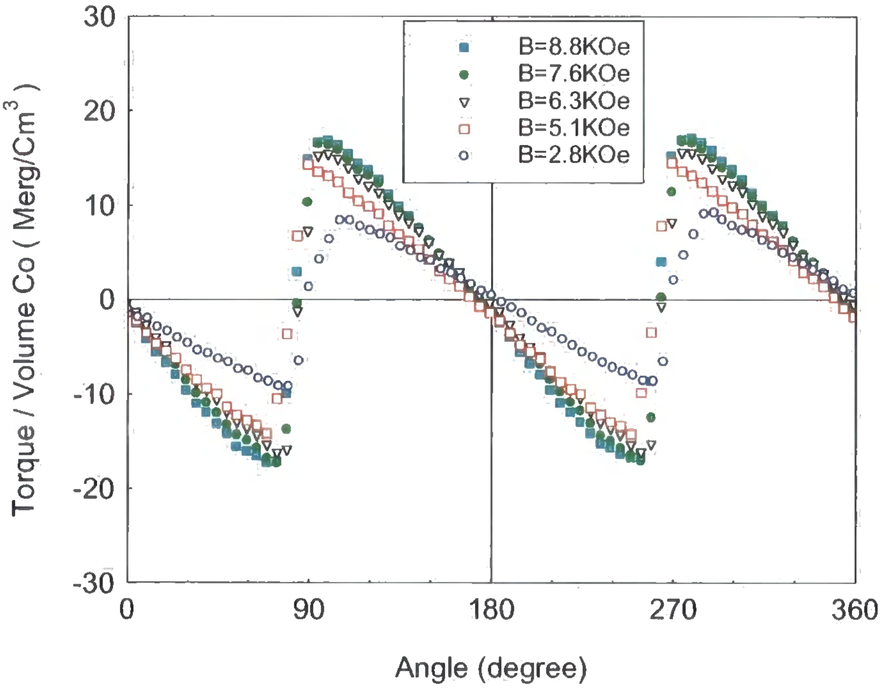

(b)

Figure 7.1 Torque curves at different magnetic fields. **(a)** 12-bilayer sample. **(b)** 15-bilayer sample.

As can be seen in Figure 7.2, the amplitude of all torque curves increased with increasing magnetic field up to 7.6 KOe and then remained constant indicating that saturation of the magnetization had been achieved.

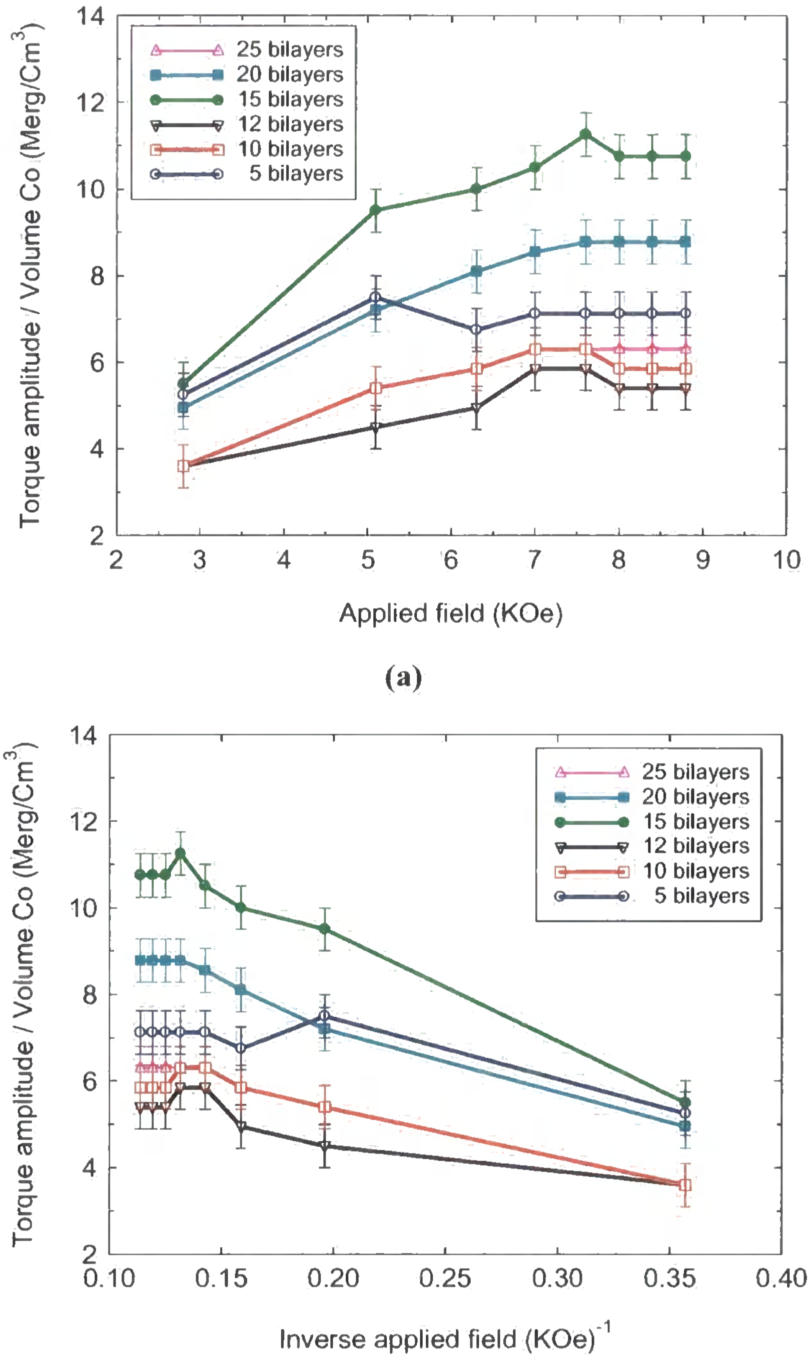

(a)

(b)

Figure 7.2 Relation between Torque and **(a)** Applied field, **(b)** Inverse applied field.

Torque curves along with a fit to Equation (6.1) for all samples, including a shear correction can be seen in Figure 7.3. Due to the large amount of experimental data only a representative selection of torque data and simulations are shown here.

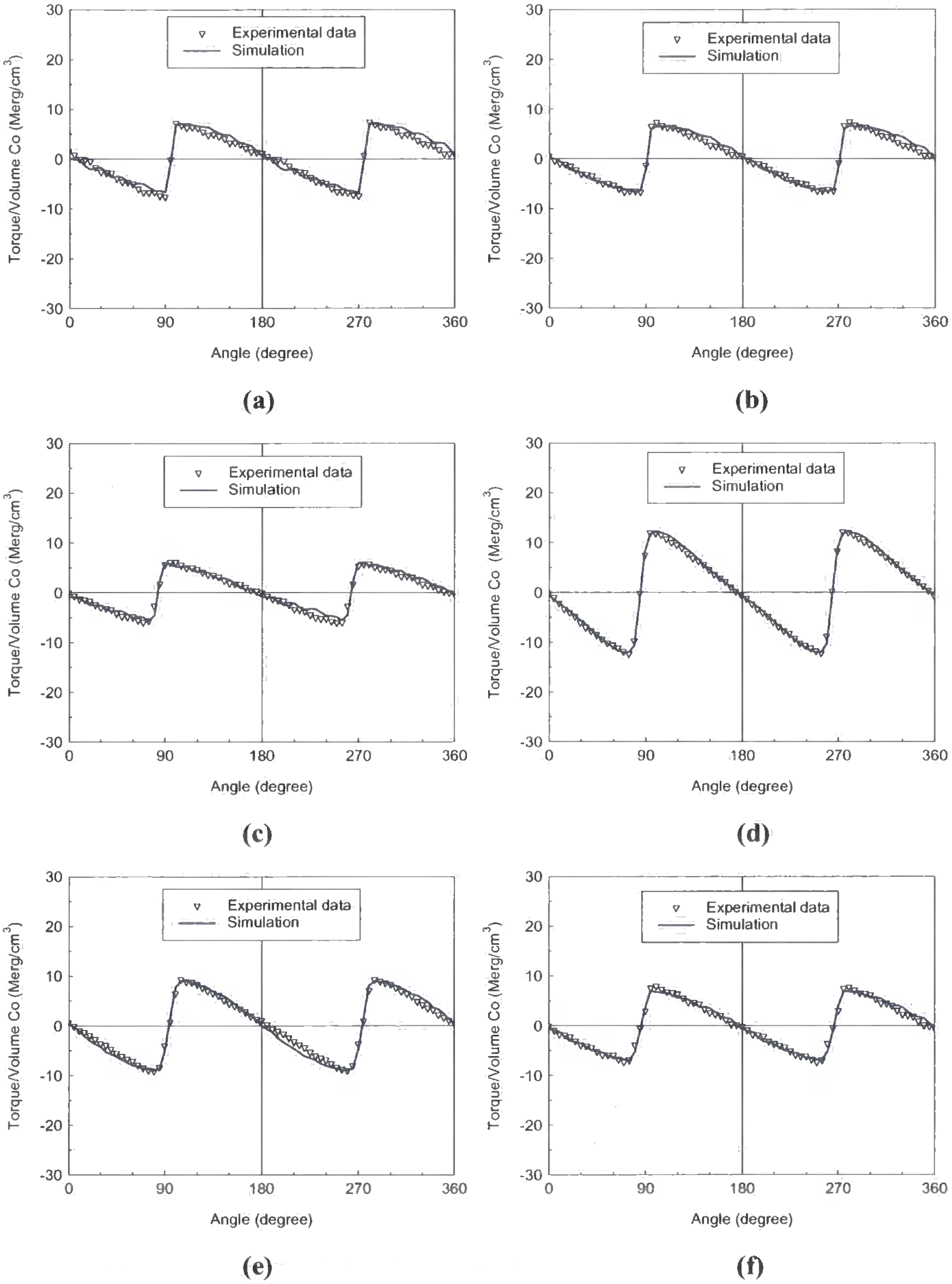

Figure 7.3 Torque curves for the samples with **(a)** 5 bilayers, **(b)** 10 bilayers, **(c)** 12 bilayers, **(d)** 15 bilayers, **(e)** 20 bilayers, and **(f)** 25 bilayers.

The negative slope at $\phi = 0$ confirms the normal to the plane of the sample as the easy direction for all samples showing that PMA is exhibited for all samples. Torque data were normalized to the magnetic volume deduced from the Co thickness determined from the x-ray reflectometry data.

As seen in Figure 7.4, the effective anisotropy (K_{eff}) is positive in all cases, again confirming that the magnetic moments are out of plane for all samples.

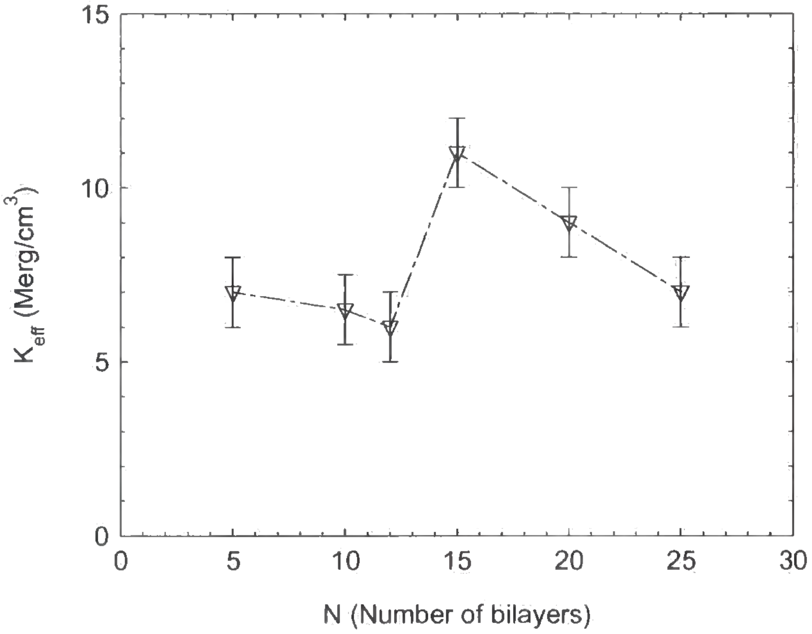

Figure 7.4 Relation between K_{eff} and number of bilayers at B = 7.6KOe.

A maximum value of $K_{eff} = (11 \pm 1)\, Merg/cm^3$ was seen for the 15 bilayer sample at $B = 7.6\, KOe$ while values for other numbers of bilayer repeats are smaller. This is midway within the range of values between 1.45 Merg/cm^3 and 35 Merg/cm^3 (depending on the deposition conditions and the type of substrate) reported by several authors [16, 17, 19-25]. K_2 was found to be zero for all samples; there was no detectable component of 4ϕ in the torque curves.

7.3.2 VSM measurements

All samples were run on the laboratory Vibrating Sample Magnetometer (VSM). VSM data showed excellent consistency with the torque magnetometry measurements and can be seen in Figure 7.5.

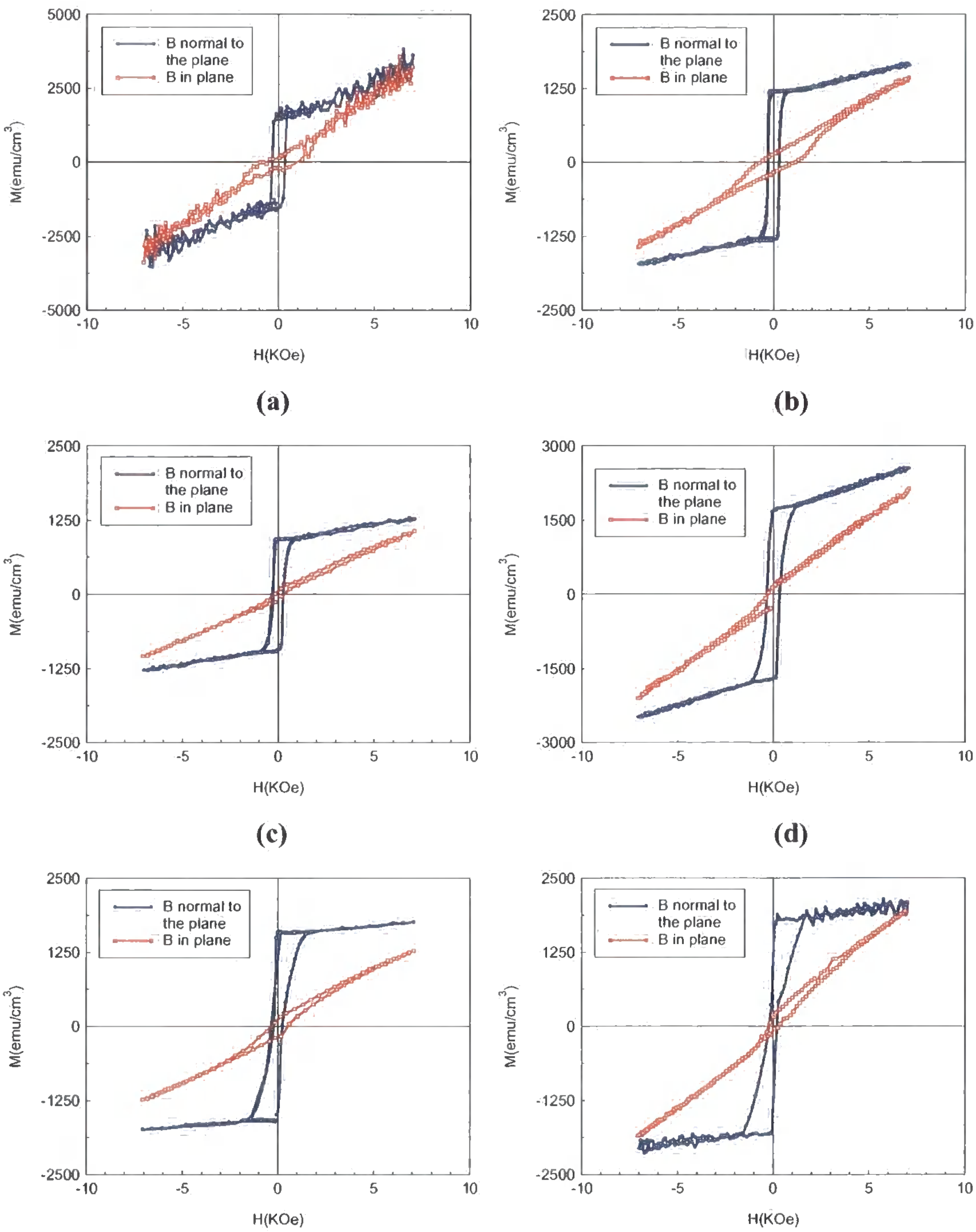

(a) **(b)** **(c)** **(d)** **(e)** **(f)**

Figure 7.5 VSM magnetization loops for samples with **(a)** 5 bilayers, **(b)** 10 bilayers, **(c)** 12 bilayers, **(d)** 15 bilayers, **(e)** 20 bilayers, and **(f)** 25 bilayers.

From the area between the in-plane and out-of-plane M-H loops, K_{eff} was calculated for all samples and the results can be seen in Figure 7.6. Again, the 15 bilayer sample has a maximum value for K_{eff}. In the out-of-plane measurements all samples were found to have low coercivities, typically 0.35 KOe. This at the low end of the values between 0.3-12.8 KOe reported in the literature [16, 17, 22-26].

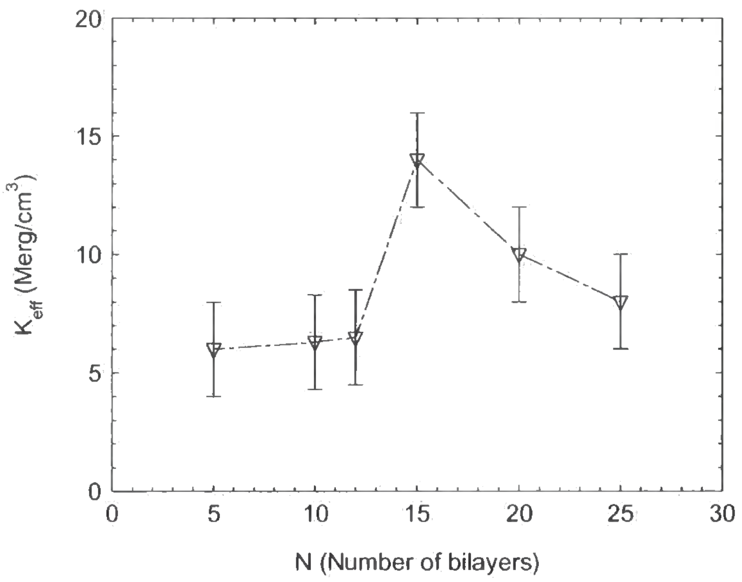

Figure 7.6 Relation between K_{eff} and number of bilayers (VSM measurements).

7.3.3 AGFM measurements

The AGFM data in this section were taken by G. Ashcroft at the University of Durham on a home-built Alternating Gradient Field Magnetometer. AGFM measurements are again in excellent consistency with TM and VSM measurements. A series of out-of-plane hystersis loops can be seen in Figure 7.7.

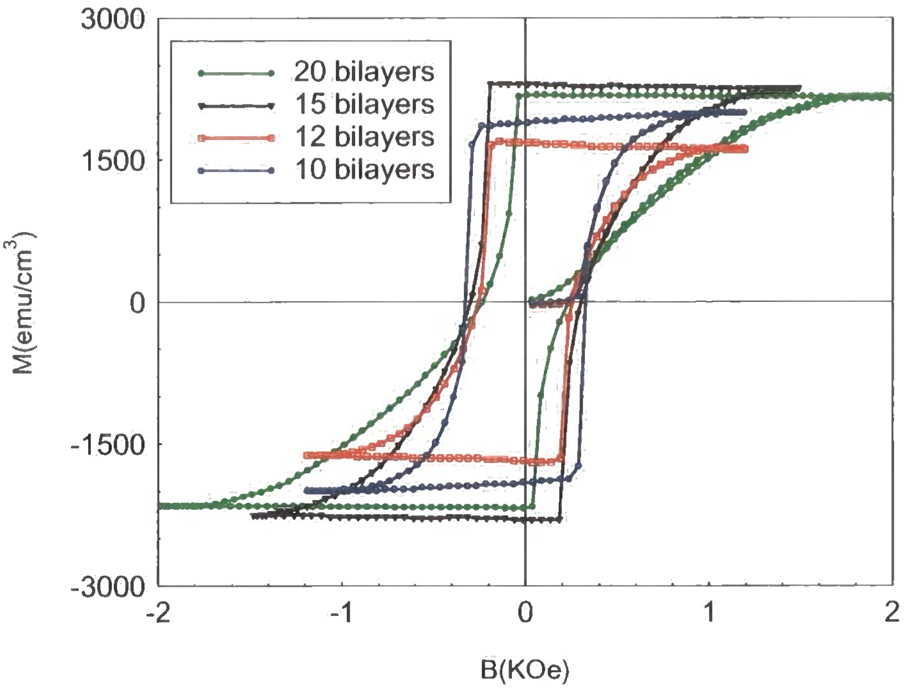

Figure 7.7 AGFM out-of plane hystersis loops (taken by G. Ashcroft, Department of Physics, University of Durham).

7.4 X-ray experiments

In this section, the x-ray data will be presented. Grazing incidence x-ray reflectivity (GIXR) and scattering (GIXS) experiments were carried out on a Bede GXR1 laboratory reflectometer using a wavelength of $\lambda = 1.393\text{Å}$ and on station 2.3 at the SRS (Daresbury). The best synchrotron radiation data were obtained at a wavelength of $\lambda = 1.3\text{Å}$, where the intensity from the monochromator is a maximum. High angle x-ray diffractometry measurements were performed on beamline BM16 at the ESRF, Grenoble.

7.4.1 GIXR results

A series of grazing incidence specular and off-specular x-ray scans along with simulations for these samples is shown in Figure 7.8. These scans provide information concerning the development of the multilayer stack as the number of bilayers was increased from 5 to 25.

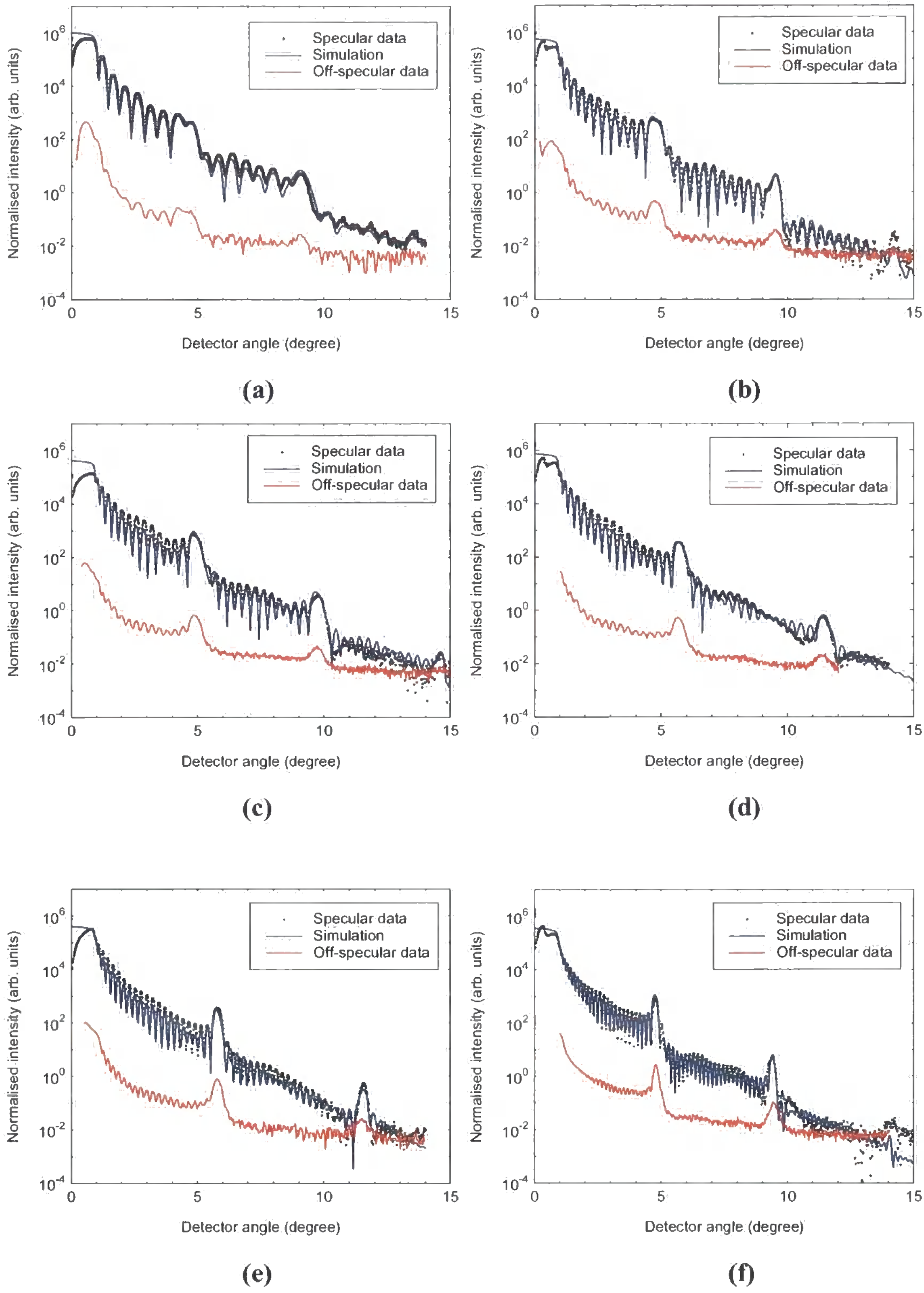

(a) **(b)** **(c)** **(d)** **(e)** **(f)**

Figure 7.8 Specular, Off-specular and simulations for samples with **(a)** 5 bilayers, **(b)** 10 bilayers, **(c)** 12 bilayers, **(d)** 15 bilayers, **(e)** 20 bilayers, and **(f)** 25 bilayers.

As can be seen in Figure 7.9, the position and spacing of the specular (Figure 7.9(a)) and off-specular (Figure 7.9(b)) Bragg peaks for the N=15 & 20 bilayer samples show the bilayers were slightly thinner than the nominal thickness. The off-specular Bragg peaks remained strong (Figure 7.9(b)), indicating that correlation in roughness between bilayers was retained up to the maximum thickness grown. Further, off-specular data (Figure 7.9(b)) and simulations (Figure 7.10) show that the Kiessig fringes are retained in all samples demonstrating that the roughness is correlated over the entire sample thickness in all cases.

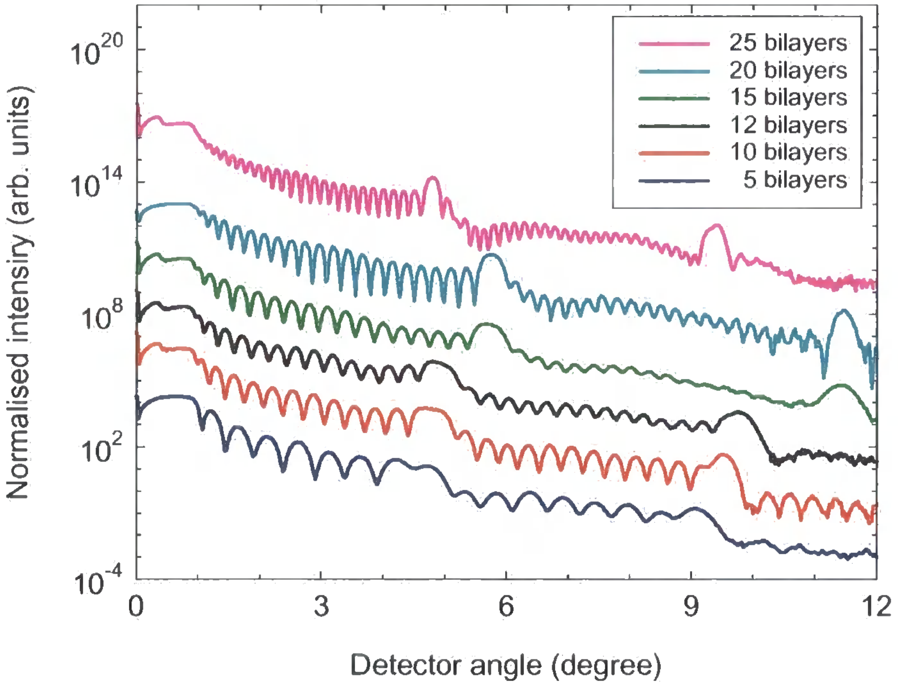

(a)

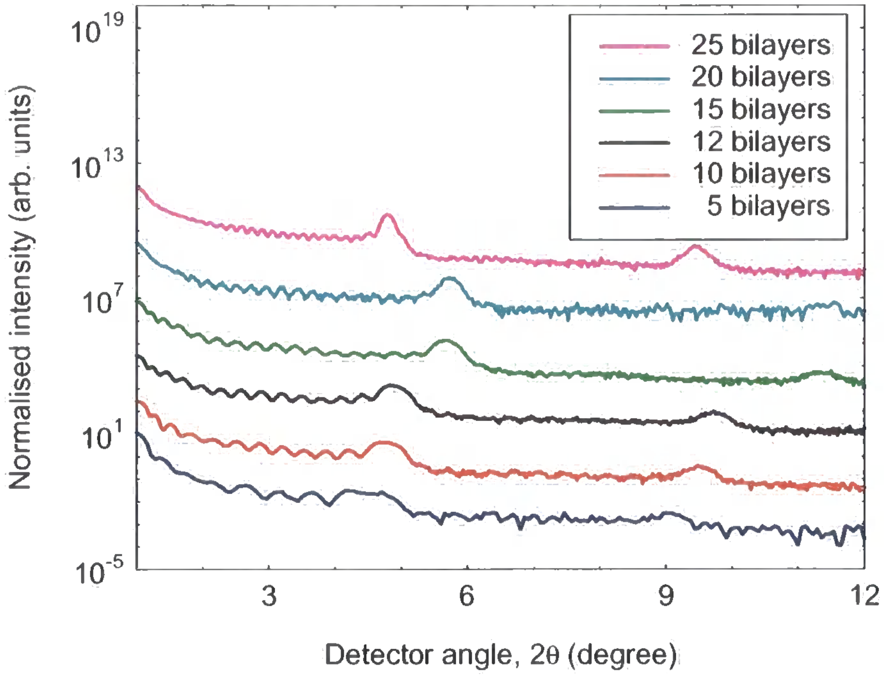

(b)

Figure 7.9 (a) A series of Co/Pt Specular scans, λ = 1.3Å. **(b)** A series of Co/Pt Off-specular scans (sample off-set -0.1°, λ = 1.3Å).

In figure 7.10 a series of off-specular simulations for Co/Pt show the effect of varying the number of bilayers form $N=5$ to $N=25$ for a system in which the interface roughness is correlated in nature. Both off-specular Kiessig fringes and Bragg peaks remain as N increases and this is clearly consistent with the actual data in figure 7.8.

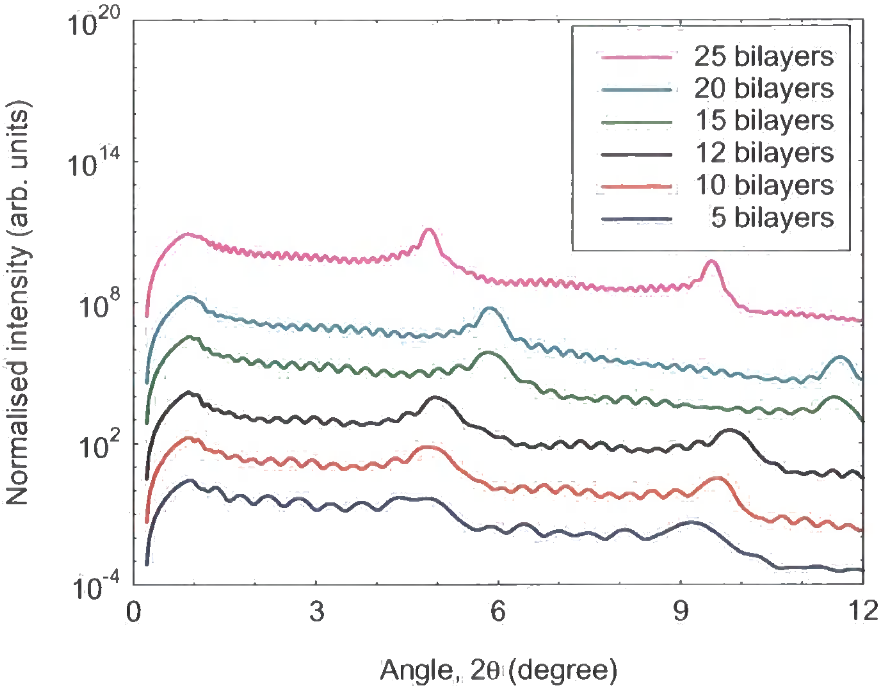

Figure 7.10 A series of Co/Pt Off-specular simulations. With out-of-plane correlation length ranging from 160Å - 400Å

Structural parameters were obtained by fitting the experimental data to simulations from a model structure. Values of thickness and interface width were first found by automatic refinement using the Bede MERCURY code for the specular data and these parameters then used to fit the diffuse scatter manually (section 7.4.2). In all cases excellent and unambiguous convergence was found, provided that the data range was sufficient to cover at least the first two Bragg peaks.

7.4.2 GIXS results

Across the series of six samples, extensive specular and transverse diffuse measurements were made. Through a combination of these scans, many aspects of the interface morphology in the multilayer structures could be characterised. Two x-ray wavelengths were used, one on the laboratory GXR1, 1.393Å, and one on the station 2.3 at the SRS, 1.3Å. For each sample, at each wavelength, 3-5 transverse diffuse scans were taken, one or two at and two or more away from the Bragg condition. These scans are primarily sensitive to correlated and uncorrelated roughness respectively. The Bede REFS code (which was used to fit the transverse diffuse data), considers four different models for interfaces. Best fits were achieved using two models for partially correlated roughness. Models I and II use out-of-plane (or vertical) correlation fraction (VCF) and out-of-plane (or vertical) correlation length respectively. In the following sub-sections, these two parameters will be determined by using the two models. Due to the large amount of experimental data obtained, only the best SRS data and simulations for each of the samples are shown here (Figures 7.11 – 7.17).

7.4.2.1 Partially correlated interfaces, model I

A series of transverse diffuse scans and simulations can be seen in Figure 7.11.

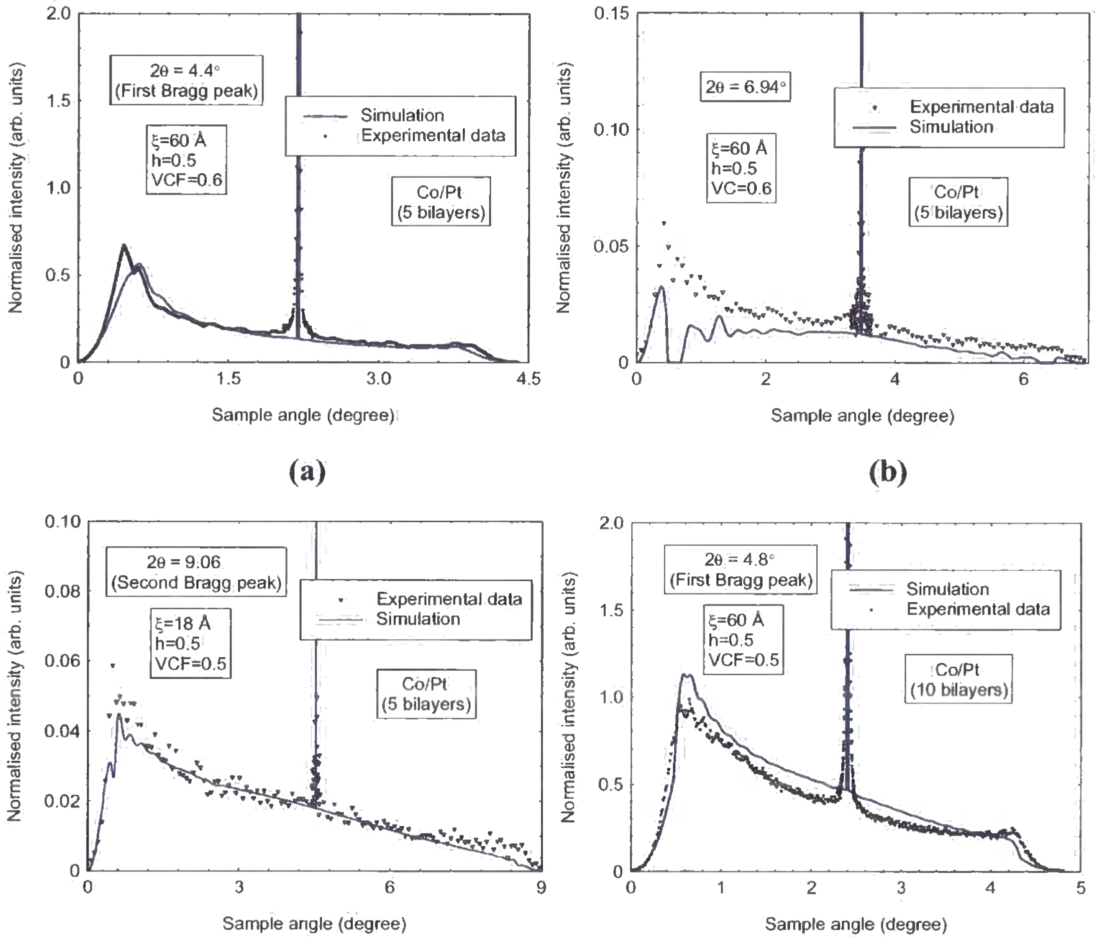

(a) (b)

(c) (d)

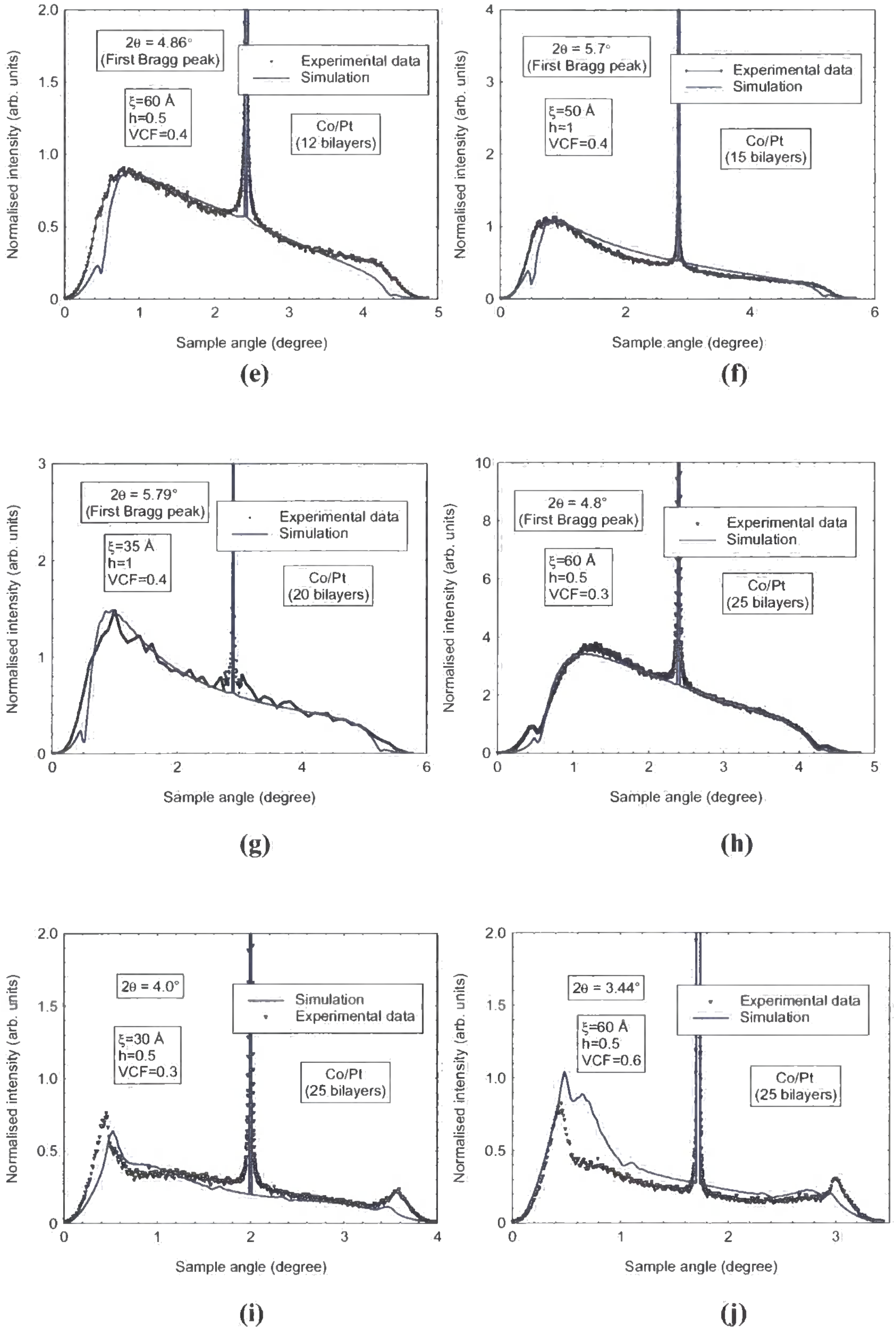

Figure 7.11 Transverse diffuse scans and simulations using Bede REFS, Model I.

As can be seen in Figure 7.11, in some cases it was not possible to achieve the best fit by using the same parameters (of the same sample) to fit all diffuse scans in different angles. This is due to the limited parameters in Model I that can be changed during the fitting process as this model assumes propagation of a fraction of conformal roughness through the layers. As stated in chapter 5, model I is best for measuring the fraction of correlated and uncorrelated roughness for each interface (*VCF*) by simulating the off-specular data.

Structural parameters, such as thickness (t), *rms* roughness (σ), in-plane correlation length (ξ), vertical correlation fraction (*VCF*) and fractal parameter (h) determined from the GIXR and GIXS fitting procedure are listed in table 6.1. No interdiffusion was detected between interfaces for all samples $(\Sigma = 0)$. Densities of all layers were fixed at 100%.

Table 7.1

Multilayer structure parameters determined from x-ray scattering simulations, Model I.

N	t_{Buffer} (±0.3Å)	t_{Co} (±0.3Å)	t_{Pt} (±0.3Å)	σ_{Co} (±0.3Å)	σ_{Pt} (±0.3Å)	*VCF* (±10%)	ξ (±10Å)	h (±10%)
5	54.3	3.1	13.0	2.5	2.5	0.6	60	0.5
10	50.5	3.2	12.5	2.9	2.9	0.5	60	0.5
12	46.8	3.7	11.6	2.2	3.0	0.5	60	0.5
15	41.9	2.3	10.7	2.4	3.1	0.4	50	1.0
20	38.6	2.3	10.7	2.5	3.2	0.4	60	1.0
25	50.5	3.0	13.0	3.0	3.0	0.3	60	0.5

7.4.2.2 Partially correlated interfaces, model II

Model II was used to achieve best fits and the results can be seen in Figures 7.12-7.17. Model I code is very fast and the simulation can be done in a few seconds while Model II is much slower (more than ten times) as many parameters have been employed to find the best fit, Among them, the value of out-of-plane correlation length.

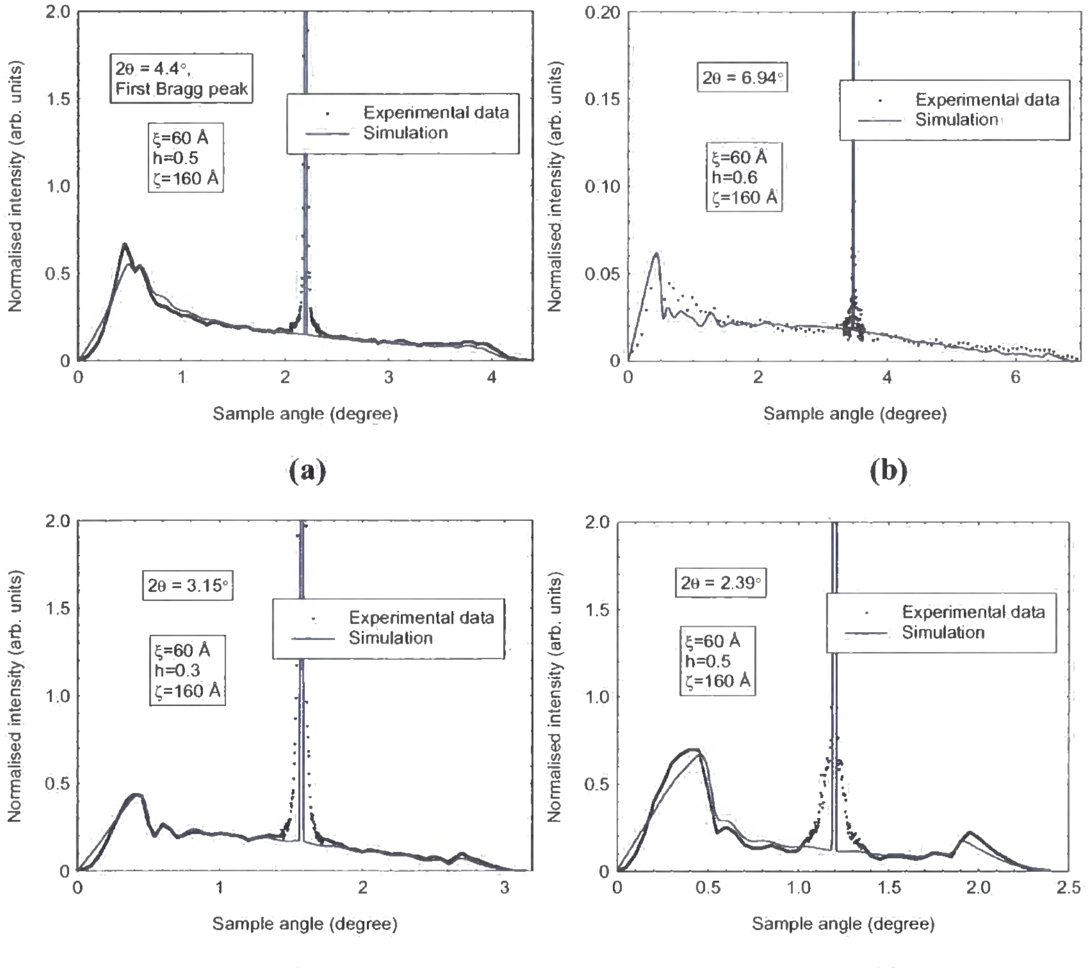

(a) (b)

(c) (d)

Figure 7.12 Transverse diffuse scans and simulations for the 5-bilayer sample.

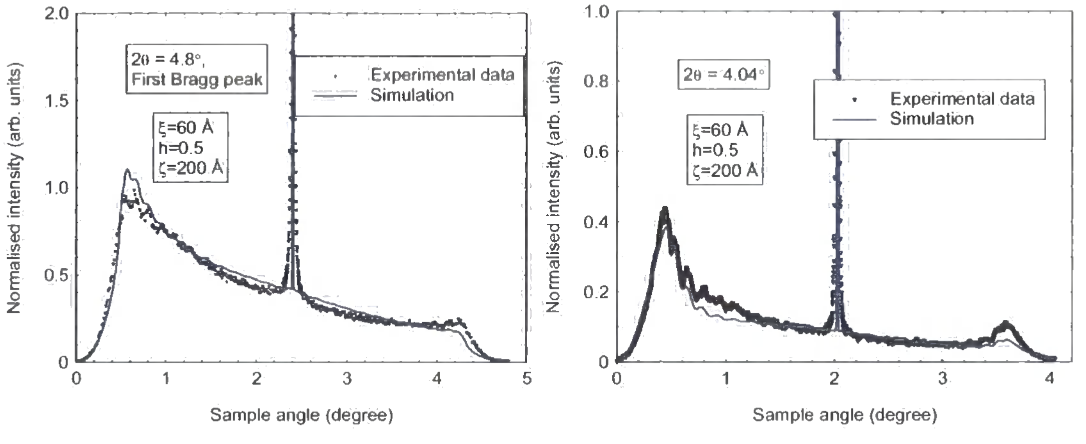

(a) (b)

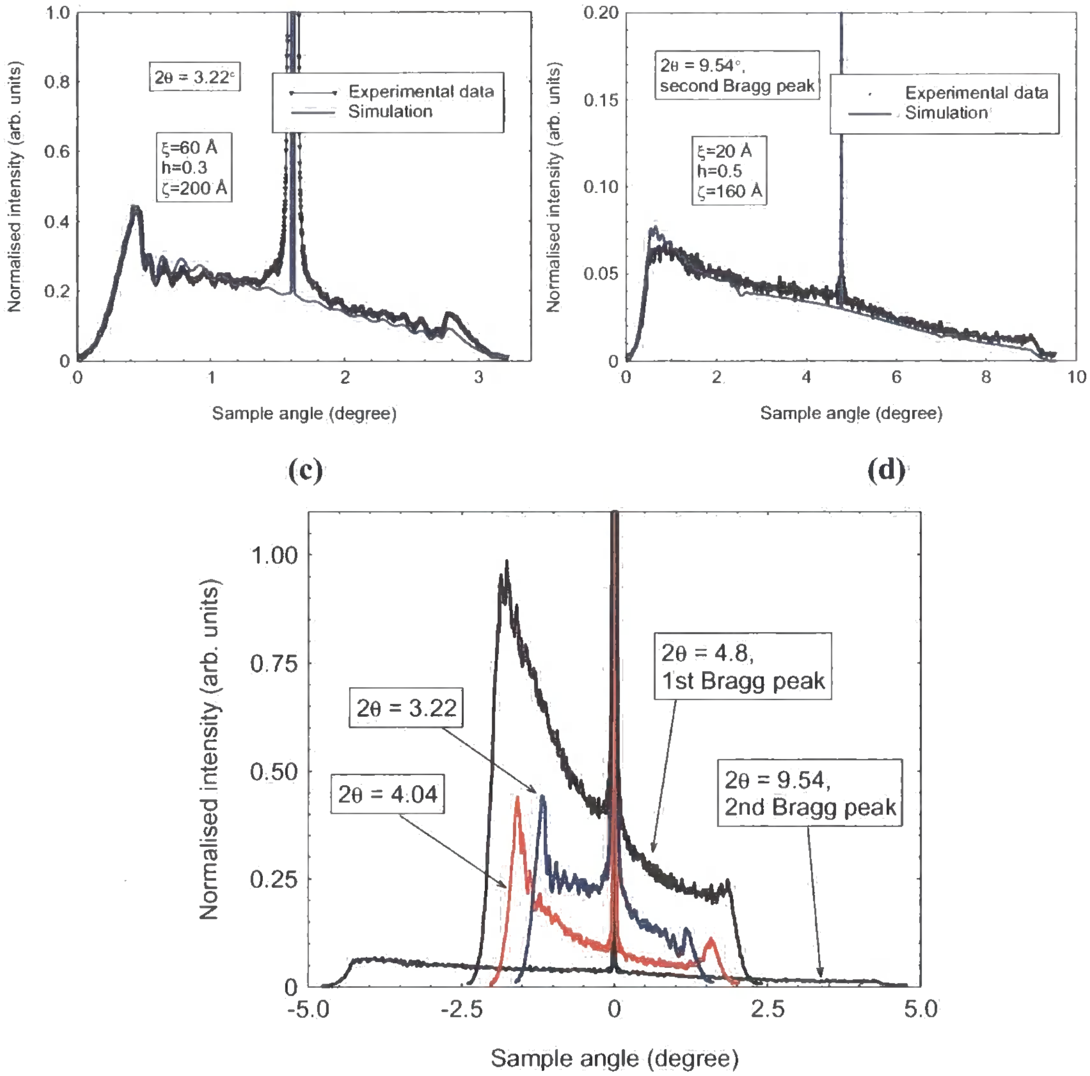

(c) (d)

(e)

Figure 7.13 Transverse diffuse scans and simulations for the 10-bilayer sample.

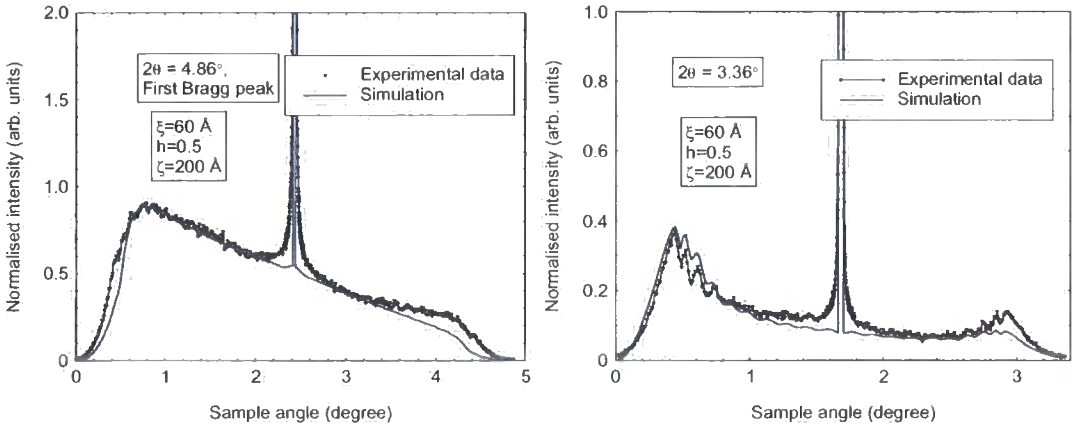

(a) (b)

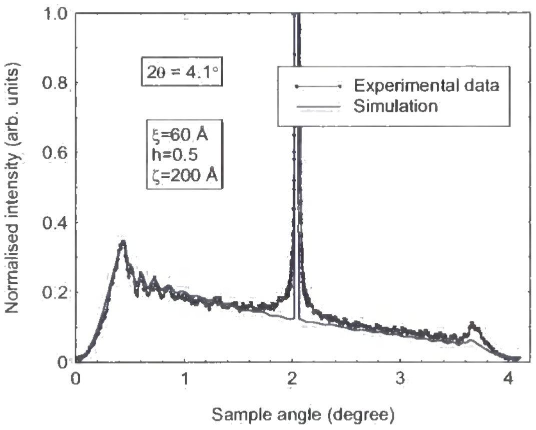

(c)

Figure 7.14 Transverse diffuse scans and simulations for the 12-bilayer sample.

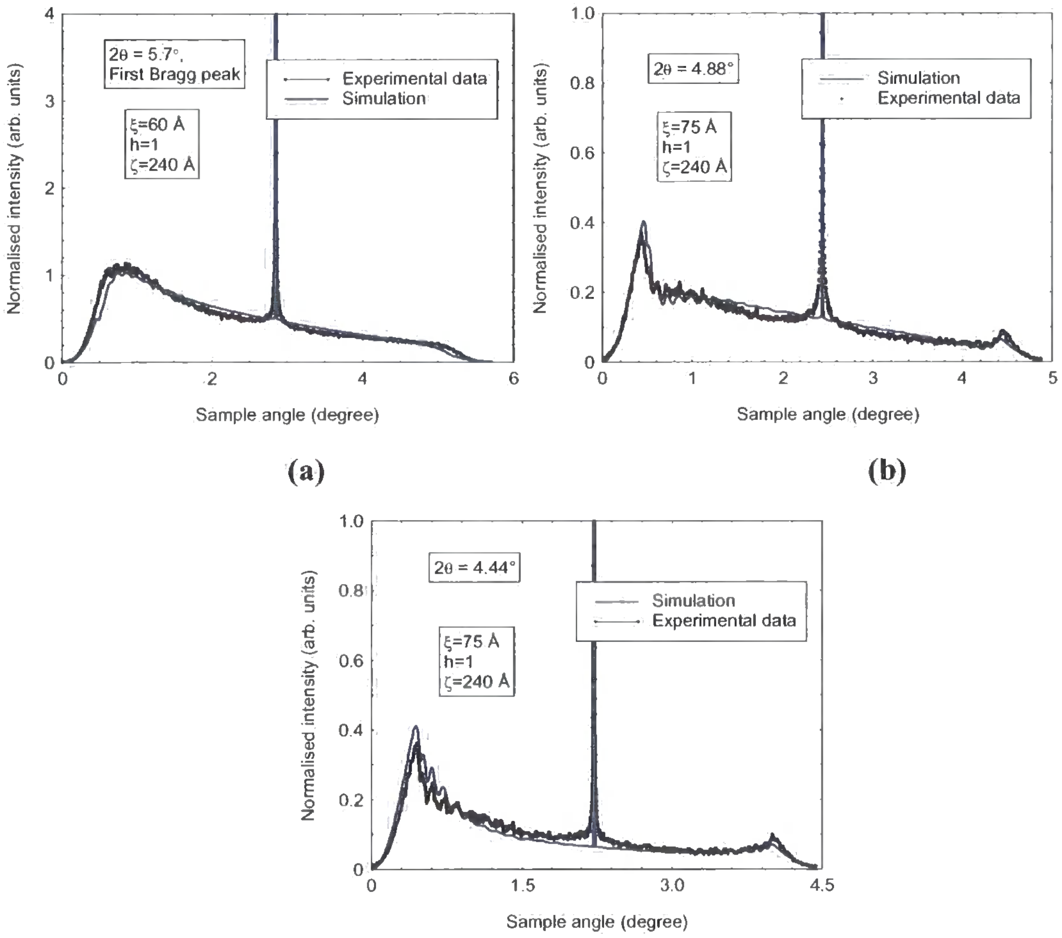

(a) (b)

(c)

Figure 7.15 Transverse diffuse scans and simulations for the 15-bilayer sample.

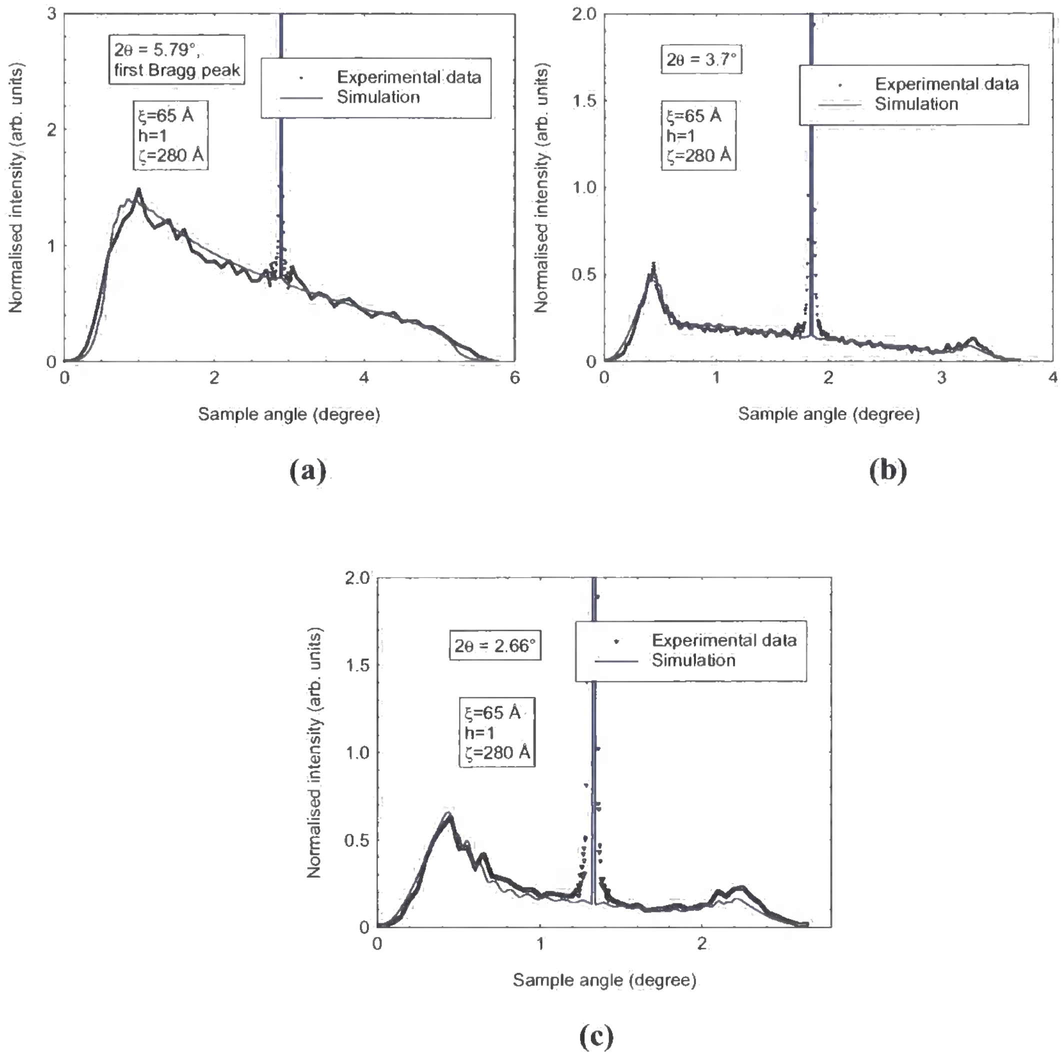

(a) **(b)**

(c)

Figure 7.16 Transverse diffuse scans and simulations for the 20-bilayer sample.

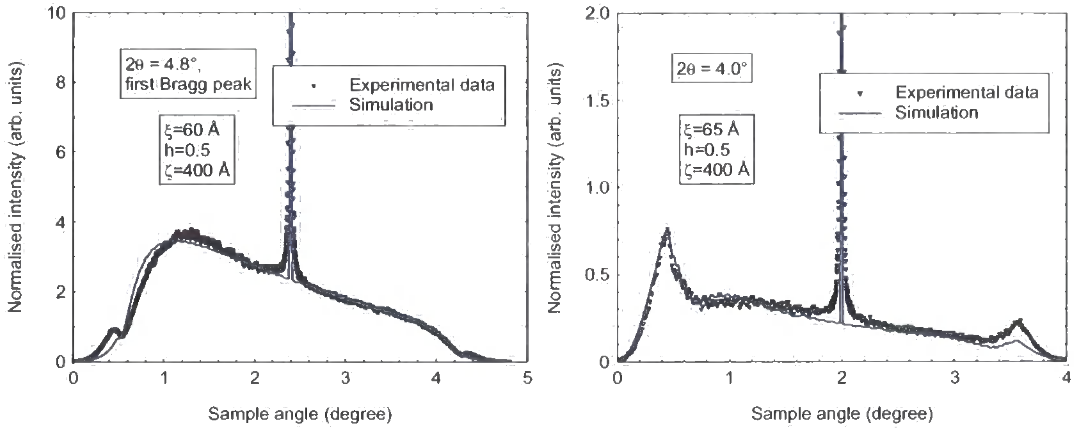

(a) **(b)**

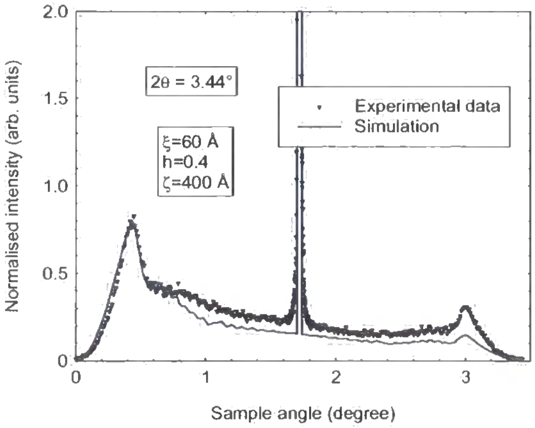

(c)

Figure 7.17 Transverse diffuse scans and simulations for the 25-bilayer sample.

Figures 7.12 – 7.17 show that excellent fits have been achieved in most cases. As can be seen in Figures 7.11(c) and 7.13(d), the in-plane correlation length has been found to be different from others. These scans were taken at the second Bragg peak in each sample. This effect is also seen in Co/Pd samples.

Structural parameters such as thickness (t), *rms* roughness (σ_{rms}), in-plane (lateral) correlation length (ξ), out-of-plane (vertical) correlation length (ζ) and fractal parameter (h), determined from the GIXR and GIXS fitting procedure (Model II) are listed in table 7.2. No interdiffusion was detected between interfaces for all samples $(\Sigma = 0)$.

Table 7.2

Multilayer structure parameters determined from x-ray scattering simulations, Model II.

N	t_{Buffer} (±0.3Å)	t_{Co} (±0.3Å)	t_{Pt} (±0.3Å)	σ_{Co} (±0.3Å)	σ_{Pt} (±0.3Å)	ζ (±10%)	ξ (±10Å)	h (±0.1)
5	54.3	3.1	13.0	2.5	2.5	160	60	0.5
10	50.5	3.2	12.5	2.9	2.9	200	60	0.5
12	46.8	3.7	11.6	2.2	3.0	200	60	0.5
15	41.9	2.3	10.7	2.4	3.1	240	75	1.0
20	38.6	2.3	10.7	2.5	3.2	280	65	1.0
25	50.5	3.0	13.0	3.0	3.0	400	60	0.5

7.4.3 HAXRD results

High angle powder diffraction was used to assess the crystallinity and texture of the samples. A high angle diffraction scan is performed in the same way as a low angle coupled $\theta/2\theta$ scan, with both the sample and detector being scanned out of the plane of the sample. In the symmetric Bragg geometry the scattering planes are parallel to the plane of the sample and measurements are therefore sensitive to bulk out-of-plane layer structure. Zero order multilayer and satellite diffraction peaks arise because of the bilayer repeats producing a pseudo lattice structure of large out-of-plane *d* spacing. The absolute position of these diffraction peaks can be calculated from the weighted average of the lattice parameters of the constituent layers via Bragg's law. Comparison of the calculated and observed peak positions therefore gives a measure of the out-of-plane strain within the deposited layers and a method by which to determine the crystalline texture of a layer. The full width at half maximum of the diffraction peaks gives a measure of the grain size within the layers via the Scherrer equation [27, 28]:

$$D = \frac{0.94\lambda}{\eta\cos\theta} \tag{7.1}$$

where D is the grain size in Å, η the FWHM of the diffraction peak in radians and θ the Bragg angle corresponding to the peak. The sharpness and number of observed satellite diffraction peaks also gives an indication of the quality of the deposited epitaxial layers, with a loss of higher order peaks observed because of a reduction in the layer quality and abruptness of the interface.

As illustrated in Figure 7.18, the bilayer satellites were prominent and consistent in position with the low angle data. No significant difference in texture was found between samples. By using the Scherrer formula on the width of the Pt peak in the symmetric $\theta / 2\theta$ scan, the out-of-plane grain size was found to be comparable with the total stack thickness (~ 280Å for the20-bilayer sample), consistent with columnar growth of crystallites [18].

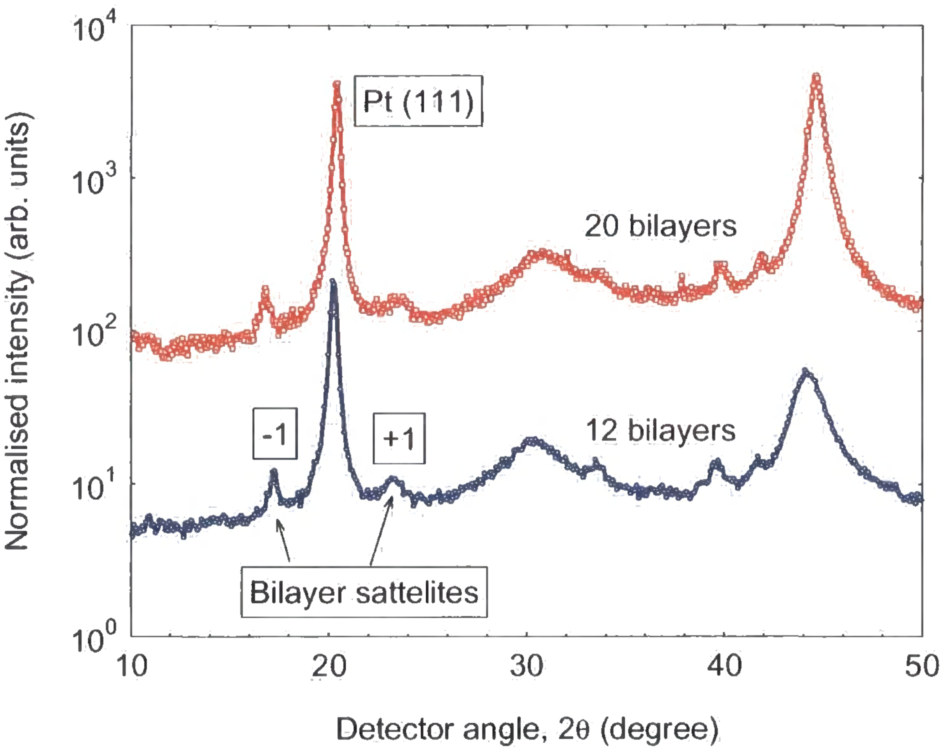

Figure 7.18 HAXRD powder scan for samples with 12 and 20 bilayers, $\lambda = 0.8$Å.

7.5 Discussions

The maximum in PMA observed in both torque and magnetometry data for 15 bilayers is consistent with a previous report of high values of K_{eff} between 10 and 20 bilayers for a series of (Co 4Å/ Pt 20Å) multilayers grown on Si [16]. These new data indicate that such an increase in PMA in this region is not confined to a specific value of the Pt thickness. The VSM data show a saturation magnetization, scaled to Co volume, greater than that of pure Co and some variation was found in the moment enhancement

[9] within the sequence. However, the torque magnetometry results for the anisotropy do not rely on measurement of the magnetization. The good agreement between VSM and torque anisotropy data gives confidence in the calibration.

Previous off-specular grazing incidence x-ray scattering measurements of (Co 4Å/ Pt 20Å) multilayers grown on Si [16] and on glass [18] showed that the conformality was lost for the samples with $N \geq 15$. The correspondence with the maximum in the anisotropy values suggested that these effects might be connected. However, matching of simulations to the present experimental off-specular $\theta/2\theta$ scans shows that the correlated roughness is retained for all samples although the degree of conformality decreases when the number of bilayers increase. This is illustrated in Figures 7.19 and 7.20 by using the interface parameters taken from Table7.1.

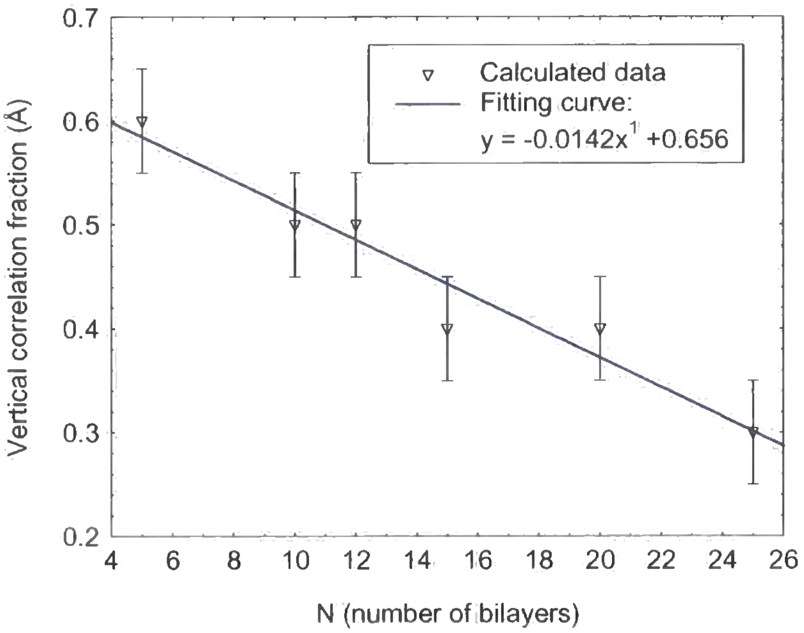

Figure 7.19 Relation between vertical correlation fraction (*VCF*) and number of bilayers.

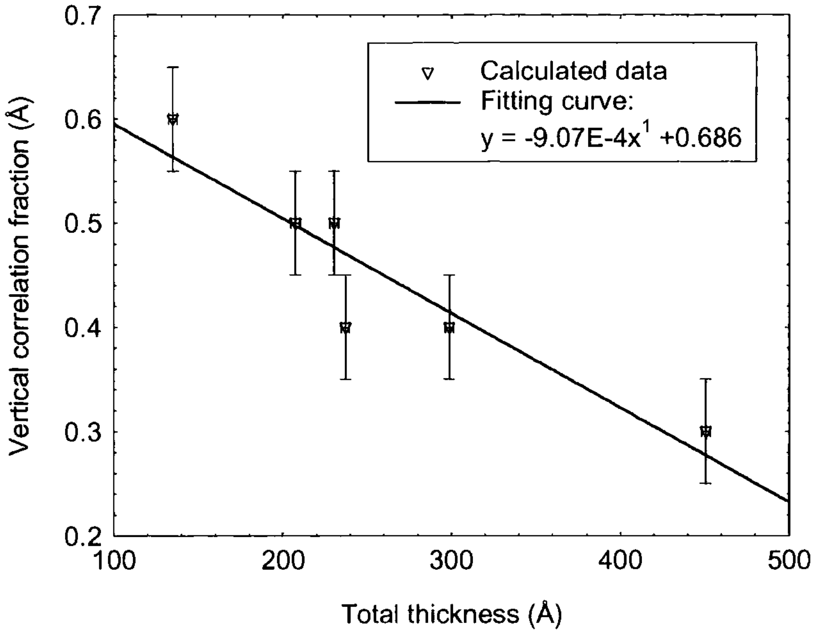

Figure 7.20 Relation between vertical correlation fraction and the total thickness.

The presence of strong Kiessig fringes in the off-specular scatter from N = 25 shows that the out-of-plane correlation length of the roughness is not lower than the thickness of this sample. Longitudinal and transverse diffuse data and simulations show that there is a large increase in the out-of-plane correlation length, ζ, as a function of bilayer repeat (Figures 7.21 and 7.22).

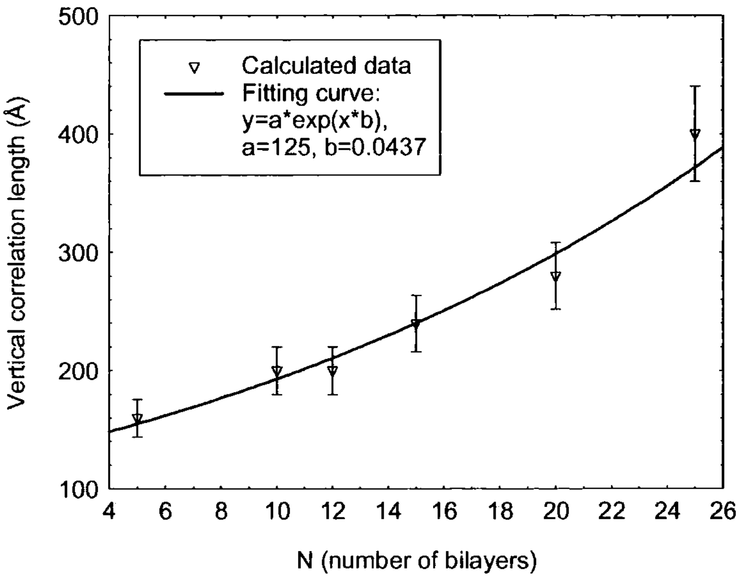

Figure 7.21 Relation between vertical correlation length (ζ) and number of bilayers.

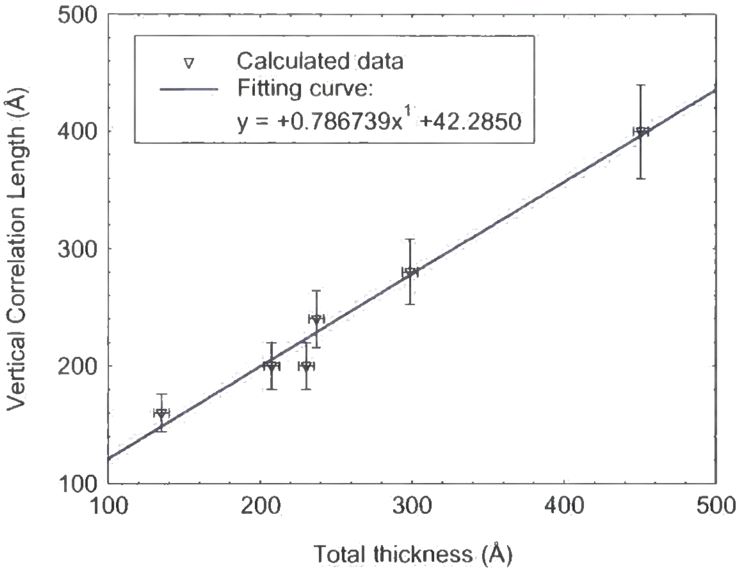

Figure 7.22 Relation between vertical correlation length (ζ) and the total thickness.

The previous study of Co/Pt sputtered multilayers on glass [18] showed that the conformality in Co/Pt (Co 4Å / Pt 20 Å) system is lost beyond a certain out-of-plane length scale. It has been possible to estimate this length scale to be of the order of 360Å (by direct measurement of the inverse FWHM of specular and off-specular Bragg peak), which in turn places the critical bilayer number for conformal growth at around 15 in that system (Figure 7.23).

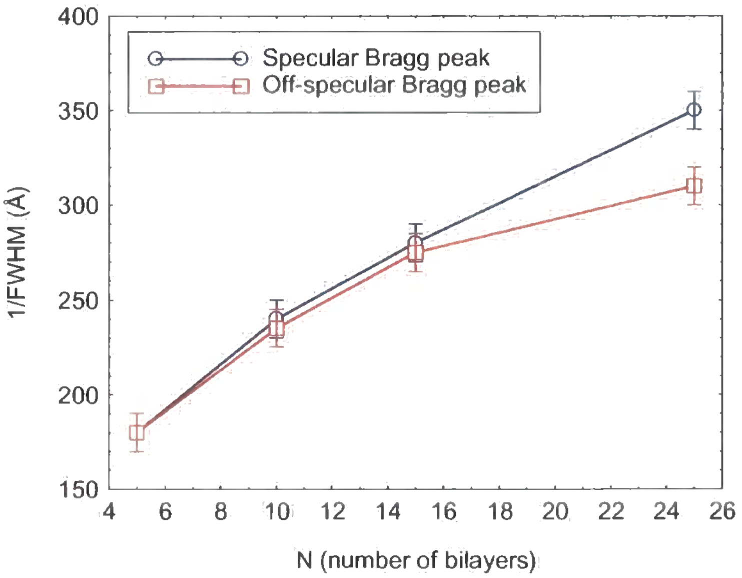

Figure 7.23 Inverse FWHM of the specular and off-specular Bragg peak as a function of bilayer number, N for Co/Pt samples on glass [18, 29].

On the other hand, similar measurements of the inverse FWHM of specular and off-specular Bragg peaks (first and second) for Co/Pt samples on Si show that the conformality is retained up to 25 bilayers (Figure 7.24); in good agreement with the results of the transverse diffuse scatter simulations (Figure 7.21). The specular Bragg peak becomes sharper and more intense as the bilayer number increases, as expected due to the increase in the number of coherently scattering layers. Figure 7.24(a) shows that the inverse FWHM for off-specular Bragg peak is equal to the specular peak, marking the point that the correlation of interface roughness is complete up to $N = 25$. As can be seen in Figure 7.24(b), the off-specular second Bragg peak scales with the specular second Bragg peak but is not equal. Moreover, the variation of the inverse FWHM for the second Bragg peak is different from the first Bragg peak. This effect was also seen in the transverse diffuse scatter simulations through second Bragg peak. At around 15 bilayers (samples with higher PMA), a drop in the inverse FWHM for the second Bragg peak can be seen in Figure 7.24(b).

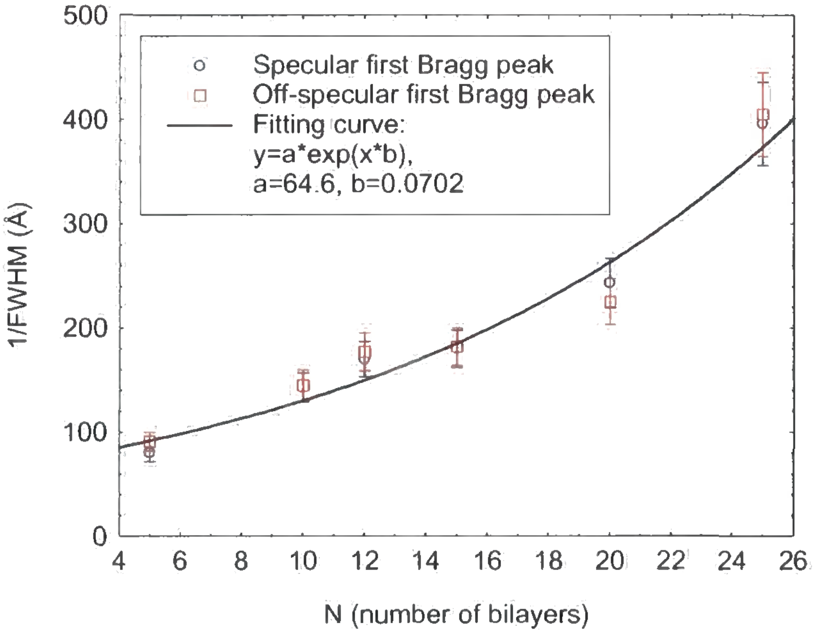

(a)

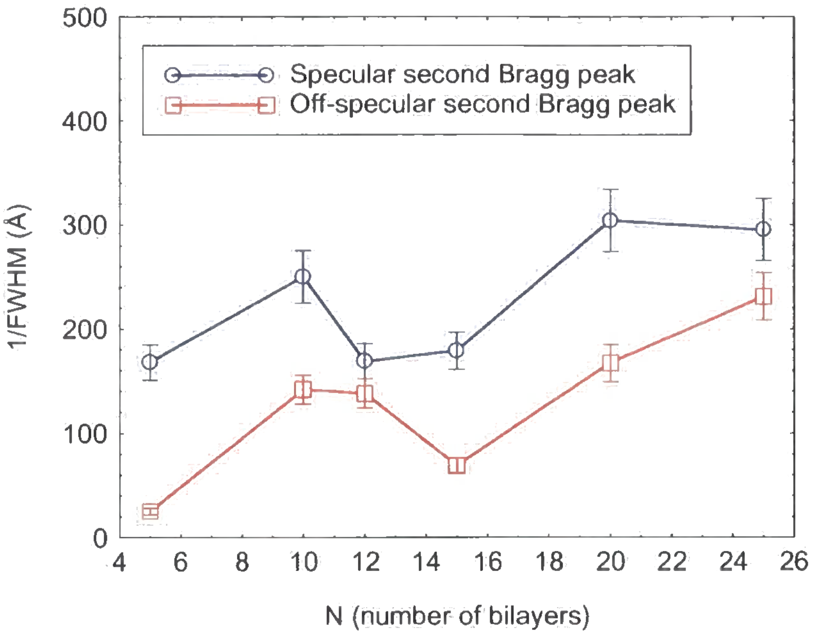

(b)

Figure 7.24 Inverse FWHM of the specular and off-specular **(a)** First and **(b)** Second Bragg peak as a function of bilayer number, N for Co/Pt samples on Si.

The origin of the maximum in the PMA as a function of bilayer repeat number is not associated with changes in interdiffusion as the growth time of the samples extends. Transverse diffuse data (Figure 7.12 – 7.17) and associated simulations show that there is no detectable interdiffusion contribution to the interface width in any of the samples and almost all of the effective roughness corresponds to genuine geometric roughness. This is consistent with a recent work reported by Huang *et al* [30]. There is found to be a large increase in the diffuse scatter when the detector angle is twice the Bragg angle for the low order diffraction peaks from the artificial multilayer structure (Figure 7.13). This is characteristic of the majority of the roughness being conformal (Table 7.2) and demonstrates that most of the diffuse scatter arises from the interfaces rather than from the surface of the sample.

The Bede REFS code uses Sinha's fractal model [31-33] for the interface structure. In this model, the nature of the surface is defined by the fractal exponent, h. As h tends to zero, the surface become more three dimensional in nature; as h tends to unity, the surface becomes more two dimensional [34]. By fitting the diffuse scatter at (at least), three different scattering vectors the ambiguity in determining the fractal parameter can be greatly reduced [35] and the confidence level in this fit increases. The results can be seen in Table 7.1 (model I), and Table 7.2 (model II) and reveal that h is approximately 0.5 for all the samples except for those with $N = 15$ and 20, those exhibiting high PMA. For these multilayers, the fractal parameter was found to be close to unity. Based on Sinha's model, a Lorentzian correlation function relates to $h = 0.5$ and Gaussian correlation function relates to $h = 1.0$, a two dimensional surface. Moreover, the in-plane correlation length was found to be independent of N (almost). As can be seen in Figures 7.12-7.17, the best fits were achieved using the Bede REFS, Model II. It has been possible to measure the vertical correlation lengths (Figure 7.21) in good agreement with the measurements of inverse FWHM (Figure 7.24). It is meaningful to conclude that the Model II of Bede REFS code was better model for defining the structure of the Co/Pt samples than Model I.

As can be seen in Table 7.2, the Co thickness was found to be ~2.3Å for the samples with $N = 15$ and 20, significantly lower than that of the remainder of the samples. Previously published work has shown that the magnetic properties of Co/Pt multilayers depend on the Co layer thickness [36]. A maximum in the PMA has been observed at about 4Å Co thickness, so the effect of reduced thickness would be to lower the anisotropy. Further, the curvature in the region of the maximum is small [23] and the variation in anisotropy for Co thickness between 2 and 5Å is negligible. The high values of PMA in the samples with $N = 15$ and 20 do not therefore seem to be the result of the lower Co thickness. The relation between K_{eff} and thickness of Co layer (with the bilayer number fixed) taken from two references can be seen in Figure 7.25.

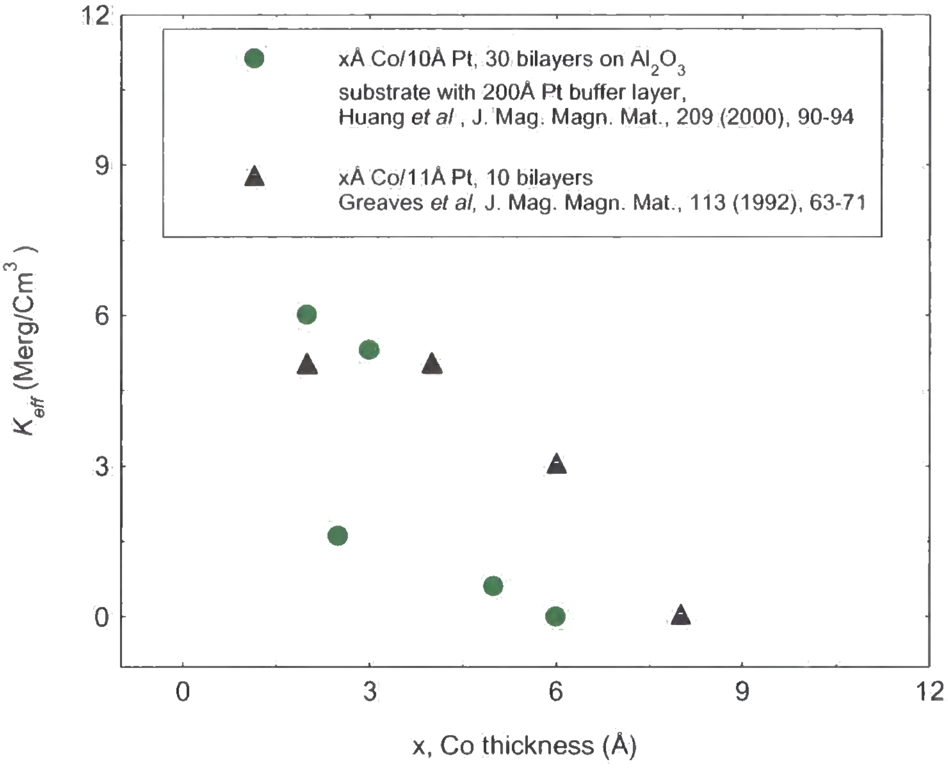

Figure 7.25 The relation between K_{eff} and the Co thickness.

A similar enhanced PMA is reported in Co/Pt multilayers grown on GaAs (111) substrate with N=15 [37], and on Al_2O_3 substrate with N=30 [38] when the Co thickness reaches ~3Å.

The Pt layer thickness for $N = 15 \& 20$, was also found to be thinner than the nominal value and the other samples. It is consistent with a work done by Stamps *et al* [39]. They reported a strong dependence of PMA on Pt within the bilayer thickness. A possible explanation is the strain in the Co induced by lattice mismatch at the interface with the Pt.

Although the buffer layer thickness was found to be different for the samples with $N = 15 \& 20$, there was no evidence in the high angle data that this affected the crystallinity and texture of these samples. In all cases, we observed quite strong HAXRD satellites confirming the conclusion from the grazing incidence data that the interfaces were well defined. The high angle data indicates that there is little crystallographic disorder at the interfaces in any of the samples.

7.6 Conclusions

The main aim of this chapter has been to study the relation between the perpendicular magnetic anisotropy and interface structure in Co/Pt multilayers sputtered on Si. The magnetic measurements have confirmed the enhanced perpendicular anisotropy seen in other sample sets when the bilayer repeat number is about 15. However, the out-of-plane correlation length of the interface roughness is larger than observed previously and no changes in roughness amplitude, in-plane correlation length or crystallographic texture were found as a function of bilayer number. Although the thickness of Co and Pt layers of the samples with enhanced anisotropy differs from the other samples, the effect appears to be a reduction in PMA rather than an enhancement. The only difference observed in the interface structure was a change in the dimensionality of the roughness of the interfaces, seen in the change in fractal parameter. There therefore appears to be little evidence for variation of perpendicular magnetic anisotropy with interface structure in Co/Pt multilayers. A similar result has recently been observed in Fe/Tb multilayers [40].

REFERENCES

[1] P. F. Carcia, A. D. Meinhaldt, and A. Suna, *Appl. Phys. Lett.*, **47 (2)**, 178-180 (1985).

[2] A. J. Freeman and R. Q. Wu, *J. Magn. Magn. Mater.*, **99** , 71 (1991).

[3] C. Chappert and P. Bruno, *J. Appl. Phys.*, **64 (10)**, 5736-5741 (1988).

[4] B. Zhang, K. M. Krishnan, C. H. Lee, and R. F. C. Farrow, *J. Appl. Phys.*, **73 (10)**, 6198-6200 (1993).

[5] B. N. Engel, C. D. England, R. A. Vanleeuwen, M. H. Wiedmann, and C. M. Falco, *J. Appl. Phys.*, **70 (10)**, 5873-5875 (1991).

[6] B. N. Engel, C. D. England, R. A. Vanleeuwen, M. H. Wiedmann, and C. M. Falco, *Phys. Rev. Lett.*, **67 (14)**, 1910-1913 (1991).

[7] J. G. Ha, K. Kyuno, and R. Yamamoto, *J. Phys.-Condes. Matter*, **8 (6)**, 677-684 (1996).

[8] P. F. Carcia, *J. Appl. Phys.*, **63 (10)**, 5066-5073 (1988).

[9] F. J. A. den Broeder, H. C. Donkersloot, H. J. G. Draaisma, and W. J. M. Dejonge, *J. Appl. Phys.*, **61 (8)**, 4317-4319 (1987).

[10] S. J. Greaves, P. J. Grundy, and R. J. Pollard, *J. Magn. Magn. Mater.*, **121 (1-3)**, 532-535 (1993).

[11] P. Bruno, *J. Phys.: F*, **18 (6)**, 1291-1298 (1988).

[12] P. Bruno, *J. Appl. Phys.*, **64 (6)**, 3153-3156 (1988).

[13] F. J. A. den Broeder, D. Kuiper, A. P. Vandemosselaer, and W. Hoving, *Phys. Rev. Lett.*, **60 (26)**, 2769-2772 (1988).

[14] A. M. Baker, A. Cerezo, and A. K. Petford-Long, *J. Magn. Magn. Mater.*, **156 (1-3)**, 83-84 (1996).

[15] H. S. Oh and S. K. Joo, *IEEE Trans. Magn.*, **32 (5)**, 4061-4063 (1996).

[16] C. J. Tatnall, D. E. Joyce, P. J. Grundy, J. P. Schille, and G. van der Laan, *J. Magn. Magn. Mater.*, **177** , 1181-1182 (1998).

[17] C. J. Tatnall, J. P. Schille, P. J. Grundy, and D. G. Lord, *J. Magn. Magn. Mater.*, **165 (1-3)**, 391-393 (1997).

[18] B. D. Fulthorpe, D. E. Joyce, T. P. A. Hase, A. S. H. Rozatian, B. K. Tanner, and P. J. Grundy, *J. Phys.-Condes. Matter*, **11 (43)**, 8477-8487 (1999).

[19] R. J. Pollard, M. J. Wilson, and P. J. Grundy, *J. Appl. Phys.*, **76 (10)**, 6090-6092 (1994).

[20] G. A. Bertero and R. Sinclair, *IEEE Trans. Magn.*, **31 (6)**, 3337-3342 (1995).

[21] M. T. Johnson, R. Jungblut, P. J. Kelly, and F. J. A. den Broeder, *J. Magn. Magn. Mater.*, **148 (1-2)**, 118-124 (1995).

[22] P. F. Carcia, Z. G. Li, and W. B. Zeper, *J. Magn. Magn. Mater.*, **121 (1-3)**, 452-460 (1993).

[23] S. J. Greaves, A. K. Petfordlong, Y. H. Kim, R. J. Pollard, P. J. Grundy, and J. P. Jakubovics, *J. Magn. Magn. Mater.*, **113 (1-3)**, 63-71 (1992).

[24] W. B. Zeper, H. W. Vankesteren, B. A. J. Jacobs, J. H. M. Spruit, and P. F. Carcia, *J. Appl. Phys.*, **70 (4)**, 2264-2271 (1991).

[25] P. J. Grundy, *J. Alloy. Compd.*, **326 (1-2)**, 226-233 (2001).

[26] D. Weller, L. Folks, M. Best, E. E. Fullerton, B. D. Terris, G. J. Kusinski, K. M. Krishnan, and G. Thomas, *J. Appl. Phys.*, **89 (11)**, 7525-7527 (2001).

[27] *X-ray diffraction in Crystals, Imperfect Crystals and Amorphous Bodies*, A. Guinier, Dover Pub. (1994).

[28] *X-ray Diffraction*, P. E. Warren, Dover Pub. (1990).

[29] B. D. Fulthorpe, *Ph. D. Thesis,* University of Durham (1999).

[30] J. C. A. Huang, C. H. Lee, and K. L. Yu, *J. Appl. Phys.*, **89 (11)**, 7059-7061 (2001).

[31] S. K. Sinha, *Curr. Opin. Solid State Matter. Sci.*, **1 (5)**, 645 (1996).

[32] S. K. Sinha, *Acta Phys. Pol. A*, **89 (2)**, 219-234 (1996).

[33] D. K. G. de Boer, *Phys. Rev. B*, **49 (9)**, 5817-5820 (1994).

[34] K. N. Stoev and K. Sakurai, *Spectroc. Acta Pt. B-Atom. Spectr.*, **54 (1)**, 41-82 (1999).

[35] B. K. Tanner, T. P. A. Hase, B. D. Fulthorpe, J. Clarke, G. M. Luo, S. K. Halder, A. S. H. Rozatian, and S. B. Wilkins, *Mater. Res. Soc. Symp. Proc.*, **615**, G 2.1.1-G 2.1.12 (2000).

[36] W. B. Zeper, F. Greidanus, and P. F. Carcia, *IEEE Trans. Magn.*, **25 (5)**, 3764-3766 (1989).

[37] K. M. Krishnan, *Acta Mater.*, **47 (15-16)**, 4233-4244 (1999).

[38] J. C. A. Huang, L. C. Wu, M. M. Chen, T. H. Wu, J. C. Wu, Y. W. Huang, C. H. Lee, and C. M. Fu, *J. Magn. Magn. Mater.*, **209 (1-3)**, 90-94 (2000).

[39] R. L. Stamps, L. Louail, M. Hehn, M. Gester, and K. Ounadjela, *J. Appl. Phys.*, **81 (8)**, 4751-4753 (1997).

[40] A. Paul, *J. Magn. Magn. Mater.*, **240**, 497-500 (2002).

Chapter 8

Interfaces in Co/Pd Multilayers

8.1 Introduction

Co/Pd magnetic multilayer thin films have received a great deal of attention in the last few years as components in high-density perpendicular magnetic recording media [1-14]. Kim *et al* [15] studied the interfaces of Co/Pd multilayers by Polarized Extended X-ray Absorption Fine Structure (PEXAFS) analysis and observed the presence of a Co-Pd alloy-like phase at the interface. In a more recent paper, Kim *et al* [16] reported that the alloy-like character is dominant at interfaces in typical Co/Pd multilayers and yields PMA through the strain anisotropy of Co atoms. They found that the broken symmetry, generally considered as the origin of PMA, was not definitely necessary for the presence of PMA in Co/Pd multilayers.

The effects of surface and interface roughness on magnetic properties were studied by Palasantzas *et al* [17] and Macrander *et al* [18]. They worked out theoretically that knowledge of the demagnetizing factor allowed a more precise determination of roughness effects on coercivity, domain wall width, and domain size. They suggested that a precise determination of film roughness as well as its growth mechanism using x-ray and electron diffraction is a necessary step in correlating microstructural disorder with magnetic properties.

The effect of underlayer on magnetic properties of Co/Pd multilayers has been studied by several authors [19-28]. Onoue *et al* reported that the Co/Pd multilayer media with C or Si underlayer possessed good thermal stability with a high value of coercivity [20, 22]. Kawaji *et al* observed an enhancement of magnetic properties of Co/Pd magnetic multilayers by using Pd/Si dual seed layer [19].

An enhancement of coercivity by underlayer control in Co/Pd multilayers has been reported by Oh and Joo [29]. They found that the coercivity of Co/Pd multilayers was strongly dependent on the sputtering pressure of the underlayer and could be increased by increasing the sputtering pressure of the Pd underlayer.

In this chapter, the structural and interface parameters and their relation to the magnetic properties of four series of Co/Pd multilayers is studied. The results will also be compared with the Co/Pt multilayers grown on Si (chapter 7) and Fe/Au multilayers (chapter 6). The experimental results for each series of samples will be presented and discussed in separate sections. For all samples, anisotropy measurements were obtained by recording in-plane and out-of-plane M-H loops using a vibrating sample magnetometer [30]. All magnetic measurements were performed at room temperature. X-ray experiments were carried out on a Bede GXR1 laboratory reflectometer and on station 2.3 at the SRS (Daresbury, UK) and the XMaS beamline (BM 28) at the ESRF (Grenoble, France).

8.2 Samples

Four series of {Pd 30Å / (Co xÅ / Pd 30Å)*N} multilayer films were grown on single crystal (001) oriented silicon using the magnetron sputtering technique at the University of Leeds by C. H. Marrows. The number of bilayers, N, was varied between 2 and 30. The growth conditions (including the values of Ar gas pressure, sputtering current, and sputtering power) for all samples are as follows:

Series 1:	3 mTorr Ar; Co 100 mA, 33 W; Pd 50 mA, 17 W
Series 2:	3 mTorr Ar; Co 100 mA, 34 W; Pd 50 mA, 17 W
Series 3:	3 mTorr Ar; Co 100 mA, 33 W; Pd 50 mA, 16 W
Series 4:	7.5 mTorr Ar; Co 100 mA, 28 W; Pd 50 mA, 15 W

It is worth mentioning that the layer thicknesses are controlled by adjusting the deposition time. Details of the preparation of multilayers have been described in Ref. [31].

8.3 Series 1

In this section, the x-ray data and magnetic measurements for the first series of samples will be presented. All samples were nominally:

$$\mathrm{SiO_2} / 30\ \text{Å Pd} / N \times \{5\ \text{Å Co} / 30\ \text{Å Pd}\} \quad \text{where } N = 2, 4, 6..., 30$$

8.3.1 X-ray experiments

8.3.1.1 GIXR results

A series of grazing incidence specular and off-specular x-ray scans along with simulations for these samples is shown in Figure 8.1. These scans provide information concerning the development of the multilayer stack as the number of bilayers was increased from 2 to 30. In all cases excellent and unambiguous convergence was found, provided that the data range was sufficient. For most samples, this covered the first four Bragg peaks.

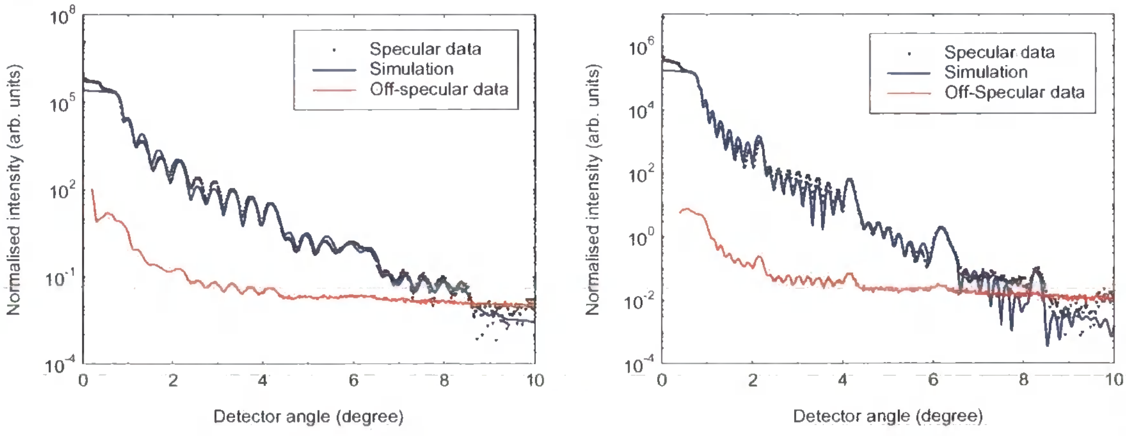

(a) (b)

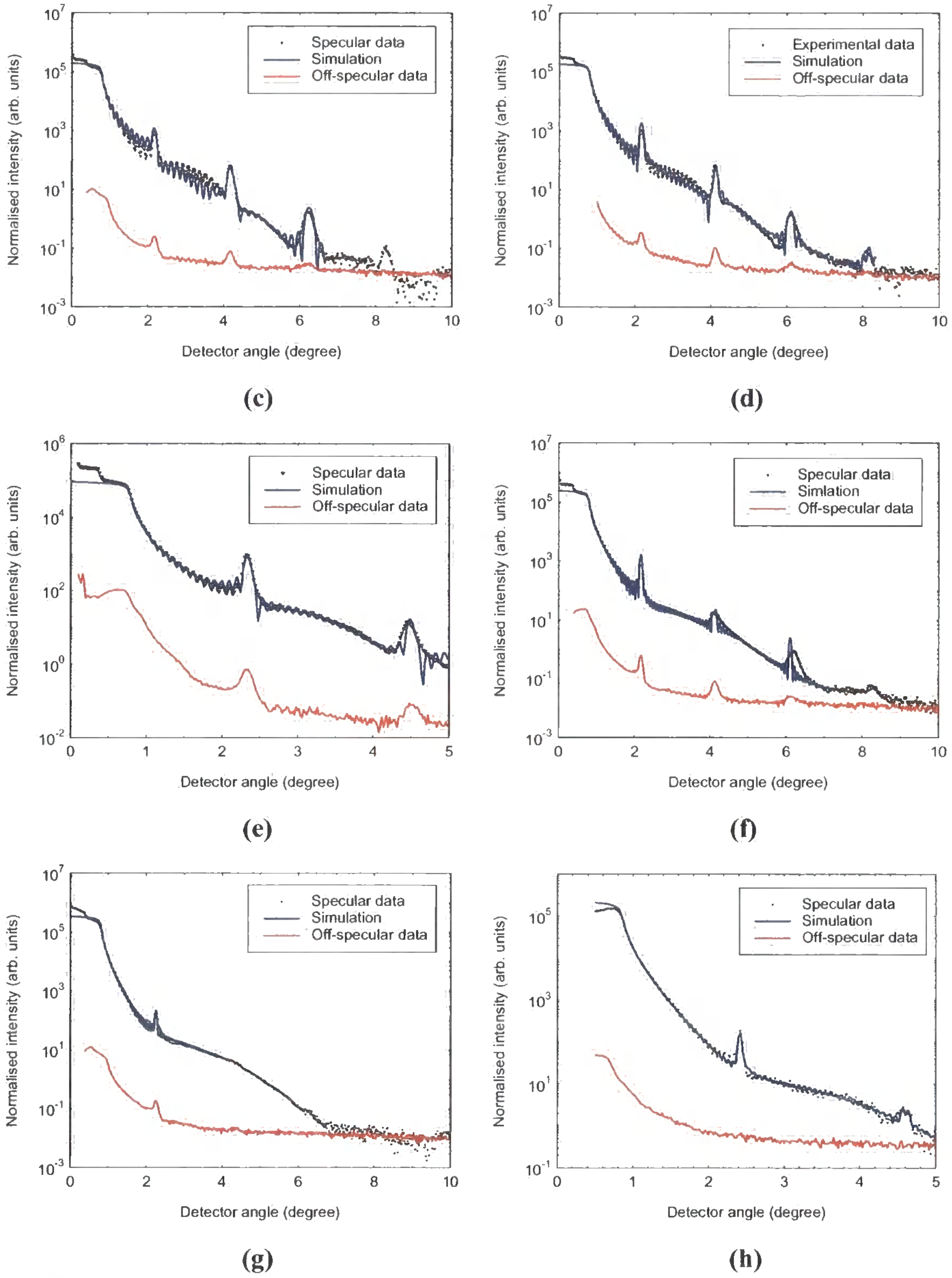

(c) (d)

(e) (f)

(g) (h)

Figure 8.1 Specular and Off-specular data and simulations for samples with **(a)** 4 bilayers, **(b)** 8 bilayers, **(c)** 12 bilayers, **(d)** 16 bilayers, **(e)** 20 bilayers, **(f)** 24 bilayers, **(g)** 30 bilayers, synchrotron data with $\lambda = 1.3\text{Å}$ and **(h)** 30 bilayers, laboratory data with $\lambda = 1.393\text{Å}$

The off-specular Bragg peaks can be seen in all cases except in Figure 8.1(h). These data were taken on the GXR1 reflectometer using λ = 1.393 Å where the signal was too low to resolve the second off-specular Bragg peak from the noise. As can be seen in Figure 8.1(g), the second specular Bragg peak did not appear distinctly in the synchrotron data (due to alignment difficulties) while it could clearly be seen in the laboratory data (Figure 8.1(h)). The reason for this is not totally clear but it may be that the alignment, which is critical in the synchrotron experiments, was such that the sample slid off the specular ridge. By simulating the laboratory data, the interface parameters were found to be compatible with the model for the series 1 samples. The layer and interface parameters are given in Table 8.1.

The position and spacing of the specular (Fig 8.2(a)) and off-specular (Fig 8.2(b)) Bragg peaks for the N=20 & 30 bilayer samples show the bilayers were slightly thinner than nominal. A similar effect was observed in Co/Pt multilayers for N=15 & 20 [32]. In contrast to the previous measurements on Co/Pt multilayers, the Co/Pd layers show a different propagation of interface structure through the multilayer stack. As can be seen in Fig. 8.2(b), as the bilayer number is increased, the off-specular Bragg peak remains, indicating that out-of-plane correlation is retained within the bilayers. However, the off-specular Kiessig fringes disappear as the stack thickness increases, and the out-of-plane correlation between the interfaces at the substrate and cap is lost.

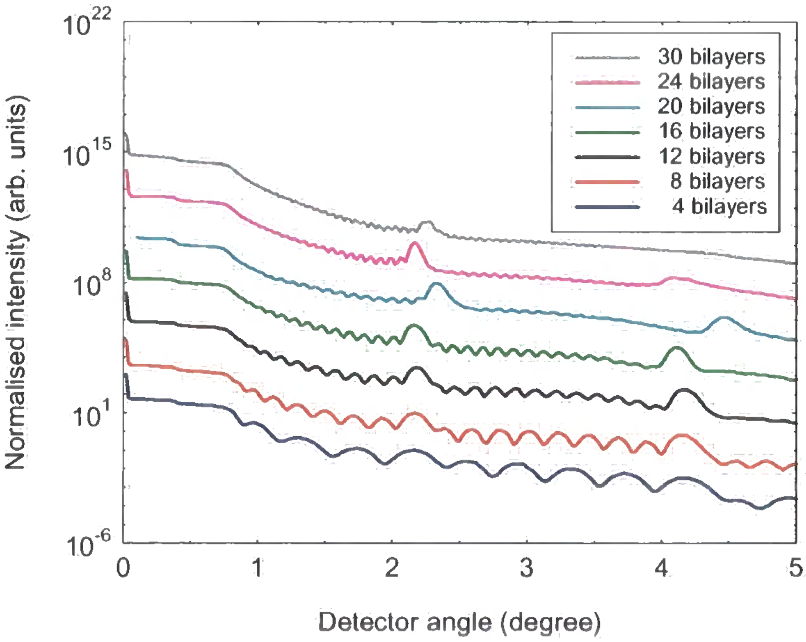

(a)

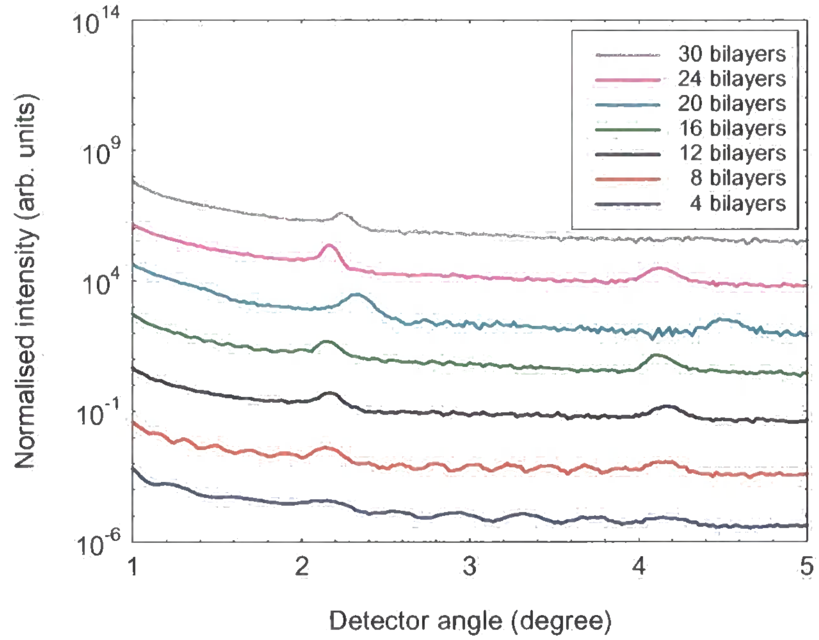

(b)

Figure 8.2 **(a)** A series of Co/Pd Specular scans, λ = 1.3Å. **(b)** A series of Co/Pd Off-specular scans (sample off-set -0.1°, λ = 1.3Å).

Structural parameters were obtained by fitting the experimental data to simulations from a model structure. Values of thickness and interface width were first found by automatic refinement using the Bede MERCURY code for the specular data and these parameters then used to fit the diffuse scatter manually (section 8.3.1.2). After several attempts for each set of data, the model structure that led to the best fits for both specular and diffuse scatter data was determined and can be seen in Figure 8.3.

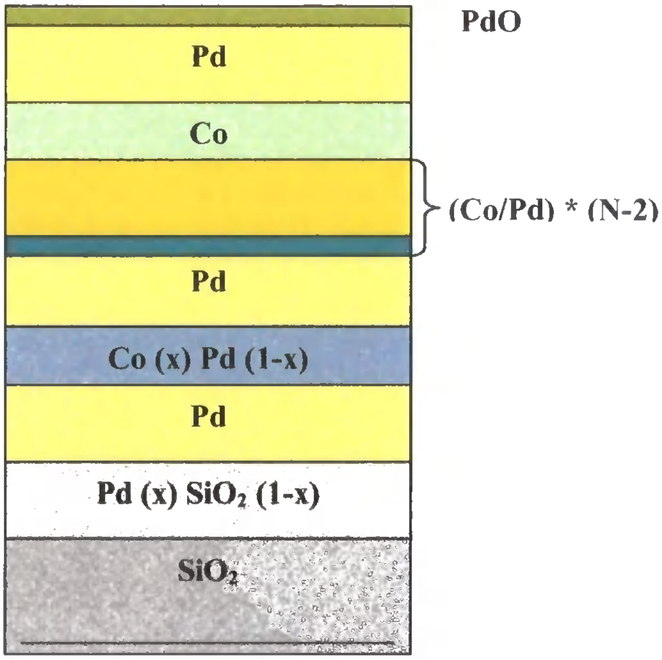

Figure 8.3 The model structure used to fit specular and diffuse scatter data. X varied from 0.1 to 0.9.

8.3.1.2 GIXS results

Across the series of fifteen samples, extensive specular and transverse diffuse measurements were made. Through a combination of these scans, many aspects of the interface morphology in the multilayer structures could be determined. Two x-ray wavelengths were used, one on the laboratory GXR1, λ=1.393Å, and one on the station 2.3 at the SRS, λ=1.3Å. For each sample, at each wavelength, at least three transverse diffuse scans were taken, one or two at and one or two away from the Bragg condition. These scans are primarily sensitive to correlated and uncorrelated roughness within the multilayer itself respectively. The Bede REFS code (which was used to fit the transverse diffuse data), considers four different models for interfaces. Best fits were achieved using a partially correlated roughness, model II (Figures 8.4 – 8.10).

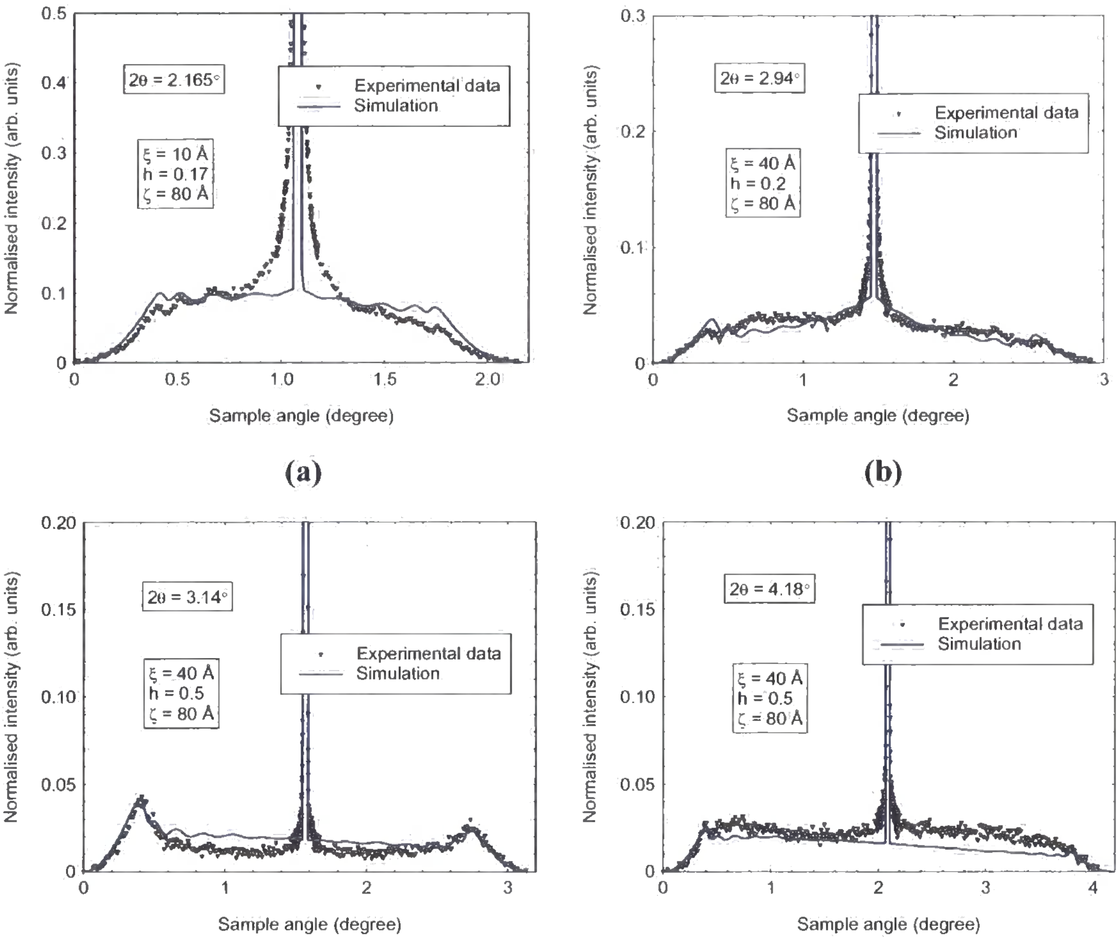

(a) (b)

(c) (d)

Figure 8.4 Transverse diffuse scans and simulations for the 4-bilayer sample, λ = 1.3Å.

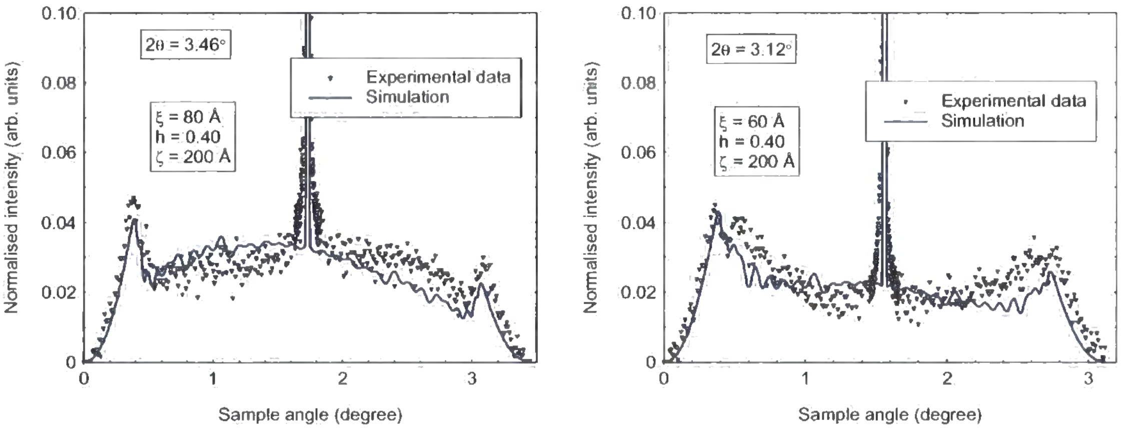

(a) (b)

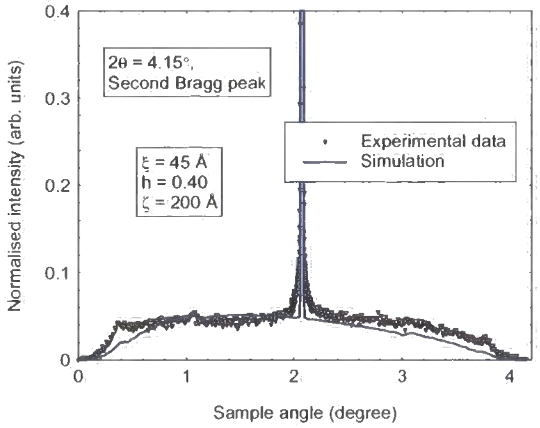

(c)

Figure 8.5 Transverse diffuse scans and simulations for the 8-bilayer sample, λ = 1.3Å.

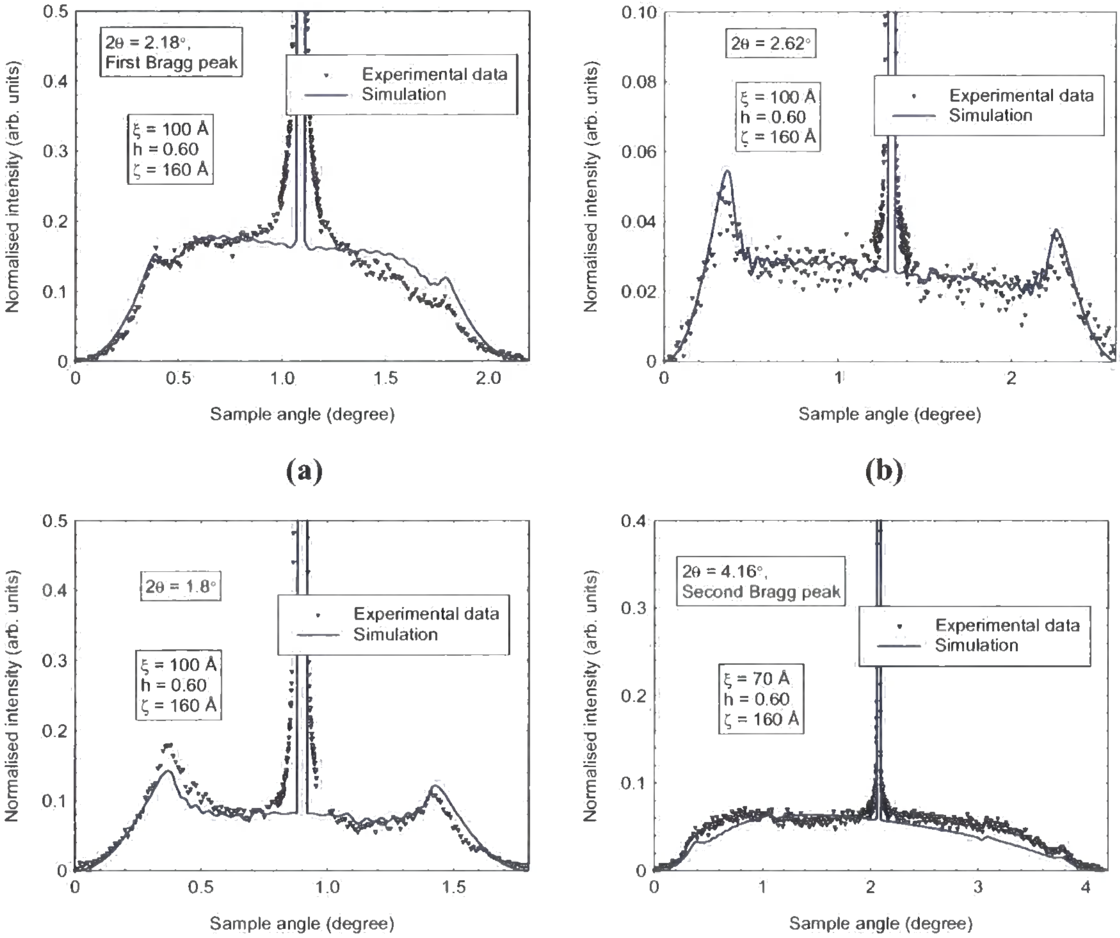

(a) (b)

(c) (d)

Figure 8.6 Transverse diffuse scans and simulations for the 12-bilayer sample, λ = 1.3Å.

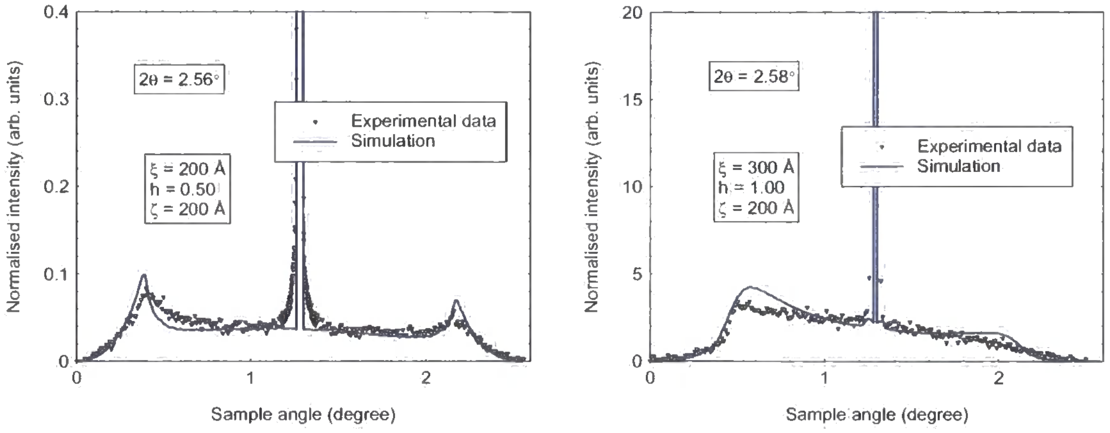

(a) **(b)**

Figure 8.7 Transverse diffuse scans and simulations for **(a)** The 16-bilayer sample, $\lambda = 1.393$Å and **(b)** The 20-bilayer sample, $\lambda = 1.393$Å.

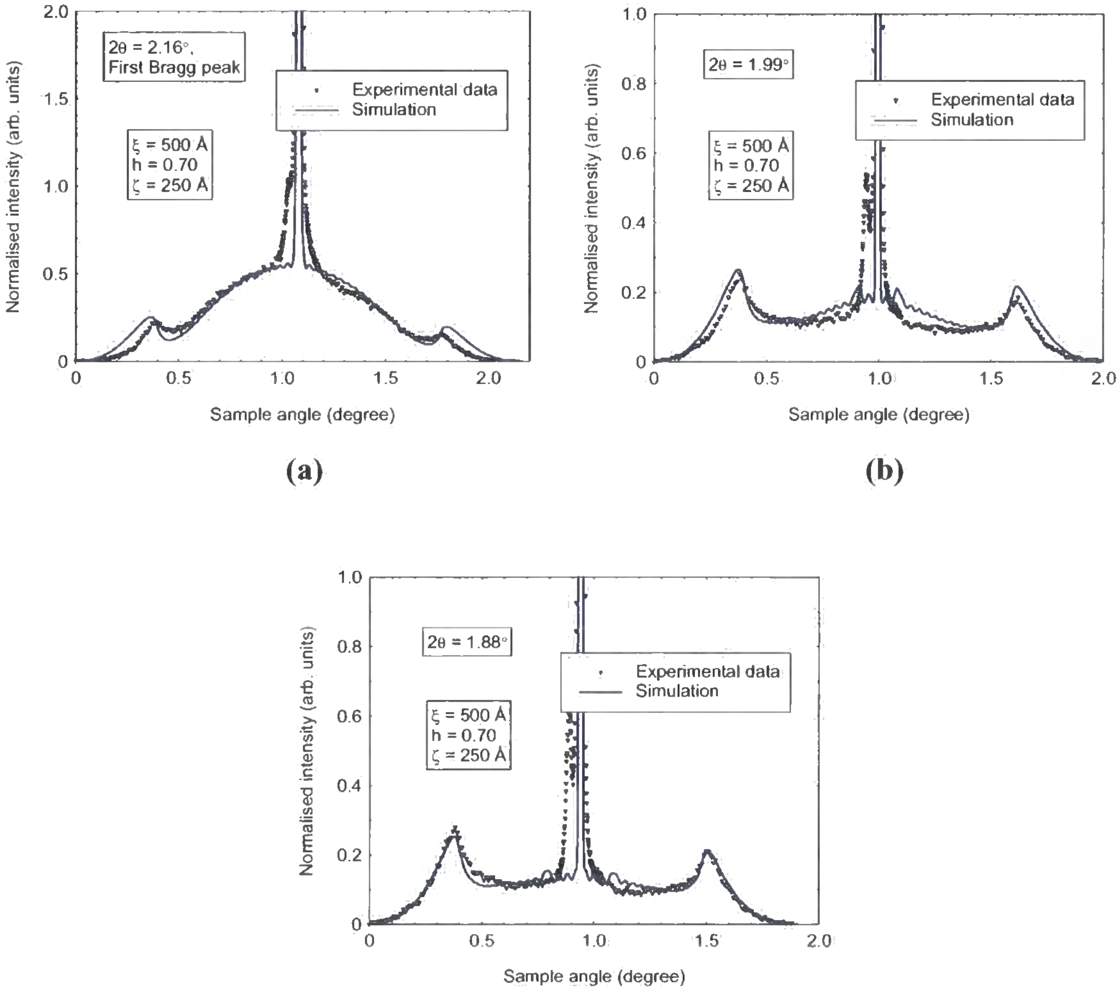

(a) **(b)**

(c)

Figure 8.8 Transverse diffuse scans and simulations for the 24-bilayer sample, $\lambda = 1.3$Å.

As seen in Figures 8.4 – 8.8, excellent fits have been achieved in most cases. As illustrated in Figures 8.5(c) and 8.6(d), the deduced in-plane correlation lengths were found to be different from those deduced from the other scans. These anomalous scans were taken at the second Bragg peak in each sample. This effect was also seen in some Co/Pt samples and no explanation is found to date.

As stated in the previous section, two sets of data were simulated for the 30-bilayer sample. In the laboratory data (Figure 8.1(h)), the second specular Bragg peak was prominent and could be simulated, while in the synchrotron data (Figure 8.1(g)) it did not appear strongly. Transverse diffuse data and simulations using the interface parameters taken from the laboratory simulated data, can be seen in Figure 8.9. The same diffuse data were simulated by using the interface parameters taken from the synchrotron data and results can be seen in Figure 8.10. Excellent fits were achieved in most cases with very different in-plane correlation lengths for the two series of simulations. A real challenge was to choose one of these two series of data to introduce the best model for the whole series 1 samples. By examining different model structures, it was finally decided to choose the interface parameters that were taken from simulating the laboratory specular data (as the data range was sufficient to cover at least the first two Bragg peaks) the possibility of misalignment in the synchrotron data is higher. Structural parameters determined by simulating the transverse diffuse data (Figure 8.9) using Model II are listed in Table 8.1.

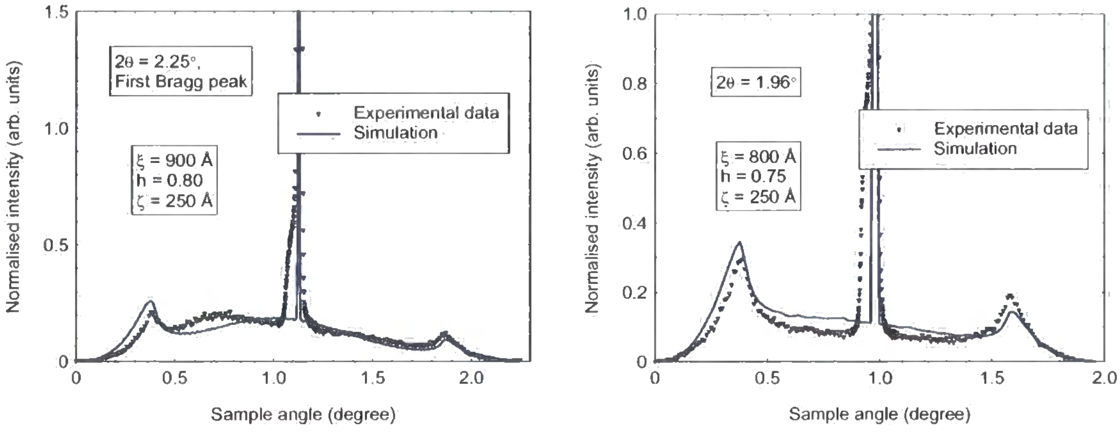

(a) **(b)**

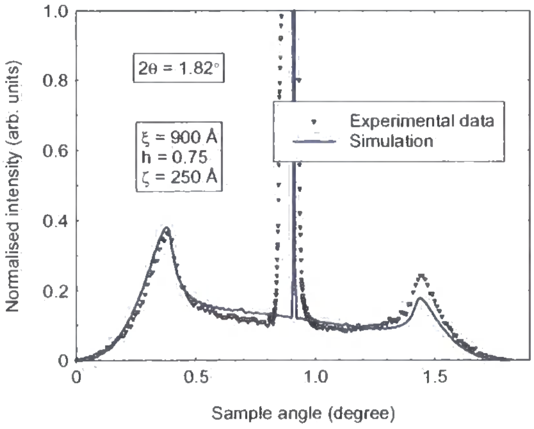

(c)

Figure 8.9 Transverse diffuse scans and simulations for the 30-bilayer sample with λ = 1.3Å using the interface parameters taken from the simulation of laboratory specular data.

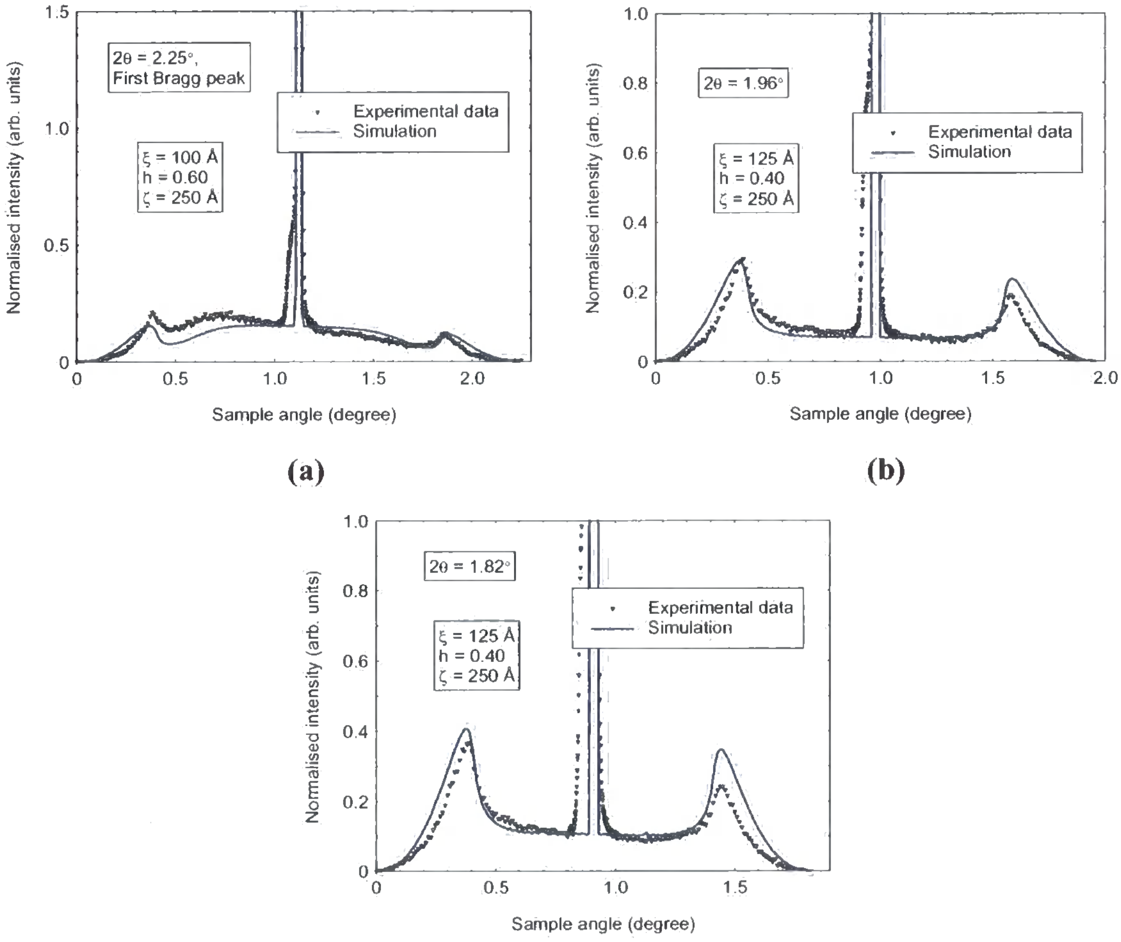

(a) (b)

(c)

Figure 8.10 Transverse diffuse scans and simulations for the 30-bilayer sample with λ = 1.3Å, using the interface parameters taken from the simulation of synchrotron specular data.

Structural parameters determined by simulating the x-ray data using Model II are listed in Table 8.1.

Table 8.1

Multilayer structure parameters determined from x-ray scattering simulations.

N-2	t_{Buffer} ±0.3Å	t_{Co} ±0.3Å	t_{Pd} ±0.3Å	σ_{Buffer} ±0.3Å	σ_{Co} ±0.3Å	σ_{Pd} ±0.3Å	VCF	ζ ±10%	ξ ±10Å	h ±10%
2	33.5	5.7	29.4	4.0	5.0	3.2	0.3	80	40	0.50
6	29.6	5.8	30.2	6.1	3.1	3.8	0.3	200	60	0.40
10	27.2	6.5	29.5	4.7	2.9	3.4	0.2	160	100	0.60
14	39.6	6.4	30.6	4.2	6.2	3.0	0.2	200	200	0.50
18	31.5	4.9	28.7	7.3	4.2	8.9	0.2	200	300	1.00
22	39.9	4.0	32.9	8.3	3.6	11.0	0.1	250	500	0.70
24	39.3	5.0	31.7	6.9	10.8	5.5	0.1	250	600	0.60
28	26.7	1.5	33.8	8.7	4.1	5.2	0.05	250	900	0.75

8.3.1.3 Diffuse intensity out of the scattering plane

Measuring the intensity out of the scattering plane allows a greater range of the in-plane component of reciprocal space to be probed, without the need to change energy. This geometry can be used to extract uniquely the fractal parameter, h [33, 34]. In the asymptotic limit $R \ll \xi$ the structure factor yields a power-law dependence with an exponent, $\gamma = -(2+2h)$. The onset of the power-law can be used to give an estimation of the in-plane correlation length, ξ. Although the technique is not particularly sensitive to the correlation length (as it is difficult to define the exact onset of the power law), a modest increase in the correlation length as a function of N was observed, $(N = 4, \xi = 115\text{Å}\ \mathit{and}\ N = 20, \xi = 250\text{Å})$ as shown in Figure 8.11. A scaling behavior was seen in all cases, with h being larger than that deduced from the GIXS data and closer to that expected from sputtered materials.

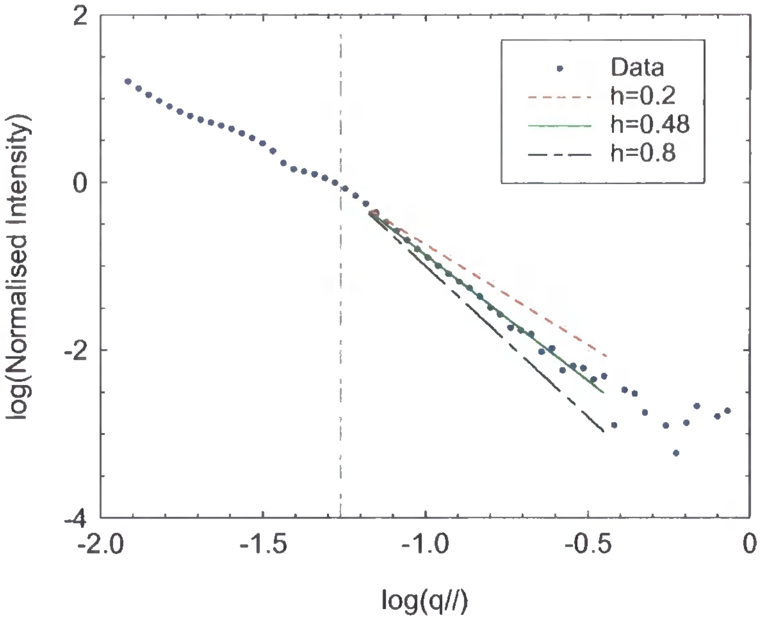

(a)

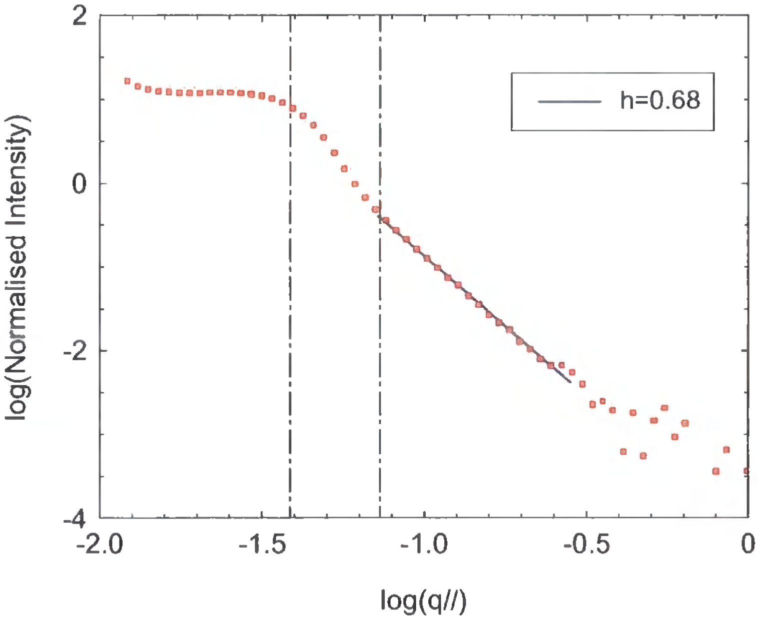

(b)

Figure 8.11 Intensity versus $q_{\parallel}$ $\left(q_{\parallel}=\sqrt{q_x^2+q_y^2}\right)$ for Co/Pd samples with **(a)** 4 bilayers and **(b)** 20 bilayers (experimental data taken at the XMaS beamline, ESRF by Prof. B. K. Tanner and Dr. T. P. A. Hase).

8.3.1.4 Reciprocal space map

The effect of the nature of the roughness on the diffuse scatter can be seen in a full reciprocal space map (FRSM) for the 20-bilayer sample in Figure 8.12 and shows that the interface roughness is partially correlated. There are some features present in this FRSM. Rather than being distributed randomly throughout reciprocal space, as is the case for uncorrelated roughness, the diffuse scatter is confined into regions termed resonant diffuse sheets (RDS) at the positions of the Bragg peaks, arising from coherent scatter within the bilayers. In this case the resonant sheets have reduced in intensity compare to the FRSM from totally correlated interfaces [35-37].

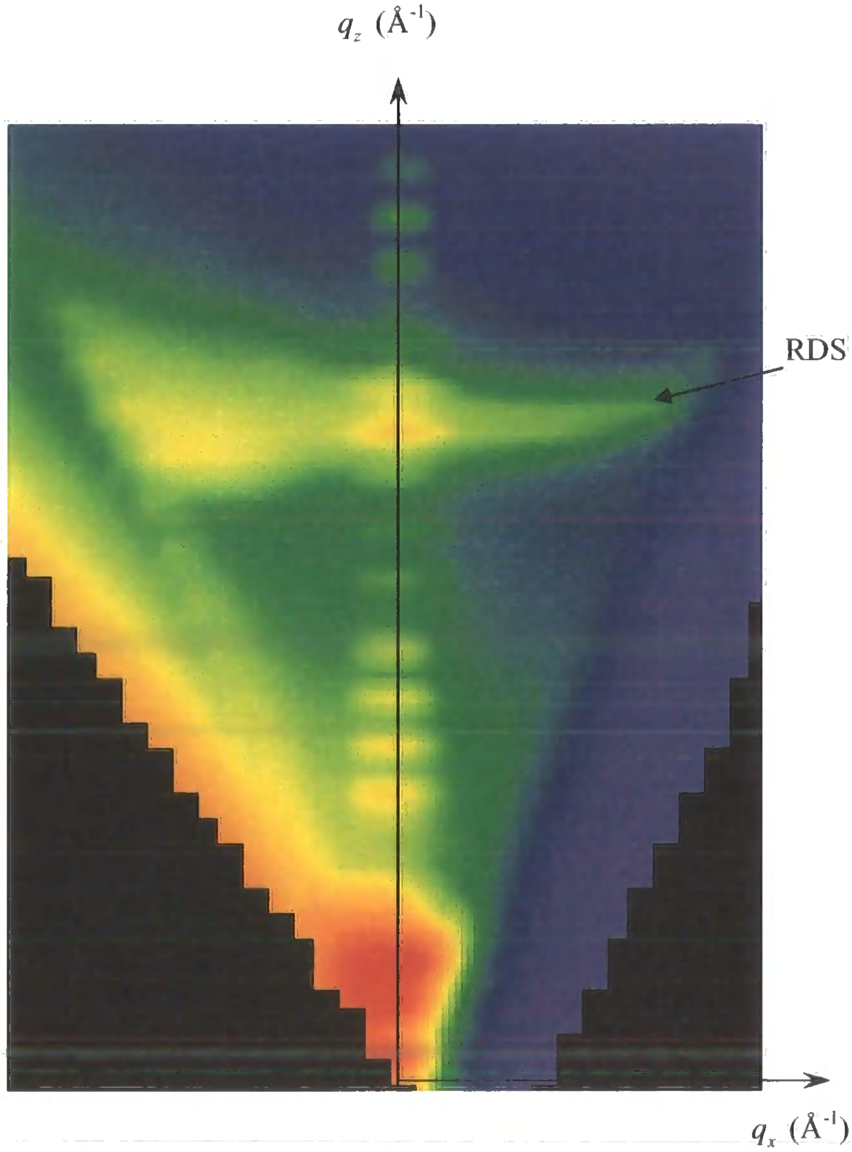

Figure 8.12 Reciprocal space map for 20-bilayer sample.

8.3.2 VSM measurements

Samples were run on the laboratory Vibrating Sample Magnetometer (VSM) and magnetization loops can be seen in Figure 8.13. All samples exhibited PMA.

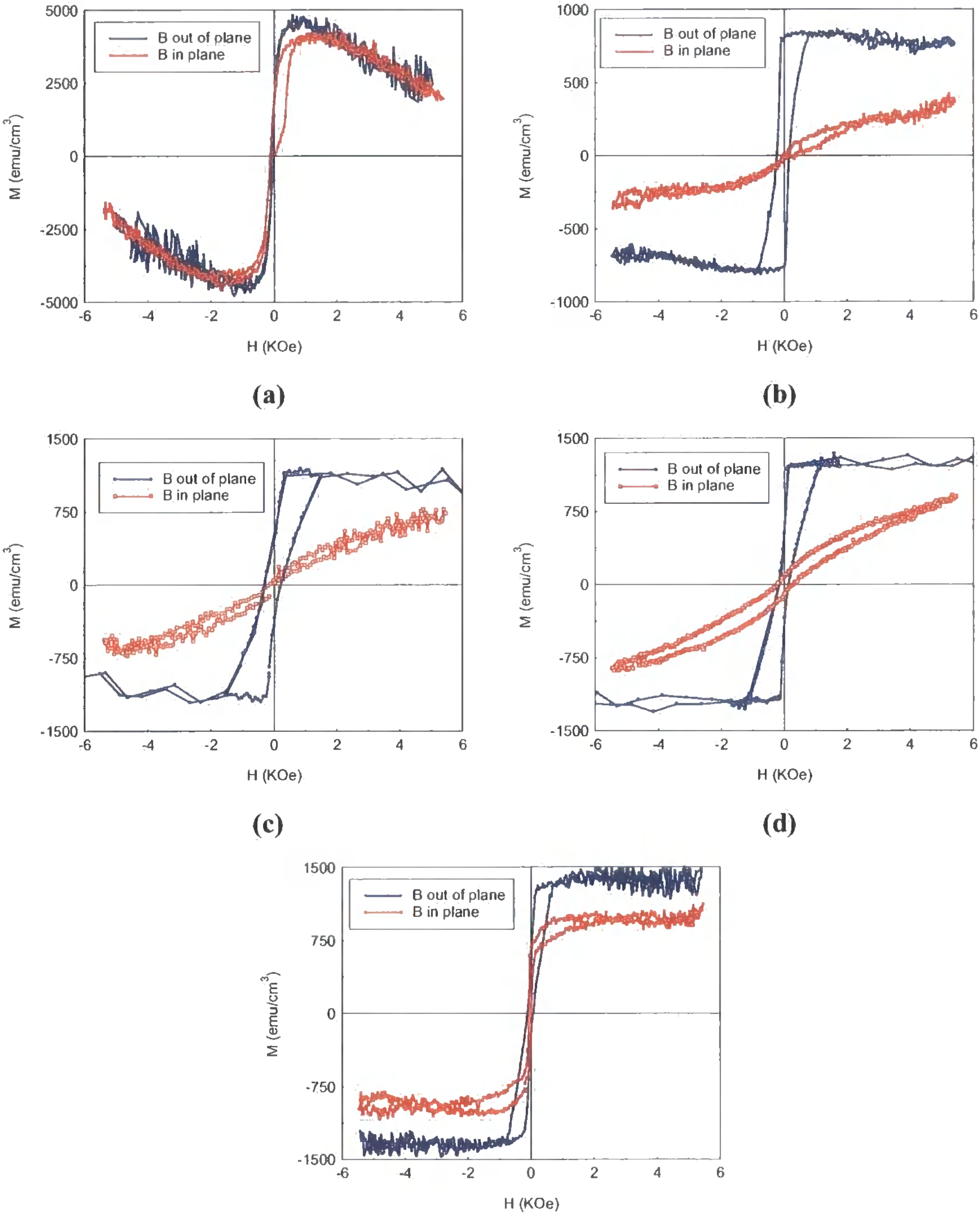

(a) **(b)** **(c)** **(d)** **(e)**

Figure 8.13 VSM magnetization loops for samples with **(a)** 2 bilayers, **(b)** 12 bilayers, **(c)** 20 bilayers, **(d)** 24 bilayers, and **(e)** 30 bilayers.

From the area between the in-plane and out-of-plane M-H loops, K_{eff} was calculated for all samples and the results can be seen in Figure 8.14. The 20 bilayer sample has a maximum value for $K_{eff} = (3.0 \pm 0.2)\ Merg/cm^3$. In the out-of-plane measurements all samples were found to have low coercivity (Figure 8.14(b)). The small coercivity is believed to be the specification of sputtered Co/Pd multilayers [6] although it has been reported for multilayers grown by other techniques [14].

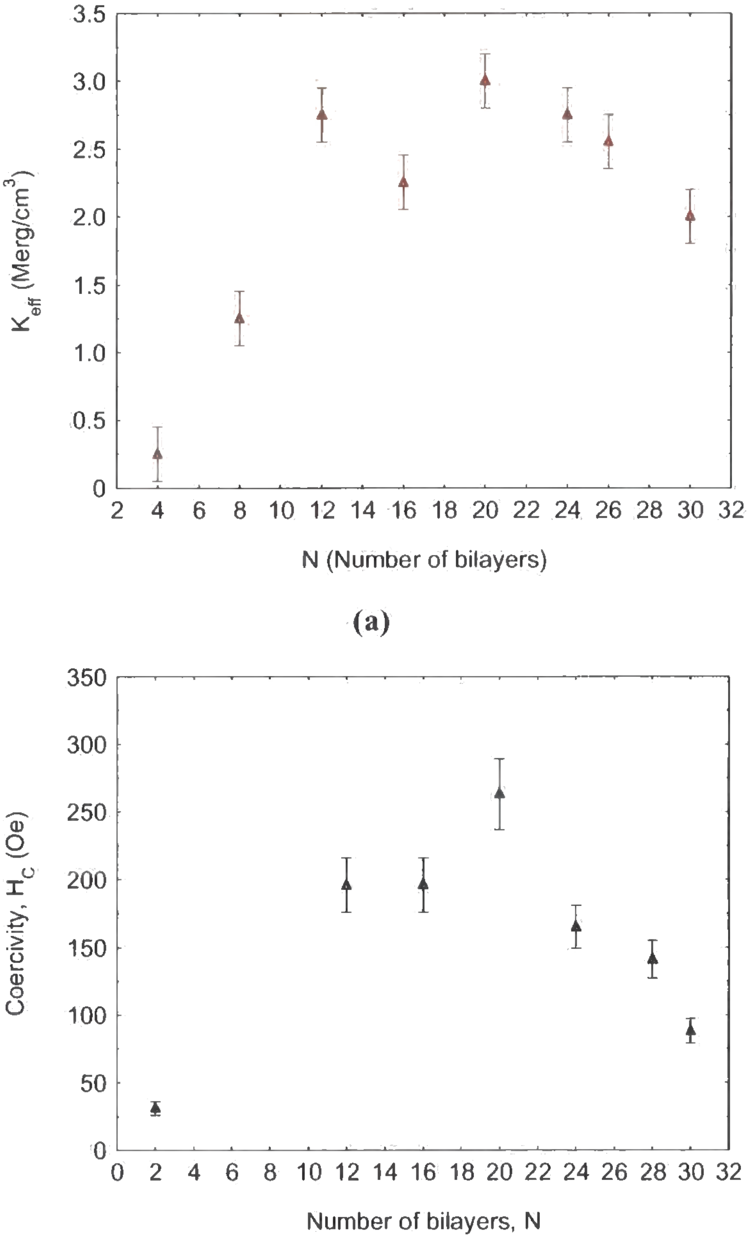

(a)

(b)

Figure 8.14 Relation between **(a)** K_{eff}, and **(b)** Coercivity and number of bilayers (VSM measurements).

8.3.3 Discussions

As can be seen in Figures 8.15, as the number of bilayers was increased, a bump appeared in the transverse diffuse scatter which corresponds to an increase in the in-plane correlation length.

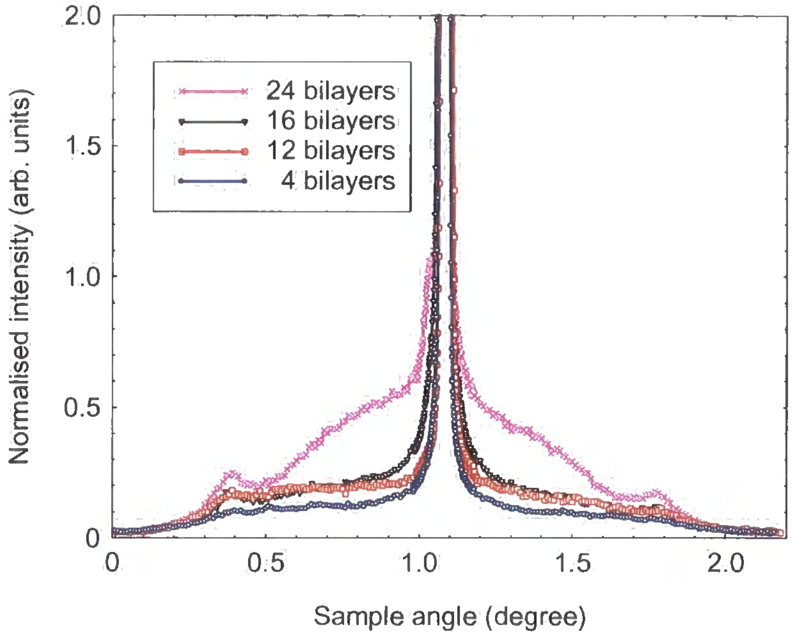

Figure 8.15 Transverse diffuse scatter data taken at the first Bragg peaks, λ= 1.3Å.

The relation between the in-plane correlation lengths and number of bilayers and total thicknesses is shown in Figure 8.16. An exponential increase of the in-plane correlation length (ξ) as a function of bilayer repeat and total thickness is observed, indicating that high frequency components of roughness propagate less readily than the lower frequency components. This effect was seen in Fe/Au multilayers (with totally uncorrelated interfaces) (chapter 6) but not in Co/Pt multilayers (with totally correlated interfaces) (chapter 7).

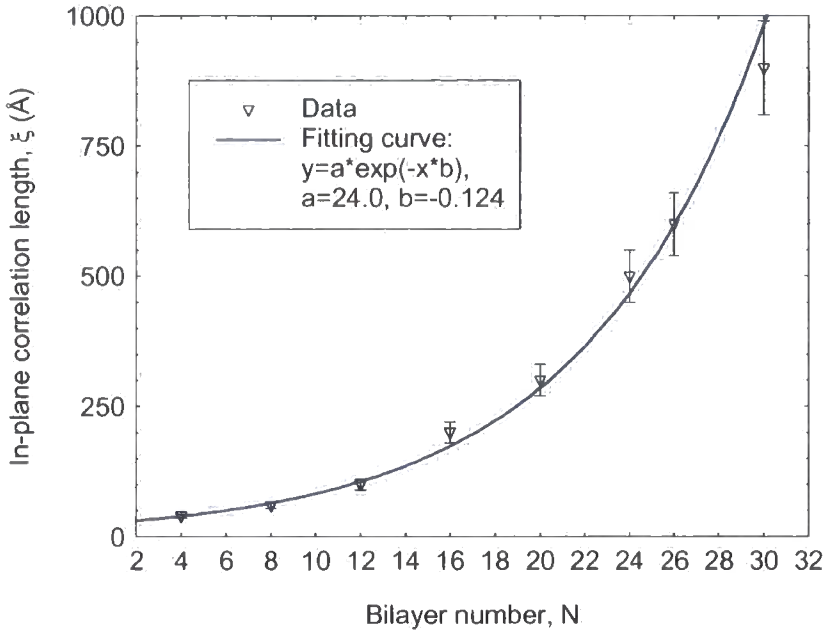

(a)

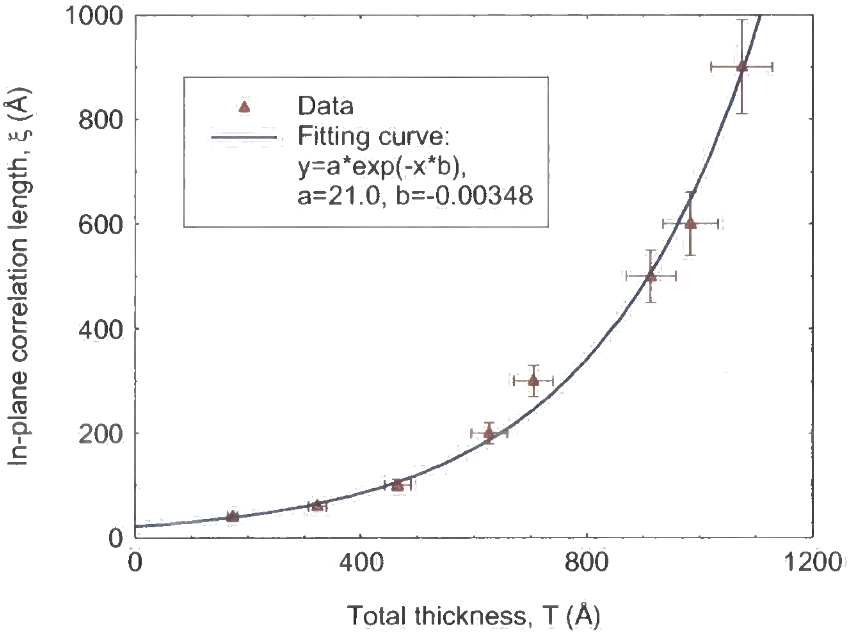

(b)

Figure 8.16 Relation between the in-plane correlation length, ξ, and **(a)** Number of bilayers, and **(b)** The total thickness.

The relation between out-of-plane correlation length (ζ) and number of bilayers (N) and total thickness (T) can be seen in Figure 8.17. The out-of-plane correlation length increases as bilayer number increases up to $N = 24$ and then remains constant.

Again, this effect was different in the Co/Pt multilayers (chapter 7) as ζ increased exponentially with N.

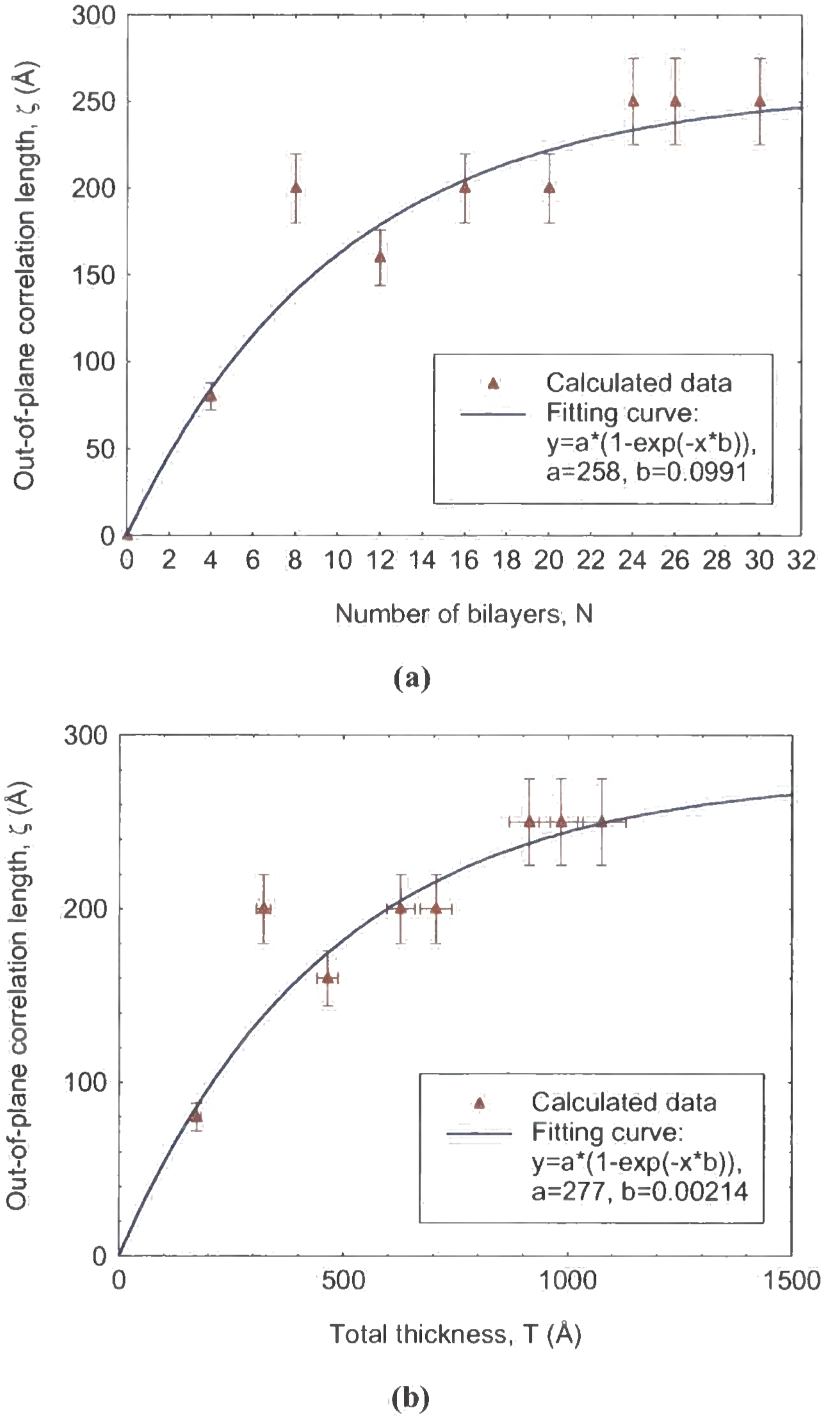

Figure 8.17 Relation between the out-of-plane correlation length and **(a)** Number of bilayers, and **(b)** The total thickness.

The inverse FWHM of the specular and off-specular first Bragg peak, as a function of N are shown in Figure 8.18. The specular Bragg peak becomes sharper and more intense as the bilayer number increases, as expected due to the increase in the number of coherently scattering interfaces. The off-specular Bragg peak follows almost the same trend. This is in contrast with the measured inverse FWHM in Co/Pt multilayers [32, 38] (chapter 7). The point at which out-of-plane correlation is lost can no longer be estimated from the changes of inverse FWHM with number of bilayers in these series of Co/Pd multilayers.

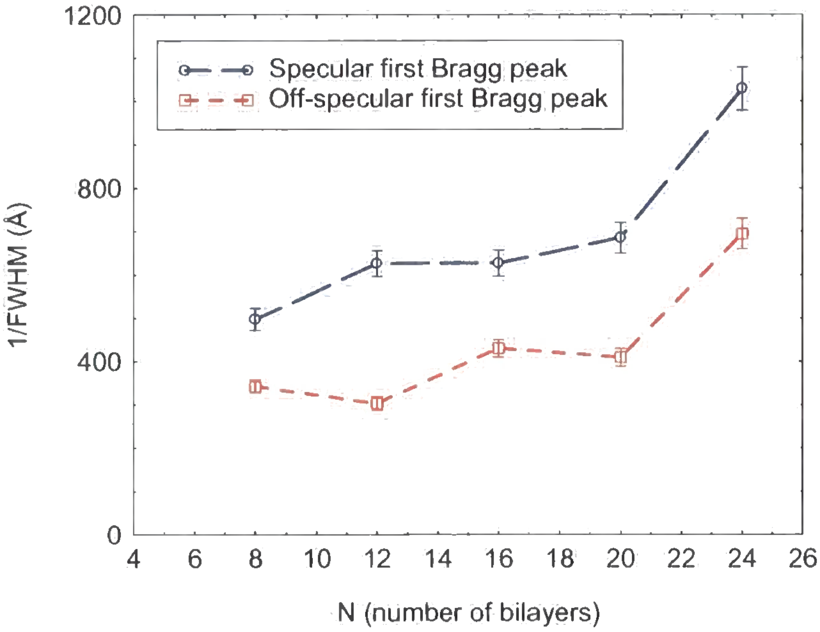

Figure 8.18 Inverse FWHM of the first specular and off-specular Bragg peaks as a function of bilayer number.

The relation between fractal parameter (h) and number of bilayers (N) can be seen in Figure 8.19. The 20-bilayer sample has a maximum value of $h=1.00$. This effect was seen in two Co/Pt multilayers with 15 and 20 bilayers.

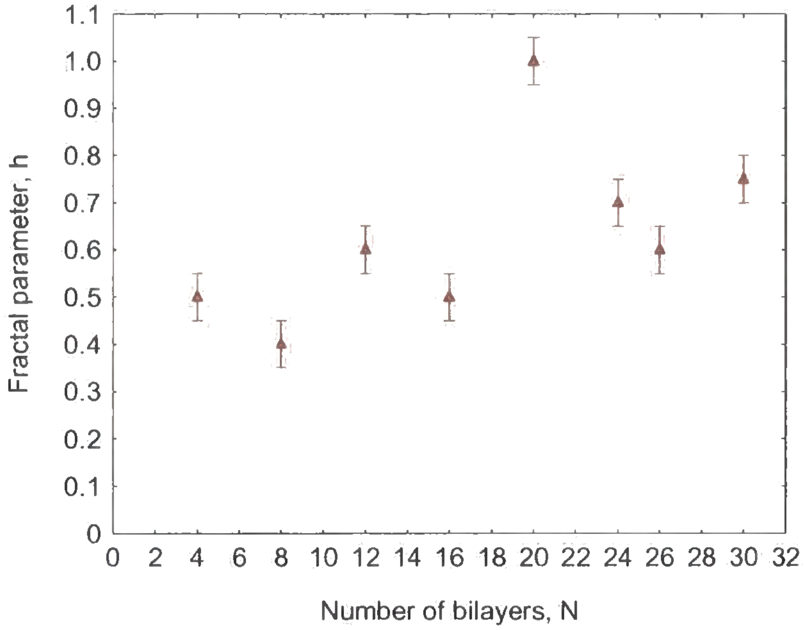

Figure 8.19 Relation between the fractal parameter and number of bilayers.

In some samples, significant interdiffusion was found at the interface between the Si substrate and the Pd buffer layer (which is typically 30Å in thickness), a feature never detected in equivalent Co/Pt multilayers. On the other hand, magnetometry measurements show that all samples exhibited PMA with smaller values for K_{eff} (effective anisotropy energy) than those for Co/Pt samples. Co/Pd multilayers exhibit PMA when $t_{Co} < 8\text{Å}$ [1]. There was a tendency for multilayers exhibiting high perpendicular magnetic anisotropy to have a large fractal parameter h (Figure 8.20). A similar, relatively weak, correlation between a more two-dimensional interface structure and high anisotropy has been observed in sputtered Co/Pt multilayers (chapter 7).

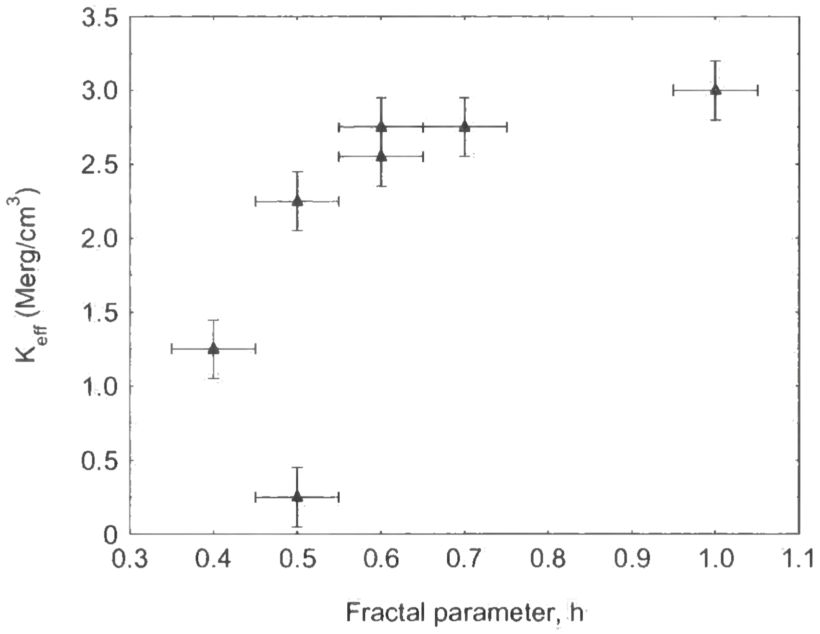

Figure 8.20 Relation between the effective anisotropy energy and fractal parameter.

In the Co/Pt system (chapter 7), the presence of the same periodic features in both the specular and off-specular scans was observed for all bilayer numbers. However, there is a marked difference in the case of Co/Pd multilayers (series 1). Initially for small bilayer number, N, the periodic features exist in both the specular and off-specular data. This, as discussed earlier, means that a high degree of conformality exists not only between each successive bilayer repeat but also across the entire multilayer stack thickness. The interface roughness is highly correlated in nature with a uniform lateral correlation length at the interface. However, in the Co/Pd system as the bilayer number reaches $N = 16$ the off-specular Kiessig fringes start to become less well defined and by $N = 20$ they are lost completely, although the off-specular Bragg peaks do remain indicating that conformality between successive repeats is retained. Loss of the Kiessig fringes and, by definition, the loss of correlation between interfaces at the top and bottom of the multilayer, enables the out-of-plane length scale over which conformal growth to be estimated. Here it is of the order of 200Å in good agreement with the value from simulations (Figure 8.17). This places the critical bilayer number for conformal growth in this system at around $N = 20$. The next stage is to attempt to visualise, and explain the cause of, a growth mode that would lead to this loss in conformality between the top and bottom surface of a multilayer stack whilst at the same time retaining the correlation between neighbouring bilayers in the stack. One possible structural explanation for this loss of conformal growth in the stack is a columnar type growth mode in the Co/Pd system which has been observed through cross sectional TEM in other studies. This growth mode has been observed previously by Junhua [39] in which a columnar type microstructure was seen to develop with increasing bilayer number in a series of Co/Pd multilayers grown on glass and on Al-NiP substrates. In structures which show a high degree of columnar growth it has been observed that the convex interface structures and column boundaries can cause the pinning of domain wall motion which, in turn, can lead to an increase in the coercivity in such systems [40-42]. However, an increase in the coercivity was observed in these Co/Pd samples as the number of bilayers changed from 2 to 20 and then decreased (Figure 8.14(b)). The increase in the coercivity may be a consequence of the more pronounced grain boundaries in a columnar structure acting as pinning centers. These observations are consistent with other studies by Zeper and Greaves [40, 43]. Further to this, as seen in Figure 8.14(a), VSM measurements indicate a maximum in the perpendicular anisotropy in these Co/Pd multilayers for a value of approximately $N = 20$.

8.4 Series 2.

Series 2 samples were nominally:

$$\mathrm{SiO_2} / 30\ \text{Å Pd} / N \times \{8\ \text{Å Co} / 30\ \text{Å Pd}\} \quad \text{where } N = 2, 4, 6..., 30$$

For convenience, the experimental data sets and their analysis have been placed in Appendix D. The summary is found in Table 8.2.

Table 8.2

Multilayer structure parameters determined from VSM measurements and x-ray scattering simulations.

N-1	t_{Buffer} ±0.3Å	t_{Co} ±0.3Å	t_{Pd} ±0.3Å	σ_{Buffer} ±0.3Å	σ_{Co} ±0.3Å	σ_{Pd} ±0.3Å	ζ ±10%	ξ ±10Å	h ±10%
7	32.5	8.9	31.9	4.1	8.8	4.0	200	40	0.15
11	31.6	8.9	32.3	8.1	4.1	4.3	300	70	0.25
N-2	t_{Buffer} ±0.3Å	t_{Co} ±0.3Å	t_{Pd} ±0.3Å	σ_{Buffer} ±0.3Å	σ_{Co} ±0.3Å	σ_{Pd} ±0.3Å	ζ ±10%	ξ ±10Å	h ±10%
14	30.4	4.5	33.8	3.8	6.6	3.6	300	25	0.15
18	36.0	6.4	29.1	7.4	5.1	5.0	300	300	0.60
28	24.1	6.9	33.5	1.9	4.4	6.3	250	1500	0.7

8.4.1 Discussions

The relation between the in-plane correlation lengths and number of bilayers is shown in Figure 8.21. An exponential increase of the in-plane correlation length (ξ) as a function of bilayer repeat is observed as the number of bilayers increased from 2 to 14. A dramatic change in ξ can clearly be seen for the 16-bilayer sample. Interestingly, the in-plane correlation length continued to increase as the number of bilayers changes from 16 to 30. As seen in Table 8.2, the Co layer thickness for samples with 16 and 20 bilayers was thinner than that for the other samples. On the other hand, magnetometry measurements showed that these samples exhibited out-of-plane magnetization, while the in-plane magnetization is observed for other samples of this series.

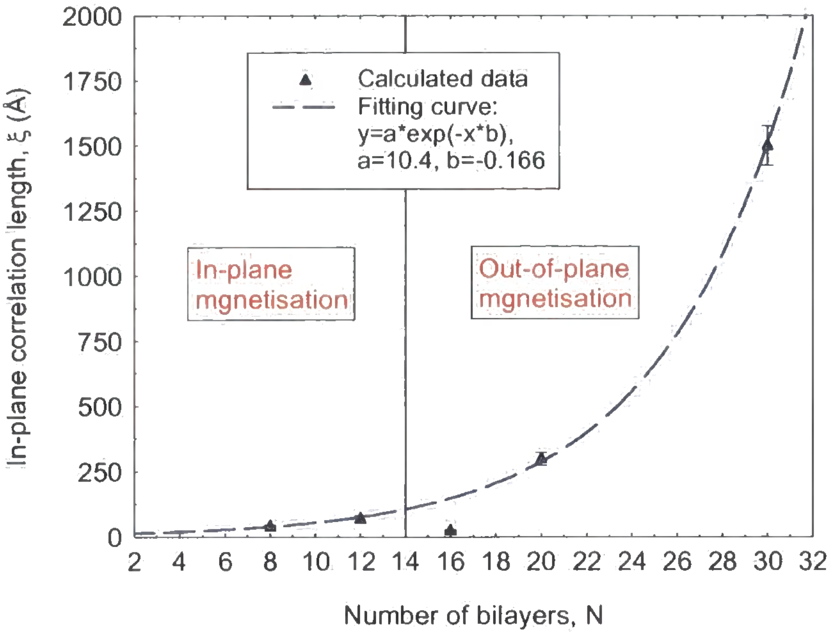

Figure 8.21 Relation between the in-plane correlation length and number of bilayers.

The relation between out-of-plane correlation length (ζ) and number of bilayers (N) can be seen in Figure 8.22. The out-of-plane correlation length increases as bilayer number increases up to $N=12$ and then remains constant. This effect was different in the Co/Pd multilayers series 1 as ζ increased exponentially with N up to $N=24$ and then remained constant. Interestingly, no change in ζ is observed for samples with $N=16\,\&\,24$ (samples with thinner Co thicknesses and magnetization out of the plane).

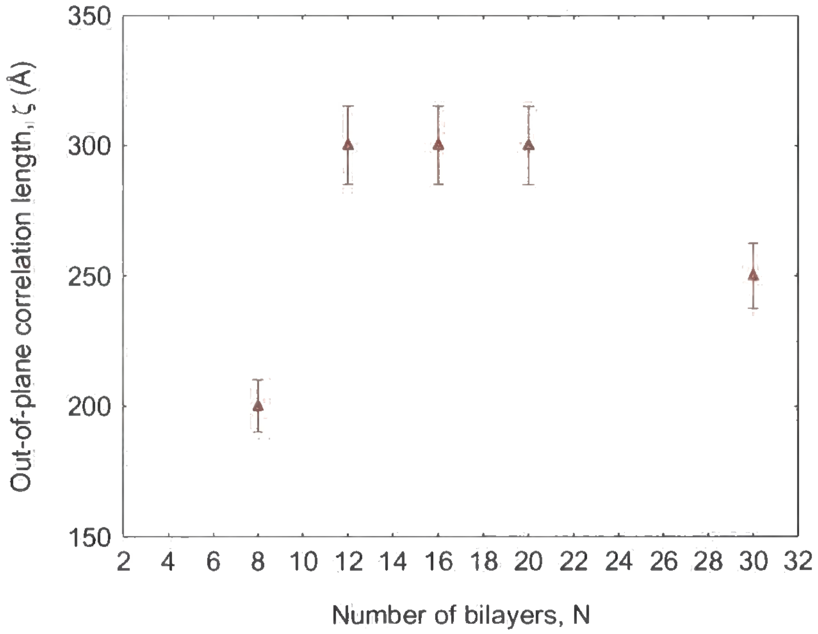

Figure 8.22 Relation between the out-of-plane correlation length and number of bilayers.

The relation between fractal parameter with number of bilayers can be seen in Figure 8.23. The 20-bilayer sample has a maximum value of $h = 0.6$. As illustrated in Figure 8.23, a transition from in-plane magnetization to the perpendicular anisotropy seems to be associated with the increase in fractal parameter. This effect was seen in 20-bilayer sample in series 1 of Co/Pd and two Co/Pt multilayers with 15 and 20 bilayers.

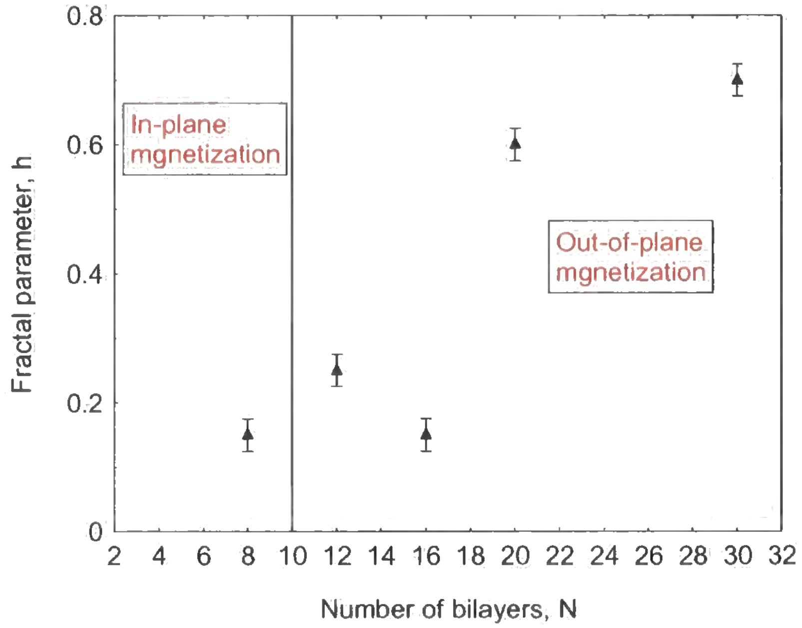

Figure 8.23 Relation between the fractal parameter and number of bilayers.

8.5 Series 3.

Series 3 samples were nominally:

SiO_2 / 30 Å Pd / N × {14 Å Co / 30 Å Pd} where $N = 2, 4, 6..., 30$

X-ray experiments showed that five samples in this series had poor interfaces. No Bragg peaks could be observed in the grazing incidence specular scans. The experimental data sets and their analysis can be found in Appendix E. The summary is shown in Table 8.3.

Table 8.3

Multilayer structure parameters determined from VSM measurements and x-ray scattering simulations.

N-1	t_{Buffer} ±0.3Å	t_{Co} ±0.3Å	t_{Pd} ±0.3Å	σ_{Buffer} ±0.3Å	σ_{Co} ±0.3Å	σ_{Pd} ±0.3Å	ζ ±10%	ξ ±10Å	h ±10%
7	33.0	14.4	29.2	3.9	3.8	3.7	200	18	0.20
9	32.8	14.6	31.0	8.0	2.6	9.1	250	60	0.20
11	35.5	14.9	30.9	3.8	3.9	3.6	250	70	0.24
15	32.0	15.4	30.1	4.8	4.2	4.2	250	120	0.15
25	32.3	13.0	30.9	7.5	4.8	8.4	250	300	0.50

8.5.1 Discussions

The relation between the in-plane correlation lengths and number of bilayers is shown in Figure 8.24. An exponential increase of the in-plane correlation length (ξ) as a function of bilayer repeat is observed indicating that high frequency components of roughness propagate less readily than the lower frequency components. This effect was seen in both series 1 and 2 of Co/Pd samples.

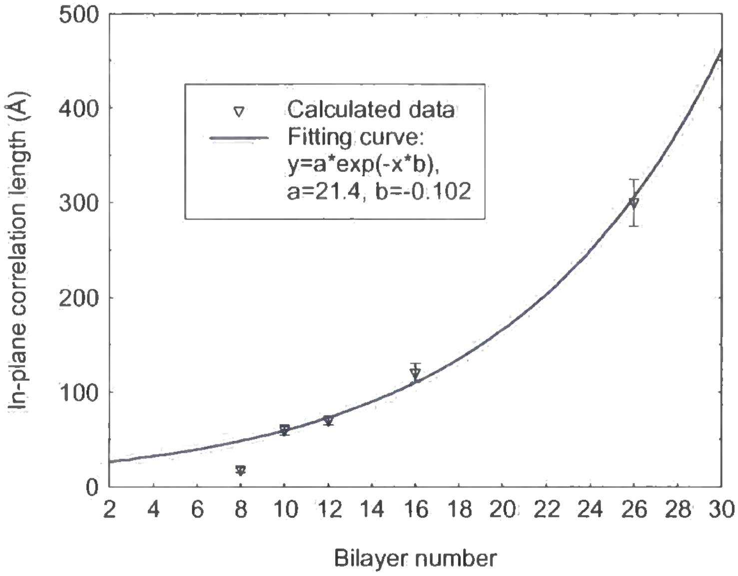

Figure 8.24 Relation between the in-plane correlation length and number of bilayers.

The relation between out-of-plane correlation length (ζ) and number of bilayers can be seen in Figure 8.25. The out-of-plane correlation length increases as bilayer number increases up to $N = 10$ and then remains constant. A similar effect was seen in series 2 while it was different in the Co/Pd multilayers, series 1, when ζ increased exponentially.

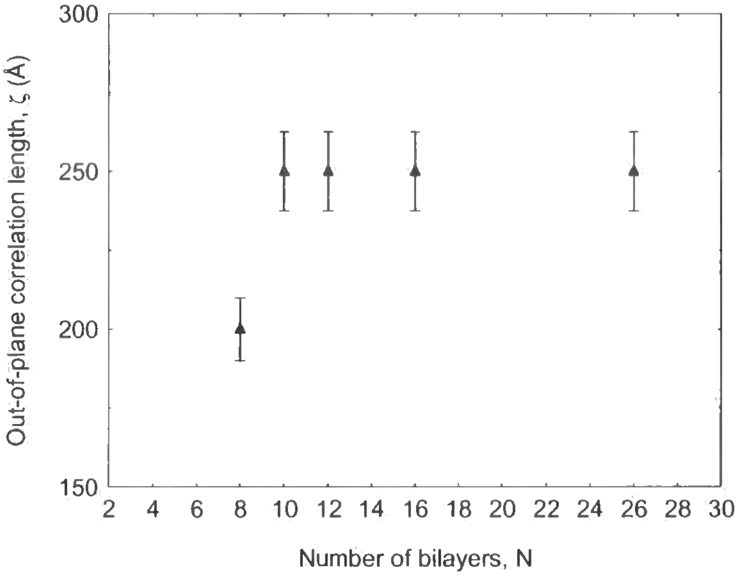

Figure 8.25 Relation between the out-of-plane correlation length and number of bilayers.

By simulating the diffuse scattering data, the fractal parameter for all series 3 samples found to be lower than 0.5. The relation between fractal parameter and number of bilayers can be seen in Figure 8.26. On the other hand, VSM measurements showed that all samples exhibited in-plane magnetization. One may conclude that, compare to series 1 and 2, the fractal parameter has a major impact on the magnetization direction.

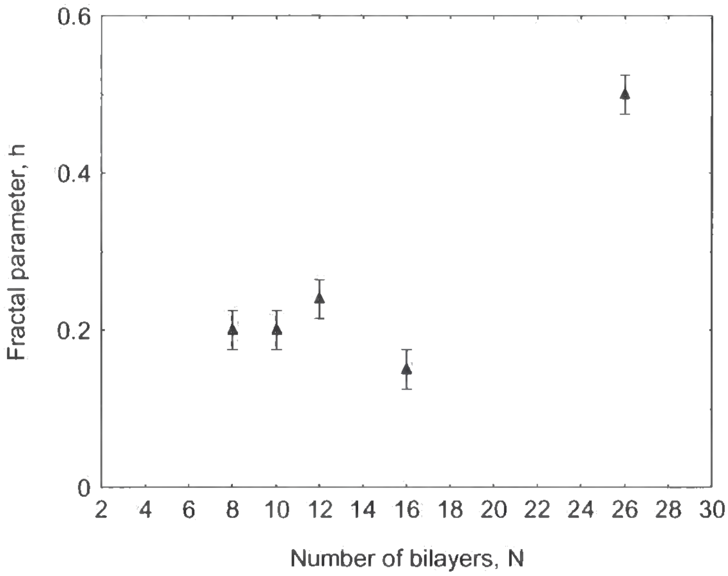

Figure 8.26 Relation between the fractal parameter and number of bilayers.

8.6 Series 4.

Series 4 samples were nominally:

SiO_2 / 30 Å Pd / $N \times$ {3 Å Co / 26 Å Pd} where $N = 2, 4, 6..., 30$

The experimental data sets and their analysis have been placed in Appendix F. The summary is found in Table 8.4.

Table 8.4

Multilayer structure parameters determined from VSM measurements and x-ray scattering simulations.

N-1	t_{Buffer} ±0.3Å	t_{Co} ±0.3Å	t_{Pd} ±0.3Å	σ_{Buffer} ±0.3Å	σ_{Co} ±0.3Å	σ_{Pd} ±0.3Å	ζ ±10%	ξ ±10Å	h ±10%
3	29.6	2.2	21.9	7.2	5.3	6.4	150	40	0.50
7	26.4	3.6	26.4	4.5	7.9	3.8	300	120	0.50
11	25.7	3.1	27.9	4.4	3.3	4.4	300	350	0.60
15	27.7	2.5	28.0	6.0	4.8	5.3	300	850	0.60
N-2	t_{Buffer} ±0.3Å	t ***Co(0.9) Cu(0.1)*** ±0.3Å	t_{Pd} ±0.3Å	σ_{Buffer} ±0.3Å	σ ***Co(0.9) Cu(0.1)*** ±0.3Å	σ_{Pd} ±0.3Å	ζ ±10%	ξ ±10Å	h ±10%
20	31.5	2.6	27.5	6.1	4.1	6.3	350	100	0.60
28	28.3	5.5	20.9	11.1	8.6	8.7	300	1500	0.25

8.6.1 Discussions

The relation between the in-plane correlation lengths and number of bilayers is shown in Figure 8.27. An exponential increase of the in-plane correlation length (ξ) is observed when the number of bilayers increased from 2 to 20. A dramatic change in ξ is seen for the 22-bilayer sample. Samples with $N \geq 20$ were found to become accidentally contaminated with Cu, as reported by the Leeds group.

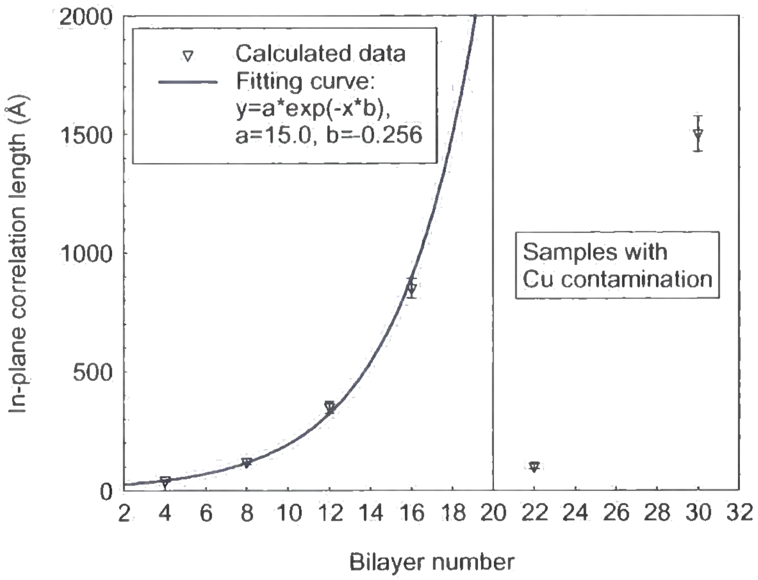

Figure 8.27 Relation between the in-plane correlation length and number of bilayers.

The relation between out-of-plane correlation length (ζ) and number of bilayers (N) can be seen in Figure 8.28. The out-of-plane correlation length increases as bilayer number increases up to $N = 8$ and then remains constant.

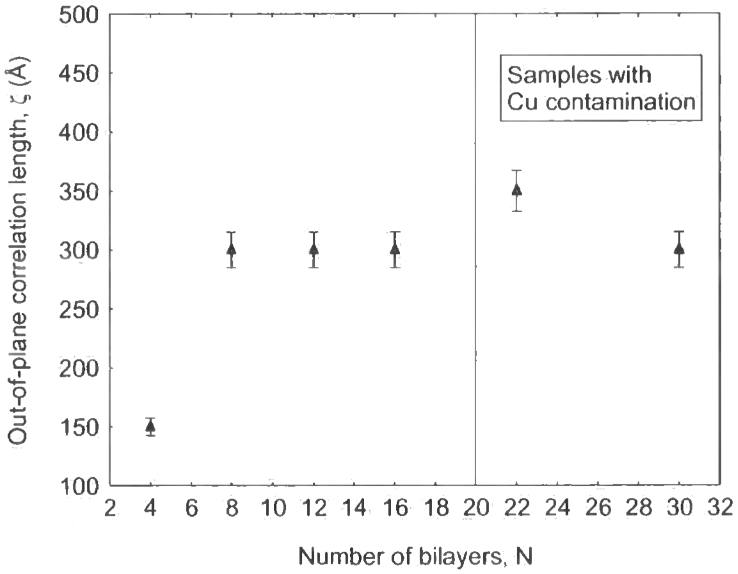

Figure 8.28 Relation between the out-of-plane correlation length and number of bilayers.

The relation between fractal parameter (h) and number of bilayers (N) can be seen in Figure 8.29.

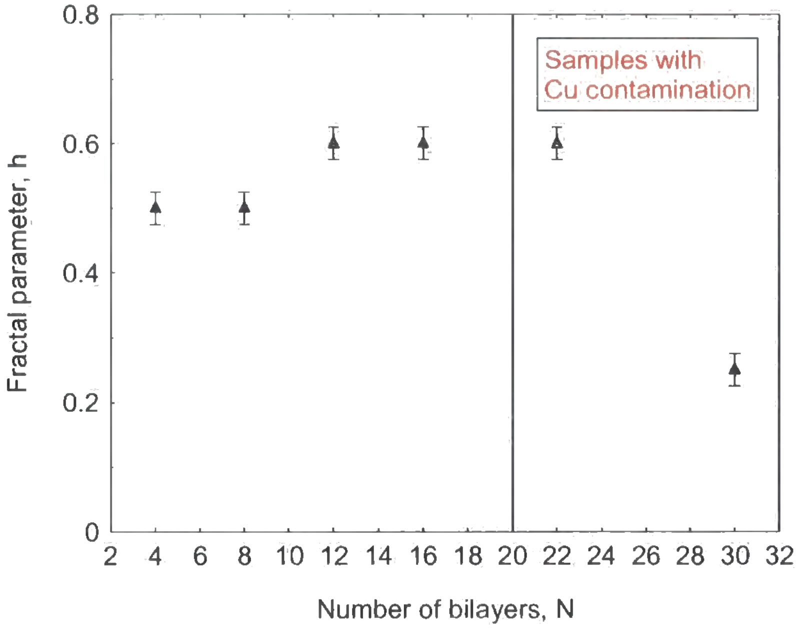

Figure 8.29 Relation between the fractal parameter and number of bilayers.

On the other hand, VSM measurements showed that all samples exhibited PMA. From the area between the in-plane and out-of-plane M-H loops, K_{eff} was calculated and the results can be seen in Figure 8.30. Once again, samples with higher PMA seem to have a higher fractal parameter as illustrated in Figures 8.29 and 8.30.

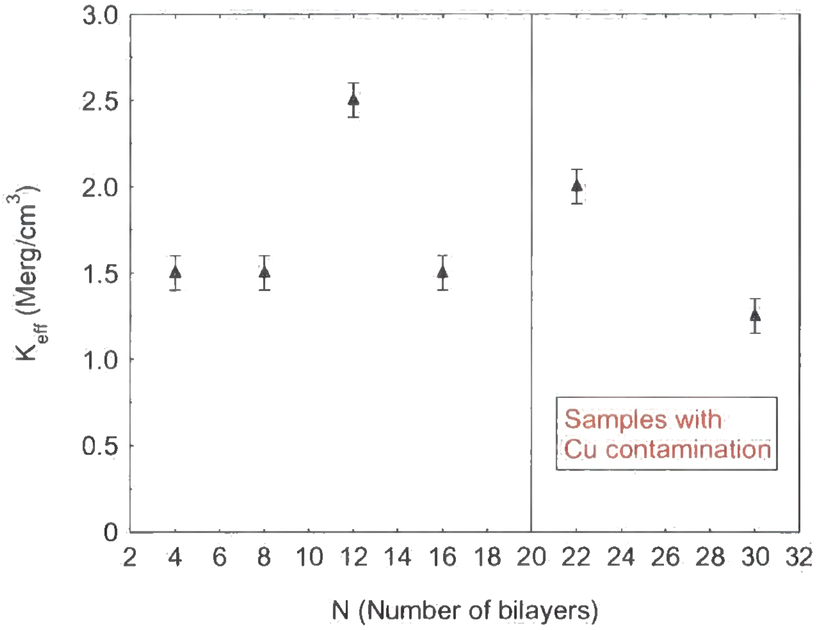

Figure 8.30 Relation between K_{eff} and number of bilayers (VSM measurements).

8.7 Conclusions

In this chapter the interface structure of four series of Co/Pd multilayer thin films have been investigated. Grazing incidence x-ray specular and diffuse scattering studies in all four series of samples showed that a large increase in the in-plane correlation length, ξ, was observed as a function of bilayer repeat, indicating that high frequency components of roughness propagate less rapidly than the lower frequency components. The following equation was fitted to the structural parameters:

$$\xi = a * \{\exp(-b * N)\}$$

Where ξ and N are the in-plane correlation length and number of bilayers, respectively. In some samples (with higher value for K_{eff} and coercivity), significant interdiffusion was found at the interface between the Si substrate and the Pd buffer layer, a feature never detected in equivalent Co/Pt multilayers. This is an interesting phenomena as Kawaji *et al* observed an enhancement of magnetic properties of Co/Pd magnetic multilayers by using Pd/Si dual seed layer [19]. There was a tendency for multilayers exhibiting high perpendicular magnetic anisotropy to have a large Hurst fractal parameter h. Similar correlation between a more two dimensional interface structure and high anisotropy was observed in sputtered Co/Pt multilayers.

REFERENCES

[1] P. F. Carcia, A. D. Meinhaldt, and A. Suna, *Appl. Phys. Lett.*, **47 (2)**, 178-180 (1985).

[2] F. J. A. den Broeder, H. C. Donkersloot, H. J. G. Draaisma, and W. J. M. Dejonge, *J. Appl. Phys.*, **61 (8)**, 4317-4319 (1987).

[3] H. J. G. Draaisma, F. J. A. Denbroeder, and W. J. M. Dejonge, *J. Appl. Phys.*, **63 (8)**, 3479-3481 (1988).

[4] P. F. Carcia, *J. Appl. Phys.*, **63 (10)**, 5066-5073 (1988).

[5] S. K. Kim, J. S. Kang, J. I. Jeong, J. H. Hong, Y. M. Koo, H. J. Shin, and Y. P. Lee, *J. Appl. Phys.*, **72 (10)**, 4986-4989 (1992).

[6] H. Yamane, Y. Maeno, and M. Kobayashi, *J. Appl. Phys.*, **73 (1)**, 334-338 (1993).

[7] B. M. Lairson, J. Perez, and C. Baldwin, *Appl. Phys. Lett.*, **64 (21)**, 2891-2893 (1994).

[8] F. J. A. den Broeder, W. Hoving, and P. J. H. Bloemen, *J. Magn. Magn. Mater.*, **93** , 562-570 (1991).

[9] G. H. O. Daalderop, P. J. Kelly, and M. F. H. Schuurmans, *Phys. Rev. B*, **41 (17)**, 11919-11937 (1990).

[10] C. Chappert and P. Bruno, *J. Appl. Phys.*, **64 (10)**, 5736-5741 (1988).

[11] S. Tsunashima, K. Nagase, K. Nakamura, and S. Uchiyama, *IEEE Trans. Magn.*, **25 (5)**, 3761-3763 (1989).

[12] C. H. Lee, H. He, F. J. Lamelas, W. Vavra, C. Uher, and R. Clarke, *Phys. Rev. B*, **42 (1)**, 1066-1069 (1990).

[13] B. N. Engel, C. D. England, R. A. Vanleeuwen, M. H. Wiedmann, and C. M. Falco, *Phys. Rev. Lett.*, **67 (14)**, 1910-1913 (1991).

[14] K. Kudo, K. Kobayakawa, and Y. Sato, *Electrochim. Acta*, **47 (1-2)**, 353-357 (2001).

[15] S. K. Kim, V. A. Chernov, and Y. M. Koo, *J. Magn. Magn. Mater.*, **170 (1-2)**, L7-L12 (1997).

[16] S. K. Kim and S. C. Shin, *J. Appl. Phys.*, **89 (5)**, 3055-3057 (2001).

[17] G. Palasantzas, Y. P. Zhao, J. T. M. De Hosson, and G. C. Wang, *Physica B*, **283** , 199-202 (2000).

[18] A. T. Macrander, C. Liu, R. Csencsits, R. Cook, M. Kirk, and R. Headrick, *Physica B*, **283** , 157-161 (2000).

[19] J. Kawaji, T. Asahi, T. Onoue, J. Sayama, J. Hokkyo, T. Osaka, and K. Ouchi, *J. Magn. Magn. Mater.*, **251 (2)**, 220-228 (2002).

[20] T. Onoue, T. Asahi, K. Kuramochi, J. Kawaji, T. Osaka, J. Ariake, K. Ouchi, G. Safran, and N. Yaguchi, *J. Appl. Phys.*, **92 (8)**, 4545-4552 (2002).

[21] T. Onoue, T. Asahi, K. Kuramochi, J. Kawaji, T. Homma, and T. Osaka, *J. Magn. Magn. Mater.*, **235 (1-3)**, 40-44 (2001).

[22] T. Onoue, J. Kawaji, K. Kuramochi, T. Asahi, and T. Osaka, *J. Magn. Magn. Mater.*, **235 (1-3)**, 82-86 (2001).

[23] T. Asahi, K. Kuramochi, J. Kawaji, T. Onoue, T. Osaka, and M. Saigo, *J. Magn. Magn. Mater.*, **235 (1-3)**, 87-92 (2001).

[24] A. G. Roy, D. E. Laughlin, T. J. Klemmer, K. Howard, S. Khizroev, and D. Litvinov, *J. Appl. Phys.*, **89 (11)**, 7531-7533 (2001).

[25] J. Y. Kim, B. K. Lee, G. S. Park, M. Uchida, T. Kurosawa, S. Watanabe, J. Ariake, N. Honda, and K. Ouchi, *J. Magn. Magn. Mater.*, **235 (1-3)**, 53-58 (2001).

[26] H. Ohmori and A. Maesaka, *J. Magn. Magn. Mater.*, **235 (1-3)**, 45-52 (2001).

[27] S. Matsunuma, A. Yano, E. Fujita, T. Onuma, T. Takayama, and N. Ota, *IEEE Trans. Magn.*, **38 (4)**, 1622-1626 (2002).

[28] S. Matsunuma, A. Yano, E. Fujita, T. Onuma, T. Takayama, and N. Ota, *J. Appl. Phys.*, **91 (10)**, 8073-8075 (2002).

[29] H. S. Oh and S. K. Joo, *IEEE Trans. Magn.*, **32 (5)**, 4061-4063 (1996).

[30] S. R. Hoon and S. N. M. Willcock, *J. Phys. E.: Sci. Instrum.*, **21 (8)**, 772 (1988).

[31] C. H. Marrows, *Ph. D. Thesis,* University of Leeds (1997).

[32] A. S. H. Rozatian, B. D. Fulthorpe, T. P. A. Hase, D. E. Read, G. Ashcroft, D. E. Joyce, P. J. Grundy, J. Amighian, and B. K. Tanner, *J. Magn. Magn. Mater.*, **256** , 365-372 (2003).

[33] T. Salditt, D. Lott, T. H. Metzger, J. Peisl, G. Vignaud, P. Hoghoj, O. Scharpf, P. Hinze, and R. Lauer, *Phys. Rev. B*, **54 (8)**, 5860-5872 (1996).

[34] T. Salditt, D. Lott, T. H. Metzger, J. Peisl, R. Fischer, J. Zweck, P. Hoghoj, O. Scharpf, and G. Vignaud, *Europhys. Lett.*, **36 (8)**, 565-570 (1996).

[35] V. Holý and T. Baumbach, *Phys. Rev. B*, **49 (15)**, 10668-10676 (1994).

[36] B. D. Fulthorpe, *Ph. D. Thesis,* University of Durham (1999).

[37] T. P. A. Hase, *Ph. D. Thesis,* University of Durham (1998).

[38] B. D. Fulthorpe, D. E. Joyce, T. P. A. Hase, A. S. H. Rozatian, B. K. Tanner, and P. J. Grundy, *J. Phys.-Condes. Matter*, **11 (43)**, 8477-8487 (1999).

[39] W. Junhua, *Nanotechnology*, **13** , 720-724 (2002).

[40] W. B. Zeper, H. W. Vankesteren, B. A. J. Jacobs, J. H. M. Spruit, and P. F. Carcia, *J. Appl. Phys.*, **70 (4)**, 2264-2271 (1991).

[41] S. Hashimoto, Y. Ochiai, and K. Aso, *J. Appl. Phys.*, **66 (10)**, 4909-4916 (1989).

[42] S. Honda, H. Tanimoto, J. Ago, M. Nawate, and T. Kusuda, *J. Appl. Phys.*, **70 (10)**, 6047-6049 (1991).

[43] S. J. Greaves, P. J. Grundy, and R. J. Pollard, *J. Magn. Magn. Mater.*, **121 (1-3)**, 532-535 (1993).

Chapter 9

Summary, Conclusions and Further Work

The physical processes underlying the Perpendicular Magnetic Anisotropy (PMA) effect in magnetic multilayers, namely the spin–orbit interaction is widely believed to exhibit a strong dependence upon multilayer structure. The aim of the work presented in this thesis was to utilise x-ray scattering techniques in an attempt to determine the dominant structural factors, both interfacial and bulk, controlling the magnitude of the PMA in these systems. Experimentally, many factors such as roughness, formation of interface alloys, or patchiness of ultrathin layers may cause a reduction in PMA.

The important role of the roughness of the interfaces on the PMA is evidence of the work in chapter 6. It was found that in a series of MBE grown Fe/Au multilayers the easy axis remained in the plane with constant effective anisotropy energy in all cases. X-ray scattering data and simulations showed that the interface roughness was high and it is postulated that this results in the easy axis of magnetization remaining in the plane. However, the formation and propagation of uncorrelated roughness followed a systematic trend for surface growth. From the long period fringes in the specular and off-specular data, it was found that there was a high degree of vertical correlation of the interfaces throughout the layer stack in all samples. The in-plane correlation length associated with the correlated roughness, ξ_c, was determined to be about equal in all samples while ξ_{uc} (in-plane correlation length associated with the uncorrelated roughness) increased as the number of bilayers increased. On the other hand, x-ray data and simulations for a single 100-bilayer sample showed that although the Fe and Au layers have the thickness close to that of the other samples in the first series, the interfaces are much better defined with significantly lower roughness. This was the only sample to show perpendicular anisotropy supposing the suggestion that the absence of PMA in all other samples is associated with high interface roughness.

The work of chapter 7 builds on the observation of the highly correlated interfaces of Co/Pt multilayers and looks at the way this conformality is retained with increasing bilayer number. Longitudinal and transverse diffuse measurements show that a high degree of interface conformality is retained with increasing bilayer number, suggesting that if a limiting out-of-plane length scale for conformal growth does exist then it must be considerably greater than 400Å. The magnetic measurements have confirmed the enhanced perpendicular anisotropy seen in other sample sets when the bilayer repeat number is about 15. However, the out-of-plane correlation length of the interface roughness is larger than observed previously and no changes in roughness amplitude, in-plane correlation length or crystallographic texture were found as a function of bilayer number. Although the thickness of Co and Pt layers of the samples with enhanced anisotropy differs from the other samples, the effect of this difference trends to be a reduction in PMA rather than an enhancement. The only difference observed in the interface structure was a change in the dimensionality of the roughness of the interfaces, seen in the change in fractal parameter becoming close to unity.

Such observations are of importance with regard to high density magnetic recording media, in which perpendicular anisotropy is favoured. Further work could be done on Co/Pt multilayers (as well as ordered or disordered CoPt alloys) grown on different substrates with (or without) intentionally alloyed layers to improve the magnetic and magneto-optic features of Co-Pt multilayers as such system is shown to have good tolerance against oxidation and corrosion.

A large proportion of the work in this thesis relates to the Co/Pd multilayer system. Four series of Co/Pd multilayers grown, by magnetron sputtering on thin Si (001) buffer layers, were found to exhibit very different magnetic anisotropy. Grazing incidence x-ray specular and diffuse scattering were applied to the study of the interface structure in each series. There is a large increase in the in-plane correlation length ξ as a function of bilayer repeat, indicating that high frequency components of roughness propagate less readily than the lower frequency components. In series 1, in contrast to previous measurements on Co/Pt, the roughness had a low fraction of correlated roughness normal to the film surface. No significant interdiffusion could be measured at the interfaces; almost all of the interface width determined from fitting the specular scatter to a model structure using the Bede REFS-MERCURY code was identified as topological roughness by fitting the diffuse scatter to Sinha's fractal model. The *rms* amplitude of the interface roughness of the Pd/Co interfaces increased with increasing bilayer repeat number, but no corresponding variation was found for the Co/Pd interfaces. In some samples, significant interdiffusion was found at the interface between the Si substrate and the Pd buffer layer, a feature never detected in equivalent Co/Pt multilayers. There was a tendency for multilayers exhibiting high perpendicular magnetic anisotropy to have a large fractal parameter, h (Figure 8.20).

In series 2, an exponential increase of the in-plane correlation length (ξ) as a function of bilayer repeat and total thickness is observed as the number of bilayers increased from 2 to 14. A dramatic change in ξ can clearly be seen for the 16-bilayer sample. Interestingly, the in-plane correlation length continued to increase as the number of bilayers changed from 16 to 30 (Figure 8.21). The Co layer thickness for samples with 16 and 20 bilayers was found to be thinner than that for the other samples. Magnetometry measurements showed that these samples exhibited out-of-plane magnetization, while in-plane magnetization is observed for other samples of this series.

Magnetometry measurements on the Co/Pd multilayers, series 3 and 4 showed that all samples exhibited in-plane magnetization. X-ray data and simulations showed that the out-of-plane correlation length increased as bilayer number increased up to $N=10$ in series 3 and $N=8$ in series 4 and then remained constant. A similar effect was seen in series 2 while it was different in the Co/Pd multilayers, series 1, as ζ increased exponentially with N up to $N=24$.

Future research efforts on Co/Pd multilayers could be directed at enhancing the coercivity of the hard magnetic layer, fabricating soft magnetic underlayers of high moment and creating special seed layers to control the segregation of the grains.

In summary, diffuse scattering x-ray measurements on Co/Pt and Co/Pd show interface roughness σ independent of bilayer repeat number. For Co/Pt, the in-plane correlation length ξ was independent of bilayer number (Figure 9.1) while for Co/Pd and Fe/Au it increased. We note the saturation of ξ for the Au/Fe system, where island growth of the Au occurs. The out-of-plane correlation length ζ increased with bilayer repeat for Co/Pt and Co/Pd (Figure 9.2).

More work is needed in order to confirm these observations (i.e. diffuse x-ray scattering studies of MAR ccd images which is under way). In order to study the evolution of the interface morphology in thin films, one can employ different theoretical models mentioned briefly in Appendix G.

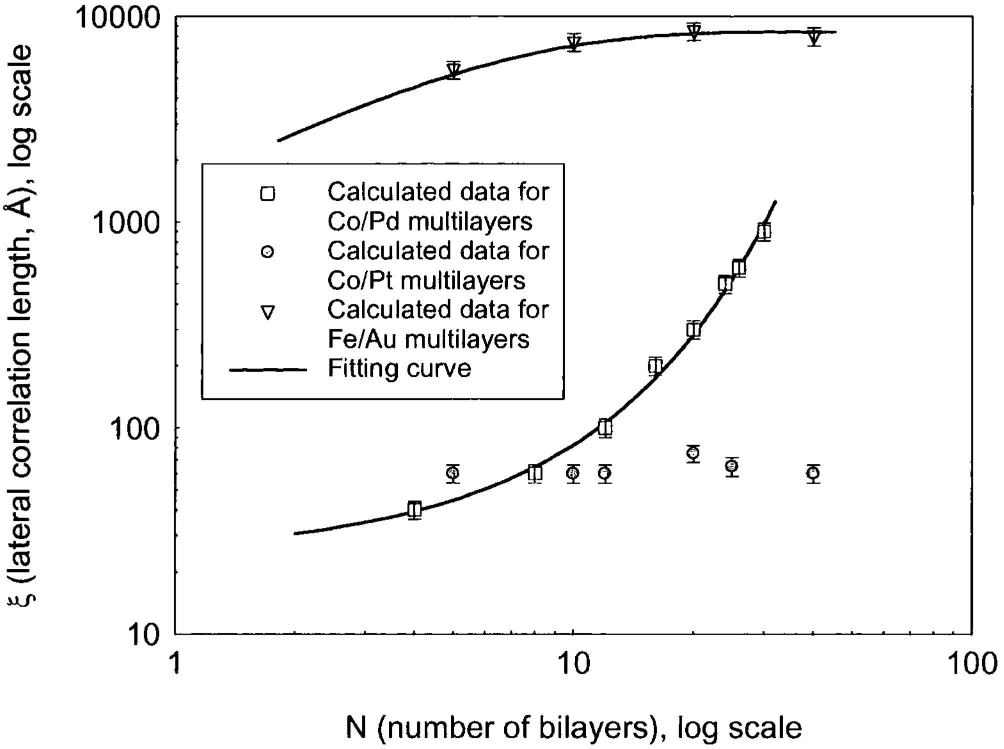

Figure 9.1 The relation between lateral (in-plane) correlation length, ξ and number of bilayers in Fe/Au, Co/Pt, and Co/Pd multilayers.

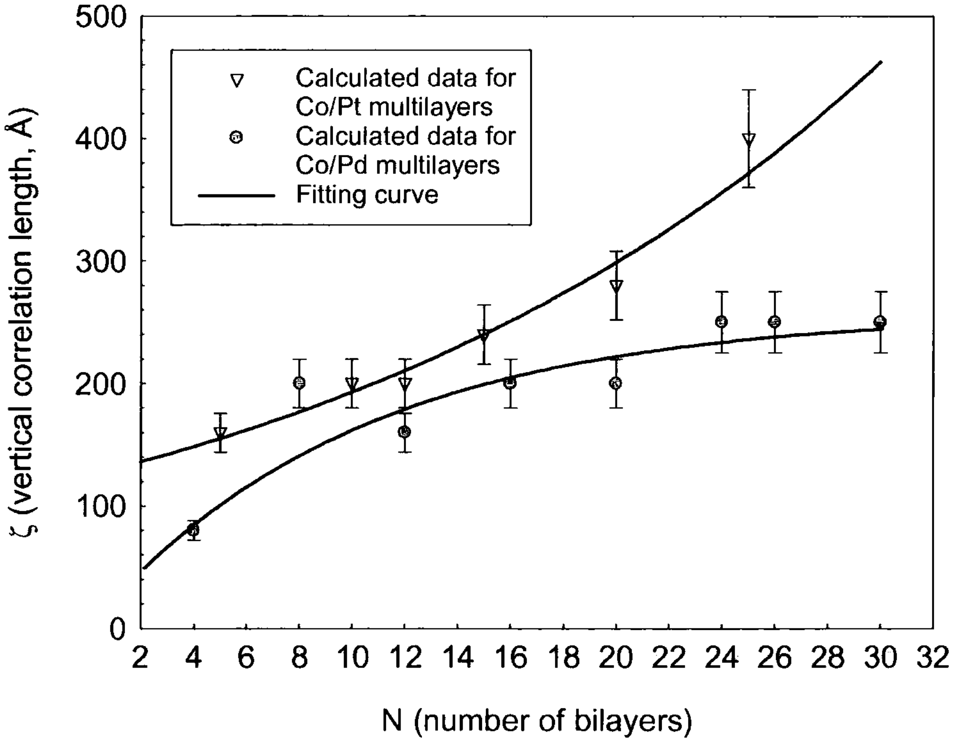

Figure 9.2 The relation between out-of-plane correlation length, ζ and number of bilayers in Co/Pt and Co/Pd multilayers.

In addition to the further work arising from the observations already discussed, there are other, closely related areas of interest that are ideally suited to x-ray scattering techniques.

The Co/Ru system exhibits extremely strong antiferromagnetic interlayer coupling that seems to be independent of interface condition, unlike the much more heavily studied Co/Cu, and which also shows the switch from in-plane to perpendicular anisotropy for low Co layer thickness. X-ray reflectivity studies could be used to probe the interface morphology in these systems in order to see how the interface roughness and conformality compares with that found for other systems. Moreover, the evolution of the interface morphology during the growth of thin films and multilayers has a major impact on the overall magnetic and transport properties and can be studied by means of the scattering distribution out of the incidence plane at high scattering vector. Measurement out of the incidence plane (by using a two-dimensional detector) enables a wider range of reciprocal space to be sampled, not limited thorugh cut-off by the sample surface. From these data it will be possible to determine if the surface is fractal and the scaling exponent. Although a rough estimation may be made of the magnitude of the in-plane correlation length, the x-ray reflectivity type of experiment, where the data are fitted to a model structure, is a much more reliable means of obtaining this parameter.

Appendix A

The Reciprocal Space

If a series of atoms are held within a periodic crystal lattice, the electron density within that crystal will also be periodic in nature. Scattering of x-rays from atoms is proportional to the Fourier transform of the electron density, and can therefore be expanded as a series over Fourier space. Within this Fourier, or reciprocal space, any periodic function is represented by a single point. All spatial frequencies in real space are converted, via a Fourier transform, to points in reciprocal space, the direction of a point corresponding to the direction of propagation of that frequency in real space.

The three primitive vectors describing the reciprocal lattice, b_1, b_2 and b_3, are linked to the three real lattice vectors, a_1, a_2, a_3, via the relations:

$$\begin{aligned} b_1 &= \frac{a_2 \times a_3}{a_1 \cdot a_2 \times a_3} \\ b_2 &= \frac{a_3 \times a_1}{a_1 \cdot a_2 \times a_3} \\ b_3 &= \frac{a_1 \times a_2}{a_1 \cdot a_2 \times a_3} \end{aligned} \tag{A.1}$$

In the Ewald construction, shown in figure A.1, the angle of the sample with respect to the beam, θ defines the incident wave vector, k_{in}. Similarly the scattering angle, φ defines the exit wavevector, k_{out}. The scattering vector is the difference between these incoming and outgoing vectors. For elastic scattering, the magnitude of each of these vectors is the same, such that:

$$|k_{in}| = |k_{out}| = |k| = \left(\frac{2\pi}{\lambda}\right) \qquad \text{(A.2)}$$

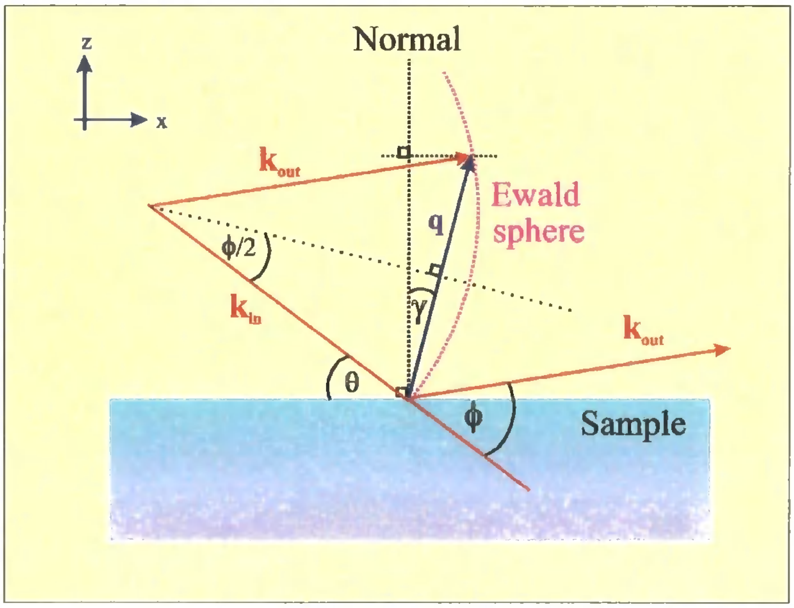

Figure A.1 Ewald construction showing the origin of the transforms between real and reciprocal space.

The scattering vector, q can be expressed solely in terms of the angle φ such that:

$$q = \left(\frac{4\pi}{\lambda}\right)\sin\left(\frac{\varphi}{2}\right) \qquad \text{(A.3)}$$

For any scattering vector, the out-of-plane, q_z, and in-plane, q_x, scattering components can then be expressed in terms of an additional angle, γ, where $\gamma = \theta - \left(\frac{\varphi}{2}\right)$. The general transforms for scattering vectors then become:

$$\begin{aligned} q_x &= \left(\frac{4\pi}{\lambda}\right)\sin\left(\frac{\varphi}{2}\right)\sin\gamma \\ q_z &= \left(\frac{4\pi}{\lambda}\right)\sin\left(\frac{\varphi}{2}\right)\cos\gamma \end{aligned} \tag{A.4}$$

Appendix B

The Kinematical Theory

It is possible to consider the scattering of x-rays by electrons from either a classical or quantum mechanical standpoint. As it is only the elastic scattering of electrons that will be considered here, discussion will proceed via the classical formalism. Any charged particle will be accelerated, and set into forced oscillation, by the electromagnetic radiation field associated with an x-ray incident upon it. The charged particle, for example an electron, will then re-radiate with the same frequency as the incident wave but with a phase shift of π upon scattering. This process is known as elastic Thomson scattering. For an incident beam, of intensity I_0 the intensity of the scattered beam is given by:

$$I_S = I_0\left(\frac{e^2}{mc^2}\right)^2\left(\frac{P}{R^2}\right)$$
$$P = \begin{cases} 1 & \textit{for } \mathrm{s} \textit{ polarisation} \\ \cos 2\theta & \textit{for } \mathrm{p} \textit{ polarisation} \end{cases} \qquad \text{(B.1)}$$

where P is a polarisation factor, dependent on whether the incident beam is polarised in the plane (s), or perpendicular to it (p), and R is the distance between the particle and the observer. The Thomson scattering length is defined as $\left(e^2/mc^2\right)$ and is equal to 2.82×10^{-3}Å.

A typical atom represents a many electron system in which the electrons are spread out, in a continuous distribution, over a considerable volume, leading to differences in the phase of the scattered radiation from different parts of the atom. The atomic number of an atom is therefore the number of electrons per unit volume element, ρ, integrated over the entire volume such that:

$$Z = \int_V \rho(r) dV \qquad \text{(B.2)}$$

Away from any absorption edges within the material, the atomic scattering factor, f is then defined as the Fourier transform of this electron density such that:

$$f = \int_v \rho(r) \exp^{[ik.r]} dV \qquad \text{(B.3)}$$

Appendix C

Scan Types in Reciprocal Space

The characterization of a sample using grazing incidence techniques will typically lead to the use of three principal types of scan; the specular, longitudinal diffuse and transverse diffuse scans. In all of these cases, the detector is scanned out of the plane of the sample and probes only two dimensions within reciprocal space.

A common factor of $\left(\frac{4\pi}{\lambda}\right)\sin\left(\frac{\varphi}{2}\right)$, dependent only upon the scattering angle, exists in both the q_x and q_z transform equations. The transforms differ only in the treatment of the γ term. In the case of $\gamma = 0$ the q_x term disappears and only q_z, the component normal to the surface, is non zero. This occurs whenever the sample angle, θ is half of the detector angle, φ. A scan in which the detector and sample axes are coupled so that $\varphi = 2\theta$ at all times, probes the specular scatter as a function of q_z only.

The diffuse scatter close to the specular condition can be measured as a function of q_z by means of a small initial off-set in the sample angle. A coupled scan similar to the specular scan is then performed, mapping out a straight line in reciprocal space with a small angular off-set to the specular scan, figure C.1. This type of scan is referred to as a longitudinal diffuse or off-specular.

A scan of the in-plane component of reciprocal space, q_x, can be performed by fixing the detector position. This maintains a constant value of φ while the sample angle, θ, is scanned from 0 to φ. Although the out-of-plane component does vary slightly during this type of scan, as a function of $\cos\gamma$, the variation is small in this low angle regime. This transverse diffuse scan can therefore often be considered as a q_x only scan at fixed q_z.

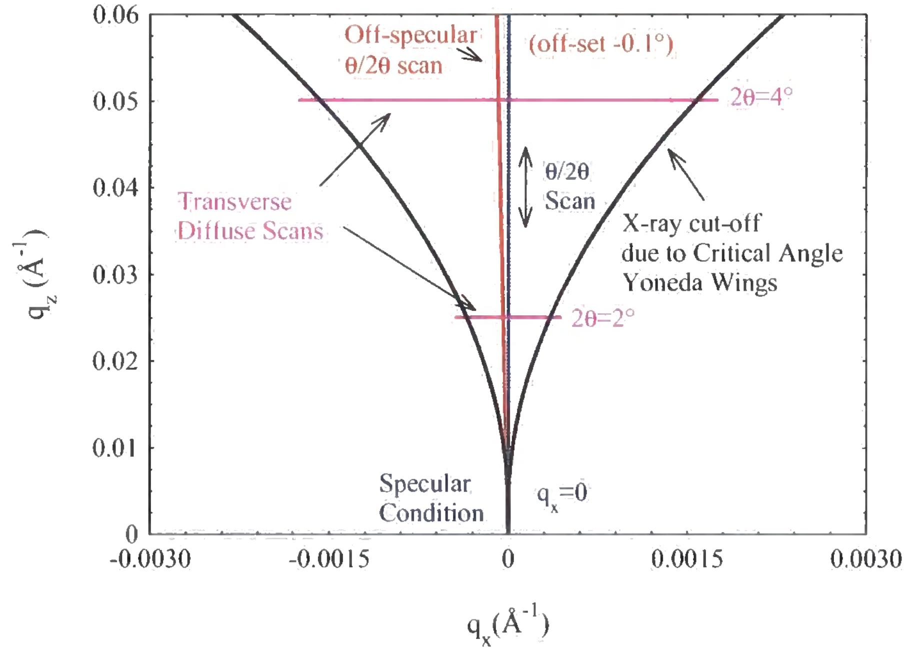

Figure C.1 Plan of reciprocal space showing the specular, off-specular and transverse diffuse scan modes. Simulated for a Si layer at λ=1.3926Å.

A plan of reciprocal space is shown in figure C.1, illustrating the various scan types. The arcs that mark the limit of observation are due to the incident and scattered x-rays existing only below the sample surface. A typical data set for a sample would include a specular scan (q_z only), an off-specular scan, which is then subtracted from the specular to obtain the true specular scatter, and two or three diffuse scans.

Appendix D

Co/Pd Multilayers, Series 2 data sets

In this appendix, the X-ray data and magnetic measurements for the second series of samples will be presented. All samples were nominally:

SiO_2 / 30 Å Pd / $N \times$ {8 Å Co / 30 Å Pt} where $N = 2, 4, 6..., 30$

D.1 X-ray experiments

D.1.1 GIXR results

A series of grazing incidence specular and off-specular x-ray scans along with simulations for these samples is shown in Figure D.1. These scans provide information concerning the development of the multilayer stack as the number of bilayers was increased from 2 to 30. In all cases excellent and unambiguous convergence was found, provided that the data range was sufficient to cover the first three Bragg peaks except for the samples with 20 and 30 bilayers. These data were taken on the GXR1 laboratory reflectometer.

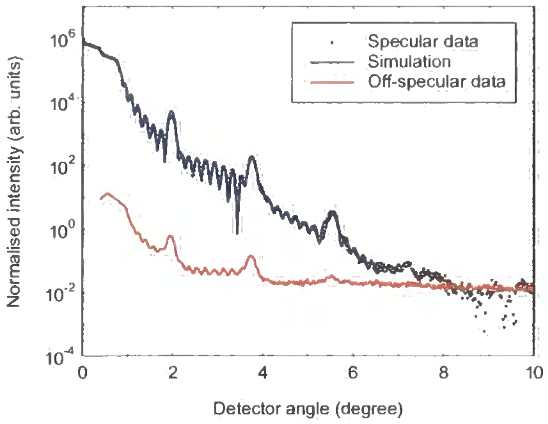

(a)

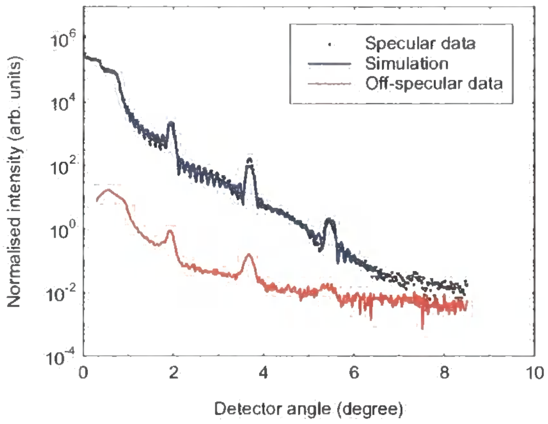

(b)

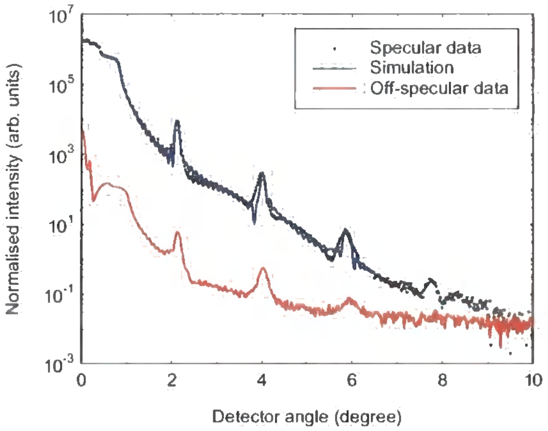

(c)

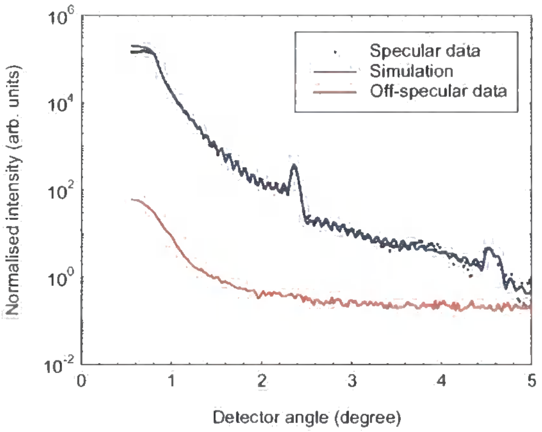

(d)

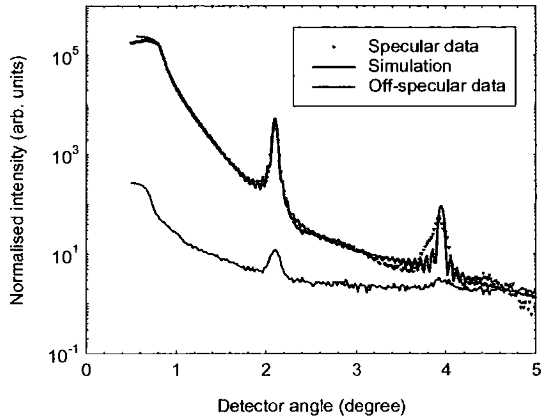

(e)

Figure D.1 Specular and Off-specular data and simulations for samples with **(a)** 8 bilayers, **(b)** 12 bilayers, **(c)** 16 bilayers, synchrotron data with λ = 1.3Å, **(d)** 20 bilayers, and **(e)** 30 bilayers, laboratory data with λ = 1.393Å.

The off-specular Bragg peaks can be seen in all cases except in Figure D.1(d). These data were taken on the GXR1 reflectometer using λ = 1.393 Å where the signal was too low to resolve the off-specular Bragg peaks from the noise. By simulating the laboratory data, the interface parameters were found to be compatible with the model for the series 2 samples.

As can be seen in Fig. D.2 (b), as the bilayer number is increased, the off-specular Bragg peak remains, indicating that out-of-plane correlation is retained within the bilayers. However, the off-specular Kiessig fringes disappear as the stack thickness increases, and the out-of-plane correlation between the interfaces at the substrate and cap is lost. The position and spacing of the specular (Fig D.2 (a)) and off-specular (Fig D.2 (b)) Bragg peaks for the N=16 & 20 bilayer samples show the bilayers were slightly thinner than the other samples.

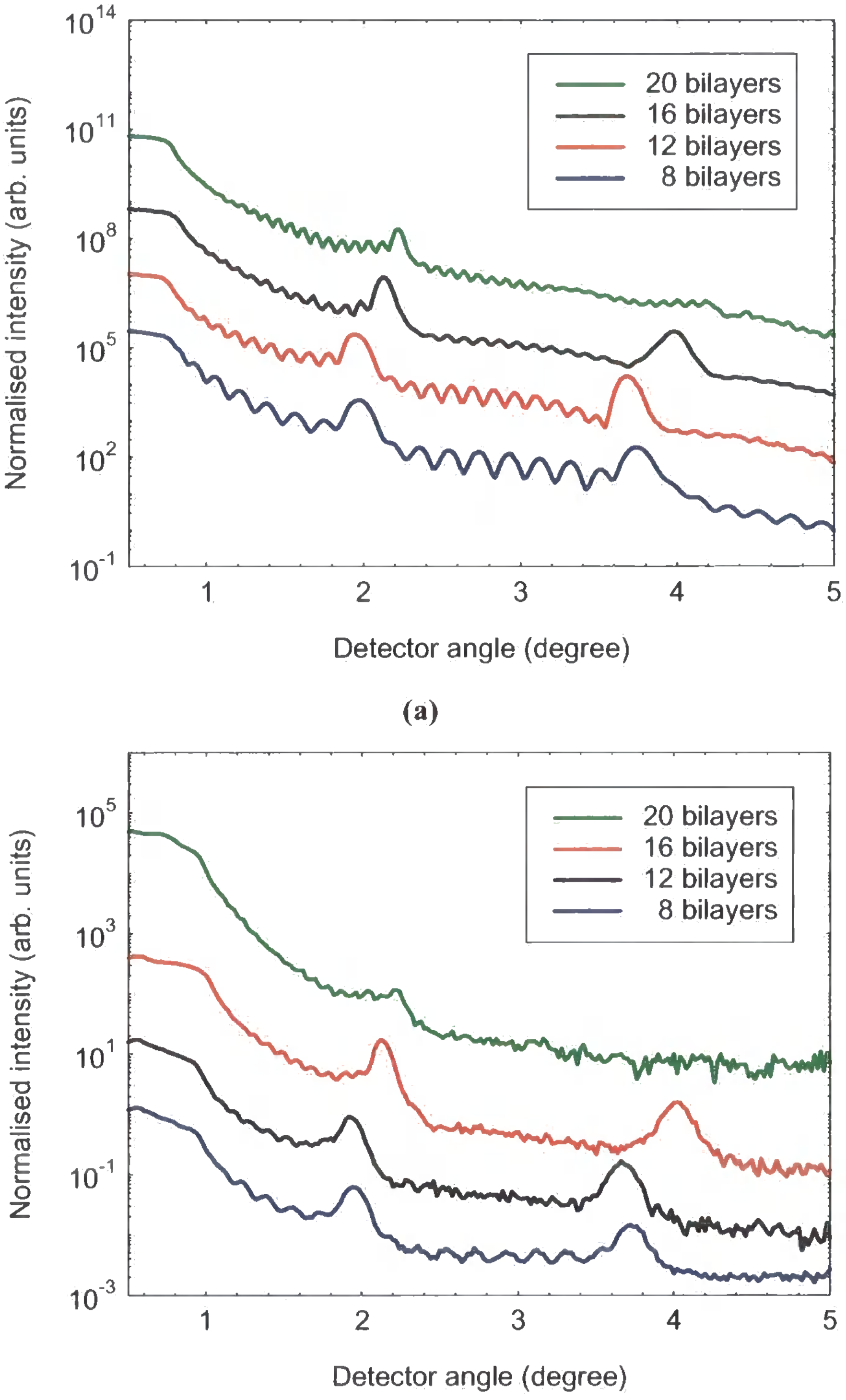

(a)

(b)

Figure D.2 **(a)** A series of Co/Pd Specular scans, λ = 1.3Å. **(b)** A series of Co/Pd Off-specular scans (sample off-set -0.1°, λ = 1.3Å).

Structural parameters were obtained by fitting the experimental data to simulations from a model structure. Values of thickness and interface width were first found by automatic refinement using the Bede MERCURY code for the specular data and these parameters then used to fit the diffuse scatter manually. After several attempts for each set of data, the model structure that led to the best fits for both specular and diffuse scatter data was determined and can be seen in Figure D.3.

(a)

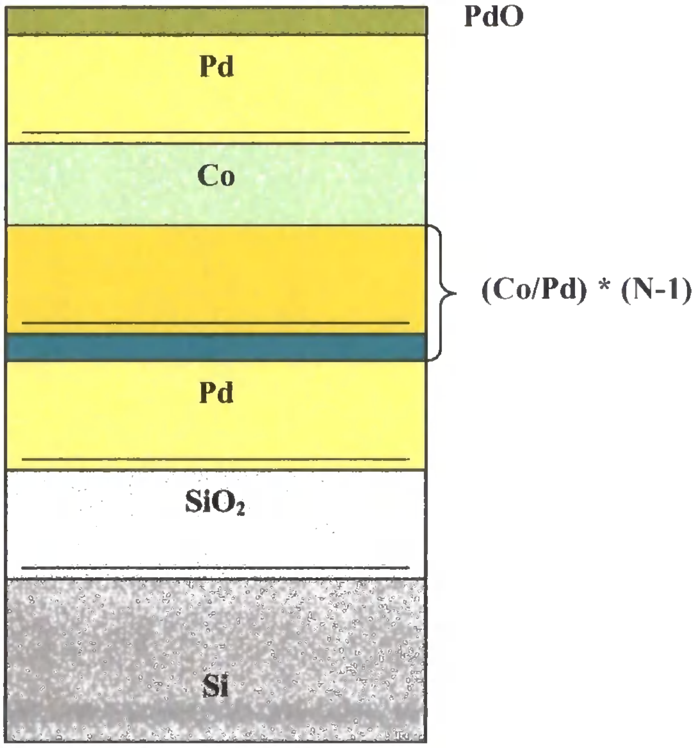

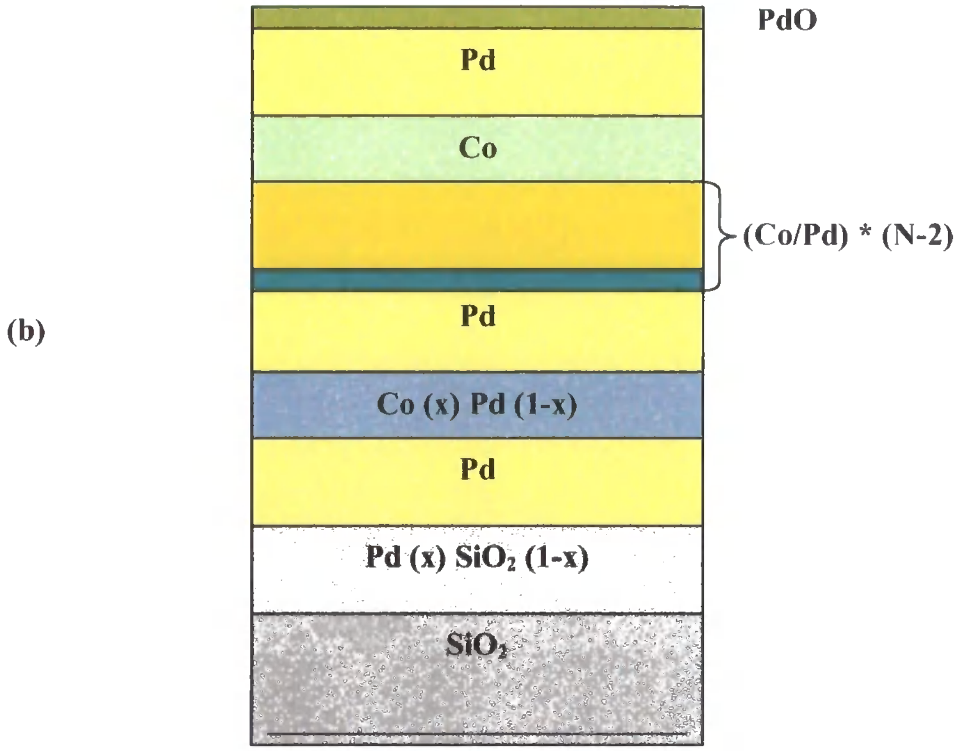

Figure D.3 The model structure used to fit specular and diffuse scatter data for samples with **(a)** In-plane and **(b)** Out-of-plane magnetization. X varied from 0.1 to 0.9.

D.1.2 GIXS results

Across the series of fifteen samples, extensive specular and transverse diffuse measurements were made. Through a combination of these scans, many aspects of the interface morphology in the multilayer structures could be determined. Two x-ray wavelengths were used, one on the laboratory GXR1, 1.393Å, and one on the station 2.3 at the SRS, 1.3Å. For each sample, at each wavelength, at least three transverse diffuse scans were taken, one or two at and one or two away from the Bragg condition. These scans are primarily sensitive to correlated and uncorrelated roughness respectively. The Bede REFS code (which was used to fit the transverse diffuse data), considers four different models for interfaces. As can be seen in Figures D.4 – D.6, best fits were achieved using a partially correlated roughness; model II.

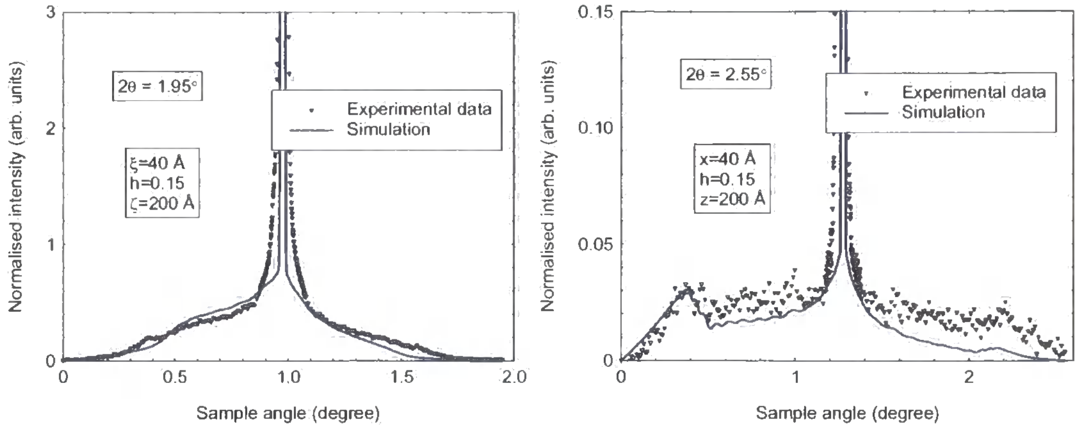

(a) **(b)**

Figure D.4 Transverse diffuse scans and simulations for the 8-bilayer sample, λ = 1.3Å.

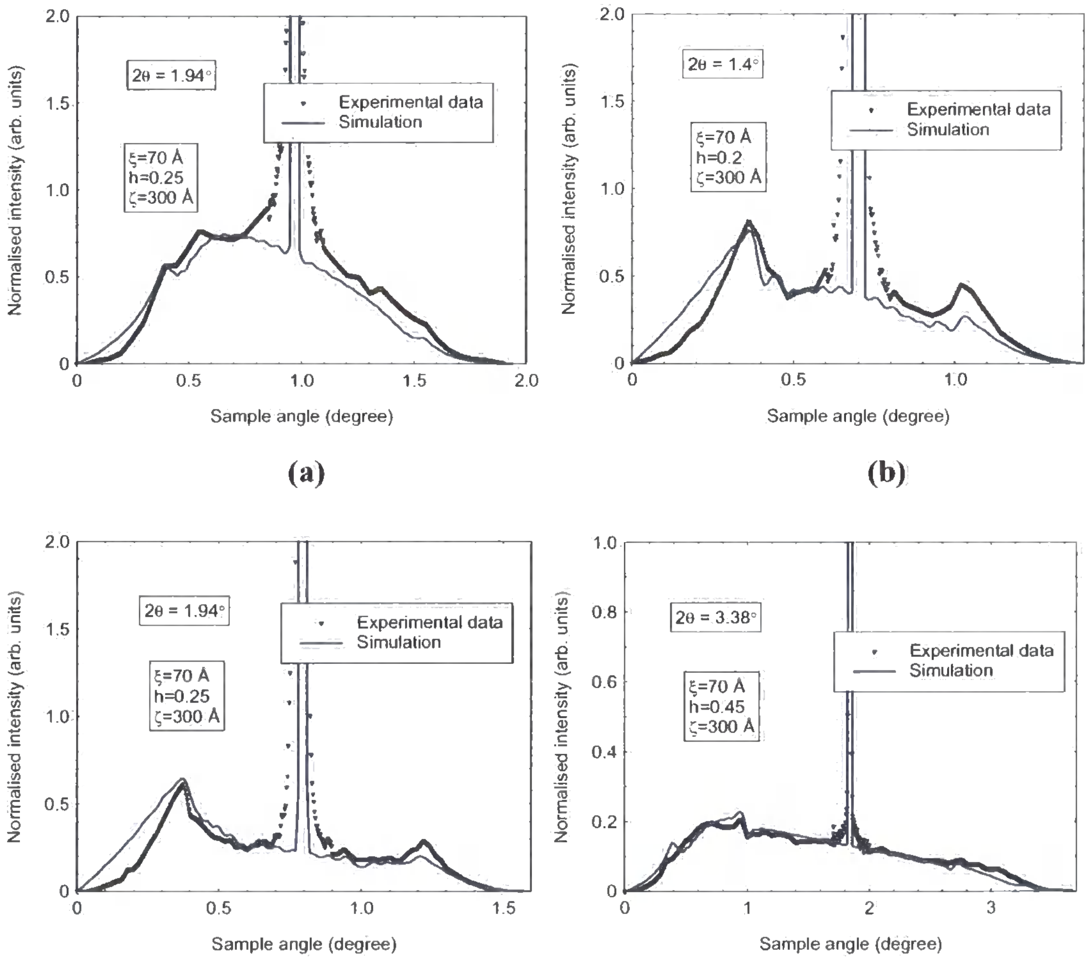

(c) **(d)**

Figure D.5 Transverse diffuse scans and simulations for the 12-bilayer sample, λ = 1.3Å.

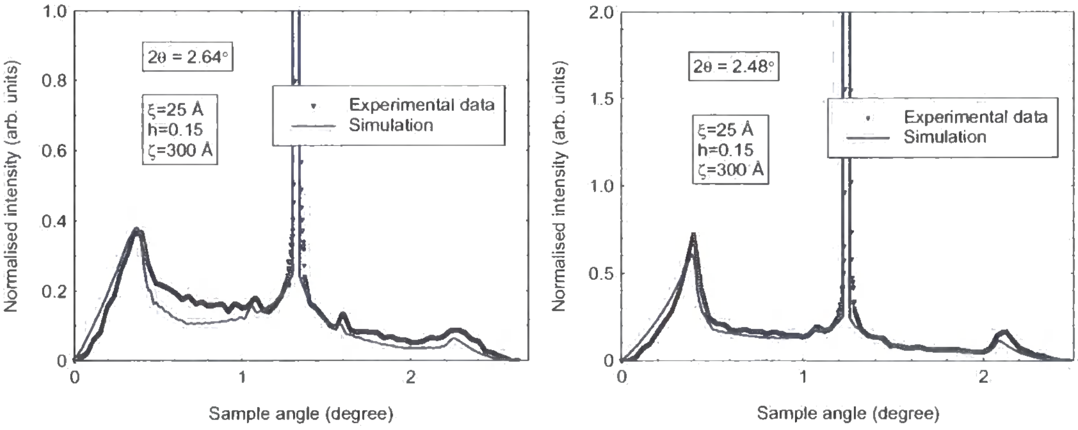

(a) **(b)**

Figure D.6 Transverse diffuse scans and simulations for the 16-bilayer sample, $\lambda = 1.3\text{Å}$.

D.2 VSM measurements

Samples were run on the laboratory Vibrating Sample Magnetometer (VSM) and can be seen in Figure D.7. Some samples exhibited PMA. From the area between the in-plane and out-of-plane M-H loops, K_{eff} was calculated for samples with 16 and 20 bilayers.

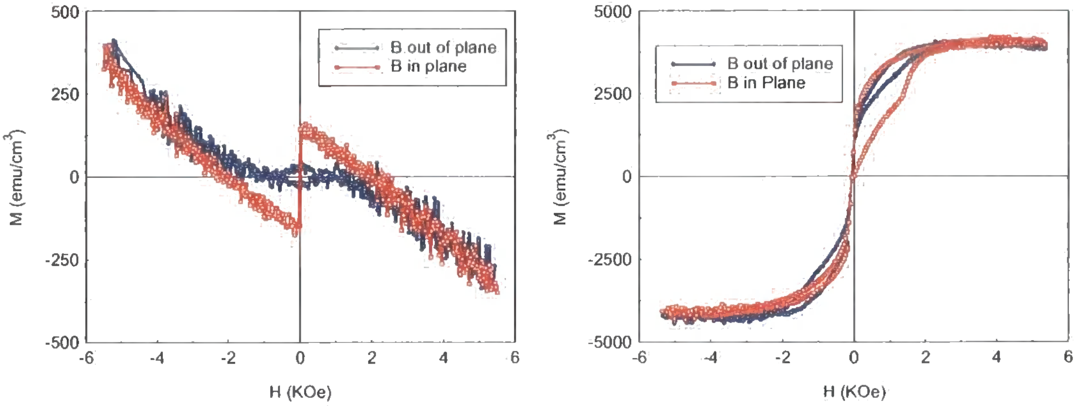

(a) **(b)**

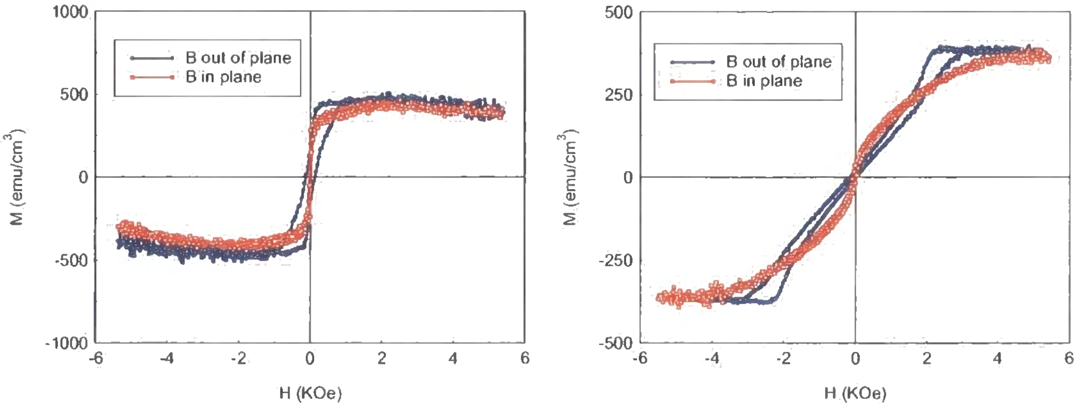

(c) **(d)**

Figure D.7 VSM magnetization loops for samples with **(a)** 2 bilayers, **(b)** 16 bilayers, **(c)** 20 bilayers, and **(d)** 30 bilayers.

Appendix E

Co/Pd Multilayers, Series 3 data sets

In this appendix, the x-ray data and magnetic measurements for the third series of samples will be presented. All samples were nominally:

$$SiO_2 / 30\ \text{Å Pd} / N \times \{14\ \text{Å Co} / 30\ \text{Å Pt}\} \quad \text{where } N = 2, 4, 6..., 30$$

E.1 X-ray experiments

E.1.1 GIXR results

A series of grazing incidence specular and off-specular x-ray scans along with simulations for these samples is shown in Figure E.1. These scans provide information concerning the development of the multilayer stack as the number of bilayers was increased from 2 to 30. In all cases excellent and unambiguous convergence was found, provided that the data range was sufficient to cover the first four Bragg peaks except for the samples with 26 and 30 bilayers. These data were taken on the GXR1 laboratory reflectometer.

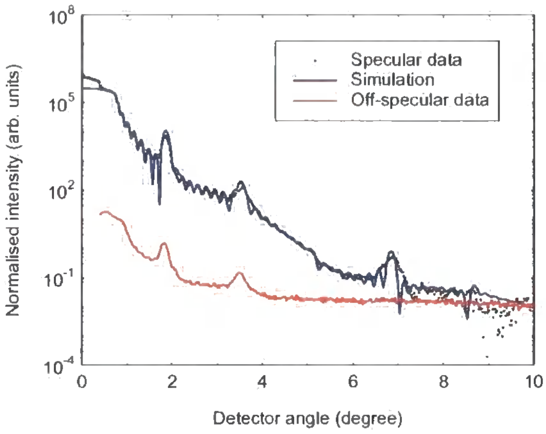

(a)

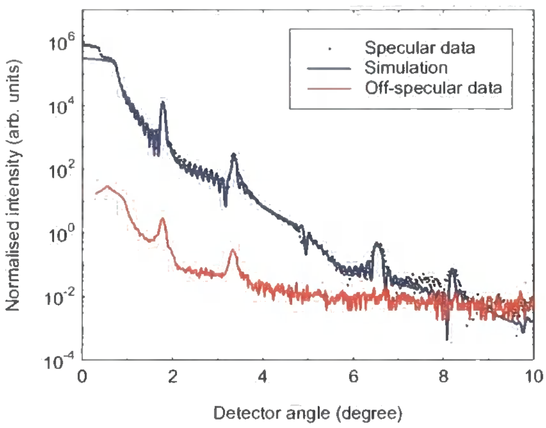

(b)

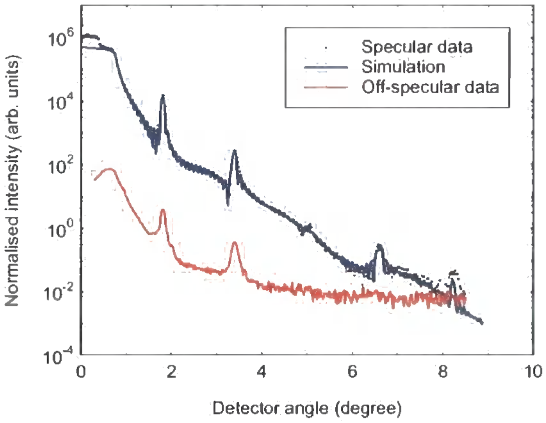

(c)

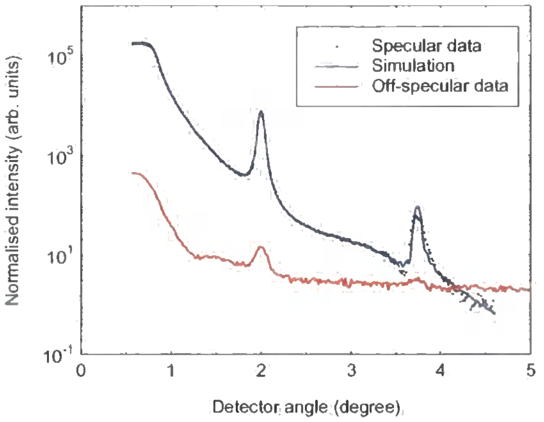

(d)

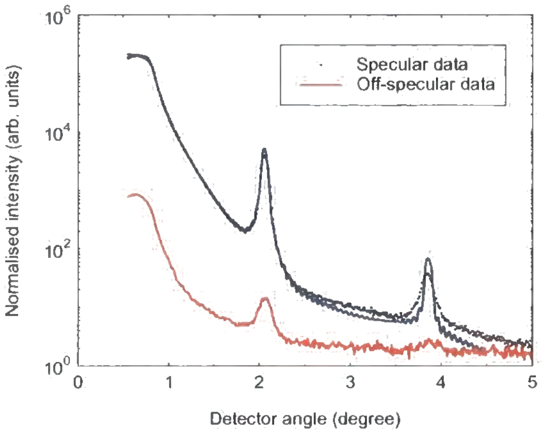

(e)

Figure E.1 Specular and Off-specular data and simulations for samples with **(a)** 8 bilayers, **(b)** 12 bilayers, **(c)** 16 bilayers, synchrotron data with λ = 1.3Å, **(d)** 26 bilayers, and **(e)** 30 bilayers laboratory data with λ = 1.393Å.

The off-specular Bragg peaks can be seen in all cases. By simulating the laboratory data, the interface parameters were found to be compatible with the model for the series 2 samples.

As can be seen in Fig. E.2(b), as the bilayer number is increased, the off-specular Bragg peak remains, indicating that out-of-plane correlation is retained within the bilayers. However, the off-specular Kiessig fringes disappear as the stack thickness increases, and the out-of-plane correlation between the interfaces at the substrate and cap is lost. Unlike the Co/Pt samples (chapter 7) and other series of Co/Pd multilayers, the position and spacing of the specular (Fig E.2(a)) and off-specular (Fig E.2(b)) Bragg peaks show that the bilayer thicknesses were close to nominal values for all samples of series 3.

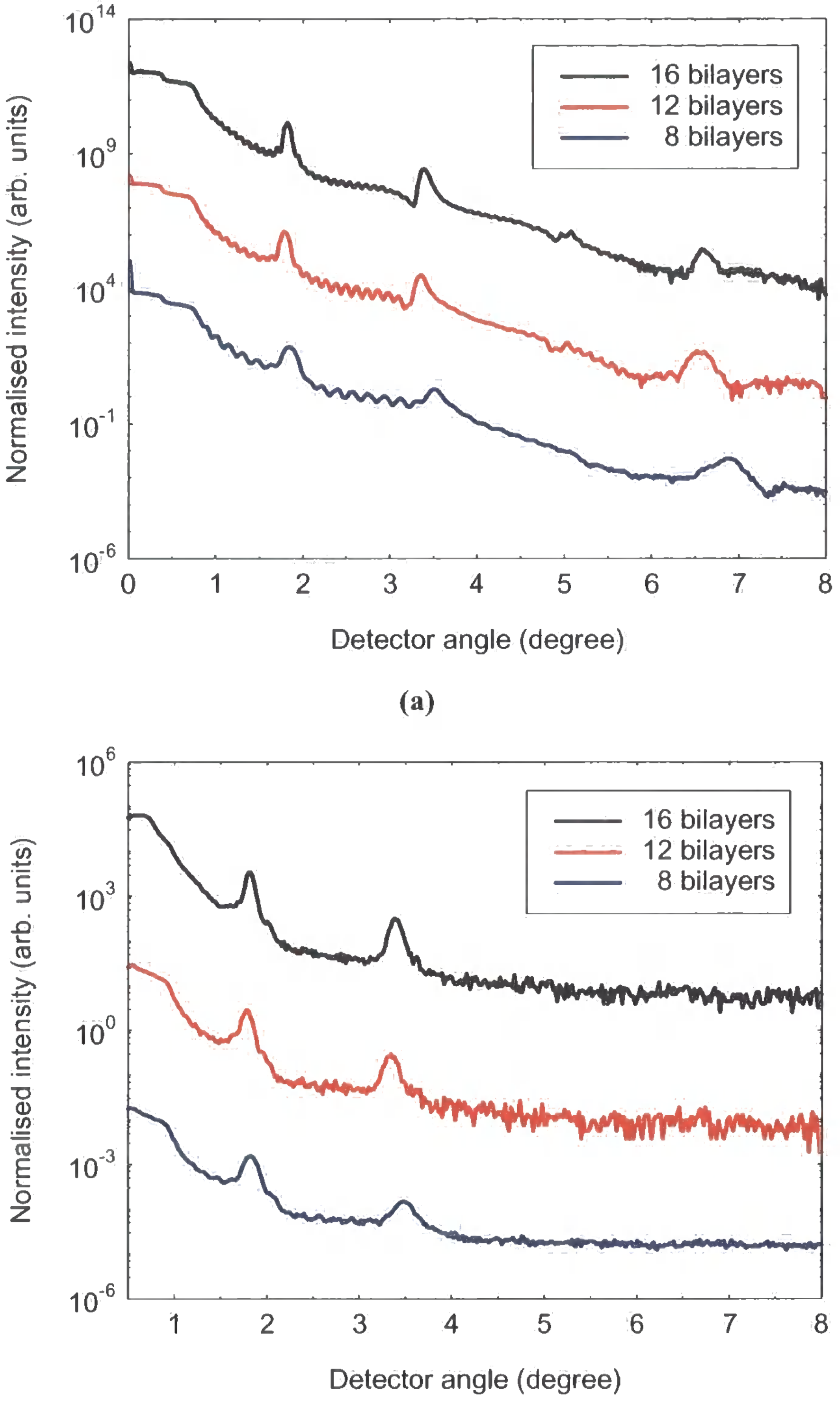

(a)

(b)

Figure E.2 (a) A series of Co/Pd Specular scans, λ = 1.3Å. **(b)** A series of Co/Pd Off-specular scans (sample off-set -0.1°, λ = 1.3Å).

Structural parameters were obtained by fitting the experimental data to simulations from a model structure. Values of thickness and interface width were first found by automatic refinement using the Bede MERCURY code for the specular data and these parameters then used to fit the diffuse scatter manually. After several attempts for each set of data, the model structure that led to the best fits for both specular and diffuse scatter data was determined and can be seen in Figure E.3.

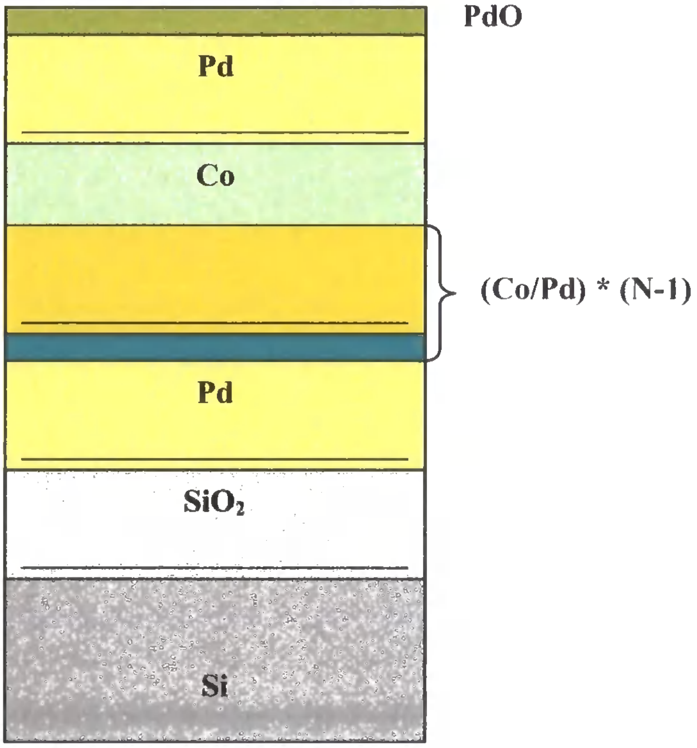

Figure E.3 The model structure used to fit specular and diffuse scatter data for samples.

E.1.2 GIXS results

Across the series of fifteen samples, extensive specular and transverse diffuse measurements were made. Through a combination of these scans, many aspects of the interface morphology in the multilayer structures could be determined. Two x-ray wavelengths were used, one on the laboratory GXR1, 1.393Å, and one on the station 2.3 at the SRS, 1.3Å. For each sample, at each wavelength, at least three transverse diffuse scans were taken, one or two at and one or two away from the Bragg condition. These scans are primarily sensitive to correlated and uncorrelated roughness respectively. The Bede REFS code (which was used to fit the transverse diffuse data), considers four different models for interfaces. As can be seen in Figures E.4 – E.7, satisfactory fits were achieved using a partially correlated roughness; model II.

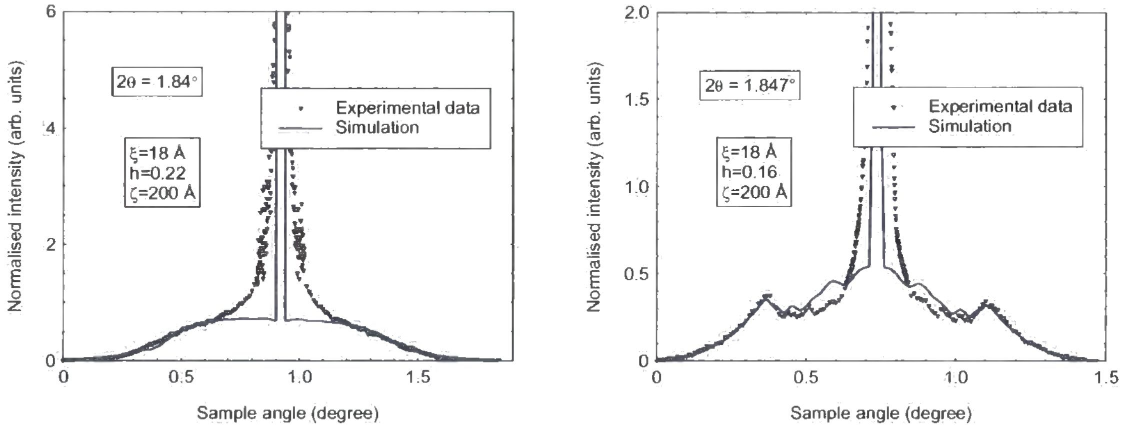

(a) **(b)**

Figure E.4 Transverse diffuse scans and simulations for the 8-bilayer sample, λ = 1.3Å.

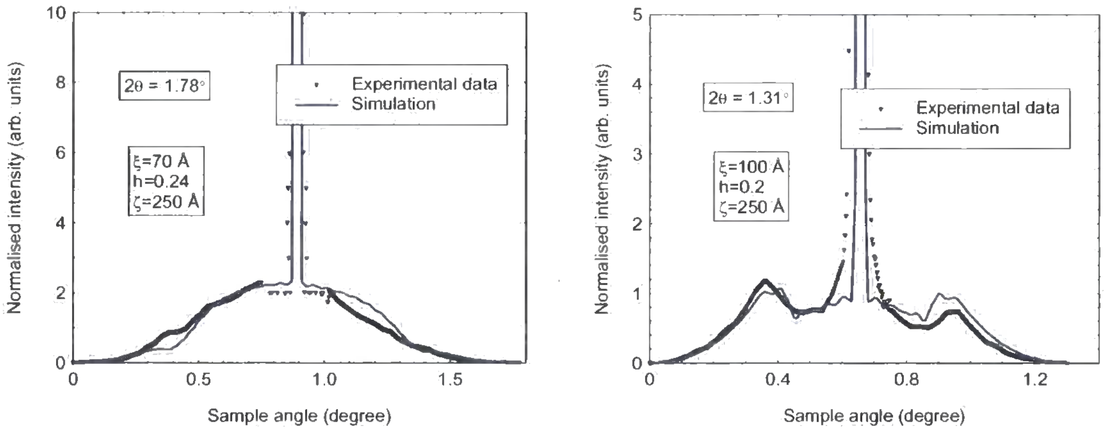

(a) **(b)**

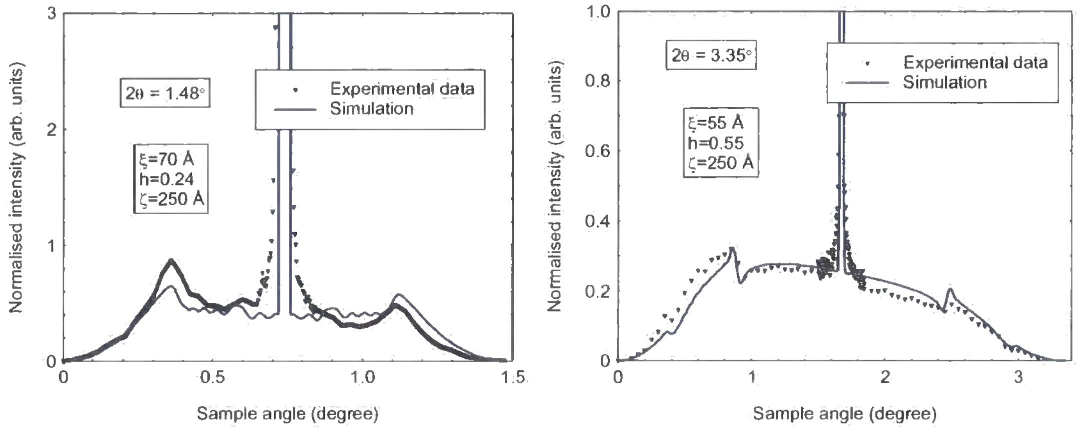

(c) **(d)**

Figure E.5 Transverse diffuse scans and simulations for the 12-bilayer sample, λ = 1.3Å.

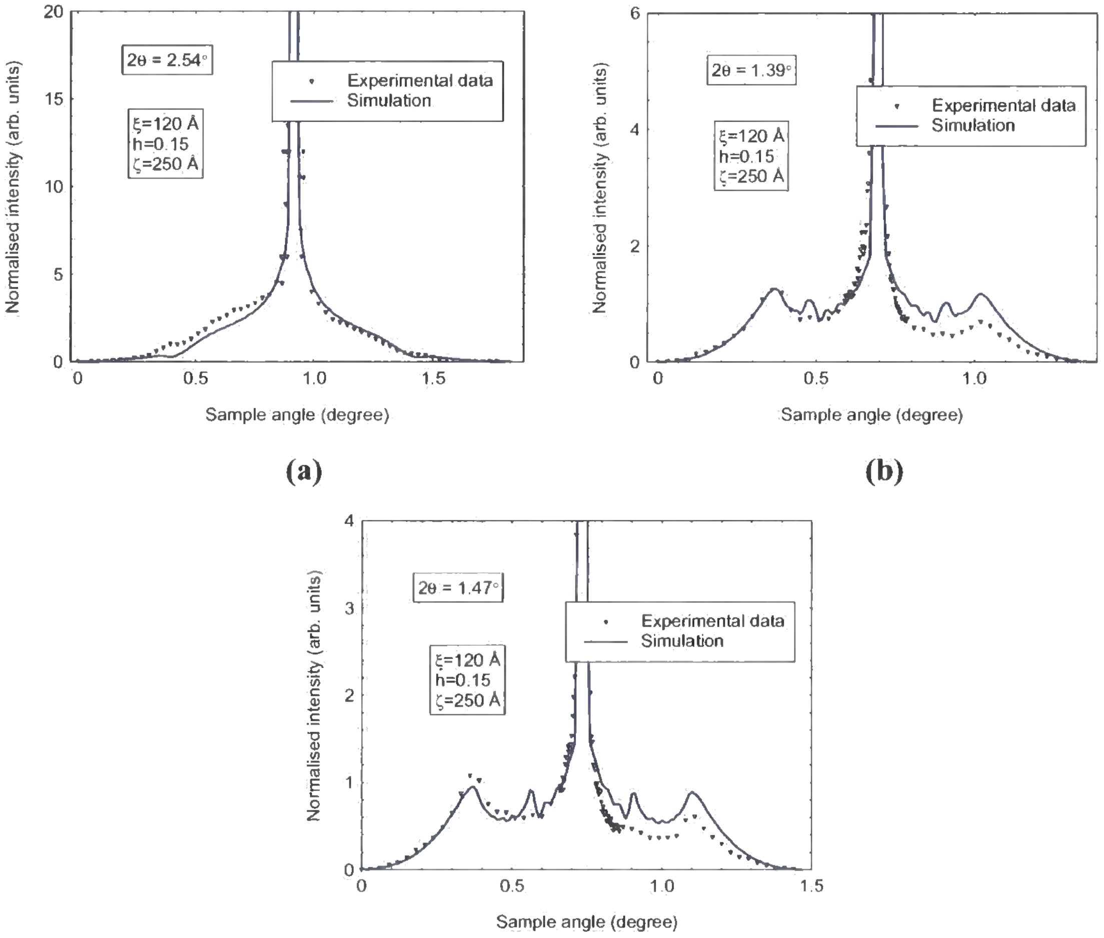

(a) **(b)**

(c)

Figure E.6 Transverse diffuse scans and simulations for the 16-bilayer sample, λ = 1.3Å.

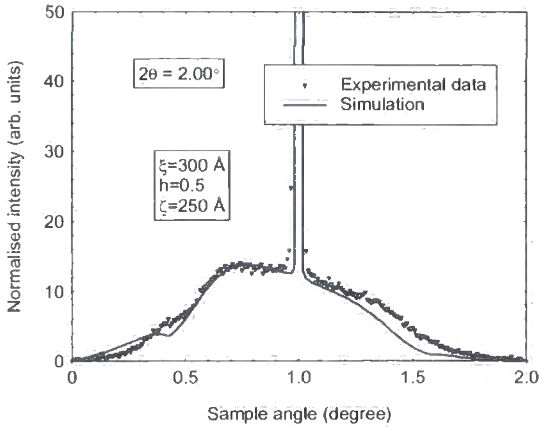

Figure E.7 Transverse diffuse scans and simulations for the 26-bilayer sample, λ = 1.393Å.

E.2 VSM measurements

Samples were run on the laboratory Vibrating Sample Magnetometer and can be seen in Figure E.8. All samples exhibited in-plane magnetization.

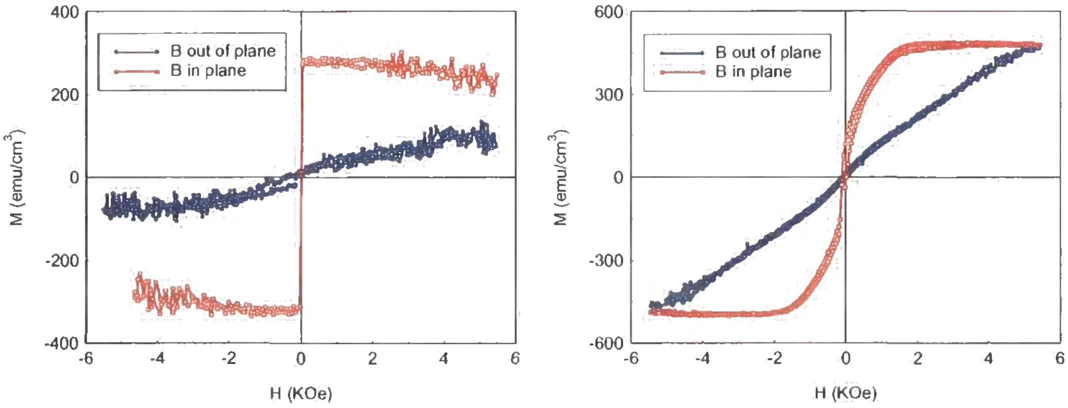

(a) **(b)**

Figure E.8 VSM magnetization loops for samples with **(a)** 6 bilayers, **(b)** 30 bilayers.

Appendix F

Co/Pd Multilayers, Series 4 data sets

In this appendix, the x-ray data and magnetic measurements for the third series of samples will be presented. All samples were nominally:

SiO_2 / 30 Å Pd / $N \times$ {3 Å Co / 26 Å Pt} where $N = 2, 4, 6..., 30$

F.1 X-ray experiments

F.1.1 GIXR Results

A series of grazing incidence specular and off-specular x-ray scans along with simulations for these samples is shown in Figure F.1. These scans provide information concerning the development of the multilayer stack as the number of bilayers was increased from 2 to 30.

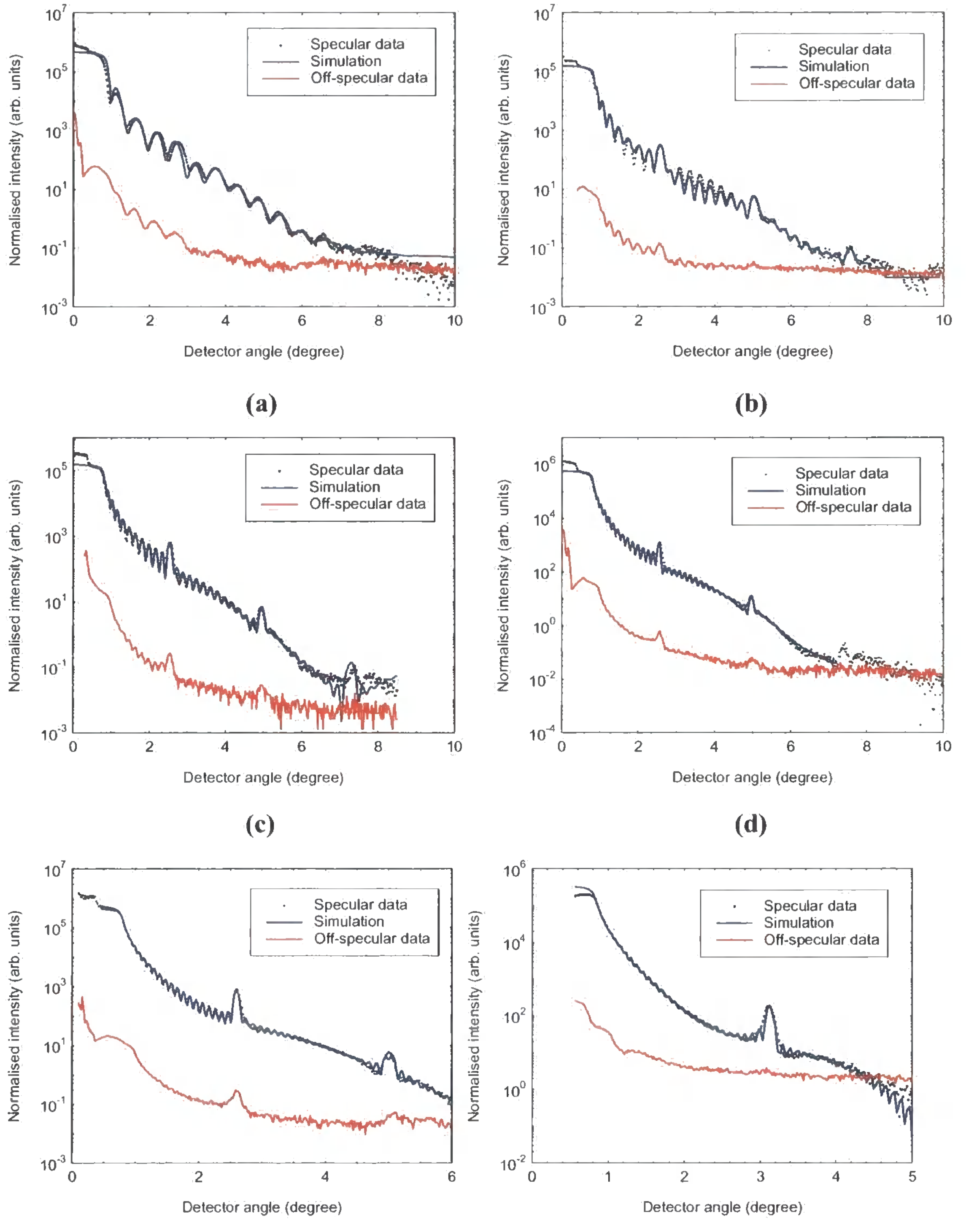

(a) **(b)**

(c) **(d)**

(e) **(f)**

Figure F.1 Specular and Off-specular data and simulations for samples with **(a)** 4 bilayers, **(b)** 8 bilayers, **(c)** 12 bilayers, **(d)** 16 bilayers, **(e)** 22 bilayers, synchrotron data with $\lambda = 1.3$Å, and **(f)** 30 bilayers laboratory data with $\lambda = 1.393$Å.

The off-specular Bragg peaks can be seen in all cases. By simulating the laboratory data, the interface parameters were found to be compatible with the model for the series 2 samples.

As can be seen in Fig. F.2(b), as the bilayer number is increased, the off-specular Bragg peak remains, indicating that out-of-plane correlation is retained within the bilayers. However, the off-specular Kiessig fringes disappear as the stack thickness increases, and the out-of-plane correlation between the interfaces at the substrate and cap is lost. The position and spacing of the specular (Fig F.2(a)) and off-specular (Fig F.2(b)) Bragg peaks show that the bilayer thicknesses were remain close to nominal values for all samples of series 4. The same effect was observed in series 3 of Co/Pd samples only.

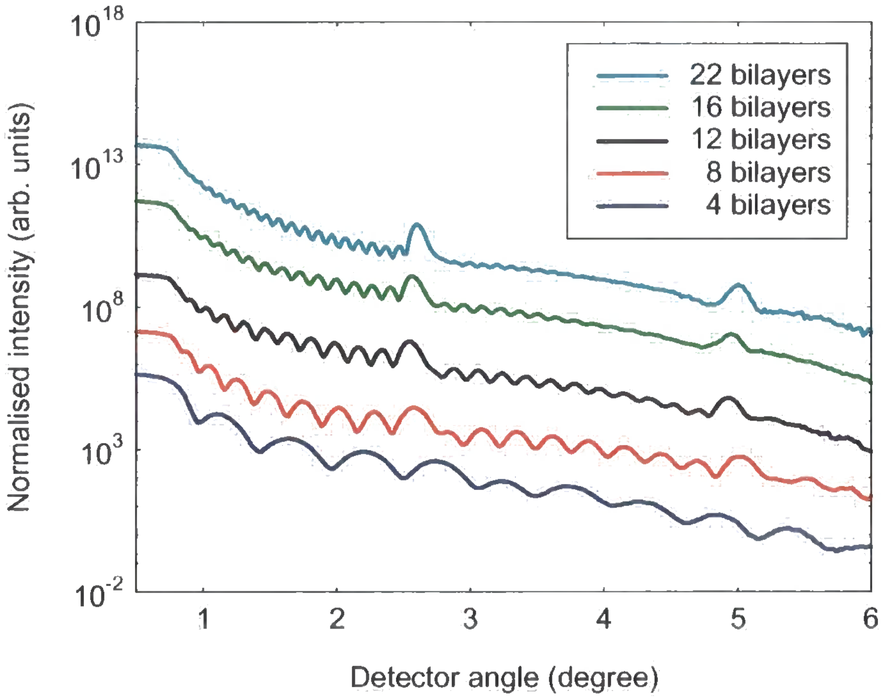

(a)

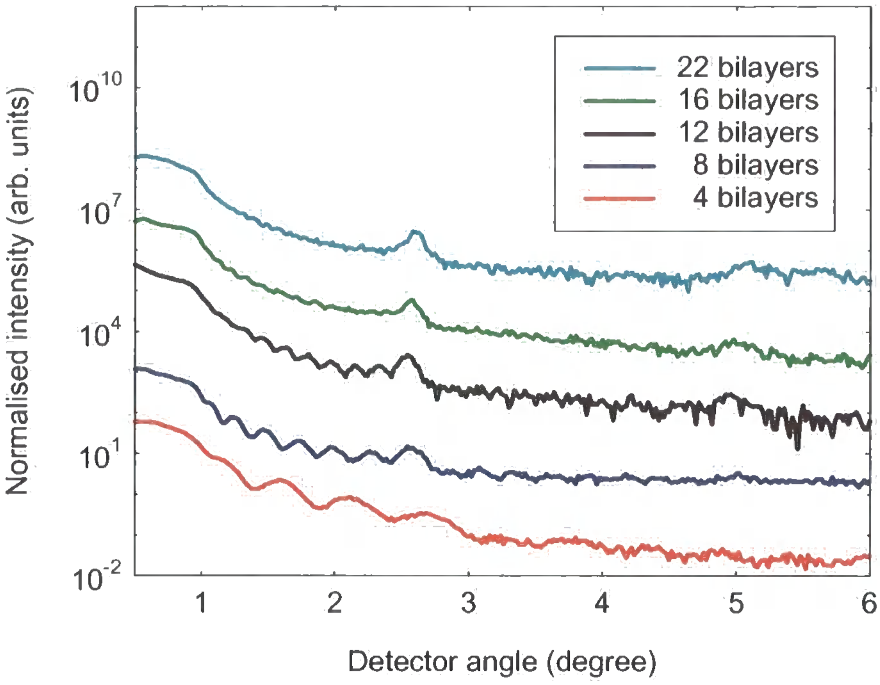

(b)

Figure F.2 (a) A series of Co/Pd Specular scans, λ = 1.3Å. **(b)** A series of Co/Pd Off-specular scans (sample off-set -0.1°, λ = 1.3Å).

Structural parameters were obtained by fitting the experimental data to simulations from a model structure. Values of thickness and interface width were first found by automatic refinement using the Bede MERCURY code for the specular data and these parameters then used to fit the diffuse scatter manually. After several attempts for each set of data, the model structure that led to the best fits for both specular and diffuse scatter data was determined and can be seen in Figure F.3.

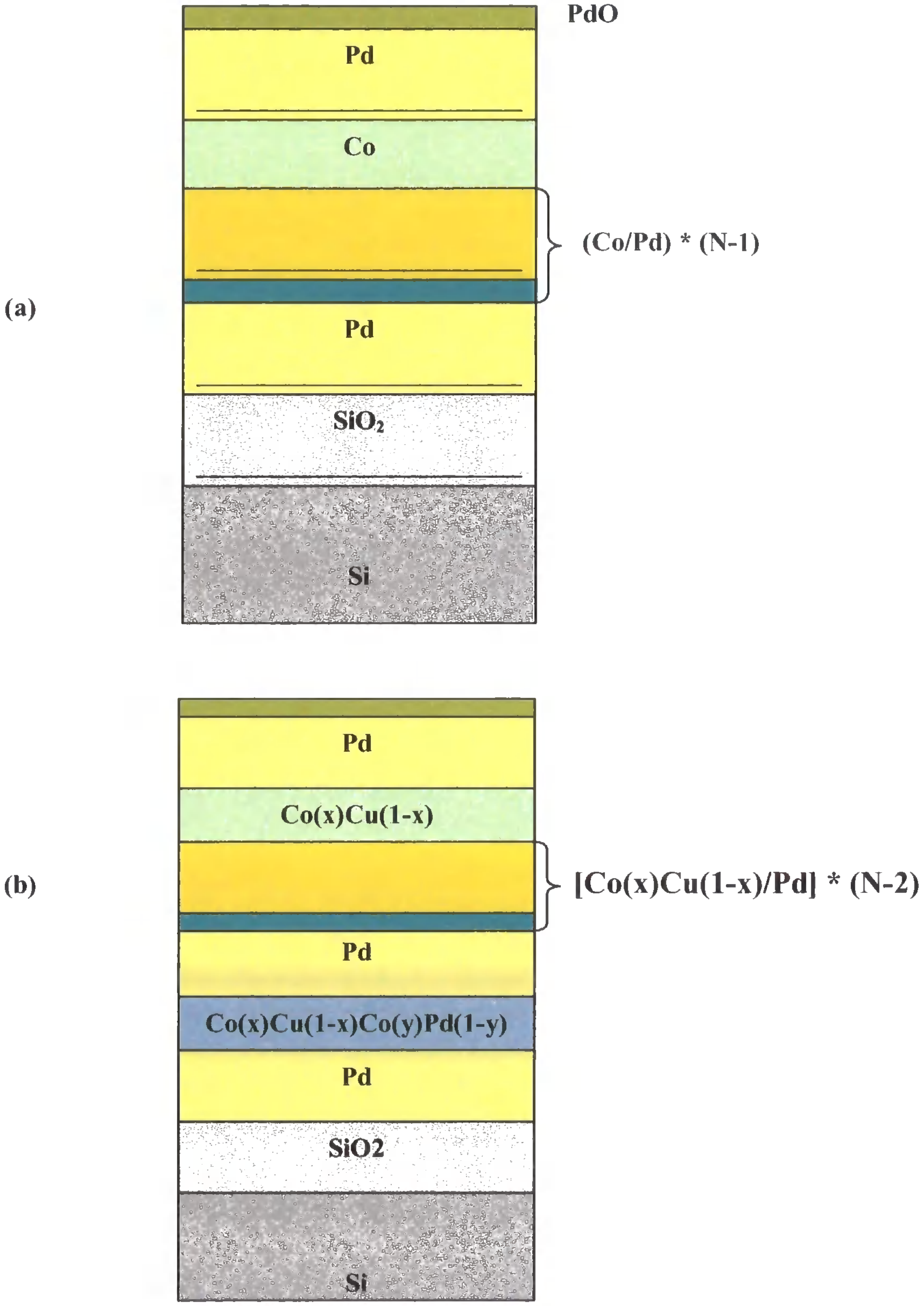

Figure F.3 The model structure used to fit specular and diffuse scatter data for samples with **(a)** $N < 20$, and **(b)** $N \geq 20$ with Cu contamination.

F.1.2 GIXS Results

Across the series of fifteen samples, extensive specular and transverse diffuse measurements were made. Through a combination of these scans, many aspects of the interface morphology in the multilayer structures could be determined. Two x-ray wavelengths were used, one on the laboratory GXR1, 1.393Å, and one on the station 2.3 at the SRS, 1.3Å. For each sample, at each wavelength, at least three transverse diffuse scans were taken, one or two at and one or two away from the Bragg condition. These scans are primarily sensitive to correlated and uncorrelated roughness respectively. The Bede REFS code (which was used to fit the transverse diffuse data), considers four different models for interfaces. GIXS data and simulations using a partially correlated roughness; model II can be seen in Figures F.4 – F.8.

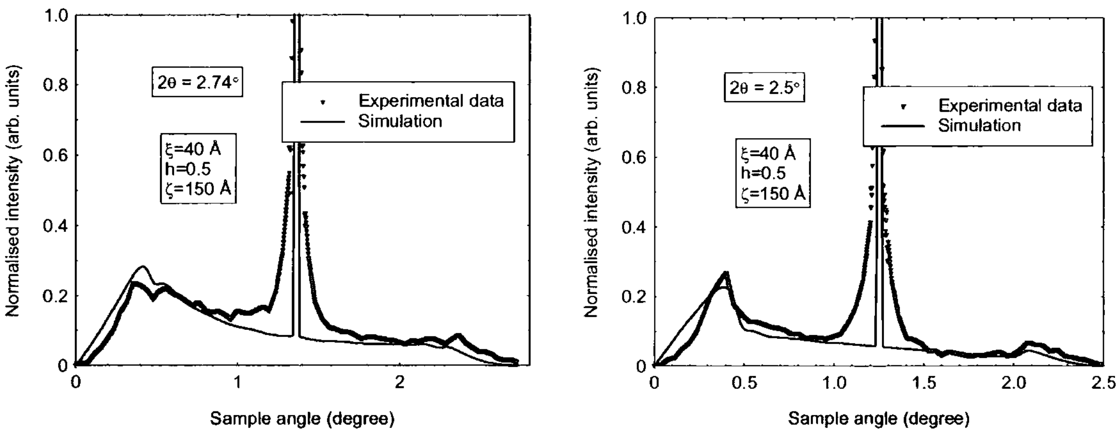

(a) (b)

Figure F.4 Transverse diffuse scans and simulations for the 4-bilayer sample, $\lambda = 1.3$Å.

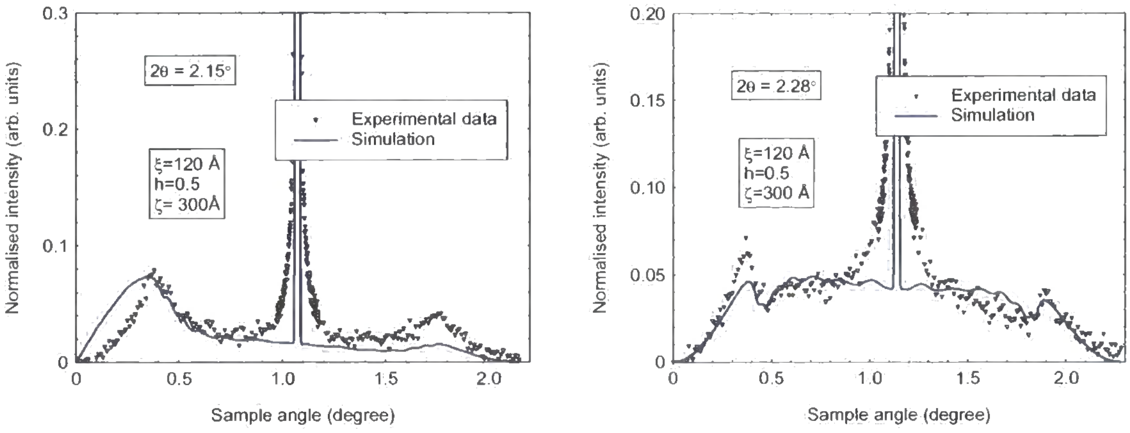

(a) **(b)**

Figure F.5 Transverse diffuse scans and simulations for the 8-bilayer sample, λ = 1.3Å.

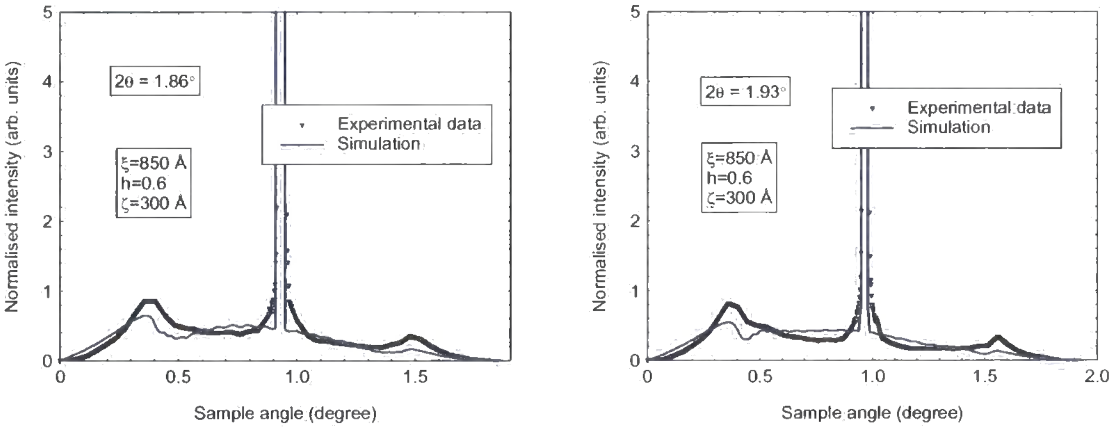

(a) **(b)**

Figure F.6 Transverse diffuse scans and simulations for the 16-bilayer sample, λ = 1.3Å.

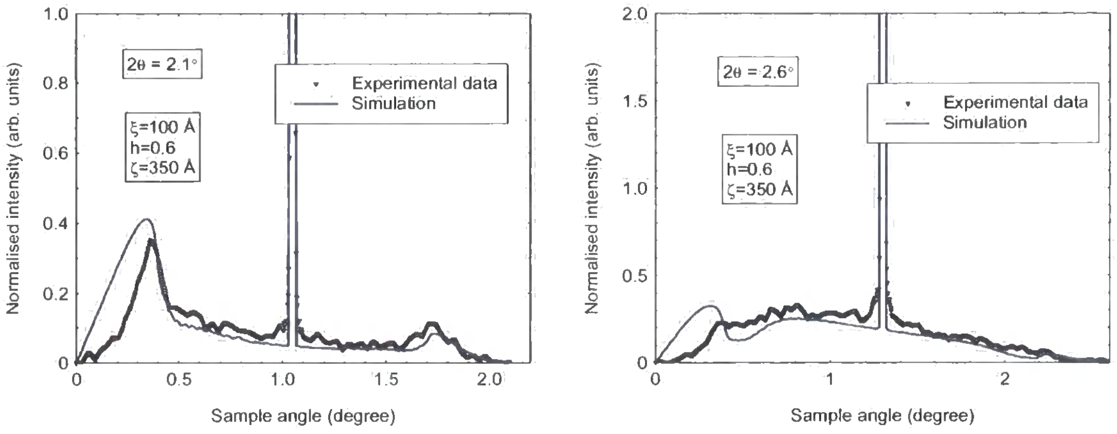

(a) **(b)**

Figure F.7 Transverse diffuse scans and simulations for the 22-bilayer sample, λ = 1.3Å.

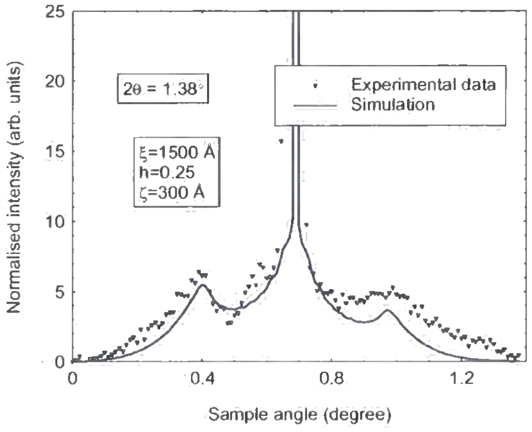

Figure F.8 Transverse diffuse scans and simulations for the 30-bilayer sample, λ = 1.393Å.

F.2 VSM measurements

Samples were run on the laboratory Vibrating Sample Magnetometer and can be seen in Figure F.9. All samples exhibited perpendicular magnetization.

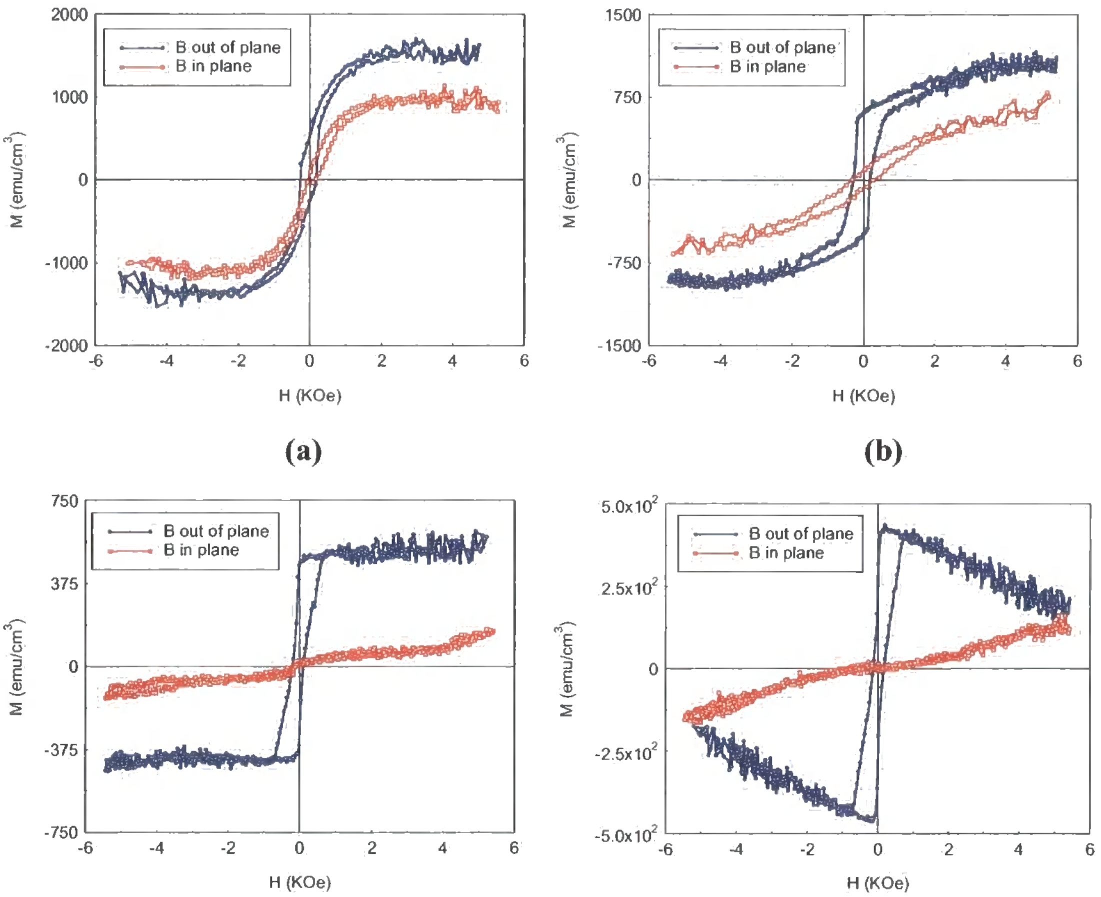

(a) (b)

(c) (d)

Figure F.9 VSM magnetization loops for samples with **(a)** 6 bilayers, **(b)** 20 bilayers, **(c)** 28 bilayers, and **(d)** 30 bilayers.

Appendix G

Evolution of the Interface Morphology

The evolution of the interface morphology during the growth of thin films and multilayers has a major impact on the overall magnetic and transport properties. In particular, the mechanism of roughness propagation from the substrate to the surface has been the focus of a number of experimental and theoretical studies. The model of Holý and Baumbach [1] assumes a conformal roughness component that propagates completely between interfaces, a separate component of uncorrelated roughness being added sequentially at successive interfaces. That of Spiller *et* al [2] assumes that roughness components with larger in-plane length scales propagate preferentially. Depending on the values of the various parameters, the overall roughness amplitude may increase or decrease with the number of repeats in a multilayer. The Ming model [3] assumes that the roughness is self-affine and that propagation does not depend on the in-plane length scale. The roughness propagation is characterised by a single out-of-plane correlation length ζ. Controlled ballistic deposition leads to a self-affine surface morphology whose scaling behaviour corresponds to the Kardar-Parisi-Zhang (KPZ) equation [4], which is one of the most general local models of growth:

$$\frac{\partial H(x,t)}{\partial t} = F + \nu \nabla^2 H(x,t) + \frac{\lambda}{2}\left[\nabla H(x,t)\right]^2 + \eta(x,t) \tag{G.1}$$

The variation of the local height of the surface $H(x,t)$ is basically a function of the local shape of the surface itself. Its time derivative depends mainly on the interfacial tension $\nu \nabla^2 H$ (which tends to smooth the interface, for $\nu > 0$) and on an uncorrelated noise term $\eta(x,t)$. The term $(\lambda/2)\left[\nabla H(x,t)\right]^2$ is due to the assumption that the growth has a component normal to the local surface and F is the flux of atoms deposited on the substrate.

Most important for the characterization of the interfacial morphology are the roughness exponents that are obtained from this model. The height difference function increases as a function of in-plane length according to $\left\langle \left[H(R) - H(0)\right]^2 \right\rangle_R \propto R^{2\alpha}$, until it saturates ($\left\langle \left[H(R)\right]^2 \right\rangle = \sigma^2$, when $R \to \infty$, where σ is the maximum interfacial width) for $R \sim \xi$, (where ξ, is the in-plane correlation length) [5]. An analogous scaling relation is obtained for the height–height correlation function $\left\langle H(R)H(0) \right\rangle$ since:

$$\left\langle H(R)H(0) \right\rangle = \sigma^2 - \left\langle \left[H(R) - H(0)\right]^2 \right\rangle / 2 \tag{G.2}$$

For partially correlated interfaces, $R < \xi$:

$$\left\langle H(R)H(0) \right\rangle = \sigma^2 - AR^{2\alpha} \tag{G.3}$$

And for the case of uncorrelated roughness, $R >> \xi$:

$$\langle H(R)H(0)\rangle \rightarrow 0 \tag{G.4}$$

The maximum interfacial width increases as a function of growth time according to $\sigma(t) \propto t^{\beta}$ and the in-plane correlation (cut-off) length increases following $\xi(t) \propto t^{1/z}$ ($\alpha, \beta, and\ z$ define as roughness components with $z = \alpha / \beta$ and for the KPZ equation: $\alpha + z = 2.0$) [6]. Since the time evolution of $\sigma(t)$ and $\xi(t)$ may not be accessible, the dynamic exponent z may be alternatively obtained from the dependence of the saturation time as a function of roughness feature size $t_{sat}(R)$. $t_{sat}(R)$ is the time taken for a feature of lateral size R to disappear during the growth of the thin film. Intuitively one may expect smaller features to be less replicated than larger ones. Very large features are almost perfectly replicated from layer to layer. The scaling behavior of the saturation time as a function of size R also depends on the roughness exponent z, following $t_{sat}(R) \propto R^{z}$ [6]. If the film is grown at a constant deposition rate, the thickness of the thin film is directly proportional to the deposition time. t_{sat} can therefore be translated into a growth (out-of-plane) correlation length $\zeta(R)$ which also scales as $\zeta(R) \propto R^{z}$ [7].

The choice of a particular model function for the fit of the in-plane diffuse profile is not arbitrary. Several model functions that incorporate the expected asymptotic behavior of $\langle H(R)H(0)\rangle$ have been proposed [8]. The average in-plane correlation function, $\langle H(R)H(0)\rangle$ can be written as [8]:

$$\langle H(R)H(0)\rangle = \sigma^{2}\left\{1-\left[1-e^{-(R/\xi)^{2}}\right]^{\alpha}\right\} \tag{G.5}$$

Paniago *et al* modelled the diffuse profile of a series of Fe/Au multilayers by fitting of the Fourier transform of this model function and observed a decrease in the interfacial slope (simulations of surface growth starting from a rough surface, showed the action of the surface tension in smoothing the growth front) [9]. By comparing the theoretical predictions of KPZ equation and AFM (Atomic-force microscopy) measurements, they showed that sputtered Fe/Au multilayers followed the KPZ equation for surface growth.

REFERENCES

[1] V. Holý and T. Baumbach, *Phys. Rev. B*, **49 (15)**, 10668-10676 (1994).

[2] E. Spiller, D. Stearns, and M. Krumrey, *J. Appl. Phys.*, **74 (1)**, 107-118 (1993).

[3] Z. H. Ming, A. Krol, Y. L. Soo, Y. H. Kao, J. S. Park, and K. L. Wang, *Phys. Rev. B*, **47 (24)**, 16373-16381 (1993).

[4] M. Kardar, G. Parisi, and Y. C. Zhang, *Phys. Rev. Lett.*, **56 (9)**, 889-892 (1986).

[5] S. K. Sinha, E. B. Sirota, S. Garoff, and H. B. Stanley, *Phys. Rev. B*, **38 (4)**, 2297-2311 (1988).

[6] *Fractal Concepts in Surface Growth*, A.-L. Barabasi and H. E. Stanley, Cambrige University Press (1995).

[7] T. Salditt, D. Lott, T. H. Metzger, J. Peisl, G. Vignaud, P. Hoghoj, O. Scharpf, P. Hinze, and R. Lauer, *Phys. Rev. B*, **54 (8)**, 5860-5872 (1996).

[8] G. Palasantzas and J. Krim, *Phys. Rev. B*, **48 (5)**, 2873-2877 (1993).

[9] R. Paniago, P. C. Chow, R. Forrest, and S. C. Moss, *Physica B*, **248** , 39-47 (1998).